IMAGING PHOSPHOLIPASE D ACTIVITIES IN LIVE CELLS WITH A REAL-TIME, BIOORTHOGONAL APPROACH AND ITS APPLICATIONS TO UNDERSTAND CELL SIGNALING AND PHOSPHOLIPID TRAFFICKING

A Dissertation

Presented to the Faculty of the Graduate School

of Cornell University

In Partial Fulfillment of the Requirements for the Degree of

Doctor of Philosophy

by

Dongjun Liang

December 2021

IMAGING PHOSPHOLIPASE D ACTIVITIES IN LIVE CELLS WITH A REAL-TIME, BIOORTHOGONAL APPROACH AND ITS APPLICATIONS TO UNDERSTAND CELL SIGNALING AND PHOSPHOLIPID TRAFFICKING

Dongjun Liang, Ph. D.

Cornell University 2021

Localized production of signaling agents is an essential feature for living cells. Many of these signaling molecules are lipid entities. However, due to their hydrophobic nature and highly diverse cellular functions, certain potent, low-abundance lipids that act as signaling agents remain understudied with traditional biochemical techniques. Thus, the advancement of modern chemical biology tools represents a promising perspective to tackle these complex biological problems. Chapter 1 summarizes the challenges and recent advancement to study phospholipid signaling and discusses its relevance towards cell signaling and lipid trafficking.

In Chapter 2, the author discusses the design, synthesis and characterization of a novel, bioorthogonal chemistry-based strategy, termed RT-IMPACT, to image the biosynthesis of a specific signaling lipid called phosphatidic acid (PA). With fast chemical kinetics and optimal enzyme specificity, PA produced by phospholipase D (PLD) enzyme activity can be visualized in living cells in real-time. The author further demonstrates that RT-IMPACT is capable of accurately reporting subcellular locations of PA production in response to different upstream stimuli.

In Chapter 3, the author applies RT-IMPACT tools to investigate PTHR signaling that are previously underexplored. The author shows that PLD activation is specifically downstream of PTHR-G_q protein signaling. Moreover, the G_q signaling pathway, in stark contrast to the G_s pathway, is transient and localized on the plasma membrane as revealed by time-resolved imaging of PLD activities. Lastly, through inhibition of endocytic pathways, a competitive relationship between the G_q and G_s pathway is revealed.

In Chapter 4, the author characterizes a family of lipid transfer proteins—ESyts—that are responsible for trafficking of unnatural fluorescent lipids from PM to ER. A positive correlation between the expression levels of ESyts and trafficking rates from PM to ER is established. Next, through protein engineering, lipid transfer activities of ESyts are shown to be directly responsible for removal of unnatural fluorescent lipids from the PM.

In the final chapter, the author summarizes the major findings and significance of this work towards understanding of physiologically relevant pathways. Several potential future directions, including screening for potential upstream stimuli and identifying other lipid transfer proteins, are briefly described.

BIOGRAPHICAL SKETCH

Dongjun Liang was born and raised in Tianjin, a harbor city in northeast China blended with modern architectures and ancient lifestyles. During his childhood, Dongjun was attracted to learn and play Chinese Chess, which constantly demands the best possible solutions out of ever-changing situations. Since middle school, he was fascinated by science subjects, especially chemistry, where starting molecules break apart and reassemble into new arrangements. For his undergraduate studies, Dongjun was determined to reach the farthest possible school within his capabilities and arrived at Hong Kong Polytechnic University to study chemistry as his major. Throughout his college years, he fell in deeper love with the beauty of organic chemistry and how physiologically active medicines can be designed and synthesized, mimicking the power of nature. For his undergraduate thesis research, he conducted inorganic synthesis and photophysical characterizations of novel lanthanide-ligand complexes with potential biological applications under the mentorship of Prof. Ga-Lai Law. He then extended his reach towards understanding physiologically relevant cellular processes with chemical probes by joining Prof. Jeremy Baskin's lab at Cornell University. There, he contributed his chemical expertise towards understanding of elusive lipid signaling pathways, which traditional biochemistry fail to decipher. Thanks to the resourceful laboratory environment and supportive mentorship by his thesis committee, especially Jeremy, Dongjun is now a step closer towards searching for the best possible way to visualize lipid signaling, as well as the ultimate meaning of life. After graduation from Cornell University, Dongjun will join the workspace of Process Development Scientist at a major pharmaceutical company to learn about protein production and technology transfer from discoveries in life sciences to serving the people in need.

Dedicated to my family, my mentors, everyone who has helped me along the way, and Yimeng, who shed light into my life and brought about my best possible self.

ACKNOWLEDGMENTS

I am deeply grateful to my parents and grandparents, who gave me the best possible support that they could ever give throughout all stages of my life. They have been my harbor when I am down, my lighthouse to guide me forward. They were my primary role models for shaping a healthy outlook of values in life.

I am also greatly indebted to my elementary school teacher Mrs. Jinzhi Zhao, for establishing an everlasting figure of positivity and energy in my heart. I would also thank my middle school teachers Rong Lv and Gang Huang, and my high school teachers Zhengxue Cai, Ting Liu, Yongxin Teng, Ran Li, Zuwang Zheng, Mengying Liu and Lianchun Jiang for shaping my interests in learning science and English. They have been instrumental for my smooth transitions in my early career of science in an international environment.

I am also immensely grateful towards the faculty members of Hong Kong Polytechnic University, especially Prof. Wing-yiu Yu, Prof. Fuk-yee Kwong and Prof. Ga-lai Law for their diligent teaching efforts, career guidance and support throughout my undergraduate studies.

Looking back, I felt extremely fortunate to have joined the lab of Prof. Jeremy Baskin as the nascent lab gradually took shape. I was nurtured with all essential aspects of success in graduate school: hands-on training from Jeremy's direct mentorship, resourceful laboratory environment at the Weill Institute, and constructive relationships with fellow graduate researchers in the lab. The transition from chemistry to biology was never easy, but his constant support, gentle attitude coupled with comprehensive scientific knowledge has been the vital catalyst to this process. On the same note, I would also express my gratitude towards my

committee members Prof. Hening Lin and Prof. Frank Schroeder, for their helpful advice throughout my graduate research.

Furthermore, I am honored to be accompanied by talented fellow undergraduate, graduate and postdoctoral researchers throughout the years. I could not have accomplished my doctoral research without the help of Kane Wu, a talented undergraduate with whom I worked together closely; Reika Tei, who is the most versatile person I have met and good at numerous advanced molecular biology tools; Dr. Tim Bumpus and Dr. Jessica Daughtry, who are senior graduate students that are experts of synthetic chemistry; Dr. Adnan Shami Shah and Dr. Alex Batrouni, who constantly provide insightful advice for my experiments; Weizhi Yu, Xiaofu Cao, Dylan Chiu, Dr. Hongyan Sun and Dr. Brittany White, who contributed to critical evaluation of my research from different perspectives. I am especially impressed by their scientific acumen, growth mindset, and can-do attitude towards research. I am optimistic that they will succeed in their areas of research or other endeavors in the future.

Last but not least, I can never express enough gratitude towards my partner, Yimeng Sun, for her unconditional support during the pandemic lockdown and her soothing company as we treaded through hardships together.

TABLE OF CONTENTS

CHAPTER 1: Introduction

Challenges in studying phosphatidic acid produced by phospholipase D enzymatic activity[1]

Lipids are fascinating, structurally diverse, and vitally important biomolecules. They comprise the key membrane barriers between cells and the surrounding environment, serve as primary energy stores, and play numerous signaling roles. Despite this tremendous physiological importance, lipids have proven exceptionally challenging to study due to their redundant biosynthetic pathways, their nature as non-genetically encoded metabolites, and their immiscibility with aqueous environments [1]. In addition to highly abundant lipids such as cholesterol, phosphatidylcholine, and sphingomyelin, which are essential for membrane structure and cellular homeostasis, cells generate a variety of short-lived and/or low-abundance lipid second messengers in a spatiotemporally controlled manner, which precisely intersect and interact with the cell's signaling cascades [2,3].

Among the wide spectrum of signaling lipids, phosphatidic acid (PA) is a pleiotropic lipid second messenger that elicits a variety of changes in cell behaviors. Aberrant PA-dependent signaling has been linked to several pathological conditions, including various types of cancers [4,5]. A full understanding of the precise physiological effects of localized PA production requires a robust set of methods for visualizing and perturbing PA biosynthesis. Despite the widespread and sustained interest in the biology of PA, there remain a number of

[1] A portion of this section is currently published as a book chapter by Timothy W. Bumpus, Dongjun Liang, and Jeremy M. Baskin in *Methods in Enzymology*.

challenges associated with studying this lipid, which can be produced by three distinct biosynthetic enzyme families: lysophosphatidic acid acyltransferases, diacylglycerol kinases, and phospholipase Ds (PLD) (Fig. 1.1) [6,7]. First, affinity-based biosensors for PA exhibit only moderate specificity and frequently rely on coincidence detection of other lipids or proteins within the membrane [8]. Critically, even in an idealized form, biosensors cannot differentiate newly synthesized PA from the total pool, nor can they distinguish between pools of PA generated by each of the three biosynthetic pathways [1]. Second, whereas fluorescently tagging specific PA-producing enzymes may mitigate the aforementioned challenges, this approach fails to reveal the active subset of enzymes, many of which exhibit dynamic localizations after stimulation [9].

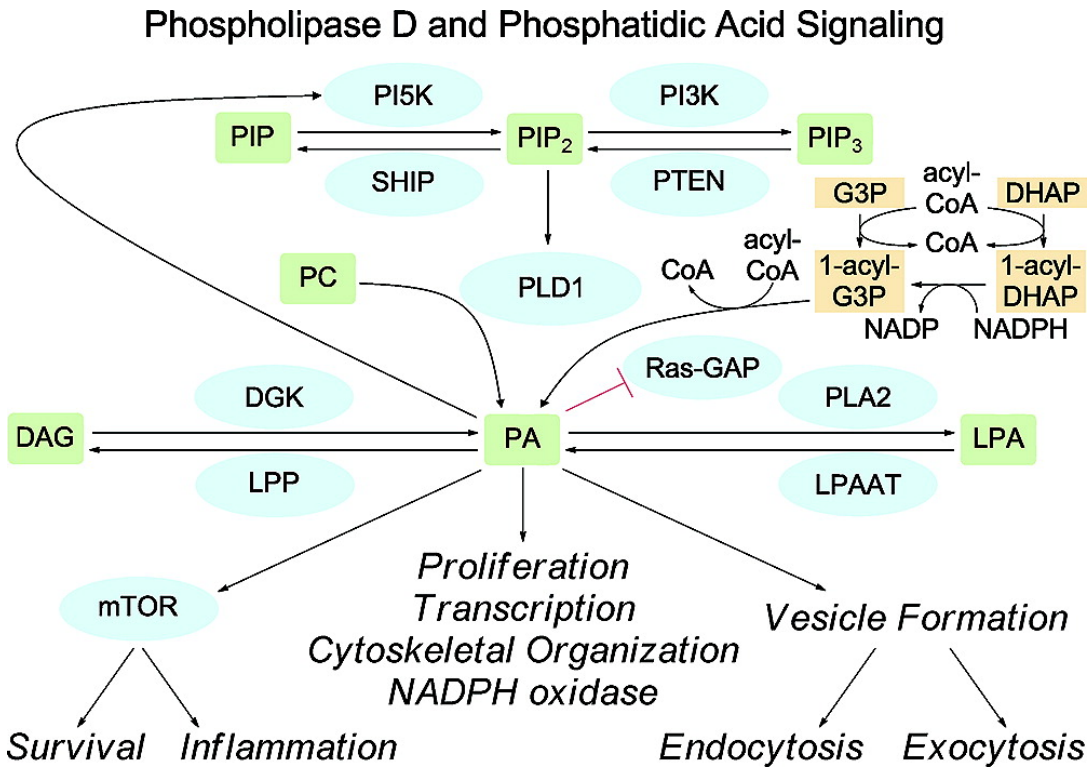

Figure 1.1: A scheme of major biosynthetic pathways of phosphatidic acid (PA) and several the signaling functions mediated by PA. Reproduced from [6].

***Recent advances of imaging phospholipase D activities with clickable alcohols in live cells*[2]**

To address these challenges, we sought to develop tools that would enable visualization and quantification of PA production by a specific pathway. We focused our efforts on PA generated by PLD enzymes, which are important in both physiological and pathological cell signaling [5]. Due to the proliferating role of PA signaling in promoting cell migration and survival (Fig. 1.2), elevated expression and activities of PLD enzymes are frequently associated with various types of cancer, including breast [10], kidney [11], brain [12,13] and colon cancer [14].

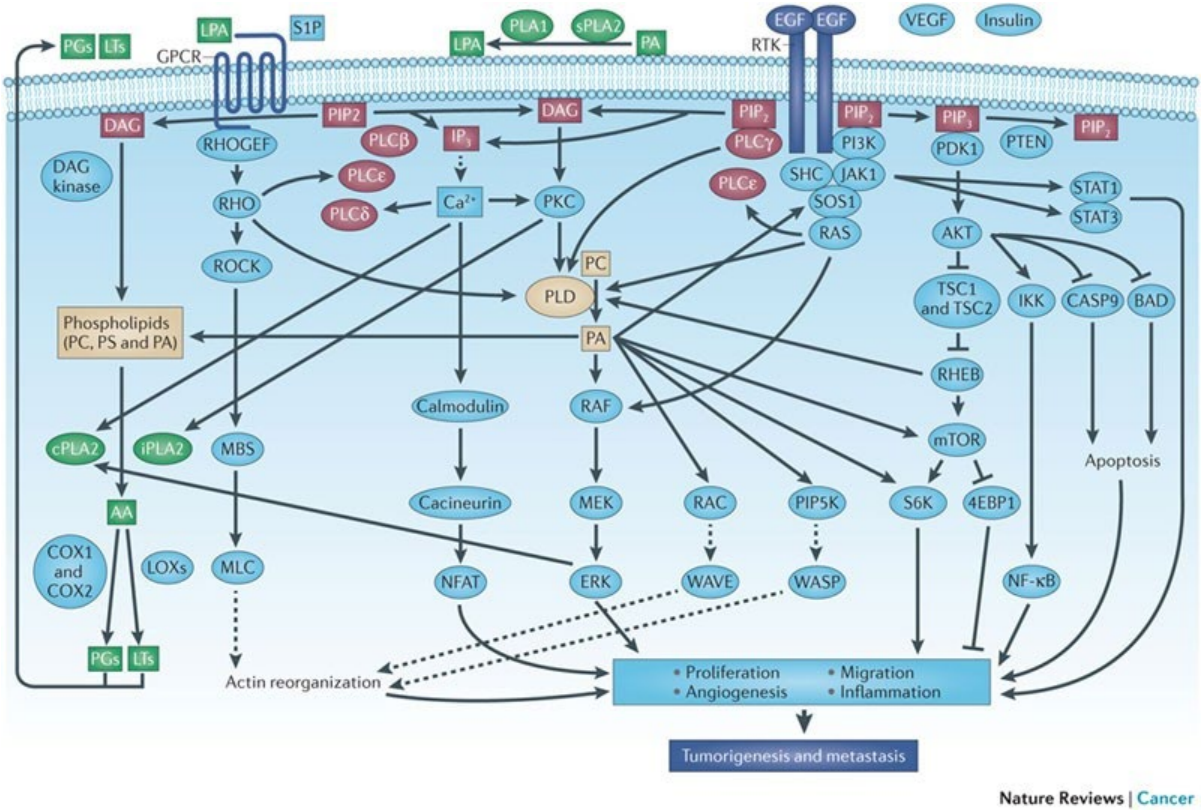

[2] A portion of this section is currently published as a book chapter by Timothy W. Bumpus, Dongjun Liang, and Jeremy M. Baskin in *Methods in Enzymology*.

Figure 1.2: An overview of phospholipase signaling networks and pathways. Reproduced from [15]. A suite of primary messengers bind to and activate cell-surface receptors, such as families of receptor tyrosine kinases (RTKs) and G protein-coupled receptors (GPCRs).

PLDs generate PA by the hydrolysis of phosphatidylcholine, the most abundant phospholipid in cellular membranes, upon activation by several upstream factors, including many families of cell-surface receptors and intracellular GTPases and kinases [6,16,17]. Classic biochemical assays for PLD activity rely on a second reaction that PLDs can catalyze, transphosphatidylation, wherein the water molecule that performs hydrolysis is replaced with an exogenous primary alcohol, enabling PLD-mediated generation of phosphatidyl alcohol lipids, whose abundance reports directly on PLD activity [18,19]. Typically, these transphosphatidylation-based methods use radio- or stable isotope-labeling, followed by bulk biochemical measurements (e.g., thin layer chromatography or mass spectrometry) [6,18,19]. Thus, whereas the phosphatidyl alcohols are generated in cells at precise subcellular membrane locations where endogenous PLDs are activated, this spatial information is lost during sample workup steps.

We aimed to develop a method based on this ability of PLDs to perform transphosphatidylation reactions that would preserve and reveal the localizations of PLD activity, at the single-cell and even subcellular levels. To accomplish this goal, we devised a two-step labeling strategy termed IMPACT (Imaging Phospholipase D Activity with Clickable Alcohols via Transphosphatidylation) [20–23]. Our method uses a functionalized primary alcohol for the transphosphatidylation reaction that enables us to subsequently install a fluorescent tag or other detection reagent, via a click chemistry reaction, to the phosphatidyl alcohol reporter,

within intact cells. Thus, the two-step IMPACT protocol enables the visualization of membranes containing active PLD enzymes within intact and—in many variants of the protocol—live cells.

Here, we describe two versions of IMPACT that we have optimized for different applications for quantifying and imaging PLD activity (Fig. 1.3). First, we describe our original version of IMPACT, using azide-containing alcohols for transphosphatidylation and click chemistry tagging via a [3 + 2] strain-promoted azide-alkyne cycloaddition (SPAAC) reaction. This reaction happens spontaneously in aqueous media and, coupled with desirable cell permeability of the probes, is ideal for measuring PLD activity at the bulk population or the single-cell levels (Fig. 1.3B, top). Second, to accurately visualize PLD activity at the subcellular, organelle-membrane level in a time-resolved manner, we describe a real-time variant of IMPACT (RT-IMPACT) that utilizes inverse electron-demand Diels-Alder (IEDDA) reaction, or commonly known as tetrazine ligation. The tetrazine ligation has virtues of fast chemical kinetics as well as fluorogenic responses, which results in a fluorescence 'turn-on' of the non-fluorescent tetrazine after the reaction, enabling real-time imaging of PLD activities. Specifically, the RT-IMPACT uses a trans-5-oxocene (oxoTCO) alcohol as the transphosphatidylation substrate and a quenched tetrazine-BODIPY fluorophore for fluorogenic tagging via the IEDDA click chemistry reaction (Fig. 1.3B, bottom). Chapter 1 elaborates on the design, development and applications of RT-IMPACT in visualizing endogenous PLD enzyme activities in real-time under live-cell conditions.

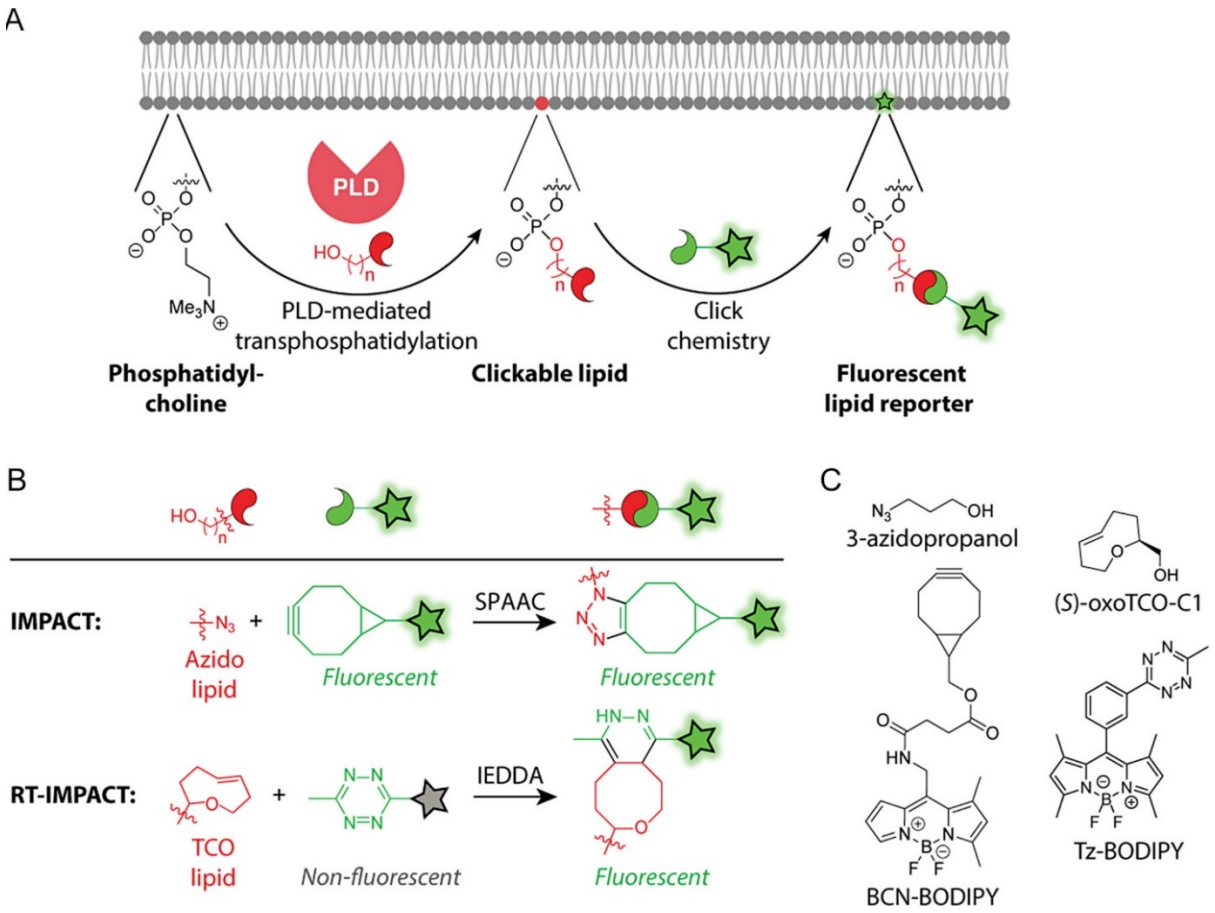

Figure 1.3. (A) Schematic of the IMPACT methods for detecting cellular PLD activity. PLD catalyzes the transphosphatidylation of phosphatidylcholine with an exogenous alcohol, producing a clickable lipid product that can then be detected following the introduction of a fluorophore using a click chemistry tagging reaction. (B and C) Structures of reagents, reactions, and reaction products utilized in IMPACT and RT-IMPACT.

GPCR-Gaq pathways that are upstream of PLD activations

Cell surface receptors serve as the mediator of cell signaling by transducing extracellular hormones and growth factors into specific intracellular pathways. G protein-coupled receptors (GPCRs) are arguably the most important class of cell surface receptors and many important

signaling pathways downstream of GPCRs intersect with PLD enzymes (Fig. 1.4). In the absence of ligands, inactive GPCRs form complexes with heterotrimeric G proteins, consisting of Gα and Gβγ subunits, on the cell surface. Ligand binding on the extracellular leaflet results in conformational changes in the GPCRs, which lead to GDP-GTP exchange in the Gα subunits. The GTP-bound Gα subunits then dissociate from inactive heterotrimeric G proteins into activated Gα and Gβγ subunits, which are responsible for distinct downstream cell signaling events. In canonical GPCR-G protein signaling which are tightly regulated, the activated GPCRs will then quickly be internalized through phosphorylation by GRKs and binding to β-arrestins to initiate clathrin-mediated endycytosis, which terminates GPCR signaling [24].

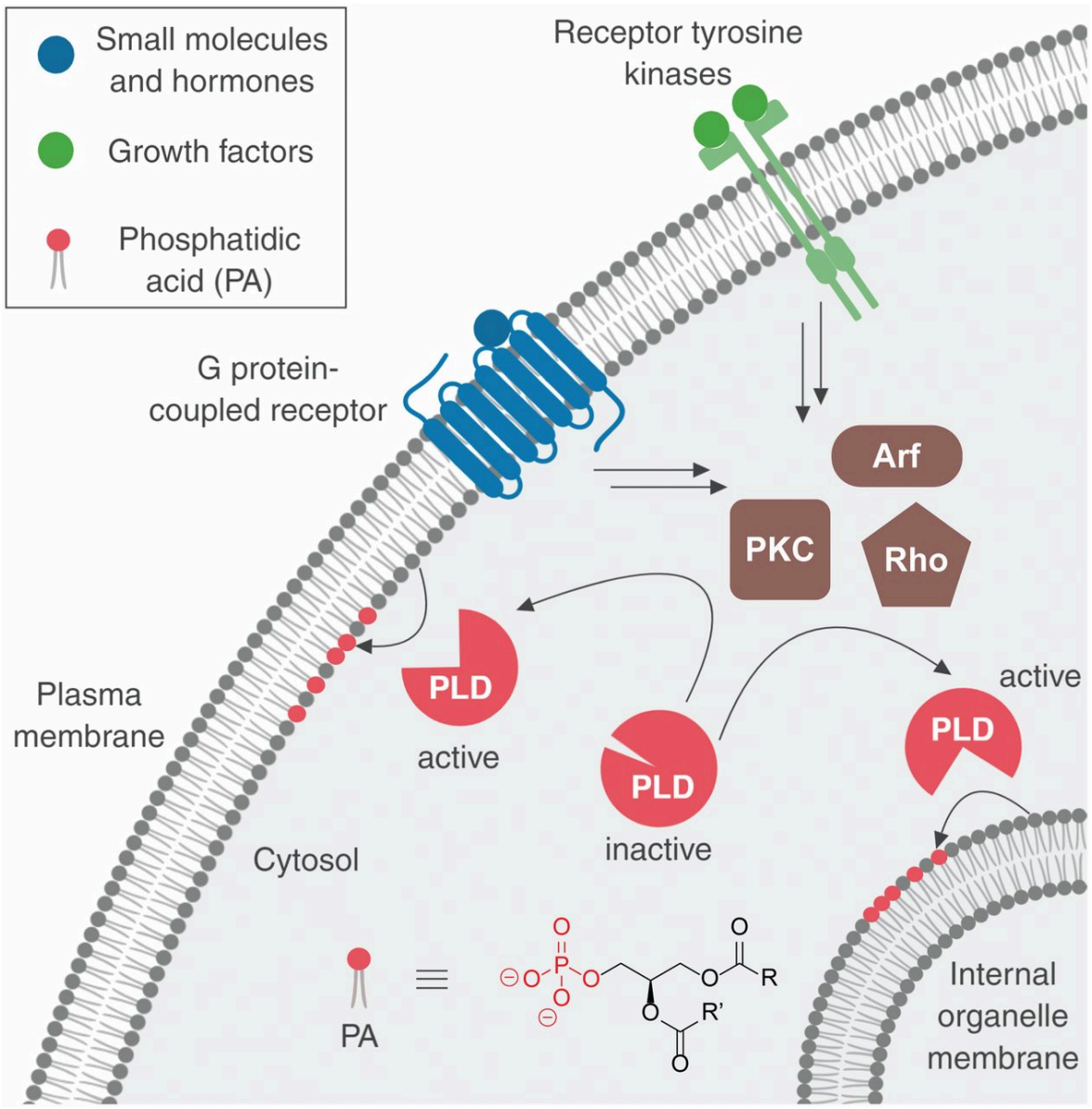

Figure 1.4: Phospholipase D (PLD) enzymes are stimulated by different classes of cell-surface receptors. Reproduced from [23]. Cell surface receptors activate PLDs through intracellular effectors including those from the protein kinase C (PKC), Rho GTPase, and Arf GTPase families, to catalyze phosphatidic acid (PA) formation at different intracellular membrane locations. R and R' denote the fatty acyl tails.

All major classes of Gα proteins (G_q, G_s, G_i, $G_{12/13}$) were somewhat linked with activation of PLD enzymes, but the extent of activation varies significantly. Among them, G_q is the arguably the strongest and most common activator of PLDs. G_q binds to and activates PLCβ on the plasma membrane, leading to hydrolysis of $PI(4,5)P_2$ in to diacylglycerol (DAG) and inositol-trisphosphate (IP_3). DAG is a known activator of PKC, which activates PLD and results in translocation towards the plasma membrane. In addition, $PI(4,5)P_2$ is an activator of PLD and IP_3 can lead to an increase in subcellular concentration of Ca^{2+}, which activates PKC as well. Studies have shown that pharmacological inhibitors of PKC can attenuate PLD activation [25] and that overexpression of a PLD mutant that are PKC-resistant dramatically reduces the overall PLD activity downstream of a GPCR-G_q pathway [26]. These studies indicate that PKC is an important mediator for the activation of PLD in the signaling pathway of G_q-PLCβ.

Other G protein pathways can also lead to PLD activation, to a less extent. G_s activates adenylyl cyclase and enhances production of cAMP, which then activates PKA and ERK. It has been reported that a cAMP derivative activates PLD through a pathway mediated by Ras and Src [27]. G_i is associated with inhibition of adenylyl cyclase, however, evidence indicates that it can also activate PLDs through RhoGEF and Arf proteins in certain G_i-activating receptors [28]. $G_{12/13}$ can initiate cytoskeleton rearrangement through activation of Rho family of GTPases, which subsequently stimulate PLDs [29].

Apart from Gα subunits, dissociated Gβγ subunits are known to activate PI3Kβ, which catalyzes the formation of PIP_3 on the plasma membrane [30]. This process was shown to facilitate recruitment of β-arrestin binding to GPCRs, which leads to endocytosis of the GPCRs and

subsequently terminates canonical GPCR signaling [31]. However, some GPCRs show extended signaling even after receptor internalization. The parathyroid receptor 1 (PTHR1) is among the first several examples discovered to form ternary complexes with β-arrestin that can signal through G_s-cAMP pathway persistently at endosomes. Such unconventional activities are physiologically relevant and play crucial roles in regulating calcium homeostasis with implications for proper bone developments [32,33]. Because PTHR1 is known to activate both G_q and G_s, with the former being poorly understood in its relation to Gas signaling, it is of vital importance to dissect dynamics of G_q pathways with high spatiotemporal resolutions. Chapter 3 addresses this challenge in the context of PTHR1-G_q protein signaling system using RT-IMPACT probes, which measures PLD activities downstream of the G_q-PLC axis.

Non-vesicular lipid trafficking events mediated by lipid transfer proteins residing at ER-PM contact sites

Compartmentalization is a fundamental feature within subcellular organization. Lipid membranes in the cell form physical barriers to facilitate certain cellular processes in specific regions, known as organelles. Different organelle membranes can be characterized by their distinct lipid compositions, which in turn determine the cellular functions of the membrane. For example, the plasma membrane is the primary boundary that separates the subcellular environment from the extracellular space. It is also where the cells transduce extracellular cues into intracellular signaling through cell surface receptors such as GPCRs and RTKs. One of the major signaling lipids that is relatively enriched in PM is $PI(4,5)P_2$. By comparison, the ER membrane is the place of biosynthesis of many types of lipids and is especially enriched in

intermediates and end-products of lipid biosynthetic pathways (e.g., DAG, PA and lysophospholipids) [34].

As membrane functions are partly determined by their lipid compositions, lipid homeostasis is essential for proper cellular processes and is tightly maintained under healthy conditions [35]. Furthermore, disruption of lipid homeostasis is frequently associated with regulated cell deaths [36]. Therefore, cells deploy a wide range of mechanisms to regulate lipid homeostasis including lipid metabolism and inter-organelle lipid trafficking. For example, under acute signaling conditions, such as those caused by activation of GPCRs through ligand binding, $PI(4,5)P_2$ on plasma membrane can be quickly depleted through activation of G_q-PLC pathway. This will lead to an abrupt increase in diacylglycerol (DAG) composition, which is a potent signaling molecule that will lead to activation of protein kinase C (PKC) and turn on many signaling pathways, including PLD-mediated PA synthesis. To counteract such effects of acute DAG production in the plasma membrane, cells can metabolize DAG by converting it to PA through DGKζ [37].

Alternatively, cells can transport DAG to the ER at membrane contact sites (MCSs). MCSs are regions where membranes of two organelles are in close apposition to facilitate non-vesicular lipid transport and frequently involve the ER (Fig. 1.5) [38]. Recent research efforts have revealed the functional significance of MCSs coupled by molecular mechanisms. The defining features of MCSs are 1. The membranes of two organelles are tethered, as opposed to fused, in proximity (within 10-80 nm). 2. MCSs facilitate certain cellular functions, such as lipid and ion transfer. 3. MCSs are formed and maintained by certain proteins to carry out the aforementioned tethering and trafficking activities [39].

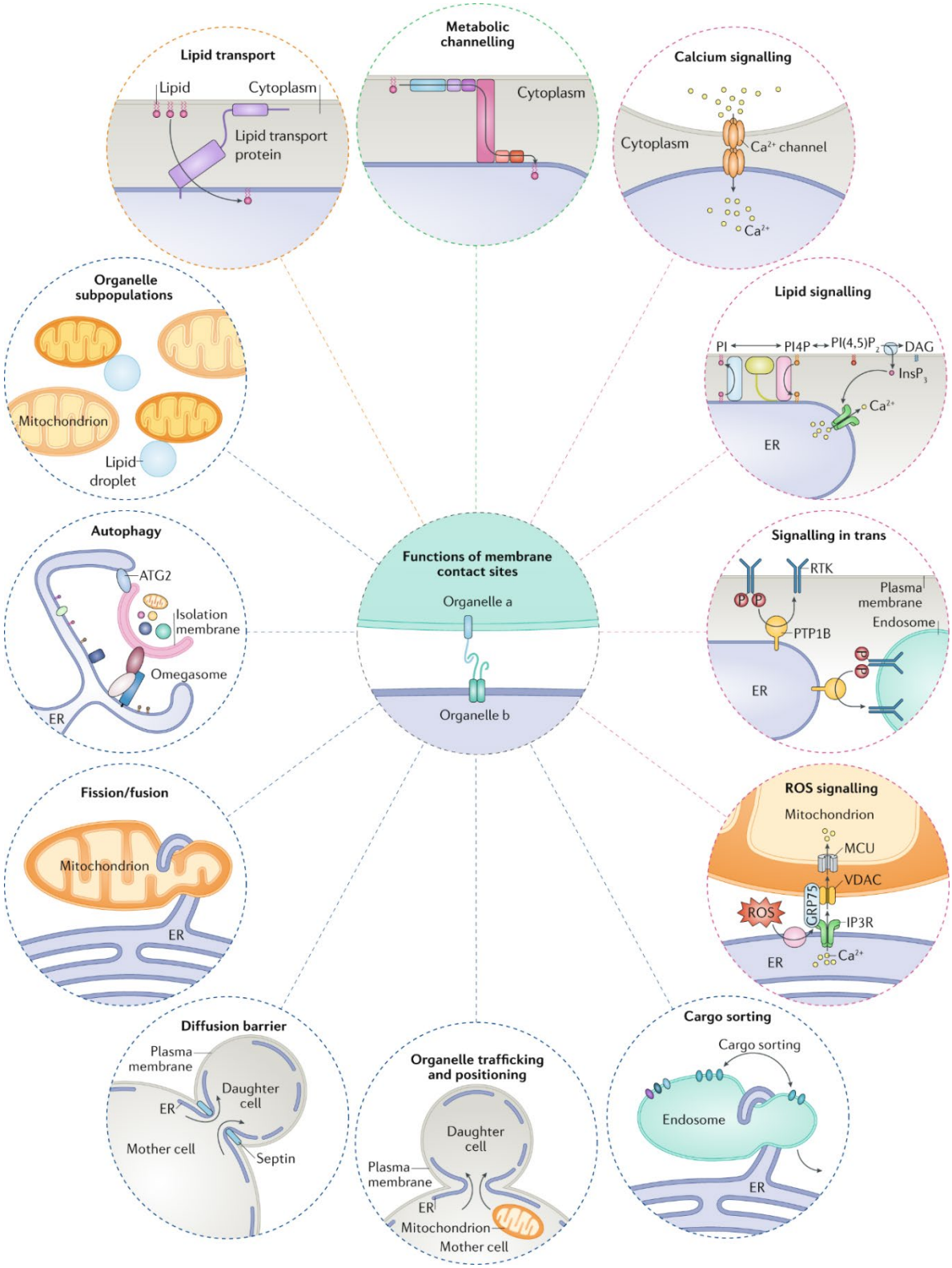
Functions of membrane contact sites
Organelle a
Organelle b
Lipid transport
Lipid
Cytoplasm
Lipid transport protein
Metabolic channelling
Cytoplasm
Calcium signalling
Cytoplasm
Ca2+ channel
Ca2+
Organelle subpopulations
Mitochondrion
Lipid droplet
Lipid signalling
PI
PI4P
PI(4,5)P2
DAG
InsP3
Ca2+
ER
Autophagy
ATG2
Isolation membrane
Omegasome
ER
Signalling in trans
RTK
P
P
Plasma membrane
Endosome
PTP1B
ER
Fission/fusion
Mitochondrion
ER
ROS signalling
Mitochondrion
MCU
VDAC
GRP75
ROS
IP3R
ER
Ca2+
Diffusion barrier
Plasma membrane
Daughter cell
ER
Mother cell
Septin
Organelle trafficking and positioning
Daughter cell
Plasma membrane
ER
Mitochondrion
Mother cell
Cargo sorting
Cargo sorting
Endosome
ER

Figure 1.5: Overview of various functions of membrane contact sites. Reproduced from [39]. Each image is a representative display of a specific function of membrane contact sites. These functions are categorized into four subsets: lipid transport (orange dotted circle), signaling (pink), regulation of organelle membrane dynamics (blue), and metabolic channeling (green). Specific examples and/or general mechanisms of the function are depicted within individual images.

Specifically, non-vesicular lipid trafficking events are an emerging mechanistic pathway of lipid transport, which is mediated by lipid transfer proteins (LTPs) at MCSs, as compared to classical vesicular trafficking mediated by COPI/II vesicles [35]. Numerous families of LTPs have been discovered to be highly enriched at MCSs, although many of their molecular mechanisms of lipid transport remain elusive [40]. Extended synaptotagmins (ESyts) are an important class of MCS proteins that mediate tethering of PM-ER contact sites and facilitate non-vesicular lipid transport between the two membranes [41,42]. Due to limitations of available biochemical tools to study non-vesicular lipid transfer mechanisms in live cells, direct visualization of lipid trafficking at physiological MCSs remains largely unachievable. However, by virtue of doping the plasma membrane with unnatural fluorescent lipids and observing lipid trafficking events in real-time under live-cell conditions, e.g., through RT-IMPACT labeling, the dynamics of non-vesicular trafficking can be directly visualized in real-time. Such lipid trafficking events originating from the PM to the ER via non-vesicular mechanisms were first observed in real-time imaging of PLD activities in Chapter 2 and then further interrogated and reconstituted with characterizations of ESyts in Chapter 4.

References

1 Bumpus TW, Baskin JM. Greasing the Wheels of Lipid Biology with Chemical Tools. *Trends Biochem Sci* 2018;**43**:970–83. https://doi.org/https://doi.org/10.1016/j.tibs.2018.09.011.

2 Hannun YA, Obeid LM. Principles of bioactive lipid signalling: Lessons from sphingolipids. *Nat Rev Mol Cell Biol* 2008:139–50. https://doi.org/10.1038/nrm2329.

3 Sunshine H, Iruela-Arispe ML. Membrane lipids and cell signaling. *Curr Opin Lipidol* 2017:408–13. https://doi.org/10.1097/MOL.0000000000000443.

4 Brown HA, Thomas PG, Lindsley CW. Targeting phospholipase D in cancer, infection and neurodegenerative disorders. *Nat Struct Mol Biol* 2017. https://doi.org/10.1038/nrd.2016.252.

5 Nelson RK, Frohman MA. Physiological and pathophysiological roles for phospholipase D. *J Lipid Res* 2015;**56**:2229–37. https://doi.org/10.1194/jlr.R059220.

6 Selvy PE, Lavieri RR, Lindsley CW, Brown HA. Phospholipase D: enzymology, functionality, and chemical modulation. *Chem Rev* 2011;**111**:6064–119. https://doi.org/10.1021/cr200296t.

7 Shulga Y V., Topham MK, Epand RM. Regulation and functions of diacylglycerol kinases. *Chem Rev* 2011;**111**:6186–208. https://doi.org/10.1021/cr1004106.

8 Kassas N, Tanguy E, Thahouly T, Fouillen L, Heintz D, Chasserot-Golaz S, *et al.* Comparative characterization of phosphatidic acid sensors and their localization during frustrated phagocytosis. *J Biol Chem* 2017;**292**:4266–79. https://doi.org/10.1074/jbc.M116.742346.

9 Du G, Altshuller YM, Vitale N, Huang P, Chasserot-Golaz S, Morris AJ, *et al.* Regulation of phospholipase D1 subcellular cycling through coordination of multiple membrane association motifs. *J Cell Biol* 2003;**162**:305–15. https://doi.org/10.1083/jcb.200302033.

10 Noh DY, Ahn SJ, Lee R a., Park I a., Kim JH, Suh PG, *et al.* Overexpression of phospholipase D1 in human breast cancer tissues. *Cancer Lett* 2000;**161**:207–14. https://doi.org/10.1016/S0304-3835(00)00612-1.

11 Zhao Y, Ehara H, Akao Y, Shamoto M, Nakagawa Y, Banno Y, *et al.* Increased

activity and intranuclear expression of phospholipase D2 in human renal cancer. *Biochem Biophys Res Commun* 2000;**278**:140–3. https://doi.org/10.1006/bbrc.2000.3719.

12 Molenaar JJ, Koster J, Zwijnenburg DA, Van Sluis P, Valentijn LJ, Van Der Ploeg I, *et al.* Sequencing of neuroblastoma identifies chromothripsis and defects in neuritogenesis genes. *Nature* 2012;**483**:589–93. https://doi.org/10.1038/nature10910.

13 Pugh TJ, Weeraratne SD, Archer TC, Pomeranz Krummel DA, Auclair D, Bochicchio J, *et al.* Medulloblastoma exome sequencing uncovers subtype-specific somatic mutations. *Nature* 2012:106–10. https://doi.org/10.1038/nature11329.

14 Saito M, Iwadate M, Higashimoto M, Ono K, Takebayashi Y, Takenoshita S. Expression of phospholipase D2 in human colorectal carcinoma. *Oncol Rep* 2007;**18**:1329–34. https://doi.org/10.3892/or.18.5.1329.

15 Park JB, Lee CS, Jang JH, Ghim J, Kim YJ, You S, *et al.* Phospholipase signalling networks in cancer. *Nat Rev Cancer* 2012;**12**:782–92. https://doi.org/10.1038/nrc3379.

16 Du G, Altshuller YM, Kim Y, Han JM, Ryu SH, Morris AJ, *et al.* Dual requirement for rho and protein kinase C in direct activation of phospholipase D1 through G protein-coupled receptor signaling. *Mol Biol Cell* 2000;**11**:4359–68. https://doi.org/10.1091/mbc.11.12.4359.

17 Hammond S, Jenco J, Nakashima S, K. Characterization of two alternately spliced forms of phospholipase D1. *J Biol Chem* 1997;**272**:3860–8. https://doi.org/10.1074/jbc.272.6.3860.

18 Brown HA, Henage LG, Preininger AM, Xiang Y, Exton JH. Biochemical Analysis of Phospholipase D. *Methods Enzymol* 2007:49–87. https://doi.org/10.1016/S0076-6879(07)34004-4.

19 Philip F, Ha EE, Seeliger MA, Frohman MA. Measuring Phospholipase D Enzymatic Activity Through Biochemical and Imaging Methods. *Methods Enzymol* 2017;**583**:309–25. https://doi.org/10.1016/bs.mie.2016.09.041.

20 Bumpus TW, Baskin JM. A Chemoenzymatic Strategy for Imaging Cellular Phosphatidic Acid Synthesis. *Angew Chem Int Ed* 2016;**55**:13155–8. https://doi.org/10.1002/anie.201607443.

21 Bumpus TW, Baskin JM. Clickable Substrate Mimics Enable Imaging of Phospholipase D Activity. *ACS Cent Sci* 2017;**3**:1070–7. https://doi.org/10.1021/acscentsci.7b00222.

22 Bumpus TW, Liang FJ, Baskin JM. Ex Uno Plura: Differential Labeling of Phospholipid Biosynthetic Pathways with a Single Bioorthogonal Alcohol. *Biochemistry* 2018;**57**:226–30. https://doi.org/10.1021/acs.biochem.7b01021.

23 Liang D, Wu K, Tei R, Bumpus TW, Ye J, Baskin JM. A real-time click chemistry imaging approach reveals stimulus-specific subcellular locations of phospholipase D activity. *Proc Natl Acad Sci U S A* 2019;**116**:15453–62. https://doi.org/10.1073/pnas.1903949116.

24 Gurevich V V., Gurevich E V. GPCR signaling regulation: The role of GRKs and arrestins. *Front Pharmacol* 2019;**10**:. https://doi.org/10.3389/fphar.2019.00125.

25 Meacci E, Vasta V, Donati C, Farnararo M, Bruni P. Receptor-mediated activation of phospholipase D by sphingosine 1-phosphate in skeletal muscle C2C12 cells. A role for protein kinase C. *FEBS Lett* 1999;**457**:184–8. https://doi.org/10.1016/S0014-5793(99)01033-9.

26 Xie Z, Ho WT, Spellman R, Cai S, Exton JH. Mechanisms of regulation of phospholipase D1 and D2 by the heterotrimeric G proteins G13 and Gq. *J Biol Chem* 2002;**277**:11979–86. https://doi.org/10.1074/jbc.M109751200.

27 Yoon MS, Jun BK, Hwang JH, Ki SL, Han JS. Activation of phospholipase D by 8-Br-cAMP occurs through novel pathway involving Src, Ras, and ERK in human endometrial stromal cells. *FEBS Lett* 2005;**579**:5635–42. https://doi.org/10.1016/j.febslet.2005.09.034.

28 Fensome A, Whatmore J, Morgan C, Jones D, Cockcroft S. ADP-ribosylation factor and rho proteins mediate fMLP-dependent activation of phospholipase D in human neutrophils. *J Biol Chem* 1998;**273**:13157–64. https://doi.org/10.1074/jbc.273.21.13157.

29 Plonk SG, Park SK, Exton JH. The α-subunit of the heterotrimeric G protein G13 activates a phospholipase D isozyme by a pathway requiring Rho family GTPases. *J Biol Chem* 1998;**273**:4823–6. https://doi.org/10.1074/jbc.273.9.4823.

30 Stephens LR, Eguinoa A, Erdjument-Bromage H, Lui M, Cooke F, Coadwell J, *et al.* The Gβγ/sensitivity of a PI3K is dependent upon a tightly associated adaptor, p101. *Cell* 1997;**89**:105–14. https://doi.org/10.1016/S0092-8674(00)80187-7.

31 Moore CAC, Milano SK, Benovic JL. Regulation of receptor trafficking by GRKs and arrestins. *Annu Rev Physiol* 2007:451–82. https://doi.org/10.1146/annurev.physiol.69.022405.154712.

32 Sutkeviciute I, Clark LJ, White AD, Gardella TJ, Vilardaga JP. PTH/PTHrP Receptor Signaling, Allostery, and Structures. *Trends Endocrinol Metab* 2019:860–74. https://doi.org/10.1016/j.tem.2019.07.011.

33 White AD, Fang F, Jean-Alphonse FG, Clark LJ, An HJ, Liu H, *et al.* Ca2+ allostery in PTH-receptor signaling. *Proc Natl Acad Sci U S A* 2019;**116**:3294–9. https://doi.org/10.1073/pnas.1814670116.

34 Van Meer G, Voelker DR, Feigenson GW. Membrane lipids: Where they are and how they behave. *Nat Rev Mol Cell Biol* 2008:112–24. https://doi.org/10.1038/nrm2330.

35 Jackson CL, Walch L, Verbavatz JM. Lipids and Their Trafficking: An Integral Part of Cellular Organization. *Dev Cell* 2016:139–53. https://doi.org/10.1016/j.devcel.2016.09.030.

36 Agmon E, Stockwell BR. Lipid homeostasis and regulated cell death. *Curr Opin Chem Biol* 2017:83–9. https://doi.org/10.1016/j.cbpa.2017.06.002.

37 Kim K, Yang J, Zhong XP, Kim MH, Kim YS, Lee HW, *et al.* Synaptic removal of diacylglycerol by DGKζ and PSD-95 regulates dendritic spine maintenance. *EMBO J* 2009;**28**:1170–9. https://doi.org/10.1038/emboj.2009.44.

38 Xu J, Huang X. Lipid Metabolism at Membrane Contacts: Dynamics and Functions Beyond Lipid Homeostasis. *Front Cell Dev Biol* 2020. https://doi.org/10.3389/fcell.2020.615856.

39 Scorrano L, De Matteis MA, Emr S, Giordano F, Hajnóczky G, Kornmann B, *et al.* Coming together to define membrane contact sites. *Nat Commun* 2019;**10**:. https://doi.org/10.1038/s41467-019-09253-3.

40 Wong LH, Gatta AT, Levine TP. Lipid transfer proteins: the lipid commute via shuttles, bridges and tubes. *Nat Rev Mol Cell Biol* 2019:85–101.

https://doi.org/10.1038/s41580-018-0071-5.

41 Giordano F, Saheki Y, Idevall-Hagren O, Colombo SF, Pirruccello M, Milosevic I, *et al.* PI(4,5)P2-Dependent and Ca2+-Regulated ER-PM interactions mediated by the extended synaptotagmins. *Cell* 2013;**153**:1494. https://doi.org/10.1016/j.cell.2013.05.026.

42 Saheki Y, Bian X, Schauder CM, Sawaki Y, Surma MA, Klose C, *et al.* Control of plasma membrane lipid homeostasis by the extended synaptotagmins. *Nat Cell Biol* 2016;**18**:504–15. https://doi.org/10.1038/ncb3339.

CHAPTER 2: A Real-Time, Click Chemistry Imaging Approach Reveals Stimulus-Specific Subcellular Locations of Phospholipase D Activity[1]

Abstract

The fidelity of signal transduction requires spatiotemporal control of the production of signaling agents. Phosphatidic acid (PA) is a pleiotropic lipid second messenger whose modes of action differ based on upstream stimulus, biosynthetic source, and site of production. How cells regulate the local production of PA to effect diverse signaling outcomes remains elusive. Unlike other second messengers, sites of PA biosynthesis cannot be accurately visualized with subcellular precision. Here, we describe a rapid, chemoenzymatic approach for imaging physiological PA production by phospholipase D (PLD) enzymes. Our method capitalizes on the remarkable discovery that bulky, hydrophilic *trans*-cyclooctene-containing primary alcohols can supplant water as the nucleophile in the PLD active site in a transphosphatidylation reaction of PLD's lipid substrate, phosphatidylcholine. The resultant *trans*-cyclooctene-containing lipids are tagged with a fluorogenic tetrazine reagent via a no-rinse, inverse-electron demand Diels-Alder (IEDDA) reaction, enabling their immediate visualization by confocal microscopy in real time. Strikingly, the fluorescent reporter lipids initially produced at the plasma membrane (PM) induced by phorbol ester stimulation of PLD were rapidly internalized via apparent non-vesicular pathways rather than endocytosis, suggesting applications of this

[1] Currently published as a research article by Dongjun Liang, Kane Wu, Reika Tei, Timothy W. Bumpus, Johnny Ye, and Jeremy M. Baskin in *Proceedings of the National Academy of Sciences of the United States of America*.

toolset for probing mechanisms of intracellular phospholipid transport. By instead focusing on the initial 10 seconds of the IEDDA reaction, we precisely pinpointed the subcellular locations of endogenous PLD activity as elicited by physiological agonists of G protein-coupled receptor and receptor tyrosine kinase signaling. These tools hold promise to shed light on both lipid trafficking pathways and the physiological and pathological effects of localized PLD signaling.

Introduction

Localized production of signaling molecules is a key feature of signal transduction pathways. This phenomenon enables a small, privileged set of ions, metabolites, and lipids to function as second messengers that dictate diverse downstream signaling events through not only their molecular identities but also their sites of production. Sensing the precise locations where second messengers are produced or enriched is a challenging task. Typical approaches include small-molecule, protein, or nucleic acid-based fluorescent sensors that use selective binding or covalent reactivity to localize or produce a fluorescent signal where the second messenger is produced [1–4]. Whereas these approaches have been revolutionary for sensing signals such as divalent cations, reactive oxygen species, and certain lipid second messengers, they have limitations in many contexts, particularly for targets without selective binding domains or that are produced by multiple different biosynthetic routes.

Phosphatidic acid (PA) is a multifunctional lipid that acts both as a key intermediate in de novo phospholipid biosynthesis and as a lipid second messenger [5]. In this latter function, PA is generated by one of several isoforms of phospholipase D (PLD) or diacylglycerol kinase (DGK) enzymes [6,7]. The PLD-mediated pathway is highly clinically relevant, as PLD levels are elevated in several diseases, including many cancers, viral infection, and neurological diseases [8–11], and consequently, PLD inhibition is emerging as a promising therapeutic strategy to attenuate pathological PLD signaling [12–15]. Two PLD isoforms, PLD1 and PLD2, mediate the bulk of their biological effects through the production of PA via hydrolysis of the abundant membrane phospholipid phosphatidylcholine (PC) in several organelle membranes, including the plasma membrane (PM), the Golgi apparatus, endosomes, and lysosomes [6,11,16].

Though the localizations of PLD1 and PLD2 differ and can change in accordance with their activation, it remains unknown which cellular compartments possess active PLD enzymes during different physiological stimulations [17–21]. In particular, PLD enzymes can receive input from two different classes of cell-surface receptors, G protein-coupled receptors (GPCRs) and receptor tyrosine kinases (RTKs). Both GPCRs and RTKs can stimulate PLD via activation of several different intermediary, intracellular effectors, including those from the protein kinase C (PKC), Rho GTPase, and Arf GTPase families. Ultimately, downstream of PLD activation, these pathways elicit different ultimate physiological effects on cells (Fig. 1.3) [6,22–27].

Despite much effort aimed at understanding PLD signaling, it remains unknown whether activation of PLDs by these different inputs occurs at different subcellular locations. More generally, how cells regulate the local production of PA to effect specific signaling outcomes remains an unsolved mystery, despite the many established effector proteins whose downstream signaling activities depend on PA production [16].

Existing tools for visualizing PA are inadequate for addressing these questions. First, directly tracking fluorescent protein fusions to PLDs and DGKs does not reveal where these enzymes are actively producing PA. A specialized fluorescence lifetime imaging approach, in which cells expressing fluorescently tagged PLDs are dosed with a fluorescent PC analog, reveals changes in enzyme–substrate interactions, which is an indirect measure that can correlate with enzymatic activity [28]. Conversely, PA-binding protein domains exhibit only moderate selectivity for PA and, critically, do not distinguish between different biosynthetic sources of PA [29–31]. The challenge of distinguishing between pools of PA derived from PLDs and DGKs is highly relevant, given that these enzymes can receive overlapping inputs from

upstream signaling molecules including integral membrane receptors, cytosolic enzymes, and small-molecule activators and yet impact distinct downstream targets [6,7,11]. The deficiencies in these toolsets have prompted us to address the challenge of visualizing a precise subset of PA produced for acute signaling by PLDs.

Here, we report a chemoenzymatic method to visualize the precise subcellular locations of PLD activity with high spatiotemporal resolution. Our approach relies on the ability of endogenous PLD enzymes to accept unnatural substrate analogs that are rapidly converted, in sequential enzyme-mediated and bioorthogonal tagging steps, into fluorescent lipids whose subcellular location faithfully reports on the location of active PLD enzymes. The major advances reported here address the key deficiency of earlier versions of this method, namely its poor temporal resolution that, because of trafficking of the fluorescent lipid reporters prior to imaging, prevented the visualization of the true localizations of PLD activation [32,33].

These new tools enabled us to reveal the precise organelle localizations of PLD activity as elicited by diverse physiological stimuli, including selective activators of GPCR and RTK signaling. We identified striking differences in the location of PLD activity between different stimulus treatments. Additionally, we observed rapid transport of the fluorescent lipid reporters produced at the PM to the endoplasmic reticulum (ER) and, subsequently, Golgi apparatus, highlighting both the need for these time-resolved tools to accurately visualize these dynamic molecules and suggesting additional applications to visualize rapid intracellular phospholipid trafficking occurring on the second-to-minute timescale [34,35].

Results

Conceptualization of a real-time version of IMPACT

Our approach to visualize sites of PLD-mediated PA production relies on the well-known ability of PLDs to catalyze transphosphatidylation reactions with exogenous small, linear primary alcohols, forming phosphatidyl alcohols as lipid reporters of PLD activity [36,37]. We have previously demonstrated that, when cells are supplied with alkynyl [32,38] or azido [33] alcohols, their endogenous PLD enzymes convert these bioorthogonally labeled alcohols into the corresponding alkynyl or azido phosphatidyl alcohols, which can be subsequently fluorescently tagged via Cu-catalyzed or strain-promoted azide–alkyne cycloadditions (CuAAC [39,40] and SPAAC [41,42]) using appropriately derivatized fluorophores (Fig. 2.1A). This method, termed IMPACT for Imaging Phospholipase D Activity with Clickable Alcohols via Transphosphatidylation, enabled fluorescent labeling of cellular membranes within live cells, using SPAAC tagging, as a function of their PLD activities [33].

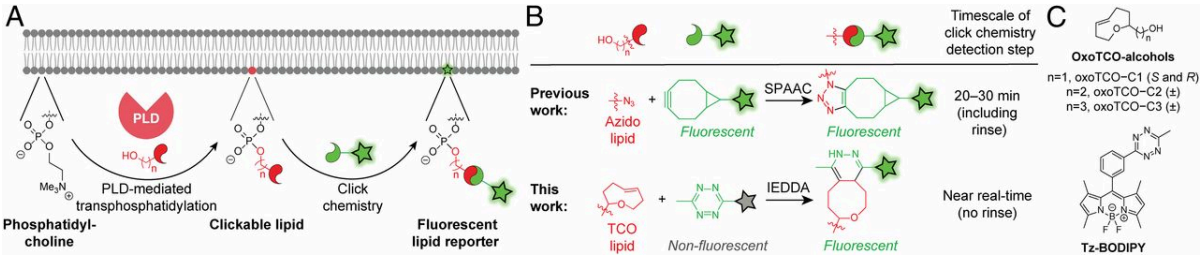

Figure 2.1: Overview of the imaging phospholipase D (PLD) activity with clickable alcohols via transphosphatidylation (IMPACT) method for visualizing PLD activity in live cells. (A) Cartoon schematic of IMPACT. (B) Comparison of established IMPACT method using azido alcohols and strain-promoted azide–alkyne cycloaddition (SPAAC) detection with the advance reported here, real-time (RT) IMPACT, using trans-cyclooctene (TCO)-containing alcohols and

inverse electron-demand Diels–Alder (IEDDA) detection using tetrazine (Tz) reagents. (C) Structures of trans-5-oxocene (oxoTCO) alcohols and the fluorogenic Tz–BODIPY conjugate used in this study.

SPAAC-based IMPACT requires 20–30 minutes for the cycloaddition and rinse-out (Fig. 2.1B, top row). This low temporal resolution makes it non-ideal for ascertaining the precise, subcellular localization of active PLD enzymes because lipid diffusion and trafficking can occur on more rapid timescales [43–45]. In particular, we noted the lack of PM-derived IMPACT fluorescence upon stimulation with phorbol 12-myristate 13-acetate (PMA), which is thought to directly stimulate PKC [23,33] and result in translocation of PLD1 to the PM [19].

We sought to substantially improve the time resolution of IMPACT by replacing SPAAC with the inverse electron-demand Diels-Alder (IEDDA) reaction of *trans*-cyclooctene (TCO) and tetrazine (Tz) reagents [46,47]. Two key advantages of this bioorthogonal reaction are its rapid reaction kinetics and the ability to perform no-rinse, real-time imaging of reaction progress using fluorogenic, or "turn-on", Tz reagents (Fig. 2.1B, bottom row) [48]. The challenges inherent in using this IEDDA reaction for IMPACT are that (i) TCO groups are substantially larger than azides or terminal alkynes, raising the question of whether endogenous PLD enzymes would accept a bulky, TCO-derivatized primary alcohol as a surrogate for water and (ii) large, hydrophobic TCO alcohols need to be both efficiently delivered to the cytosolic space, where PLDs reside, and also rinsed out from the cell after transphosphatidylation and prior to the IEDDA reaction.

Synthesis and evaluation of TCO-containing alcohols as PLD transphosphatidylation substrates

To address these challenges, we first designed and synthesized a series of carbocyclic TCO-containing primary alcohols with different linker lengths and polarities (Figs. 2.2–2.4). Remarkably, all of these TCO alcohols were transphosphatidylation substrates of both a commercially available PLD from *Streptomyces sp. PMF* (Fig. 2.5) and endogenous mammalian PLDs (Figs. 2.6 and 2.7) as evaluated by transphosphatidylation followed by *in vitro* IEDDA tagging of lipid extracts with a Tz-fluorophore conjugate and fluorescence-coupled HPLC analysis. Among these alcohols, those with aliphatic and non-polar linkers (e.g., ether) were better PLD substrates than those with more polar, bulky linkages (e.g., amide and carbamate). Unfortunately, none of these carbocyclic TCO alcohols were suitable for IMPACT, because attempts to carry out both transphosphatidylation and IEDDA tagging within cells resulted in substantial background fluorescence present in cells treated with a pan-PLD inhibitor, FIPI [49], indicating PLD-independent labeling likely due to incomplete rinse-out of the lipophilic TCO alcohols (Fig. 2.8).

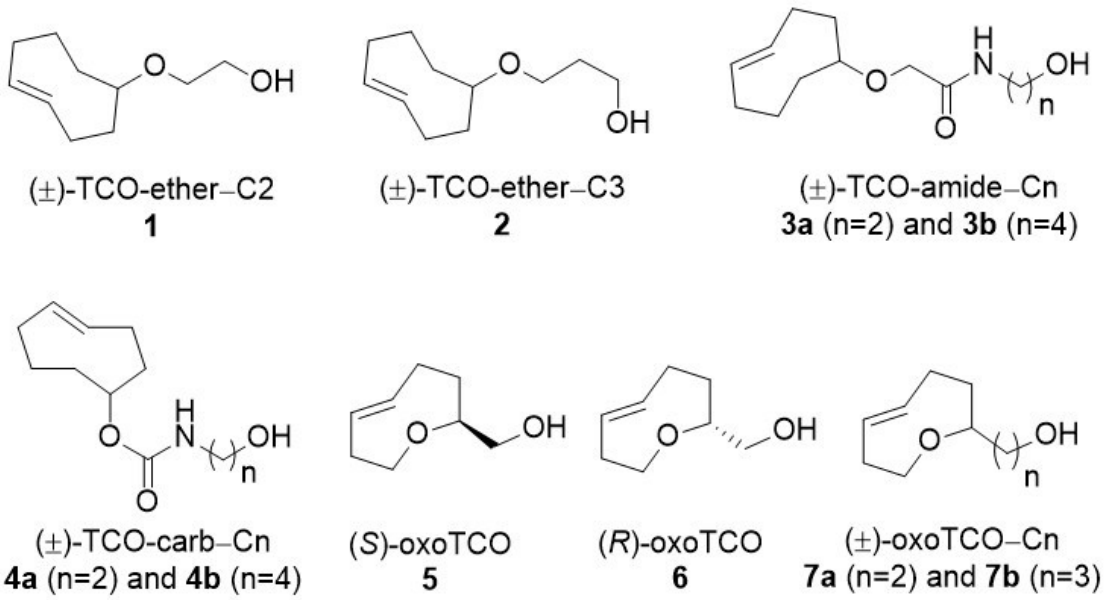

Figure 2.2: Structures of TCO and oxoTCO alcohols used in this study. Note: All trans-cyclooctene (TCO) and trans-5-oxocene (oxoTCO) alcohols were prepared as a mixture of equatorial and axial diastereomers. With the exception of the enantiomerically pure **5** and **6**, all compounds were isolated as racemates (±).

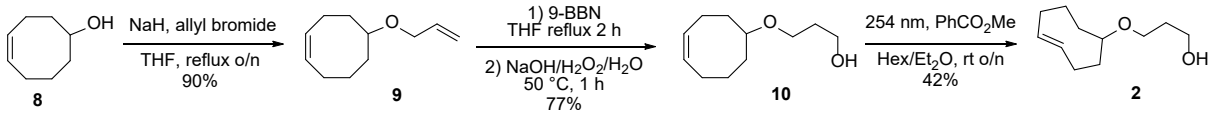

Figure 2.3: Synthesis of (±)-TCO-ether–C3.

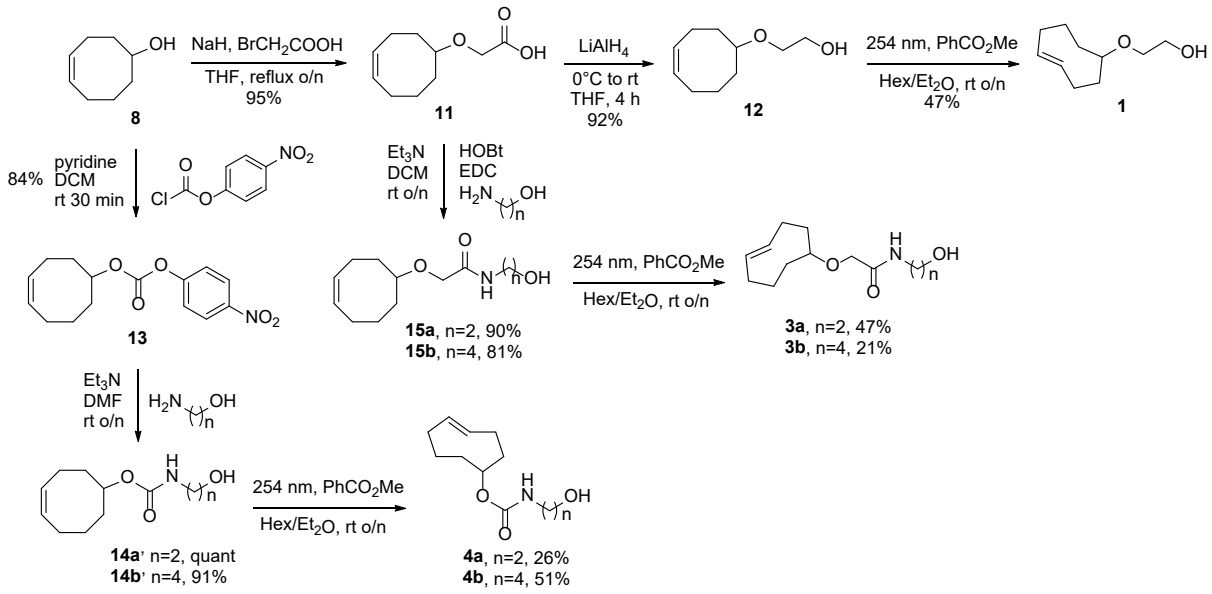

Figure 2.4: Synthesis of (±)-TCO-ether–C2, (±)-TCO-amide–Cn and (±)-TCO-carb–Cn.

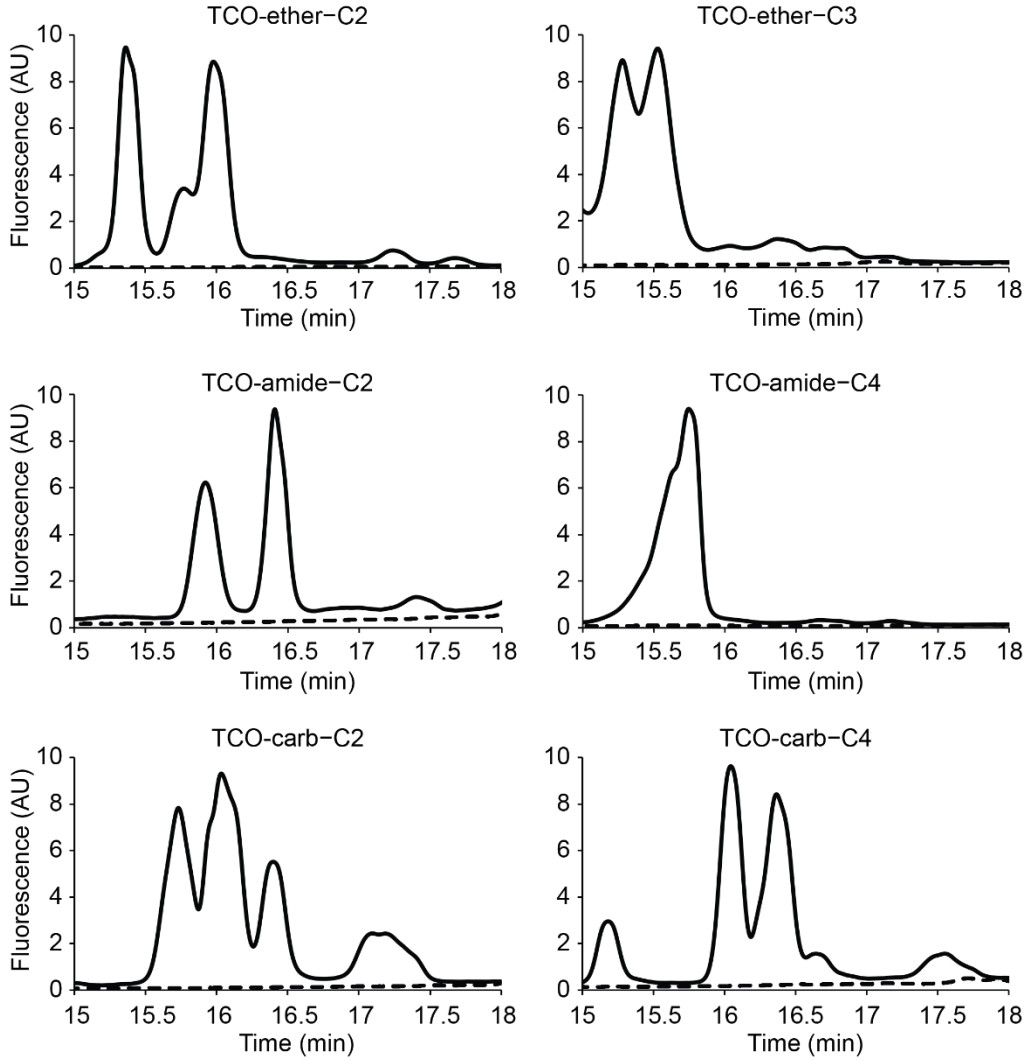

Figure 2.5: Carbocyclic TCO alcohols are PLD transphosphatidylation substrates *in vitro. In vitro* transphosphatidylation reactions catalyzed by PLD from *Streptomyces sp. PMF* were carried out with dioleoylphosphatidylcholine (DOPC) and either the indicated TCO alcohol (solid line) or no alcohol (dashed line). After a 90 min reaction at 30 ºC, lipids were extracted, dried under a stream of nitrogen, and dissolved in 100 µL of a 2:1 $CHCl_3$:MeOH mixture containing BODIPY-alkyl-Tz (25 µM) and the IEDDA reaction was performed for 5 min at 37 ºC. The reaction mixture was then analyzed by fluorescence-coupled HPLC, with

fluorescence reported in arbitrary units (AU). We note the appearance of multiple peaks, which is due to a combination of TCO isomers (each alcohol is a racemic mixture of both axial and equatorial diastereomers) and the presence of several potential isomeric dihydropyridazine and/or pyridazine products of the IEDDA reaction.

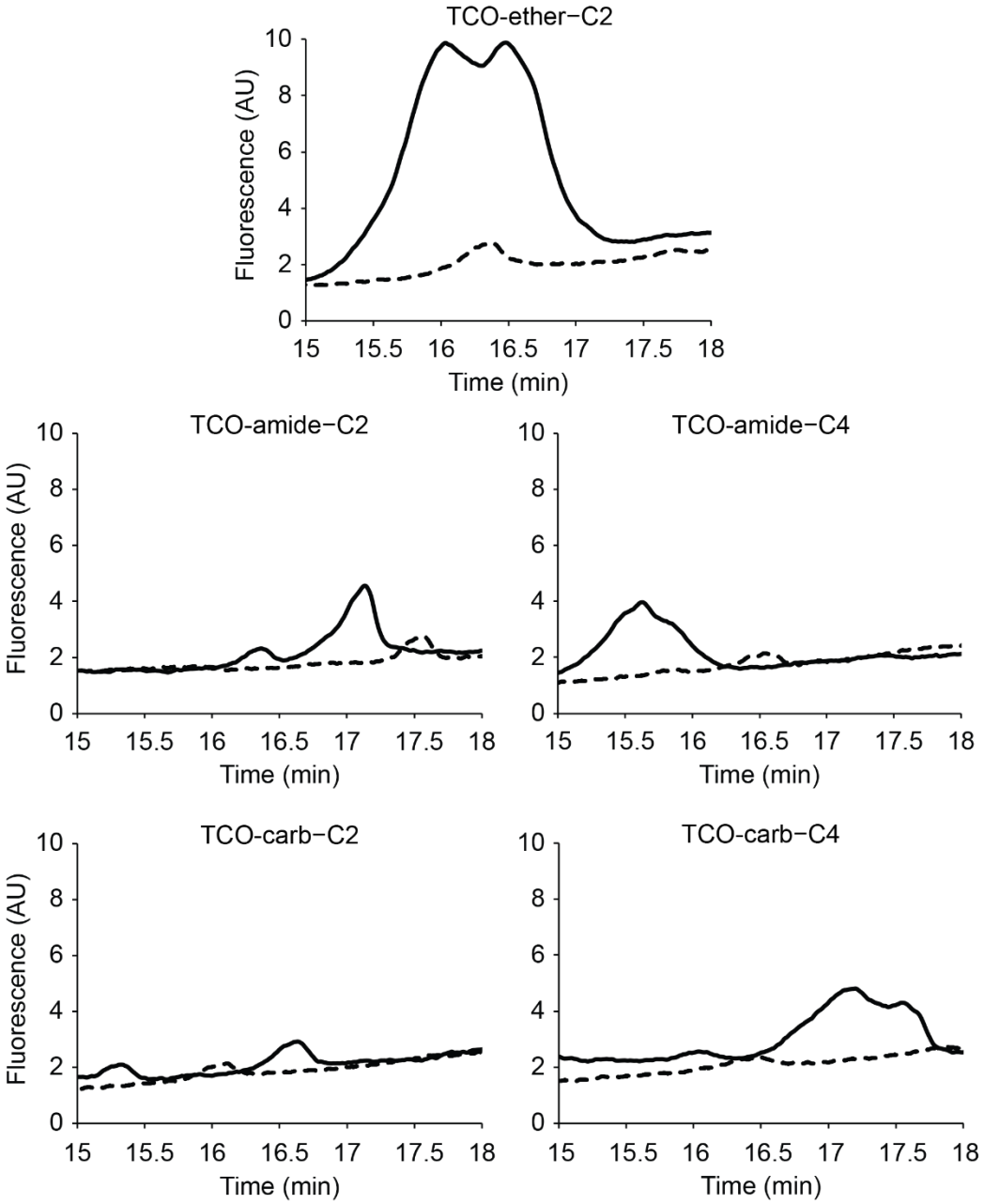

Figure 2.6: Carboxylic TCO alcohols are transphosphatidylation substrates for endogenous human PLDs. HeLa cells were incubated with PLDi (FIPI, dashed lines) or DMSO (solid lines) for 30 min and then treated with indicated TCO alcohols (7.5 mM for TCO-ether–C2 and 10 mM for all others) for 20 min, followed by PMA stimulation in the continued presence of the TCO alcohol for an additional 20 min. Following cell lysis, lipids extracts were generated, reacted with BODIPY-alkyl-Tz (25 μM) for 5 min at 37 ºC, and analyzed by fluorescence-coupled HPLC, with fluorescence intensity indicated in arbitrary units (AU). As in Figure 2.5, we note the appearance of multiple peaks, which is due to a combination of TCO isomers (each alcohol is a racemic mixture of both axial and equatorial diastereomers) and the presence of several potential isomeric dihydropyridazine and/or pyridazine products of the IEDDA reaction.

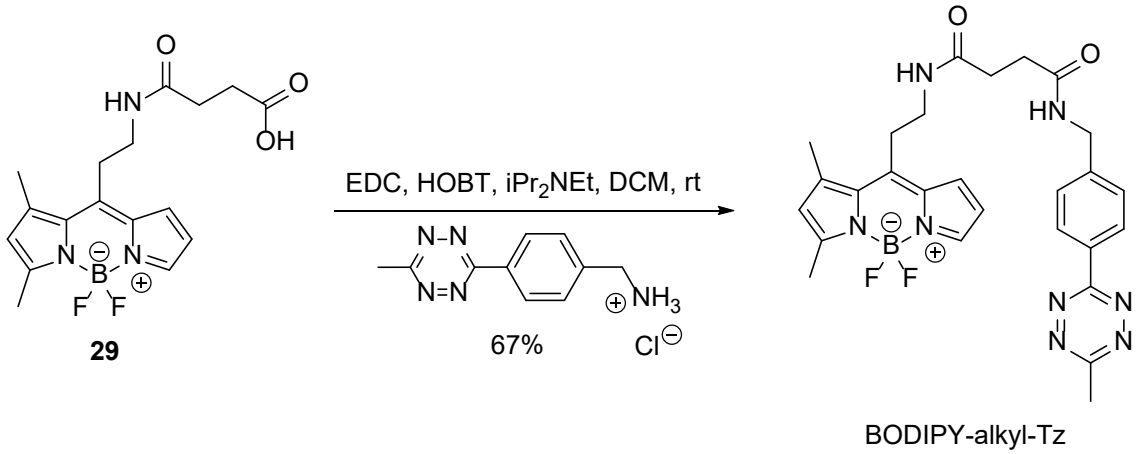

Figure 2.7: Synthesis of BODIPY-alkyl-Tz.

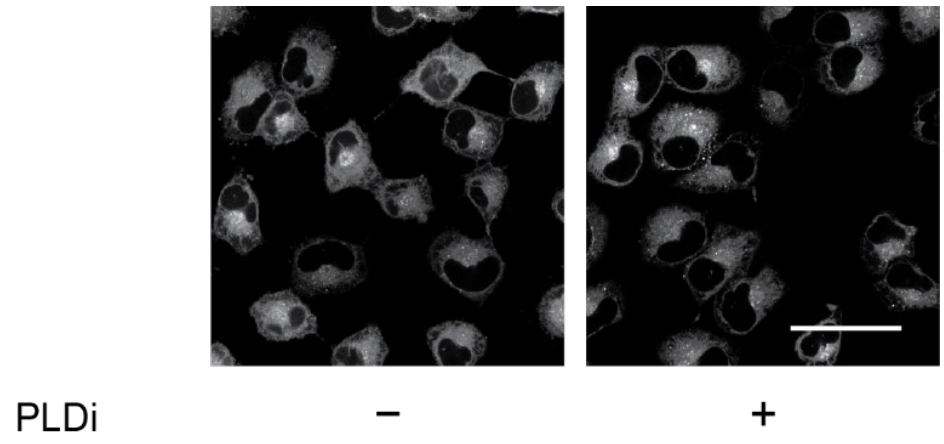

Figure 2.8: A representative carbocyclic TCO alcohol (TCO-ether−C2) is not a suitable probe for IMPACT due to high background labeling. HeLa cells were incubated with or without PLDi (FIPI) for 30 min and then treated with PMA for 20 min followed by treatment with TCO-ether–C2 (7.5 mM, 20 min) in the continued presence of PMA. After a 1 min rinse with PBS, cells were incubated with BODIPY-alkyl-Tz for 1 min, rinsed for 10 min at 37 ºC, and imaged by confocal microscopy. Scale bar: 50 μm.

At this point, we became aware of the *trans*-5-oxocene (oxoTCO, Fig. 2.1C), a more hydrophilic strained alkene that retains similarly high reactivity toward tetrazine reagents but is more polar than the carbocyclic TCOs due to the endocyclic ether functionality [50]. We prepared a group of oxoTCO-containing primary alcohols with 1- to 3-carbon aliphatic linkers: oxoTCO–C1, –C2, and –C3 (Figs. 2.1C, 2.9 and 2.10). Because the stereogenic center in oxoTCO–C1 derives from the chiral pool, we prepared both enantiomers of this compound. Excitingly, the C1 and C2 oxoTCO alcohols were all substrates of human PLDs, as confirmed by fluorescence-coupled HPLC analysis of IEDDA-tagged lipid extracts from cells stimulated with PMA in the presence of the oxoTCO alcohol (Fig. 2.11). LC–MS analysis verified that the labeled species were the expected transphosphatidylation products (Table 2.1).

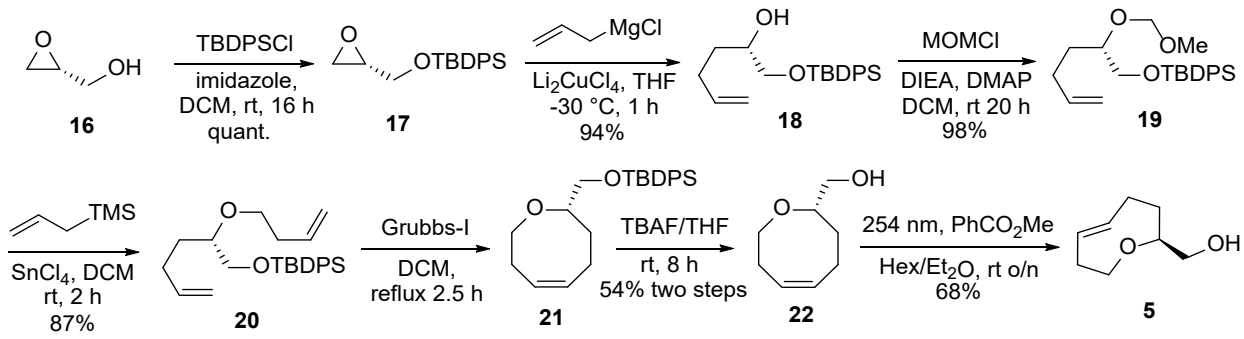

Figure 2.9. Synthesis of (*S*)-oxoTCO–C1.

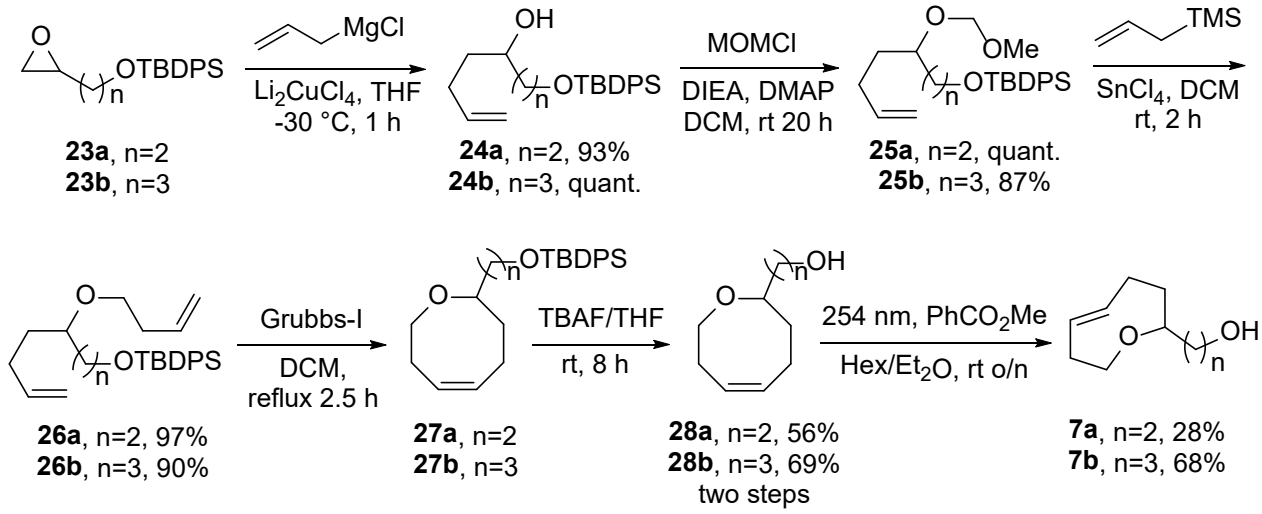

Figure 2.10: Synthesis of (±)-oxoTCO–C2 and (±)-oxoTCO–C3.

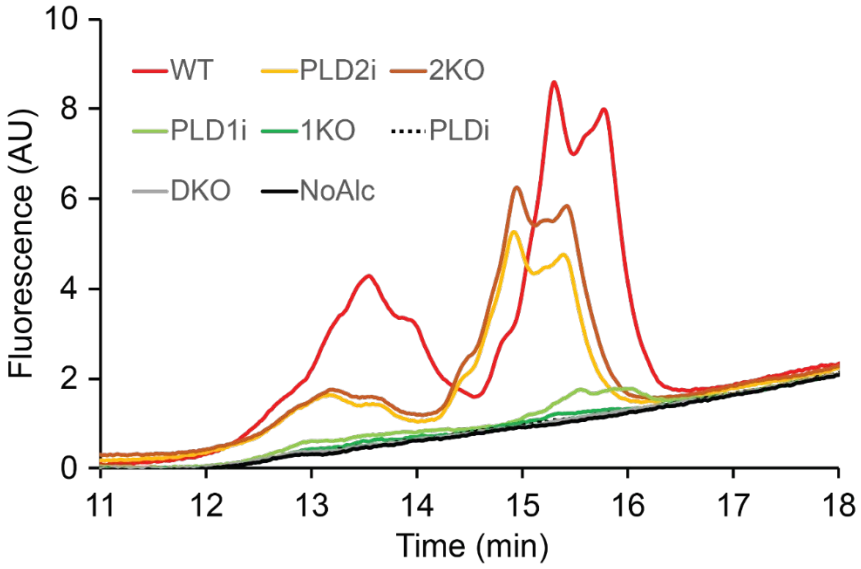

Figure 2.11: HPLC analysis of transphosphatidylation products of (S)-oxoTCO–C1 from HeLa cells. Wild-type *HeLa cells were* incubated with the indicated PLD inhibitor (PLDi, FIPI, dotted line; PLD1i, VU0359595, light green line; or PLD2i, VU0364739, yellow line) or DMSO (WT, wild-type, red line; 1KO, PLD1 knockout, dark green line; 2KO, PLD2 knockout, tan line; DKO, PLD1/2 double knockout, gray line) for 30 min. All cells were then stimulated with PMA for 20 min and then treated with (*S*)-oxoTCO–C1 (3 mM) for 20 min in the continued presence of PMA. Following cell lysis, lipids extracts were generated, reacted with Tz–BODIPY (25 μM) for 5 min at 37 ºC, and analyzed by fluorescence-coupled HPLC, with fluorescence intensity indicated in arbitrary units (AU). As in Figure 2.5, we note the appearance of multiple peaks, which is due to a combination of TCO isomers ((*S*)-oxoTCO–C1 is an enantiomerically pure mixture of both the axial and equatorial diastereomers) and the presence of several potential isomeric dihydropyridazine and/or pyridazine products of the IEDDA reaction.

Lipid species	**Calculated**	**Found**

36:1	1000.711	1000.702
36:2	998.6957	998.6956
36:3	996.6800	996.6712
36:4	994.6643	994.6646
36:5	992.6486	992.6522
34:0	974.6958	974.6888
34:1	972.6801	972.6791
34:2	970.6644	970.6671
32:0	946.6645	946.6674
32:1	944.6488	944.6512
32:2	942.6331	942.6388
30:0	918.6332	918.635
30:1	916.6175	916.623

Table 2.1. Mass spectrometry analysis of functionalized phosphatidyl alcohols isolated from cells treated with (*S*)-oxoTCO–C1. HeLa cells were incubated with PMA and (*S*)-oxoTCO–C1 (5 mM) for 60 min. Cells were rinsed for 10 min before lipid extraction. Lipid extracts were derivatized by IEDDA with methyltetrazine-amine (Click Chemistry Tools, CAS # 1345955-28-3), followed by LC-TOF-MS analysis. Indicated are calculated (Calculated) and experimentally determined (Found) masses of the functionalized phosphatidyl alcohol products,

with the lipid species classified by total number of carbons:number of double bonds in the fatty acyl tails.

(*S*)-oxoTCO–C1 is an optimal alcohol probe for monitoring PLD activity

We next assessed the ability of a fluorogenic Tz–BODIPY conjugate [51] to detect the oxoTCO-containing lipids produced by transphosphatidylation within cells. Key tools to establish the specificity of the oxoTCO alcohols for PLD enzymes was a set of knockout HeLa cell lines for PLD1 and/or PLD2 that we generated using CRISPR/Cas9-mediated mutagenesis (termed 1KO, 2KO, and DKO, for, respectively, PLD1 knockout, PLD2 knockout, and PLD1/2 double knockout). We validated these cell lines by assessing both loss of PLD proteins via Western blot (Fig. 2.12A) and extent of PMA-stimulated IMPACT labeling using azidopropanol and a cyclooctyne–fluorophore in comparison to wild-type (WT) cells treated with isoform-selective PLD inhibitors (VU0359595 [52] (PLD1i) and VU0364739 [53] (PLD2i)) by flow cytometry (Fig. 2.12B). 1KO cells had the same level of IMPACT labeling as WT cells treated with PLD1i, with similar relationships observed between 2KO cells and PLD2i treatment and between DKO cells and FIPI treatment (Figs. 2.11 and 2.12B).

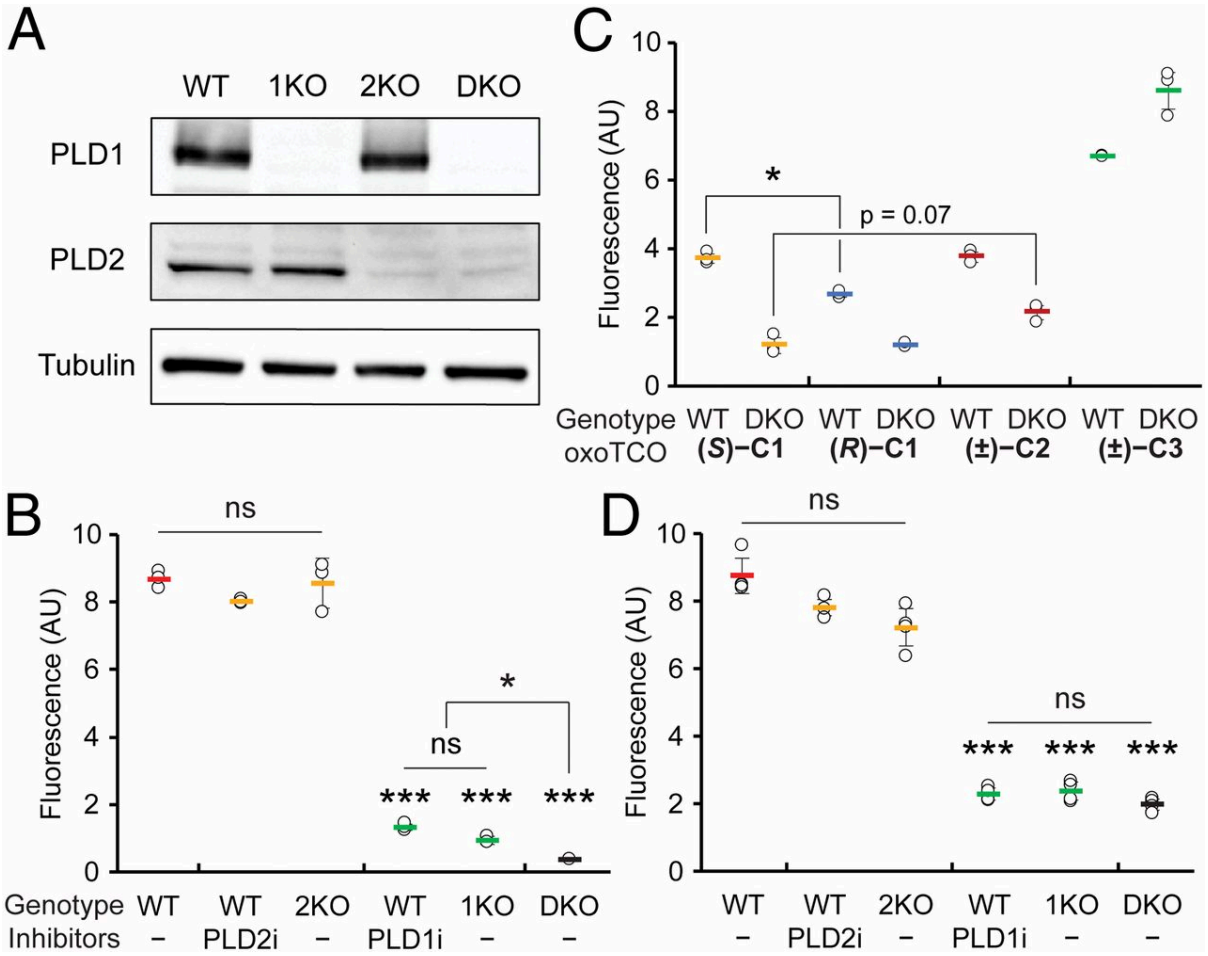

Figure 2.12: oxoTCO alcohols are effective and selective reporters of endogenous human PLD activity. (A and B) Generation and validation of PLD1 knockout (1KO), PLD2 knockout (2KO), or PLD1/2 double knockout (DKO) HeLa cells made by using CRISPR/Cas9-mediated mutagenesis. (A) Knockout was verified by Western blot analysis for PLD1, PLD2, or as a loading control, α-tubulin. (B) The indicated cells were pretreated with the indicated PLD inhibitor (PLD1i, VU0359595; or PLD2i, VU0364739) or DMSO for 30 min, followed by transphosphatidylation with 3-azido-1-propanol (1 mM) under PMA stimulation (100 nM) for 20 min, rinsing with PBS solution, and labeling with a cyclooctyne–BODIPY conjugate (1 μM) for 10 min, rinsing for 20 min, and analysis by flow cytometry. Indicated are mean fluorescence

intensities in arbitrary units (AU). (C and D) Evaluation of oxoTCO alcohols as selective probes for endogenous PLD enzymes. Shown are mean fluorescence intensities from flow cytometry experiments wherein IMPACT labeling was performed as in A, except using the indicated oxoTCO alcohol (C) or (S)-oxoTCO–C1 (3 mM, 5 min; D) in place of 3-azido-1-propanol and Tz–BODIPY (0.33 μM, 1 min, no subsequent rinse) in place of cyclooctyne–BODIPY. Statistical significance was assessed by using a 1-way ANOVA followed by Games–Howell post hoc analysis. Asterisks directly above data points denote statistical significance compared with WT without the presence of inhibitors, asterisks above horizontal lines denote statistical significance comparing the 2 indicated data groups, and error bars represent SD (*$P < 0.05$ and ***$P < 0.001$; ns, not significant).

To evaluate the panel of oxoTCO alcohols as probes for IMPACT, we performed in-cell transphosphatidylation with PMA stimulation followed by a one-minute IEDDA reaction with Tz–BODIPY and quantification by flow cytometry. Gratifyingly, the oxoTCO–C1 and –C2 were suitable probes for IMPACT in cells (Fig. 2.12C). (*S*)-oxoTCO–C1 was the most efficient alcohol, roughly 50% more efficient than (*R*)-oxoTCO–C1. Background labeling, i.e., labeling that occurred even in DKO cells or in the presence of FIPI, trended slightly higher with oxoTCO–C2 and was significantly higher with oxoTCO–C3, whose linkers are more hydrophobic. We thus used (*S*)-oxoTCO–C1 for all subsequent studies. We note that the optimized IEDDA-based IMPACT protocol does not have as high sensitivity (i.e., signal-to-background) as SPAAC-based IMPACT (Fig. 2.12B and 2.12D), likely due to differences in PLD-mediated turnover rates of the bulky (*S*)-oxoTCO–C1 in the transphosphatidylation step compared to the small, linear azidopropanol.

We then ascertained whether (*S*)-oxoTCO–C1 was a substrate of both PLD isoforms. We compared the extent of PMA-stimulated IMPACT labeling in WT cells to that in the relevant PLD knockout cells or in WT cells treated with isoform-selective PLD inhibitors and observed identical relative labeling efficiencies to those obtained using SPAAC-based IMPACT (Fig. 2.12B and 2.12D). These experiments clearly indicated that (*S*)-oxoTCO–C1 was a substrate of PLD1.

The differences in mean fluorescence intensities of cellular IMPACT fluorescence quantified by flow cytometry between PLD2i-treated or 2KO cells and WT cells (or between PLD1i-treated or 1KO cells and DKO cells), however, were subtle or not statistically significant. As to whether (*S*)-oxoTCO–C1 might be a substrate of PLD2, HPLC analysis of transphosphatidylation products from PLD1i-treated or 1KO cells were suggestive (Fig. 2.11). To gain support for this hypothesis, we turned to a gain-of-function approach to test whether (*S*)-oxoTCO–C1 was a substrate of PLD2. We assessed the level of IMPACT labeling using (*S*)-oxoTCO–C1 due to PLD2 by overexpressing fluorescently tagged PLD2 in DKO cells. Gratifyingly, we observed IMPACT labeling when overexpressing WT PLD2 but not a catalytically dead variant (K758R) (Fig. 2.13).

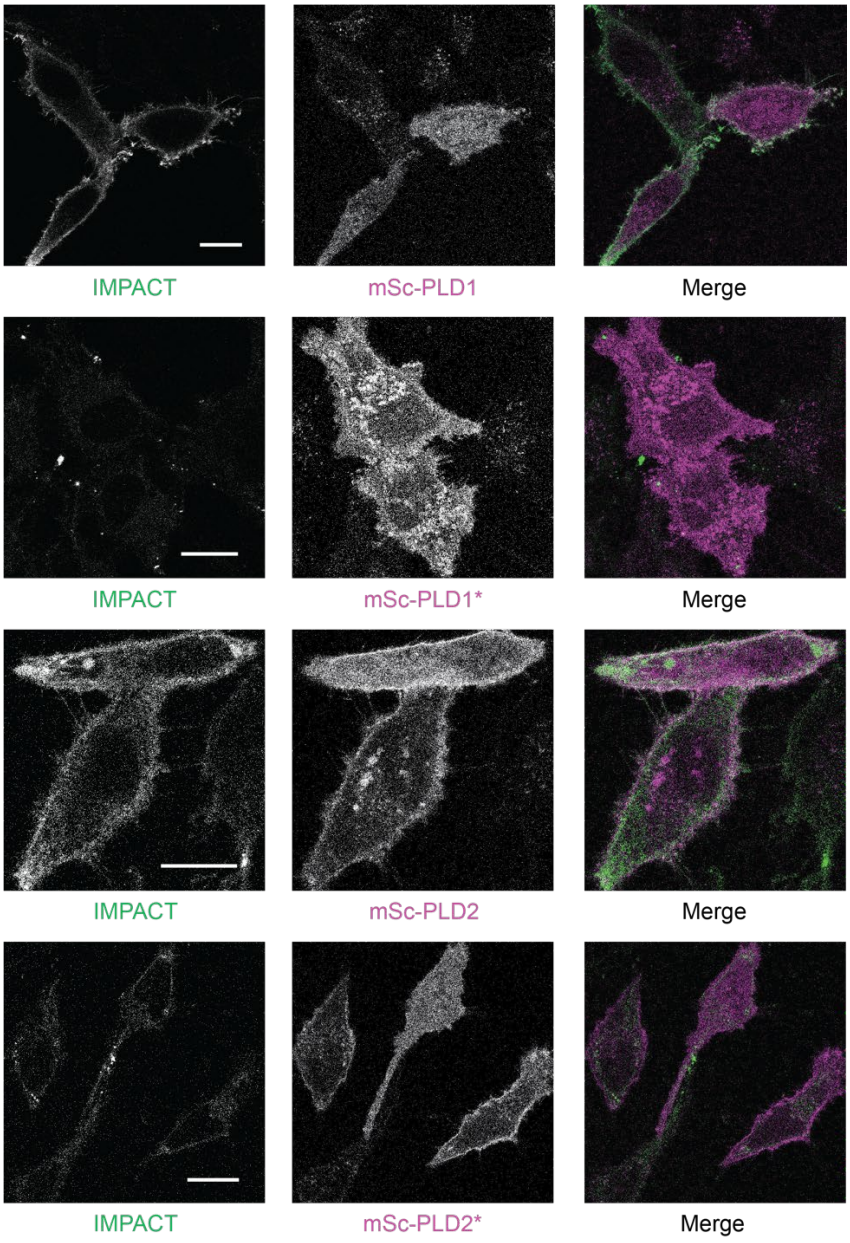

Figure 2.13: (S)-oxoTCO–C1 is a substrate of both human PLD1 and PLD2 in cells. PLD1/2 DKO HeLa cells were transfected with the indicated mScarlet-i (mSc)-tagged wild-type or catalytic dead (asterisk) variant of human PLD1 or PLD2. One day after transfection, cells were labeled via IMPACT using (*S*)-oxoTCO–C1. Briefly, cells were incubated with both (*S*)-oxoTCO–C1 (3 mM) and PMA for 5 min, rinsed for 1 min, and then Tz-BODIPY (1 μM) was

added and live-cell, time-lapse confocal imaging was performed. Shown is the 9 s timepoint of the time-lapse movie. In the merged images, IMPACT is green, PLD is magenta, and colocalization appears as white. Note the appearance of IMPACT fluorescence at the plasma membrane, the site of PMA-stimulated PLD1 activity and constitutive PLD2 activity, in cells expressing active but not catalytic-dead PLD1 and PLD2, respectively. Scale bars: 20 μm.

We note that these data do not allow us to establish whether PLD1 and PLD2 are equally efficient in using (*S*)-oxoTCO–C1 as a transphosphatidylation substrate. Ultimately, whether due to lower PLD2 expression in this cell line, less efficient activation of PLD2 by PMA [18], or (*S*)-oxoTCO-C1 being a less efficient substrate for PLD2 than for PLD1, in this setting PLD1 is the major isoform contributing to IMPACT signal.

IMPACT with (*S*)-oxoTCO–C1 reveals PM localization of active PLD

Using confocal microscopy, we evaluated the subcellular localization of IEDDA-based IMPACT using (*S*)-oxoTCO–C1 labeling with PMA stimulation followed by a one-minute IEDDA reaction with Tz–BODIPY (Fig. 2.14A). We observed substantial cellular fluorescence, and addition of FIPI during the transphosphatidylation step or the use of DKO cells abrogated the labeling, again demonstrating the specificity of our probes to active PLD enzymes (Fig. 2.14B). Excitingly, a major portion of the labeling was apparent at the PM, in contrast to SPAAC-based IMPACT using azidopropanol, which requires a 20–30 min SPAAC labeling and rinse-out and gives exclusively intracellular labeling. Colocalization analysis using both conventional confocal microscopy and super-resolution structured illumination microscopy indicated that the IEDDA-based IMPACT predominantly labeled the PM, ER, and Golgi

apparatus, with minimal labeling observed of endosomes, lysosomes, and mitochondria (Figs. 2.15 and 2.16).

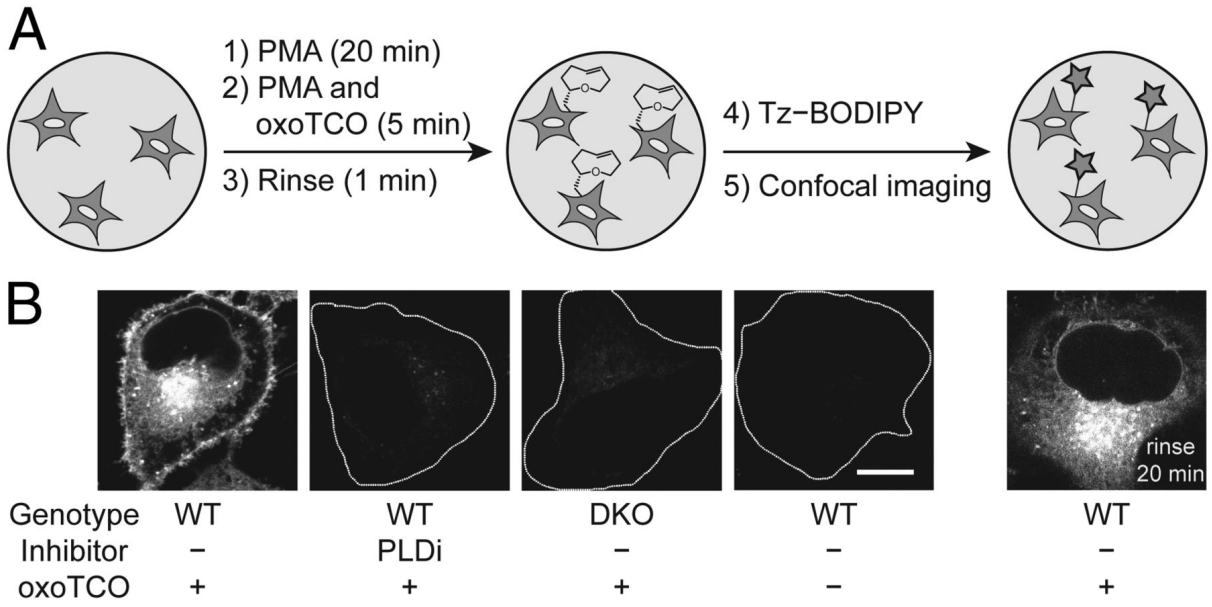

Figure 2.14: IMPACT with (S)-oxoTCO–C1 reveals the PM localization of active PLD enzymes stimulated with a phorbol ester. (A) Experimental setup: endogenous PLD enzymes were stimulated with PMA (100 nM, 20 min), followed by transphosphatidylation with (S)-oxoTCO–C1 (3 mM, 5 min, in the presence of PMA), rinse (1 min), and IEDDA reaction with Tz–BODIPY (0.33 μM, 1 min), followed by confocal microscopy imaging. (B) Representative images of HeLa cells labeled as described in A with the indicated negative controls. Where indicated, PLDi (the pan-PLD inhibitor FIPI) was applied 30 min before and during the transphosphatidylation step. DKO, PLD1/2 double knockout cells. Far right: cells were rinsed after the IEDDA reaction for 20 min before imaging. White dotted lines indicate cell outlines in the negative controls. (Scale bar: 10 μm.)

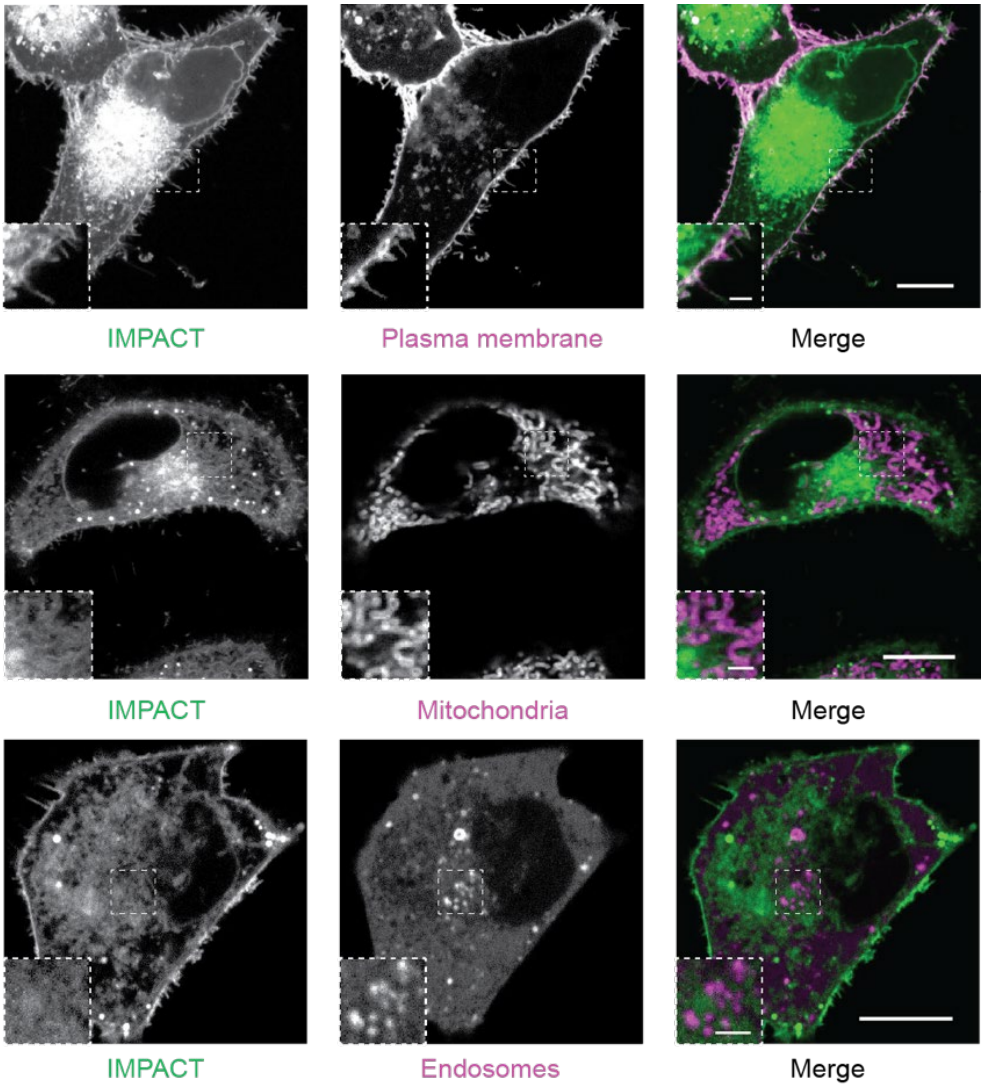

Figure 2.15: Colocalization of IEDDA-based IMPACT with organelle markers by confocal microscopy. HeLa cells were transfected with markers of various organelles (Plasma membrane: PM-mRFP; Mitochondria: OMP25(transmembrane domain)-mCherry; Endosomes: EEA1-mRFP). One day after transfection, cells were labeled via IMPACT using (*S*)-oxoTCO–C1. Briefly, cells were stimulated with PMA for 20 min and then treated with (*S*)-oxoTCO–C1 (3 mM) for 5 min in the continued presence of PMA, rinsed for 1 min, and then imaged by live-cell confocal microscopy. In the merged images, IMPACT is green, the

organelle marker is magenta, and colocalization appears as white. Note partial colocalization under this pseudo-steady state labeling protocol with a plasma membrane marker and minimal colocalization with markers of mitochondria and endosomes. Scale bars: 10 μm for full-size images and 2 μm for zoomed-in regions.

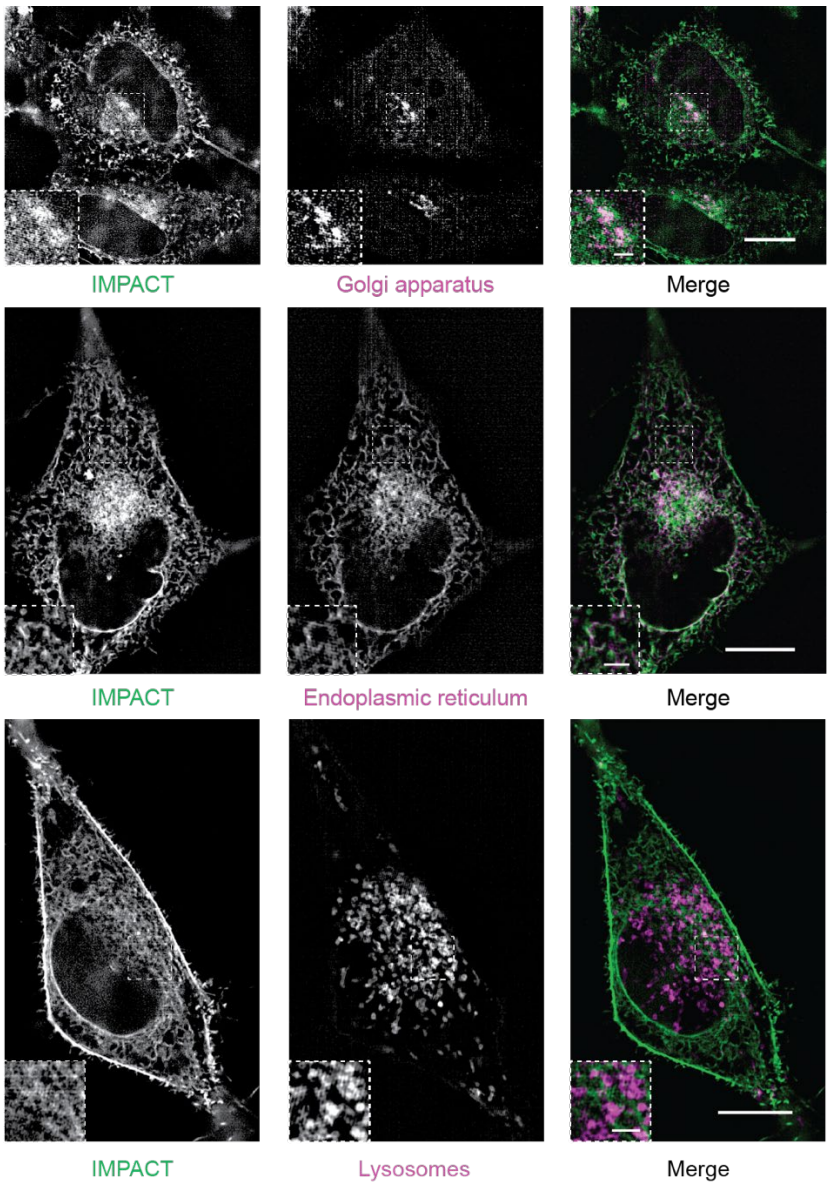

Figure 2.16: Colocalization of IEDDA-based IMPACT with organelle markers by super-resolution structured illumination microscopy. HeLa cells were transfected with markers of various organelles (Golgi apparatus: mCherry-P4M-SidM; Endoplasmic reticulum: STIM1-mRFP; Lysosomes: LAMP1-mRFP). One day after transfection, cells were labeled via IMPACT using (*S*)-oxoTCO–C1. Briefly, cells were stimulated with PMA for 20 min and then treated with (*S*)-oxoTCO–C1 (3 mM) for 5 min in the continued presence of PMA, rinsed for 1

min, and then imaged by live-cell super-resolution structured illumination microscopy. In the merged images, IMPACT is green, the organelle marker is magenta, and colocalization appears as white. Note partial colocalization under this pseudo-steady state labeling protocol with markers of the endoplasmic reticulum and Golgi apparatus and minimal colocalization with a marker of lysosomes. Scale bars: 10 μm for full-size images and 2 μm for zoomed-in regions.

We hypothesized that IEDDA-based IMPACT successfully revealed the expected PM localization of PMA-stimulated PLD activity because of the rapid timescale of the labeling: 5 min of (*S*)-oxoTCO–C1, a quick rinse, a 1-min IEDDA reaction with Tz–BODIPY, and imaging immediately afterward. To test this hypothesis, we performed a chase experiment by incubating the IMPACT-labeled cells at 37 ºC for an additional 20 min, followed by imaging, and observed entirely intracellular labeling, similar to the spatial pattern created by SPAAC-based IMPACT [33] (Fig. 2.14B, far right). These results suggested that after 20 min, the BODIPY-labeled phospholipids had been fully internalized.

Real-time IMPACT enables precise determination of PLD localization

Up to this point, we had not taken advantage of a key benefit of the TCO–tetrazine IEDDA, namely its fluorogenicity [48,54]. Tz–BODIPY is only very dimly fluorescent and experiences a 1600-fold increase in brightness upon IEDDA reaction [51]. We envisioned that we could adapt this oxoTCO-based IMPACT so that the IEDDA reaction would be monitored in real time on the microscope, allowing us to visualize the localization of fluorescent lipids with no time delay. The optimized protocol, which we termed RT-IMPACT (for real-time IMPACT), involves the identical 5-min (*S*)-oxoTCO–C1 labeling under PMA stimulation (or, as described later, stimulation with alternate agonists), followed by a quick rinse and time-lapse

imaging prior to and during the IEDDA reaction with Tz–BODIPY (Fig. 2.17A). With these tools, we would be able to visualize the precise localizations of the TCO-lipid reporters with rapid temporal resolution (seconds), limited only by microscope acquisition times and the IEDDA's intrinsic kinetics.

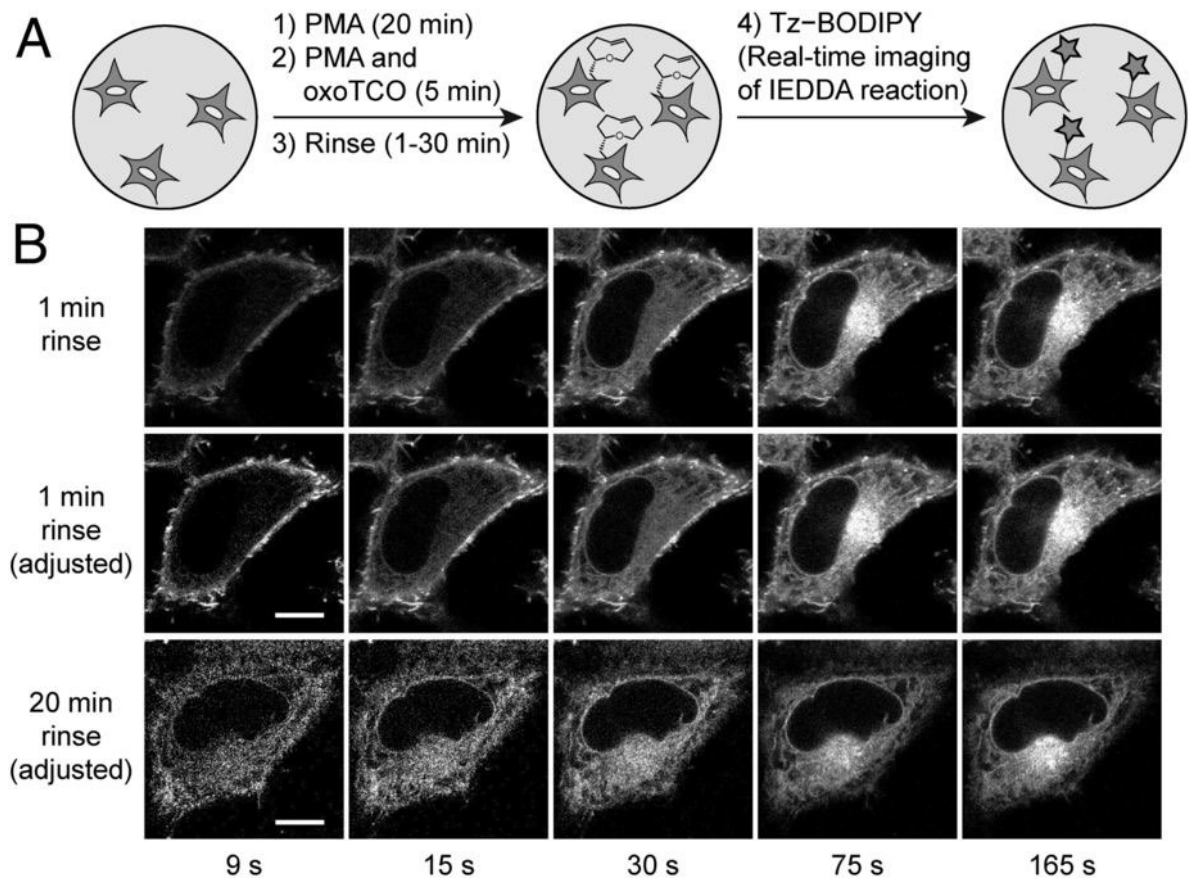

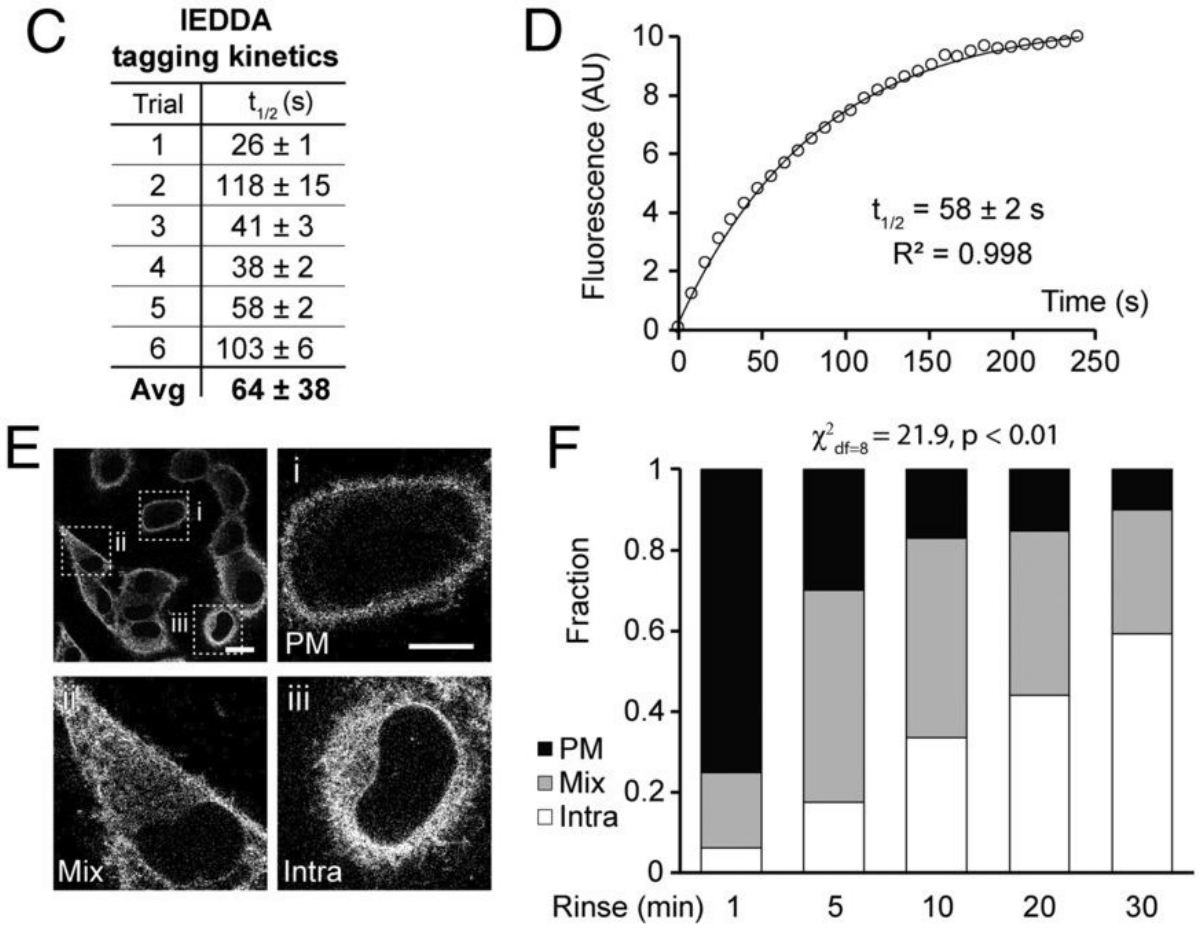

Figure 2.17: Real-time IMPACT enables precise determination of the subcellular localization of active PLD enzymes. (A) The experimental setup for RT-IMPACT is the same as indicated in Fig. 2.14 except that IEDDA reaction with Tz–BODIPY is monitored in real time by time-lapse confocal microscopy. (B) Representative images from time-lapse RT-IMPACT imaging of HeLa cells. The rinse (chase step) following the transphosphatidylation with (S)-oxoTCO–C1 and before IEDDA tagging was 1 min (Top and Middle) or 20 min (Bottom). (Top) Images are shown with identical intensity settings to facilitate visualization of reaction progress. (Middle and Bottom) Fluorescence intensities of the 9-, 15-, and 30-s time points have been brightened to facilitate visual comparison of localization of the IMPACT signal at different time points. (C and D) Quantification of the kinetics of the IEDDA tagging reaction based on total

cellular fluorescence from 6 independent experiments (where the graph represents trial 5, with circles indicating data points, the curve indicating an exponential fit, and R2 indicating the coefficient of determination of the fit) with n = 8 to 16 cells for each trial and average (Avg) reaction half-life ($t_{1/2}$) indicated as mean ± SD. (E and F) Quantification of the subcellular localizations of RT-IMPACT fluorescent signal at the 9-s time point of the IEDDA reaction as a function of the post-transphosphatidylation chase step, i.e., the rinse time after (S)-oxoTCO–C1 labeling and before IEDDA tagging. Cells were blindly scored as having plasma membrane (PM, black), intracellular (Intra, white), or a combination of PM and intracellular (Mix, gray) IMPACT fluorescence. y axis indicates fraction of cells with the indicated localization. (E, Top Left) Representative zoomed-out image of a population of cells at the 9-s time point from a 20-min rinse time point from F, with examples of PM (i), mix (ii), and intra (iii) localizations indicated in the other panels. (Scale bars: B and E, i–iii, 10 μm; E, Top Left, 20 μm.) Statistical significance was assessed by using a χ^2 test for independence, with the χ^2 value (df, degrees of freedom) and associated P value indicated. Each bar contains data of 3 to 5 biological replicates with n = 30 to 72 total cells.

Time-lapse RT-IMPACT movies, with frames acquired every 3 seconds, revealed several observations (Fig. 2.17B). First, total cellular fluorescence increased over the first minute and then stabilized, indicating that the IEDDA reaction had reached completion during that time period (Fig. 2.17B, top row). By measuring total cellular fluorescence over time, we calculated the half-life of IEDDA tagging of (*S*)-oxoTCO–C1-labeled lipids with Tz–BODIPY (0.33 μM and presumably under pseudo-first order conditions) to be 64 ± 38 s (Fig. 2.17C–D), in line with the reaction's intrinsically high kinetics [48].

Second, the fluorescence at early timepoints is almost entirely located at the PM (Fig. 2.17B, middle row). These data suggest that the bulk of PMA-stimulated PLD activity in HeLa cells is at the PM, though an alternate possibility is differential trafficking rates of PLD-generated PA compared to two different types of phosphatidyl alcohols generated via IMPACT, i.e., those whose head group is TCO or BODIPY, which we will address below. Third, when we examined cells that had been rinsed for 20 min prior to IEDDA and at an early timepoint of the time-lapse movie after addition of Tz–BODIPY (9 s), we observed a distribution of localizations, which we classified as either "PM" for predominantly plasma membrane, "intra" for predominantly intracellular, or "mix" for a mixture of PM and intra (Fig. 2.17B, bottom row, and E). This distribution of localizations at this early timepoint of the IEDDA reaction indicates that diffusion of unreacted fluorophore is not rate-limiting compared to IEDDA reaction kinetics. Put another way, the data show that TCO-lipids on intracellular organelle membranes have similar access to Tz–BODIPY compared to those at the PM.

Using this localization classification system (PM, mix, and intra), we performed pulse-chase experiments to examine TCO-lipid trafficking, using as a readout the distribution of localizations at the 9 s timepoint of a time-lapse movie. Here, the chase was a 37 ºC rinse-out after the 5-minute transphosphatidylation step and prior to the real-time IEDDA reaction. As we increased the chase time prior to IEDDA, the 9 s timepoint exhibited fewer "PM" cells and more "mix" and "intra" cells (Fig. 2.17F). We conclude that, though the TCO-lipid is internalized from the PM, the kinetics of this process, with a half-life of approximately 10 min (Fig. 2.17F), is longer than that of the optimized RT-IMPACT protocol. Thus, these data indicate that the localization of fluorescent lipids observed at the early timepoints of the IEDDA tagging reflects the sites of active PLD enzymes, prior to major trafficking of the lipid reporters.

As well, we observed RT-IMPACT-derived fluorescence at the plasma membrane at the 9 s timepoint of time-lapse movies in PMA-stimulated DKO cells overexpressing fluorescently tagged PLD1 or PLD2 but not catalytic dead versions of these enzymes (Fig. 2.13). These experiments further suggest that RT-IMPACT reveals the expected localizations of the active subsets of these enzymes, which are expected to be at the plasma membrane under PMA stimulation.

Real-time IMPACT reveals PM-to-ER trafficking

An obvious feature of the RT-IMPACT time-lapse movie is that the fluorescent lipids, which were predominantly at the PM at the early timepoints (i.e., 9 s), were rapidly internalized, first over the next 15-30 seconds to the ER and then subsequently to the perinuclear Golgi apparatus (Fig. 2.17B, middle row). This trafficking from the PM to internal organelle membranes appeared to be unidirectional (Figs. 2.14B, far right and 2.17B, bottom row).

The ability to monitor the trafficking of the labeled lipids from the very moment that they become fluorescently tagged allowed us to gain information about their internalization pathway and its kinetic properties. Notably, the first apparent intracellular destination of the IMPACT-derived fluorescent lipids was the ER, not endosomes, suggesting that they were internalized predominantly not via endocytosis (Fig. 2.17B). Based on such a localization, we propose that the lipids were internalized by vesicle-independent pathways mediated by lipid transfer proteins that largely operate at ER-PM contact sites [34,55]. These contact sites, or junctions, are assemblies where the two organelle membranes are located within 10-20 nm of each other to facilitate rapid lipid transport and other signaling processes [55].

By quantifying the extent of colocalization of the RT-IMPACT labeling with an ER marker over time, we measured the half-life of fluorescent lipid PM-to-ER trafficking, determining it to be 104 ± 36 s (Fig. 2.18 A–B). We envision that this type of RT-IMPACT-based experiment, i.e., tracking the fate of the BODIPY-labeled lipid, might prove useful for studying lipid trafficking mediated by lipid transfer proteins, suggesting applications of RT-IMPACT entirely separate from applications to visualize locations of PLD signaling. Notably, some lipid transfer proteins interact only with the lipids' hydrophobic tails and have little preference for head group, suggesting that they may transport the BODIPY-labeled phospholipids similarly to natural glycerophospholipids [56].

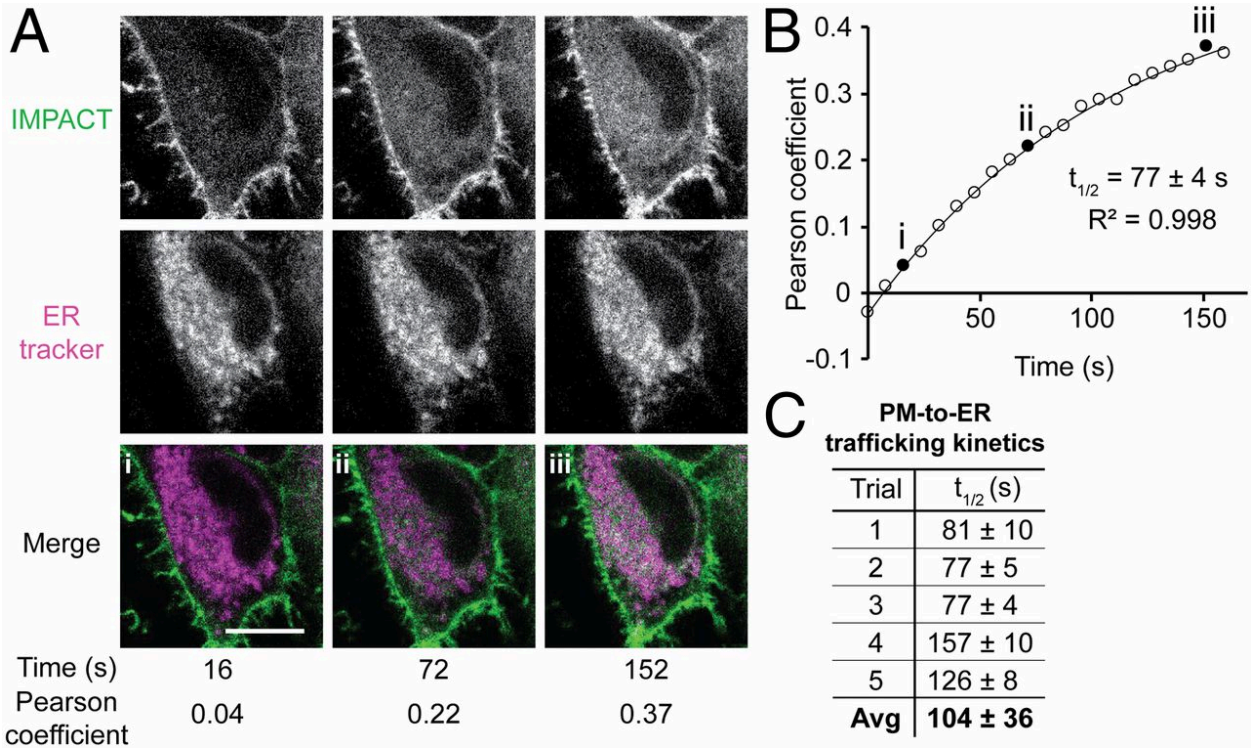

Figure 2.18: Real-time IMPACT reveals PM-to-ER trafficking of fluorescent lipids. (A) Representative images of HeLa cells from a 2-color time-lapse movie. HeLa cells were incubated with ER tracker, PMA, and (S)-oxoTCO–C1 for 5 min and rinsed for 1 min before

time-lapse imaging. Values of Pearson correlation coefficients of colocalization between IMPACT (green) and ER tracker (magenta) were determined. Colocalization appears as white in merge. (B) Representative exponential fitting of kinetics of PM-to-ER trafficking. Plotted is increase in colocalization (Pearson coefficient) between IMPACT and ER tracker over time. Circles are data points, and the curve indicates an exponential fit. Filled circles (i–iii) correspond to Pearson coefficients for the images shown in A, and R2 indicates the coefficient of determination of the fit. (C) Summary of quantification of PM-to-ER trafficking kinetics from 5 independent experiments (where the graph in B represents trial 3) with n = 8 to 16 cells for each trial and average (Avg) half-life of internalization ($t_{1/2}$) indicated as mean ± SD. (Scale bar: 10 μm.)

Applying real-time IMPACT to visualize differences in active PLD localization elicited by different stimuli

Finally, having validated RT-IMPACT, we sought to apply it to evaluate the localizations of PLD signaling activity elicited by different physiological stimuli. We focused on agonists that would specifically activate either GPCR or RTK signaling pathways, which both lead to PLD-mediated PA biosynthesis. In these experiments, localization was determined by examining the 9 s timepoint after Tz–BODIPY addition of a time-lapse movie of the IEDDA reaction, to avoid effects of fluorescent lipid trafficking, and evaluating the fraction of cells with “PM”, “mix”, and “intra” localizations. We varied two parameters: the type of stimulus and the amount of time the cells were exposed to the stimulus prior to the 5-min transphosphatidylation step.

First, to assess GPCR-mediated signaling, we generated HeLa cells stably expressing the M1 muscarinic receptor (M1R). Upon stimulation with its agonist oxotremorine-M (oxo-M), M1R activates $G_{\alpha q}$ to turn on phospholipase Cβ (PLCβ), which hydrolyzes phosphatidylinositol-4,5-bisphosphate ($PI(4,5)P_2$) to generate inositol trisphosphate and diacylglycerol [57,58], an allosteric activator of PKC. GPCR signaling also activates the RhoA GTPase, and both active PKC and RhoA can stimulate PLD activity downstream of GPCR activation [24].

RT-IMPACT revealed that, in the absence of oxo-M stimulation, HeLa cells exhibited a small amount of basal PLD activity, even under serum starvation, and its localization was intracellular (Fig. 2.19A, second vs. third sample; Fig. 2.19B, top; Fig. 2.19C, quantification). Exposure of cells to oxo-M led to an approximate doubling of PLD activity within the first 5 min of oxo-M stimulation (Fig. 2.19A, first vs. second sample), and treatment with isoform-selective PLD inhibitors revealed that this activity was predominantly due to PLD1 (Fig. 2.19A). Prolonged exposure to oxo-M led to attenuation of PLD activity, consistent with the known property of this system to desensitize under sustained oxo-M stimulation (Figs. 2.19A and 2.20A) [57,58]. The localization of PLD activity under oxo-M stimulation was nearly evenly split between PM, mix, and intra (Fig. 2.19B, bottom; Fig. 2.19C, quantification). Because this oxo-M-stimulated activity represented a roughly even mixture of M1R-derived and basal PLD activities (Fig. 2.19A), we conclude that the bulk of the M1R-stimulated PLD enzymes were located at the PM, either through translocation from intracellular locations or through activation of subsets that were previously located in this membrane.

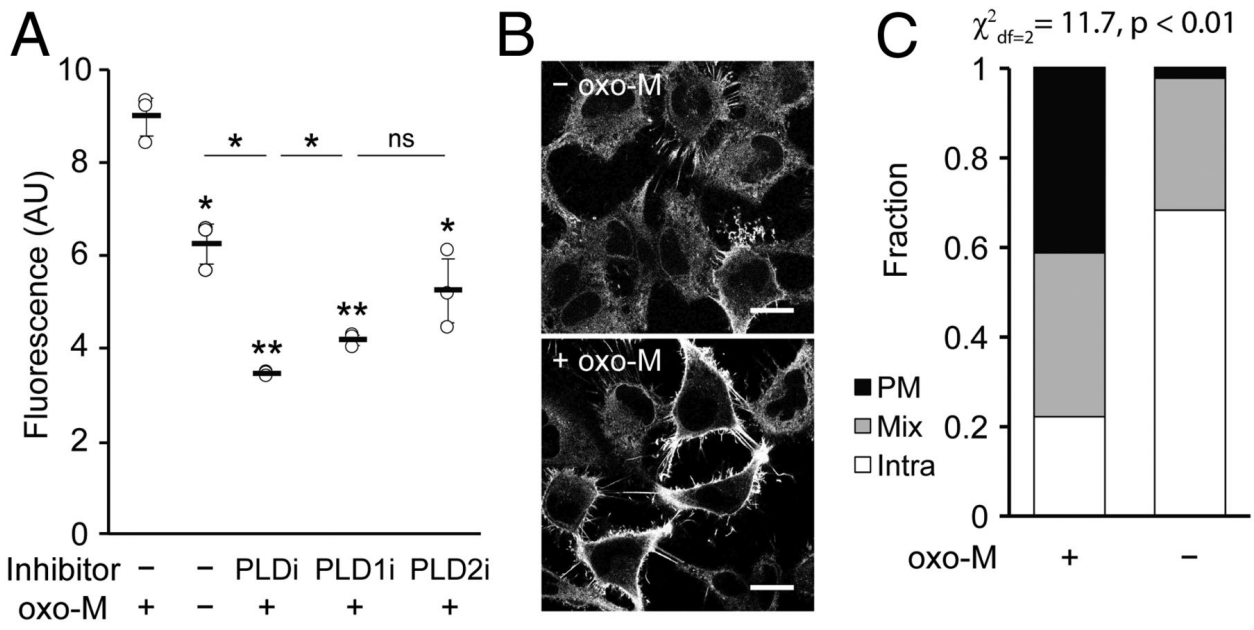

Figure 2.19: Muscarinic M1 receptor (M1R) activation leads to PLD activity that is predominantly at the plasma membrane. HeLa cells stably expressing M1R were labeled for RT-IMPACT by treatment with the indicated PLD inhibitor or DMSO for 30 min (A only) and then simultaneous treatment of (*S*)-oxoTCO–C1 in the presence or absence of oxo-M (5 min), rinsing (1 min), and IEDDA reaction with Tz–BODIPY (0.33 μM) for 1 min followed by flow cytometry analysis (A), with mean fluorescence intensity in arbitrary units (AU) indicated, or (B and C) in real time with time-lapse confocal images taken (B) and quantified (C) 9 s after the addition of Tz–BODIPY, using the PM/Mix/Intra rubric described in Fig. 2.17E−F. In B, the brightness of the –oxo-M image was increased to facilitate comparison of the localization of IMPACT-derived fluorescence in the 2 images. (Scale bars: 20 μm.) For A, statistical significance was assessed by using 1-way ANOVA followed by Games–Howell post hoc analysis. Asterisks directly above data points (*P < 0.05 and **P < 0.01; ns, not significant) denote statistical significance compared with the first sample (−inhibitor, +oxo-M), and error bars represent SD. For C, statistical significance was assessed by using a χ^2 test for

independence, with the χ^2 value (df, degrees of freedom) and associated P value indicated. Each bar contains data of 3 (−oxo-M) or 8 (+oxo-M) biological replicates, with n = 41 (−oxo-M) or 112 (+oxo-M) total cells.

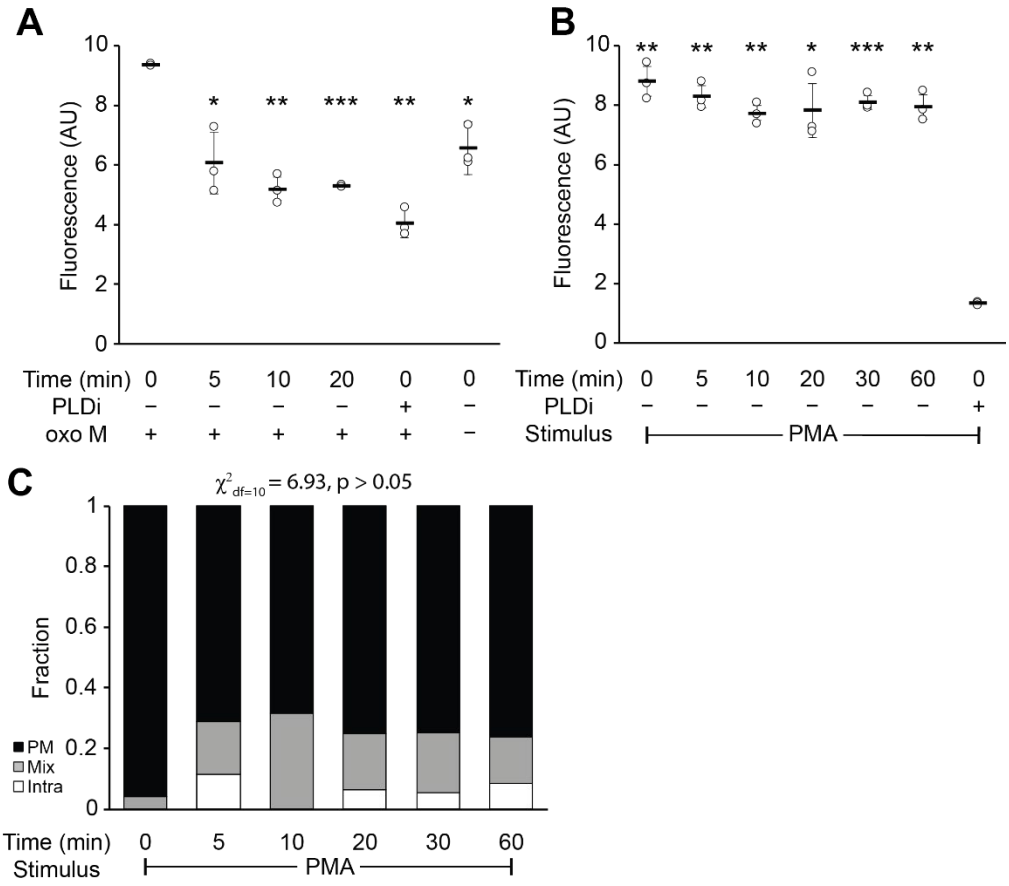

Figure 2.20: Muscarinic M1 receptor (M1R) stimulation or PMA treatment induces predominantly plasma membrane PLD activity in HeLa cells. (A) M1R stimulation activates PLD enzymes only within the first 5 min of M1R signaling. HeLa cells stably expressing M1R were treated with or without PLDi (FIPI) for 30 min and then treated with the M1R agonist oxotremorine-M (oxo-M) for the indicated amount of time, followed by treatment with (S)-oxoTCO (3 mM) for 5 min in the continued presence of oxo-M. Cells were then rinsed, treated with Tz–BODIPY (0.33 μM) for 1 min, and analyzed by flow cytometry. (B–C) PMA

stimulation of cells leads to sustained activity (B) at the plasma membrane (C). (B) HeLa cells were labeled and analyzed as in (A), substituting oxo-M for PMA. (C) HeLa cells were labeled as in (A), except that the IEDDA reaction with Tz–BODIPY was monitored in real-time by confocal microscopy. The 9 s timepoint of the IEDDA reaction was quantified using the PM/Mix/Intra rubric described in Figure 2.17E–F. For (A–B), mean fluorescence intensity is in arbitrary units (AU), each data point represents a technical replicate from a single experiment (n=3), at least two biological replicate experiments were performed, each giving similar results, and error bars, where indicated, represent standard deviation. Statistical significance was assessed using a one-way ANOVA followed by Games-Howell post-hoc analysis. Asterisks directly above data points (* $p<0.05$, ** $p<0.01$, ***, $p>0.001$) denote statistical significance compared to the first sample (– PLDi, + oxo-M) for (A) and compared to the last sample (+ PLDi) for (B). For (C), data were averaged from at least three experiments. Each bar contains data from n=3–4 biological replicates with n=42–71 total cells. Statistical significance was assessed using a chi-squared test for independence, with the chi-squared value (df = degrees of freedom) and associated p value indicated.

Second, we examined the localization of PLD signaling during RTK activation. Here, we stimulated NIH 3T3 cells with platelet-derived growth factor (PDGF), the agonist for the PDGF receptor (PDGFR), which activates PLDs through PLC-mediated $PI(4,5)P_2$ hydrolysis, but through a different PLC isoform (PLCγ) from GPCR pathways [59–61]. PDGFR additionally stimulates PLDs through activation of small Ras superfamily GTPases, including Arf, Rho, and Rac family GTPases, which can localize to several organelle membranes [62–65].

For these experiments, we varied the amount of time that the PDGF stimulus was applied prior to the RT-IMPACT labeling. We found that PDGF treatment resulted in a robust and sustained stimulation of PLD enzymes over 60 min (Fig. 2.21A) and that such activity is due predominantly to the PLD1 isoform (Fig. 2.22A). To our surprise, we discovered that the localization of the RT-IMPACT signal was predominantly intracellular for all timepoints evaluated during the time course of PDGF stimulation (Figs. 2.21B and 2.22B–C). As a control, we examined PMA stimulation in this cell line and found that, similar to in HeLa cells, it led to predominantly PM-localized PLD activity after at least 10 min of stimulation prior to RT-IMPACT (Figs. 2.21C and 2.22B–C). Thus, RT-IMPACT labeling suggests that PDGFR signaling leads to activation of predominantly intracellular pools of PLD1, in contrast to M1R signaling or PMA stimulation, which leads to activation of PLD enzymes mostly at the PM.

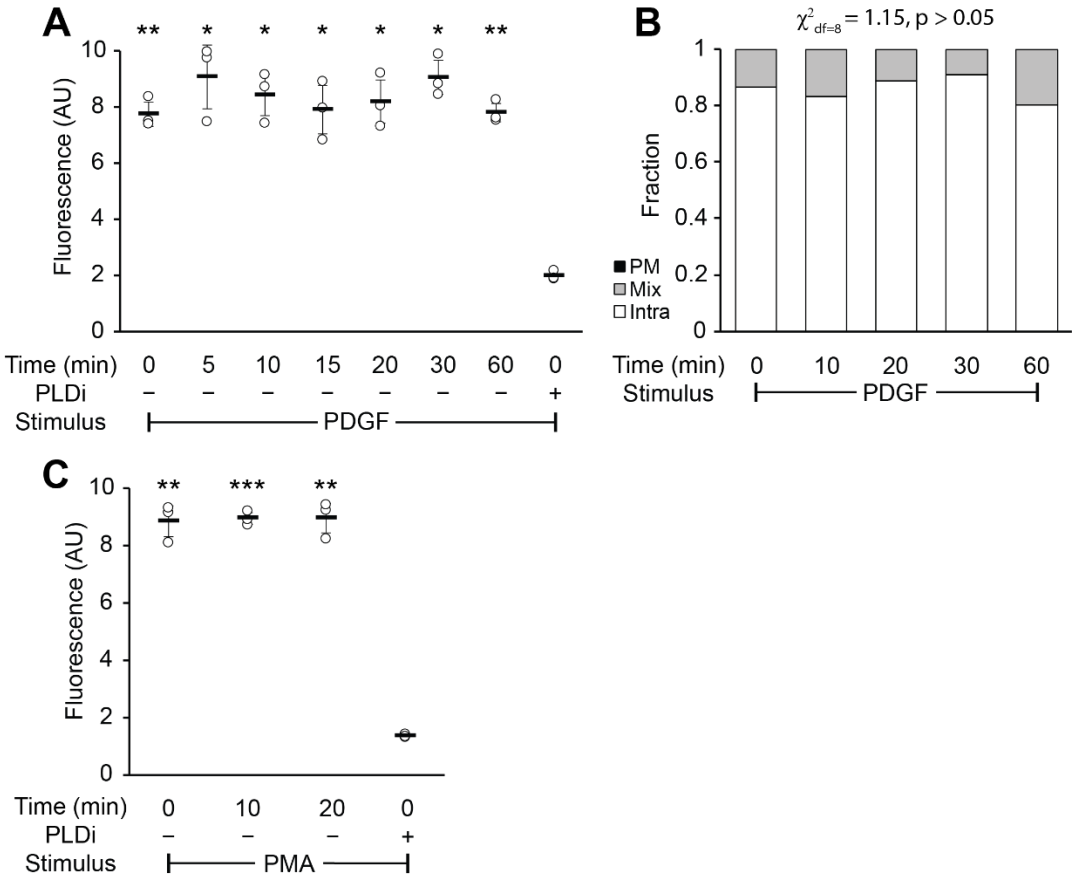

Figure 2.21: Platelet-derived growth factor (PDGF) receptor stimulation induces intracellular PLD activity in NIH 3T3 cells. (A) PDGF receptor stimulation activates PLD enzymes for at least 60 min of PDGF stimulation. NIH 3T3 cells were treated with or without PLDi (FIPI) for 30 min and then treated with PDGF for the indicated amount of time, followed by treatment with (S)-oxoTCO (3 mM) for 5 min in the continued presence of PDGF. Cells were then rinsed, treated with Tz–BODIPY (0.33 μM) for 1 min, and analyzed by flow cytometry. (B) PDGF stimulation over a 60 min time course leads to PLD activity at intracellular membranes. NIH 3T3 cells were labeled as in (A), except that the IEDDA reaction with Tz–BODIPY was monitored in real-time by confocal microscopy. The 9 s timepoint of the IEDDA reaction was quantified using the PM/Mix/Intra rubric described in Figure 2.17E–F. (C) NIH 3T3 cells

exhibit sustained PLD activity over at least 20 min of PMA stimulation. Cells were labeled and analyzed as in (A), substituting PDGF for PMA. For (A) and (C), mean fluorescence intensity is in arbitrary units (AU), each data point represents a technical replicate from a single experiment (n=3), at least two biological replicate experiments were performed, each giving similar results, and error bars represent standard deviation. Statistical significance was assessed using a one-way ANOVA followed by Games-Howell post-hoc analysis. Asterisks directly above data points (* $p<0.05$, ** $p<0.01$, ***, $p>0.001$) denote statistical significance compared to the last sample in each set (+ PLDi). For (B), data were averaged from at least three experiments. Each bar contains data from n=3–4 biological replicates with n=57–78 total cells. Statistical significance was assessed using a chi-squared test for independence, with the chi-squared value (df = degrees of freedom) and associated p value indicated.

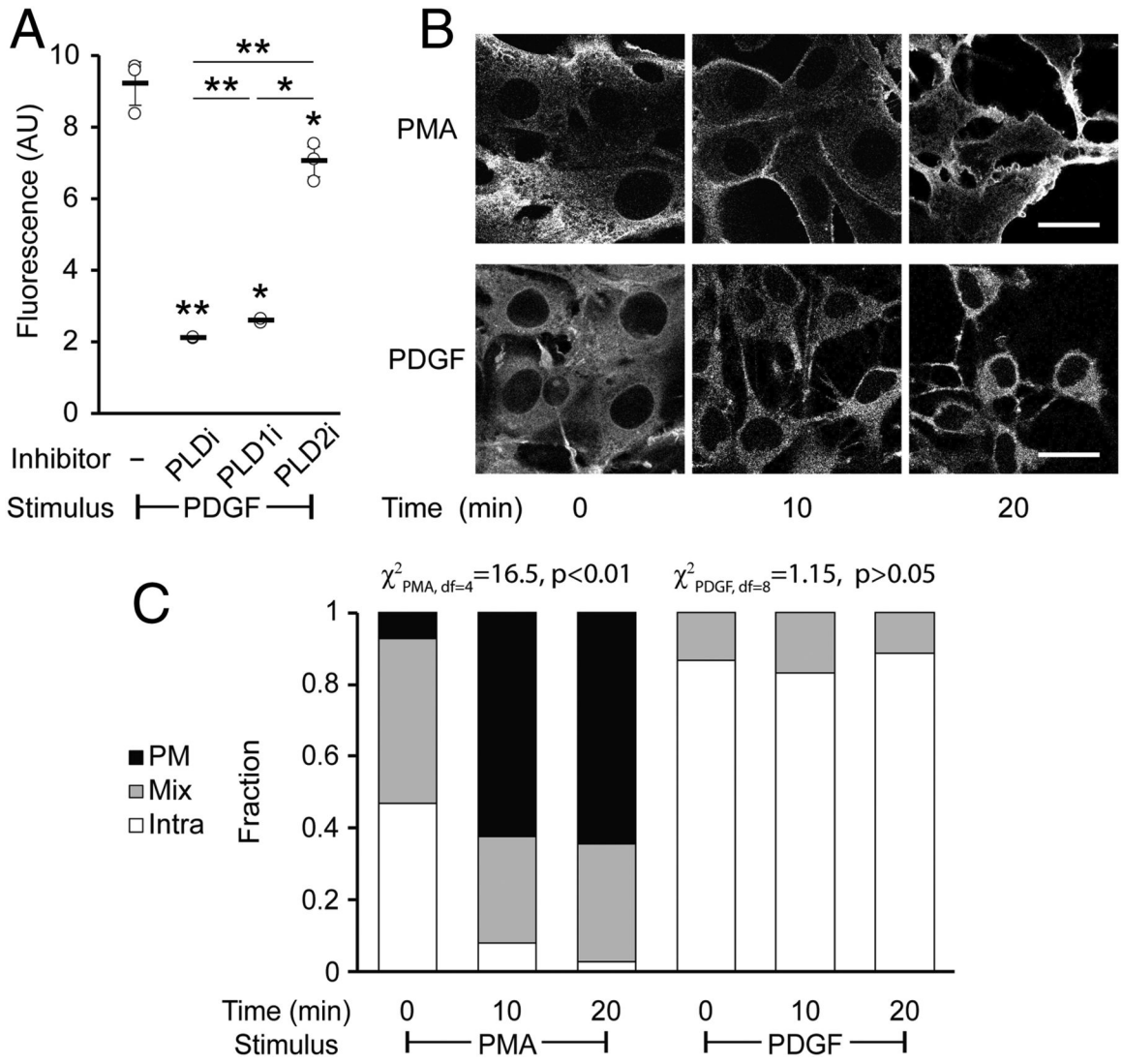

Figure 2.22: Platelet-derived growth factor (PDGF) receptor activation leads to intracellular PLD activity. NIH 3T3 cells were labeled for RT-IMPACT by treatment with the indicated PLD inhibitor or DMSO for 30 min (A only). Cells were stimulated with PDGF or PMA for the indicated time (0 to 20 min) followed by addition of (S)-oxoTCO–C1 in the continued presence of PDGF or PMA (5 min) and then rinsed (1 min), and the IEDDA reaction with Tz–BODIPY (0.33 μM) was performed for 1 min followed by flow cytometry analysis (A), with mean fluorescence intensity in arbitrary units (AU) indicated, or (B and C) in real time with

time-lapse confocal images taken (B) and quantified (C) 9 s after the addition of Tz–BODIPY, using the PM/Mix/Intra rubric described in Fig. 2.17E−F. (Scale bars: 20 μm.) For A, statistical significance was assessed by using 1-way ANOVA followed by Games–Howell post hoc analysis. Asterisks directly above data points (*P < 0.05 and **P < 0.01) denote statistical significance compared with the first sample (−inhibitor), asterisks above horizontal lines denote statistical significance comparing the 2 indicated samples, and error bars represent SD. For C, statistical significance was assessed by using a χ^2 test for independence, with the χ^2 value (df, degrees of freedom) and associated P value indicated. Each bar contains data of 3 to 4 biological replicates with n = 58 to 78 total cells for PDGF and 3 to 6 biological replicates, with n = 41 to 95 cells for PMA.

Discussion

Localized production or accumulation of intracellular signaling agents is a key feature of signal transduction pathways. Chemical imaging tools have helped pave the way to understand biological signaling pathways dependent on second messengers [2–4,66]. We initiated this study with the goal of establishing a tool to enable precise monitoring of the production of the lipid second messenger PA by PLD enzymes. Previously, we had established that PLDs, which physiologically catalyze hydrolysis of phosphatidylcholine to release PA and choline, can accept primary azido alcohols in transphosphatidylation reactions to generate azido phosphatidyl alcohol reporters of PLD activity [33]. Subsequent tagging of these azido lipids with cell-permeable cyclooctyne–fluorophore conjugates, followed by rinse-out of excess unreacted fluorophore, enabled fluorescent tagging of intracellular membranes bearing PLD activity, in a method termed IMPACT. The lack of IMPACT labeling at the PM combined with the long

labeling and rinse-out times and the knowledge that lipids can diffuse and traffic rapidly throughout the cell led us to consider an alternative approach for precisely determining the subcellular locations of PLD signaling.

Taking advantage of rapid and fluorogenic IEDDA bioorthogonal chemistry, which has proven useful for tagging and imaging highly dynamic molecules such as lipids [67–69], we report here a real-time variant of IMPACT (RT-IMPACT). We have replaced azido alcohols with a bulky, hydrophilic *trans*-5-oxocene (oxoTCO)-containing primary alcohol [50], which acts as a replacement for the water co-substrate in the PLD active site. Following this transphosphatidylation step, excess oxoTCO alcohol is quickly rinsed away, and the locations of the oxoTCO-labeled lipids are then visualized within 10 seconds using time-lapse monitoring, in real time, of a no-rinse, IEDDA reaction with a fluorogenic tetrazine–BODIPY reagent (Tz–BODIPY).

In developing these tools, we discovered that human PLDs accept a wide group of TCO-containing primary alcohols as transphosphatidylation substrates, revealing a previously unappreciated tolerance of these enzymes for large, bulky side chains on the primary alcohol. However, carbocyclic TCO alcohols and even oxoTCO alcohols with longer aliphatic side chains did not effectively rinse out of cells, likely due to hydrophobicity, even though many were substrates of PLDs. This finding highlights the challenges of using TCO-based probes for metabolic labeling with small precursors, where the physicochemical properties of the bioorthogonal group dominate those of the overall probe, which in the case of our optimal alcohol, (*S*)-oxoTCO–C1, is simply the oxoTCO with a hydroxymethyl side chain.

Because the goal of RT-IMPACT was to faithfully report on the localization of PLD signaling activity (i.e., transphosphatidylation of PC to form reporter lipids occurring simultaneously with physiological PC hydrolysis to form PA), a key challenge we faced was to establish that the timescale of RT-IMPACT was faster than the trafficking of the reporter lipids to membrane locations other than their site of generation. We found that PMA stimulation led to a strong PM localization of the RT-IMPACT signal, consistent with literature reports that phorbol esters activate PLD enzymes predominantly in this membrane. By monitoring the IEDDA reaction in real-time, we directly visualized rapid internalization of BODIPY-lipids on the second timescale to other intracellular locations. In contrast, by performing a chase prior to the IEDDA tagging and then examining the earliest IEDDA reaction timepoints, i.e., those prior to this BODIPY-lipid trafficking, we established that the oxoTCO-labeled lipids internalized on a slower timescale of 10-20 minutes.

Intriguingly, the pathways for internalization of these phosphatidyl alcohol lipids appeared to be not via classic endocytic routes but instead via vesicle-independent pathways. These routes are mediated by lipid transfer proteins, which shuttle individual lipid molecules between bilayers of different organelles [34,70,71]. For maximal efficiency of lipid transport, many of these transfer proteins have recently been proposed to operate at membrane contact sites, which are sites of close apposition between two organelles where the distance between membranes is minimized, often as little as 10-20 nm [55,72].

Because of these short distances and the rapid kinetics of lipid diffusion and transport, non-vesicular lipid transport at membrane contact sites has proven challenging to directly observe. Though some lipid transfer proteins have precise lipid preferences based on head group

binding, others primarily engage the hydrophobic tails and are thought to transport a wide variety of types of lipids [34,70,71,73]. IMPACT-derived fluorescent lipids could be substrates for these latter lipid transfer proteins. An unexpected application of RT-IMPACT is that it may serve as a useful tool for directly visualizing PM-to-ER lipid trafficking via these non-vesicular pathways, which have recently been appreciated to play important roles in lipid homeostasis [55,70].

To that end, we have investigated the internalization of two types of lipids: phosphatidyl alcohols with an oxoTCO head group (TCO-lipids) and those with a fluorescent, BODIPY head group (BODIPY-lipids). Though both appear to be internalized largely by the same route (PM to ER), the kinetics of these processes are quite different. These differences could arise from several factors beyond the differences in the membrane surface areas of the PM and ER. Different transfer proteins may mediate their trafficking, or the different chemical properties of the lipids may impact their distribution within a given membrane bilayer, affinity for transfer proteins, and/or relative affinity for origin and destination organelle membranes. A potential future direction is the application of real-time oxoTCO–tetrazine IEDDA reactions for probing the trafficking pathways of lipids labeled with oxoTCO groups by processes other than PLD activity.

Finally, we applied RT-IMPACT to interrogate the spatial control of PLD signaling, taking advantage of its ability to report on the sites of synthesis of phosphatidyl alcohols by active PLD enzymes. As test cases, we examined stimulation of two distinct physiological pathways for activation of PLD: M1R as a prototypical GPCR and PDGFR as a prototypical RTK. Though the major players in the signaling pathways to activate PLD have been

established, including different PKC isoforms, small GTPases and heterotrimeric G proteins, and lipid cofactors, they can act in parallel and at different locations. Consequently, the precise locations where PA generation occurs remained unknown. Because of different subcellular localizations of the numerous PA-binding effector proteins, the location of PLD-mediated PA synthesis could greatly impact downstream signaling outcomes.

Using RT-IMPACT, we determined that, in the cell types we investigated, the majority of M1R-dependent PLD activity appears to occur at the PM, whereas the bulk of PDGFR-dependent PLD activity appears to occur on intracellular membranes. These results suggest that unique physiological agonists may activate pools of PLD enzymes at different subcellular locations, even when operating in part through common intermediates (e.g., PKC, RhoA, Rac1, etc.).

Regarding the PDGF studies, we note that this growth factor stimulates membrane ruffle formation at the plasma membrane in a process that requires PLD-mediated PA production [65], implying that some PDGF-stimulated PLD activity is likely in this membrane. Membrane ruffles are highly dynamic structures that involve major alterations to the actin cytoskeleton, and their effects on rates of phosphatidyl alcohol trafficking are unknown. Thus, it is possible that differences in the localization of IMPACT-derived fluorescent lipids — even at the early, 9 s timepoint of RT-IMPACT time-lapse movies — could reflect different rates of phosphatidyl alcohol trafficking induced by various stimuli that also activate PLDs.

Interesting future directions will involve dissecting the biological mechanisms and implications of these findings, including differential effects on relevant PA effector proteins, as

well as potential roles of choline, the soluble head group liberated from PC by PLD, which has recently been proposed to play signaling roles of its own at the ER [74].

In conclusion, we demonstrate that synthetic oxoTCO-containing primary alcohols function as substrates of endogenous, mammalian PLD enzymes and as metabolic labels for their activity within cells. In conjunction with real-time monitoring of a fluorogenic IEDDA tagging reaction of the resultant oxoTCO-containing lipids, we imaged precise subcellular locations of PLD signaling activity. Compared with IMPACT using azido alcohols and SPAAC-based fluorescent tagging, RT-IMPACT, though it has a lower extent of labeling, affords temporal resolution of seconds, and it is thus ideally suited to applications where the precise subcellular localization of lipid synthesis is critical. As well, continuous monitoring of the trafficking of lipids generated by RT-IMPACT holds promise as a method for interrogating intracellular lipid transport pathways.

Methods and materials

General materials and methods

1,2-dioleoyl-sn-glycero-3-phosphocholine (DOPC) was purchased from Echelon Biosciences. 5-fluoro-2-indolyl deschlorohalopemide (FIPI) was purchased from Cayman Chemical. Phorbol 12-myristate 13-acetate (PMA) and oxotremorine-M were purchased from Santa Cruz Biotechnology. *Streptomyces sp. PMF* PLD was purchased from Sigma-Aldrich. Recombinant PDGF-BB was purchased from Shenandoah Biotechnology. Methyltetrazine-amine (CAS # 1345955-28-3) was purchased from Click Chemistry Tools. Azidopropanol was synthesized as reported previously [33]. HPLC analysis was performed on a Shimadzu LC-20AR HPLC equipped with an SPD20AV UV/Vis detector, an RF-20A fluorescence detector, and a

Phenomenex Luna silica 3 μm 100 Å 25 cm x 4.6 mm column. LCMS analysis was performed on an Agilent 6230 electrospray ionization–time-of-flight (ESI–TOF) MS coupled to an Agilent 1260 HPLC equipped with a Zorbax Rx-Sil normal phase silica column (2.1 x 50 mm, 1.8 μm). Dulbecco's modified Eagle medium (DMEM), phosphate-buffered saline (PBS), fetal bovine serum (FBS), and 0.05% trypsin-EDTA were purchased from Corning. ER-Tracker Red, CellMask™ Deep Red Plasma Membrane Stain, and Lipofectamine 2000 were purchased from Thermo Fisher. For all imaging experiments except those in Fig. 2.16, confocal imaging was performed on a Zeiss LSM 800 confocal laser scanning microscope equipped with 20X 0.8 NA and 40X 1.4 NA Plan Apochromat objectives, 405, 488, 561, and 640 nm solid-state lasers, and two GaAsP PMT detectors, using the Zen Blue 2.3 software. For Fig. 2.16, super-resolution structured illumination microscopy (SR-SIM) was performed on a Zeiss Elyra super-resolution microscope, and image reconstruction was performed using default parameters in the Zeiss Zen Black software. All other image analysis was performed using FIJI/ImageJ. Flow cytometry was performed on a BD Accuri C6 flow cytometer, and analysis was performed using the BD Accuri C6 analysis software. For measurements of half-life of lipid trafficking, the values of Pearson correlation coefficients were fitted in Origin Pro 8 by mono-exponential regressions.

Cell culture

HeLa cells and NIH 3T3 cells were grown in DMEM (Dulbecco's modified Eagle medium) supplemented with 10% FBS and 1% penicillin/streptomycin and were maintained in a 5% CO_2, moisture-saturated atmosphere at 37 ºC. HEK 293TN cells were grown as above and additionally supplemented with 1 mM sodium pyruvate. Cell densities were maintained between 10^5 and 1.6 x 10^6 cells/mL. For cell labeling experiments, all buffers or media were

warmed to 37 ºC or room temperature prior to addition to cells unless otherwise noted, and incubations were done at 37 ºC unless otherwise specified.

Plasmids

Plasmids were obtained from the following sources. STIM1-mRFP: Barbara Baird (Cornell University). mCherry-P4M-SidM (a marker of structures positive in phosphatidylinositol 4-phosphate, principally the Golgi apparatus and the plasma membrane): Addgene # 51471. EEA1-mRFP, OMP25(transmembrane domain)-mCherry, PM-mRFP, and LAMP1-mRFP: Pietro De Camilli (Yale University). PLDs were tagged with mScarlet-i by subcloning of mScarlet-i (from pmScarlet-i-C1 (Addgene # 85044)) in place of GFP in GFP-PLD1, GFP-PLD1* (K898R), GFP-PLD2, and GFP-PLD2* (K758R) (obtained from Mike Frohman, Stony Brook University) using SnaBI and BspEI.

***In vitro* PLD transphosphatidylation reactions**

To a 1.5 mL Eppendorf tube containing was added the desired TCO-alcohol (2 μmol, neat) and DOPC (10 μL of an 8 mg/mL solution in chloroform). The chloroform was evaporated under a stream of nitrogen. The tube was then charged with SDS (1.5 μL of a 50 mM aqueous solution), sodium acetate (3 μL of a 1 M, pH 5.6, aqueous solution), and deionized water (19.5 μL), and the solution was vortexed and centrifuged briefly. Subsequently, calcium chloride (3 μL of a 500 mM aqueous solution) and 2 μL of DI water were added and the solution was vortexed and centrifuged again. Lastly, a freshly made solution of *Streptomyces sp. PMF* PLD (1 U/μL in water, 2 μL) was added and the mixture was heated to 30 ºC for 1.5 h. The mixture was then diluted with PBS (70 μL, pH 7.4), methanol (250 μL), chloroform (250 μL), and 20 mM aqueous acetic acid (125 μL). The two-phase mixture was vortexed for 1 min and then

centrifuged for 2 min at 16,000 x g. The organic layer was then transferred to a new Eppendorf tube and another fresh 250 µL of chloroform was added to the remaining aqueous layer. The mixture was vortexed and centrifuged as before. The two organic layers were then combined, dried under a stream of nitrogen and either stored at –80 ºC or further tagged via IEDDA click chemistry tagging. The lipid residue stored in a 1.5 mL Eppendorf tube was dissolved in 100 µL of a 2:1 v/v chloroform:methanol solution, charged with 2.5 nmol of Tz–BODIPY (1.94 µL, 1.3 mM stock in DMSO), reacted for 5 min at 37 ºC and then filtered (0.45 µm) prior to HPLC analysis. Samples were analyzed by normal phase HPLC with a binary gradient elution system where solvent A was chloroform:methanol:ammonium hydroxide (95:7:0.5) and solvent B was chloroform:methanol:water:ammonium hydroxide (60:34:5:0.5). Separation was achieved using linear gradients from 100% A to 100% B over 45 min. Method: 0-5 min: 0% B; 5-21 min: 0-75% B; 21-22 min: 75-100% B; 22-27 min: 100% B; 27-29 min: 100-0% B; 29-45 min: 0% B. Detection wavelengths: 495 nm (excitation) and 510 nm (emission).

Detection of endogenous mammalian PLD activity by HPLC

HeLa cells (500,000 cells) were seeded on a 60-mm dish 24 h before experiment. On the day of the experiment, the cells were first treated with the indicated PLD inhibitor (PLDi (FIPI), 750 nM; PLD1i (VU0359595), 250 nM; PLD2i (VU0364739), 350 nM) from 1000X DMSO stock solutions or the appropriate amount of DMSO for 30 min in DMEM (1 mL). PMA (100 µM, or 1000X, stock solution in DMSO) was then added to the DMEM solution to achieve a final concentration of 100 nM, and the cells were incubated for a further 20 min. The media was aspirated and replaced with the desired freshly-prepared TCO-alcohol (3–10 mM) in the continued presence of PMA (100 nM) in DMEM (500 µL). The cells were incubated for an

additional 20 min at 37 ºC (during which the dish was swirled every 5 min to cover the entire surface due to the use of a minimal volume of labeling solution) before the treatment buffer was aspirated. The cells were rinsed with DMEM for 3 min at 37 ºC, followed by a brief rinse with PBS at 4 ºC (1 mL). The PBS was aspirated, and the cells were then subjected to a modified Bligh-Dyer extraction. In brief. Using solutions at 4 ºC, 100 µL of cold PBS, 125 µL of cold acetic acid (20 mM, aqueous), and cold methanol (250 µL) were added to the aspirated dish. The cells were then scraped off the dish and transferred to 1.5 mL conical tubes. Chloroform (250 µL) was then added to the suspension. The mixture was then vortexed for 1 min and centrifuged at 16,000 x g for 2 min. The organic layer (bottom) was removed and placed in a separate conical tube, and an additional 250 µL chloroform was added to the remaining aqueous layer. The vortexing and centrifugation steps were repeated, and the two organic layers were combined, dried under a stream of nitrogen and stored at –80 ºC or tagged by IEDDA with Tz–BODIPY and analyzed by HPLC as described above.

Identification of oxoTCO-containing phosphatidyl alcohols by LC–MS

HeLa cells were labeled with (*S*)-oxoTCO–C1 (5 mM) under PMA stimulation as described in the previous section. After isolation of cellular lipidomes, the extracts were derivatized with methyltetrazine-amine (0.01 mg, 10 mg/mL stock in DMSO) for 5 min at room temperature and then filtered (0.45 µm). LC–MS analysis was performed using normal phase HPLC with a binary gradient elution system where solvent A was chloroform:methanol:ammonium hydroxide (85:15:0.5) and solvent B was chloroform:methanol:water:ammonium hydroxide (60:34:5:0.5). Separation was achieved using a linear gradient from 0% to 100% B over 8.5 min with a flow rate of 0.5 mL/min.

Phosphatidyl alcohol species were detected using a dual ESI source operating in positive mode, acquiring in extended dynamic range from m/z 100–1700 at one spectrum per second; gas temperature: 325 ºC; drying gas 10 L/min; nebulizer: 20 psig; fragmentor 300 V.

Generation of PLD1/2 knockout cell lines

Single and double knockout cells for PLD1 and/or PLD2 (1KO, PLD1 knockout; 2KO, PLD2 knockout; DKO, PLD1/2 double knockout) were generated in HeLa cells using the LentiCRISPR v2 system. The LentiCRIPSR plasmid for PLD1 knockout was made by cloning the sgRNA (GTGAGCCCACAAATAGACGG) into the LentiCRISPRv2-Puro vector (Addgene # 52961), and the LentiCRISPR plasmid for PLD2 knockout was made by cloning the sgRNA (GGCACCGAAAGATATACCAG) into the LentiCRISPRv2-Blast vector (Addgene # 83480). The appropriate LentiCRISPR plasmid (7.5 μg) was co-transfected with packaging plasmids (5.6 μg Gag and 1.8 μg Env) into HEK 293TN cells seeded on a 10 cm dish using Lipofectamine 2000. The virus-containing medium was collected 48 h and 72 h after transfection, and cell debris were removed by passing through 0.45 μm filter. For lentiviral transduction, wild-type HeLa cells seeded on a 6-well plate were treated with transduction medium (freshly prepared by mixing 1.5 mL virus-containing medium, 0.5 mL DMEM media and polybrene (8 μg/mL) for 48 h. During transduction, transduction medium was replaced every 12 h. After transduction, cells were placed in regular media for 24 h and then re-seeded on a 10-cm dish in media containing 1 μg/mL puromycin (for PLD1 knockout, or 1KO) or 5 μg/mL blasticidin (for PLD2 knockout, or 2KO). The cells were kept in the selective medium for 3–5 days until all of the cells on a plate seeded in parallel of non-transduced cells were dead. To eliminate remaining unedited cells in the PLD1 knockout population, the 1KO cells

generated as above were labeled with SPAAC-based IMPACT [33] for fluorescence-activated cell sorting (FACS) based on PLD activity. Briefly, cells were treated with azidopropanol (1 mM) and PMA (100 nM) in Tyrode's-HEPES buffer for 30 min at 37 ºC. After three rinses with PBS, cells were treated with BODIPY-bicyclononane (1 μM) for 10 min at 37 ºC. Cells were rinsed again three times with PBS and incubated in Tyrode's-HEPES buffer (135 mM NaCl, 5 mM KCl, 1.8 mM $CaCl_2$, 1 mM $MgCl_2$, 1 mg/mL glucose, 1 mg/mL bovine serum albumin, 20 mM HEPES, pH 7.4) for 10 min at 37 ºC to further rinse out unreacted fluorophore. The cells were then lifted with trypsin, and FACS was used to exclude the minority of cells with residual IMPACT labeling (i.e., the collected cells were those whose IMPACT fluorescence was comparable to negative controls wherein azidopropanol labeling was performed in the presence of PLDi (FIPI)). To generate PLD1/2 double knockout cells (DKO), the sorted PLD1 knockout cells (1KO) cells were transduced with the PLD2 sgRNA-containing LentiCRISPR virus-containing media, followed by blasticidin selection.

IMPACT labeling with oxoTCO alcohols for live-cell imaging and flow cytometry analysis

HeLa cells (150,000) or NIH 3T3 cells (250,000) were seeded on 35 mm glass-bottom imaging dishes (MatTek) for 24 h prior to experiments. For PDGF-stimulation in NIH 3T3 cells, cells were serum-starved by incubation in DMEM + 1% penicillin/streptomycin without serum for 18 h up to and including the transphosphatidylation step of the experiment. Rinses after transphosphatidylation were performed in full media. Where indicated, the cells were then transfected with the indicated plasmid using Lipofectamine 2000 as per the manufacturer's instructions. One day after seeding (or transfection, if any), cells were first treated with the indicated PLD inhibitor or DMSO in media for 30 min. The working concentrations of the

stimuli were the following: PDGF-BB (50 ng/mL), oxo-M (10 μM), PMA (100 nM). The appropriate stimulus was then added to the media for the indicated period of time (0–60 min). Subsequently, freshly prepared (*S*)-oxoTCO–C1 (or the indicated oxoTCO alcohol) (3 mM) together with the respective stimulus and PLD inhibitor/DMSO in media (100 μL) were carefully added to cover the central glass well. *Cautionary note: oxoTCOs are reported to have limited water stability* [50]*. Therefore, all aqueous oxoTCO solutions (e.g., those in DMEM-containing media) were used within 20 min of their generation. For example, we dissolved oxoTCO in 200 μL of DMEM with PLD inhibitor/DMSO and respective stimulus and used it only for two consecutive replicates rather than make a single stock solution for an entire day of experiments at the beginning of the day.* The dish was incubated for 5 min, the treatment media was aspirated, the cells were rinsed with PBS (1 mL) briefly, and the cells were then incubated in media (500 μL) for 1 min at 37 ºC. The media was replaced with Tz–BODIPY (0.33 μM) in PBS (100 μL) for 1 min, aspirated and replaced with 100 μL Tyrode's-HEPES buffer. Cells were imaged immediately afterwards. Multicolor images were obtained in two-channel, line-switching mode. Z stacks were taken with 0.45 μm sectioning. For flow cytometry analysis, cells were instead seeded in 24 well-plates (125,000 cells/well) and labeled as described above. Following the final aspiration of Tz–BODIPY, cells were lifted with trypsin, transferred to 96-well plates, rinse twice with cold PBS + 0.5% FBS by centrifugation at 500 x g, and analyzed by flow cytometry. At least 10,000 live cells were analyzed for each well, as determined by forward/side scatter analysis.

Real-time IMPACT imaging of PLD activity

For RT-IMPACT, i.e., time-lapse imaging, cells were labeled with (*S*)-oxoTCO–C1 and the appropriate stimulus as described in the previous section. Following the transphosphatidylation step and 1 min rinse with media (500 μL), the media was aspirated and replaced with 200 μL Tyrode's-HEPES buffer onto the center of the glass well. The dish was then immediately put onto the microscope stage, and a time-lapse movie was initiated with Definite Focus engaged to maintain the correct focal plane for the duration of the movie (3 s interval in between frames for a total of 3 min). Between the 2nd and 3rd frame of the movie, Tz–BODIPY (1 μM) in PBS (100 μL) was added. All time-lapse experiments were performed with at least 3 replicates. Image analysis for the localization of the RT-IMPACT signal was performed by exporting the 3rd frame (9 s timepoint) as image files. All images were blinded, and categorization of the IMPACT fluorescence as "PM" (predominantly plasma membrane), "Intra" (predominantly intracellular), or "Mix" (combination of plasma membrane and intracellular) was carried out by an individual other than the individual who performed the image acquisition. Each image had approximately 15–20 cells in view and was treated as a single biological replicate; each condition was repeated for the indicated number of biological replicates in the appropriate figure legend (n=3–8). The final categorization was assembled into stacked bar graphs for data visualization.

Quantification of PM-to-ER trafficking of fluorescently tagged lipids

This experiment was performed in a similar fashion compared to the RT-IMPACT time-lapse imaging described in the previous section, except that ER-Tracker Red and CellMask Deep Red Plasma Membrane Stain were added to the (*S*)-oxoTCO–C1 solution for the transphosphatidylation step. Following the rinse, IEDDA using Tz–BODIPY was carried out

during a time-lapse movie acquisition as described in the previous section, with the following microscope settings: frames were acquired in a three-channel, two-track, frame-switching mode (Track 1: 488 nm and 640 nm; Track 2: 561 nm) at an interval of 8 s per timepoint (4 min total length of acquisition). The Pearson correlation coefficients between the 488 nm (IMPACT) and 561 nm (ER Tracker Red) channels were calculated for each time point, plotted against time, and a mono-exponential regression fit was generated in Origin Pro 8 to give half-life ($t_{1/2}$) of trafficking kinetics from the PM to the ER.

Statistics and reproducibility

All imaging experiments show representative images from experiments performed in at least three biological replicates on different days. Exact numbers of replicate experiments and sample sizes are provided in each figure legend. For experiments involving quantification of comparisons between more than two independent groups (Figs. 2.12B–D, 2.19A, 2.20A, 2.20B, 2.21A, 2.21C and 2.22A) significance was calculated using one-way ANOVA, followed by Games-Howell post-hoc test (for samples of unequal variance). For experiments involving quantification of comparisons between groups with fractional data (i.e., fraction of PM, intra, and mix cells, which by definition sum to 1) (Figs. 2.17F, 2.19C, 2.20C, 2.21B and 2.22C), significance was calculated using chi-squared test for independence.

Synthetic Procedures

Compound characterizations by ^{1}H and ^{13}C NMR spectra are included in the Appendix.

General synthetic methods. All reactions used ACS-grade solvents and reagents from commercial sources without further purifications. Silica gel (60 Å) was purchased from Silicycle. For ^{13}C NMR of final oxoTCO products, multiplicities were distinguished using an

APT pulse sequence: typical methylene and quaternary carbons appear ‘up’ (u); methine and methyl carbons ‘down’ (dn).

General procedure for cis-to-trans photoisomerization of cyclooctenes. This general procedure for flow chemistry-based photoisomerization was adapted from work by Lambert *et al* . Reactions were done in a quartz flask (Chemglass) in close proximity to a Honeywell Ultraviolet Air Treatment System UV lamp (Model # RUVLAMP1, 18W bulb # UC100A 1005, 254 nm) in place of the photoreactor. All other parts were purchased and connected as described in Lambert *et al* [50]. A Biotage SNAP cartridge (KP-Sil 10g, Part # FSK0-1107-0010) was used to host regular silica gel and silver-impregnated silica gel. For every 1.4 mmol cyclooctene**,** the cartridge that contained a bed of regular silica gel (~1 in.) was topped with 5.4 g of silver-impregnated silica (2.3 eq silver). Any remaining space in the cartridge was filled with cotton balls. Methyl benzoate (2 eq) was added to a solution of cis-cyclooctene in the specified percentage of diethyl ether in hexanes within the quartz reaction flask. The final concentration of cyclooctene was 0.01–0.02 M. The solution was equilibrated for 10 min through the continuous flow system at a 100 mL/min flow rate. The solution in the quartz flask was then irradiated (254 nm) under continuous flow conditions (100 mL/min) for indicated period of time (typically 16–24 h). The SNAP cartridge was flushed with ~500 mL of 1:1 ether/hexanes and then dried with compressed air. The dried silica gel was transferred to an Erlenmeyer flask. Concentrated aqueous ammonium hydroxide (100 mL) and dichloromethane (100 mL) were sequentially added to the flask. The resulting biphasic mixture was stirred vigorously for 15 min, and then filtered. The filter cake was washed with additional DCM (25 mL) and ammonium hydroxide (25 mL). This rinse was repeated three times. The combined filtrates were partitioned, and the aqueous phase was extracted with DCM (3 x 25 mL). The combined

organic layers were dried over sodium sulfate, filtered, and concentrated under reduced pressure. The crude material was purified by flash column chromatography to yield the desired trans-cyclooctene (TCO or oxoTCO) as an inseparable mixture of axial and equatorial diastereomers.

Synthesis of new compounds

Cyclooct-4-enol (**8**) has been reported previously [75].

Allyl ether **9**. Sodium hydride (0.476 g, 60 wt%, 11.9 mmol) was added into a flame-dried 100 mL two-neck round-bottom flask filled with nitrogen. Hexanes (7 mL) was added to thoroughly rinse the hydride then decanted to give white-colored solid. THF (9 mL) was added to the flask, followed by secondary alcohol **8** (0.5 g, 3.96 mmol) dissolved in 6 mL THF. The resulting suspension was heated to reflux for 1 h and then cooled to room temperature before addition of allyl bromide (0.34 mL, 3.96 mmol) in THF (15 mL). The mixture was heated to reflux overnight and then cooled to room temperature. THF was removed under reduced pressure, and water was slowly added to the ice-cooled flask until bubbling ceased. The mixture was then acidified to pH 3 with 3 M HCl and extracted with ether (3 × 15 mL). The ether layers were combined and dried with $MgSO_4$ before rotary evaporation. The crude material was obtained as a yellow oil (650 mg, 99%) and used for next step without further purification. ^{1}H NMR ($CDCl_3$, 500 MHz) δ 5.86-5.94 (ddt, J = 16.3 Hz, 10.6 Hz, 5.4 Hz, 1H), 5.69-5.56 (m, 2H), 5.28-5.24 (m, 1H), 5.15-5.13 (m, 1H), 3.99-3.89 (m, 2H), 3.41-3.37 (m, 1H), 2.39-2.31 (m, 1H), 2.20-2.09 (m, 2H), 2.08-2.01 (m, 1H), 1.98-1.91 (m, 1H), 1.85-1.65 (m, 3H), 1.55-1.48 (m, 1H), 1.44-1.35 (m, 1H). ^{13}C NMR ($CDCl_3$, 126 MHz) δ 135.65, 130.22, 129.60, 116.47, 80.04, 69.38, 34.35, 33.52, 25.96, 25.74, 22.83. HRMS (DART) m/z: $[M+H]^+$ calcd. for $C_{11}H_{19}O^+$ 167.1430; found 167.1425.

Ether alcohol **10**. Compound **9** (0.34 g, 2.04 mmol) was added to an oven-dried 100 mL 2-neck round-bottom flask and dissolved in THF (6 mL) under a nitrogen atmosphere. A solution of 9-BBN (0.5 M in THF, 4.1 mL, 2.04 mmol) was added slowly. The resulting mixture was heated to reflux for 2 h before cooling to room temperature, when NaOH (aq, 3 M, 0.6 mL) and H_2O_2 (30%, 0.6 mL) was added. The mixture was heated to 50 ºC for 1 h and then cooled to room temperature. Excess K_2CO_3 (s) was added to saturate the aqueous layer, and the organic layer was separated. The aqueous layer was extracted with pentane (3 × 15 mL). The organic layers were combined, and solvents were removed under reduced pressure. The crude was purified by flash column chromatography (50% ether in hexanes) to give 170 mg of compound **10** (77% with 141 mg compound **9** recovered) as a colorless oil. ^{1}H NMR ($CDCl_3$, 500 MHz) δ 5.67-5.51 (m, 2H), 3.70-3.68 (m, 2H), 3.59-3.55 (m, 1H), 3.50-3.46 (m, 1H), 3.28-3.32 (m, 1H), 2.95 (br, s, 1H), 2.33-2.25 (m, 1H), 2.15-2.04 (m, 2H), 2.03-1.96 (m, 1H), 1.91-1.85 (m, 1H), 1.76-1.61 (m, 5H), 1.48-1.30 (m, 2H). ^{13}C NMR ($CDCl_3$, 126 MHz) δ 130.01, 129.45, 80.97, 67.65, 62.10, 34.18, 33.23, 32.26, 25.81, 25.61, 22.60. HRMS (DART) m/z: $[M+H]^+$ calcd. for $C_{11}H_{21}O_2^+$ 185.1536; found 185.1538.

(±)-TCO-ether–C3 (**2**). The general photoisomerization procedure described above was used. 0.77 g of compound **10** in 1:1 ether/hexanes yielded compound **2** (0.36 g, 47%) as a ~2.3:1 mixture of equatorial and axial isomers after 19 h of irradiation. ^{1}H NMR ($CDCl_3$, 500 MHz) δ 5.57-5.31 (m, 2H), 4.68 (br, s, 1H), 3.79-3.76 and 3.71-3.68 (q, J = 5.5 Hz, 2H), 3.61-3.39 (m, 3H), 2.93-2.76 (m, 2H), 2.37-2.26 (m, 1H), 2.25-2.11 (m, 2H), 2.05-1.85 (m, 2H), 1.85-1.70 (m, 4H), 1.51-1.42 (m, 1H) ^{13}C NMR ($CDCl_3$, 126 MHz) Peaks due to major diastereomer: δ 135.29, 132.22, 86.17, 67.51, 62.16, 40.94, 37.90, 34.55, 33.04, 32.23, 31.77. Peaks due to

minor diastereomer: δ 135.23, 131.06, 75.41, 68.44, 62.42, 40.20, 34.56, 32.76, 32.20, 29.92, 27.84. HRMS (DART) m/z: $[M+H]^+$ calcd. for $C_{11}H_{21}O_2^+$ 185.1536; found 185.1532.

Ether acid **11** has been reported previously [76].

Ether alcohol **12**. Compound **11** (0.37 g, 2.01 mmol) was dissolved in THF (3 mL) in a flame-dried 50 mL 2-neck round bottom flask under a nitrogen atmosphere. The solution was cooled on ice before lithium aluminum hydride (1 M in THF, 6.03 mL, 6.03 mmol) was added slowly. The mixture was heated to reflux for 4 h before cooling to 0 ºC. Water (0.229 mL), NaOH (aq, 15 wt%, 0.229 mL) and water (0.687 mL) were added sequentially and slowly. The mixture was stirred vigorously for 1 h at room temperature until a large amount of white gel-like precipitate formed. The solids were filtered and washed with THF (3 × 15 mL). The filtrate was evaporated under reduced pressure to give compound **12** (0.32g, 92%) as a colorless oil. The product was used for photoisomerization without further purification. ^{1}H NMR agreed with previous literature [50].

(±)-TCO-ether–C2 (**1**) has been reported previously [50].

Carbonate **13**. Compound **8** (0.72 g, 5.71 mmol) was dissolved in DCM (32 mL) in a 100 mL 2-neck round bottom flask under a nitrogen atmosphere. Pyridine (1.15 mL, 14.3 mmol) was added, followed by p-nitrophenyl chloroformate (1.27 g, 6.28 mmol) in DCM (8 mL). The solution was stirred at room temperature for 30 min before addition of saturated NH_4Cl (aq, 40 mL). The organic layer was separated and the aqueous layer was washed with DCM (2 × 15 mL). The organic layers were combined, dried over $MgSO_4$, and concentrated under reduced pressure. The crude material was purified by flash column chromatography (5–10% ethyl acetate in hexanes) to give compound **13** (1.4 g, 84%) as a white solid. ^{1}H NMR ($CDCl_3$, 500

MHz) δ 8.29-8.25 (m, 2H), 7.40-7.25 (m, 2H), 5.74-5.64 (m, 2H), 4.86-4.81 (ddd, *J* = 10.5 Hz, 9.3 Hz, 4.6Hz, 1H), 2.45-2.37 (m, 1H), 2.21-1.90 (m, 6H), 1.80-1.68 (m, 2H), 1.64-1.57 (m, 1H). ^{13}C NMR ($CDCl_3$, 126 MHz) δ 155.69, 151.96, 145.26, 129.99, 129.27, 125.26, 121.79, 80.27, 33.64, 33.45, 25.55, 24.81, 22.04. HRMS (DART) m/z: $[M+H]^+$ calcd. for $C_{15}H_{18}NO_5^+$ 292.1179; found 292.1182.

Carbamate alcohol **14a**. Compound **13** (0.68 g, 2.33 mmol) was dissolved in anhydrous DMF (10 mL) in a flame-dried scintillation vial under a nitrogen atmosphere. Triethylamine (0.65 mL, 4.67 mmol) and ethanolamine (0.21 mL, 3.5 mmol) were added to the solution. The mixture was stirred at room temperature for 22 h before acidification with 1 M HCl until the yellow color was gone. The mixture was extracted with DCM (3 × 40 mL). The organic layers were combined, dried over $MgSO_4$, and concentrated under high vacuum. The crude product was purified by column chromatography (0–3% MeOH in DCM) to give the compound **14a** as a colorless oil (0.5 g, quant.). ^{1}H NMR ($CDCl_3$, 500 MHz) δ 5.65-5.53 (m, 2H), 5.49-5.31 (br, s, 1H), 4.71-4.59 (br, s, 1H), 3.63-3.56 (m, 3H), 3.27-3.19 (m, 2H), 2.30-2.22 (m, 1H), 2.10 (q, *J* = 6.8 Hz, 2H), 2.06-2.00 (m, 1H), 1.88-1.66 (m, 3H), 1.60-1.46 (m, 3H). ^{13}C NMR ($CDCl_3$, 126 MHz) δ 157.07, 129.62, 129.52, 76.32, 61.94, 43.35, 33.99, 33.74, 25.54, 24.75, 22.32. HRMS (DART) m/z: $[M+H]^+$ calcd. for $C_{11}H_{20}NO_3^+$ 214.1438; found 214.1441.

Carbamate alcohol **14b**. Compound **13** (0.16 g, 0.55 mmol) was dissolved in anhydrous DMF (3 mL) in a flame-dried scintillation vial under a nitrogen atmosphere. Triethylamine (0.15 mL, 1.1 mmol) and 4-amino-1-butanol (76 μL, 0.824 mmol) was added to the solution. The mixture was stirred at room temperature for 22 h before acidification with 1 M HCl until yellow color was gone. The mixture was extracted with DCM (3 × 20 mL). The organic layers

were combined, dried over $MgSO_4$, and concentrated under high vacuum. The crude product was purified by column chromatography (0–3% MeOH in DCM) to give compound **14b** as a colorless oil (0.12 g, 91%). ^{1}H NMR ($CDCl_3$, 500 MHz) δ 5.69-5.57 (m, 2H), 4.80-4.66 (m, 2H), 3.67-3.62 (m, 2H), 3.22-3.13 (m, 2H), 2.34-2.26 (m, 1H), 2.20-2.05 (m, 3H), 1.94-1.69 (m, 4H), 1.63-1.51 (m, 7H). ^{13}C NMR ($CDCl_3$, 126 MHz) δ 156.58, 129.85, 129.76, 76.11, 62.49, 40.72, 34.19, 33.99, 29.78, 26.72, 25.68, 24.89, 22.49. HRMS (DART) m/z: $[M+H]^+$ calcd. for $C_{13}H_{24}NO_3^+$ 242.1751; found 242.1753.

(±)-TCO-carb–C2 (**4a**). The general photoisomerization procedure described above was used. 0.5 g of compound **14a** in 1:1 ether/hexanes generated compound **2** (0.128 g, 26%) as a ~1.5:1 mixture of equatorial and axial isomers after 20 h of irradiation. ^{1}H NMR ($CDCl_3$, 500 MHz) δ 5.61-5.32 (m, 3H), 4.93-4.80 and 4.32-4.23 (m, 1H), 3.70-3.55 (m, 3H), 3.35-3.12 (m, 2H), 2.86 (s, 1H), 2.34-2.17 (m, 3H), 2.12-1.56 (m, 5H), 1.56-1.43 (m, 1H). ^{13}C NMR ($CDCl_3$, 126 MHz) Peaks due to major diastereomer: δ 157.05, 134.82, 132.89, 80.83, 70.29, 61.90, 41.11, 38.57, 34.25, 32.49, 30.94. Peaks due to minor diastereomer: δ 157.05, 134.82, 131.13, 61.93, 43.37, 43.31, 41.06, 34.34, 32.62, 29.94, 27.95. HRMS (DART) m/z: $[M+H]^+$ calcd. for $C_{11}H_{20}NO_3^+$ 214.1438; found 214.1435.

(±)-TCO-carb–C4 (**4b**). The general photoisomerization procedure described above was used. 0.12 g of compound **10** in 1:1 ether/hexanes generated compound **2** (0.061 g, 51%) as a ~2.4:1 mixture of equatorial and axial isomers after 17 h of irradiation. ^{1}H NMR ($CDCl_3$, 500 MHz) δ 5.60-5.44 (m, 2H), 5.03-4.71 and 4.33-4.24 (m, 2H), 3.67-3.59 (m, 2H), 3.25-3.10 (m, 2H), 2.38-2.18 (m, 4H), 2.18-2.03 (m, 1H), 2.02-1.83 (m, 2H), 1.80-1.64 (m, 2H), 1.64-1.47 and 1.27-1.11 (m, 6H). ^{13}C NMR ($CDCl_3$, 126 MHz) Peaks due to major diastereomer: δ 156.53,

134.99, 133.06, 80.55, 70.13, 62.33, 41.24, 38.74, 34.37, 32.60, 31.02, 29.74, 26.66. Peaks due to minor diastereomer: δ 156.49, 135.41, 131.84, 41.16, 40.78, 40.71, 34.39, 32.75, 30.05, 28.07, 26.69. HRMS (DART) m/z: $[M+H]^+$ calcd. for $C_{13}H_{24}NO_3^+$ 242.1751; found 242.1748.

Amide alcohol **15a**. Compound **11** (0.24 g, 1.28 mmol), EDC (0.4 g, 2.56 mmol), and HOBt (0.39 g, 2.56 mmol) were dissolved in DCM (13 mL) under a nitrogen atmosphere. The mixture was cooled to 0 ºC before addition of ethanolamine (0.12 mL, 1.92 mmol) and triethylamine (1.06 mL, 7.68 mmol). The reaction was stirred under room temperature overnight and diluted with DCM (100 mL). The organic layer was washed with 1 M HCl, saturated $NaHCO_3$ (aq), and brine (50 mL each). The organic layer was dried over $MgSO_4$ and concentrated under reduced pressure. The crude material was purified by flash column chromatography (2:1 ethyl acetate:hexanes to 100% ethyl acetate) to give the title product as a yellow oil (0.26 g, 90%). ^{1}H NMR ($CDCl_3$, 500 MHz) δ 7.07-6.95 (br, s, 1H), 5.69-5.55 (m, 2H), 3.95-3.87 (m, 2H), 3.75-3.70 (m, 2H), 3.47-3.41 (m, 3H), 2.97-2.86 (br, s, 1H), 2.39-2.30 (m, 1H), 2.19-2.00 (m, 3H), 1.98-1.89 (m, 1H), 1.89-1.75 (m, 3H), 1.57-1.49 (m, 1H), 1.45-1.35 (m, 1H). ^{13}C NMR ($CDCl_3$, 126 MHz) δ 171.76, 129.87, 129.72, 82.02, 67.94, 62.48, 42.09, 34.13, 33.35, 25.82, 25.52, 22.52. HRMS (DART) m/z: $[M+H]^+$ calcd. for $C_{12}H_{22}NO_3^+$ 228.1594; found 228.1597.

Amide alcohol **15b**. Compound **11** (0.56 g, 3.05 mmol), EDC (0.95 g, 6.1 mmol), and HOBt (0.93 g, 6.1 mmol) were dissolved in DCM (26 mL) under a nitrogen atmosphere. The mixture was cooled to 0 ºC before addition of 4-amino-1-butanol (0.42 mL, 4.58 mmol) and triethylamine (2.5 mL, 18.3 mmol). The reaction was stirred under room temperature overnight and diluted with DCM (200 mL). The organic layer was washed with 1 M HCl, saturated

$NaHCO_3$ (aq), and brine (100 mL each). The organic layer was dried over $MgSO_4$ and concentrated under reduced pressure. The crude material was purified by flash column chromatography (3% MeOH in DCM) to give the title product as a yellow oil (0.62 g, 81%). ^{1}H NMR ($CDCl_3$, 500 MHz) δ 6.77-6.61 (br, s, 1H), 5.69-5.55 (m, 2H), 3.93-3.84 (m, 2H), 3.68 (q, *J* = 5.5 Hz, 2H), 3.42 (dq, *J* = 9.2 Hz, 4.3 Hz, 1H), 3.33 (q, *J* = 6.4 Hz, 2H), 2.40-2.30 (m, 1H), 2.18-2.01 (m, 3H), 1.97-1.89 (m, 1H), 1.81-1.49 (m, 9H), 1.45-1.35 (m, 1H). ^{13}C NMR ($CDCl_3$, 126 MHz) δ 170.55, 129.90, 129.74, 81.93, 68.04, 62.54, 38.64, 34.21, 33.36, 29.85, 26.41, 25.84, 25.55, 22.54. HRMS (DART) m/z: $[M+H]^+$ calcd. for $C_{14}H_{26}NO_3^+$ 256.1907; found 256.1910.

(±)-TCO-amide–C2 (**3a**). The general photoisomerization procedure described above was used. 0.68 g of compound **15a** in 1:1 ether/hexanes generated compound **3a** (0.32 g, 47%) as a ~1.5:1 mixture of equatorial and axial isomers after 19 h of irradiation. ^{1}H NMR ($CDCl_3$, 500 MHz) δ 7.18-6.81 (br, s, 1H), 5.68-5.32 (m, 2H), 4.01-3.03 (m, 7H), 2.82-2.59 (m, 1H), 2.44-1.18 (m, 10H). ^{13}C NMR ($CDCl_3$, 126 MHz) Peaks due to major diastereomer: δ 171.66, 135.25, 132.55, 86.98, 67.81, 62.57, 42.15, 40.75, 37.85, 34.53, 32.94, 31.69. Peaks due to minor diastereomer: δ 171.52, 135.69, 131.59, 76.19, 68.42, 62.47, 41.99, 40.24, 34.47, 32.71, 29.96, 28.08. HRMS (DART) m/z: $[M+H]^+$ calcd. for $C_{12}H_{22}NO_3^+$ 228.1594; found 228.1592.

(±)-TCO-amide–C4 (**3b**). The general photoisomerization procedure described above was used. 0.62 g of compound **15b** in 1:1 ether/hexanes generated compound **3b** (0.13 g, 21%) as a ~1.8:1 mixture of equatorial and axial isomers after 20 h of irradiation. ^{1}H NMR ($CDCl_3$, 500 MHz) δ 6.79-6.56 (s, 1H), 5.61-5.33 (m, 2H), 3.97-3.76 (m, 2H), 3.74-3.01 (m, 5H), 2.43-1.44 (m, 15H). ^{13}C NMR ($CDCl_3$, 126 MHz). Peaks due to major diastereomer: δ 170.43,

135.20, 132.50, 86.91, 67.90, 62.56, 40.81, 38.66, 37.86, 34.55, 32.96, 31.70, 29.84, 26.40. Peaks due to minor diastereomer: δ 170.13, 135.31, 131.31, 75.97, 68.49, 62.53, 40.29, 38.69, 38.67, 34.49, 32.67, 30.01, 28.08, 26.47. HRMS (DART) m/z: $[M+H]^+$ calcd. for $C_{14}H_{26}NO_3^+$ 256.1907; found 256.1904.

Synthesis of compounds **17**–**22** and (*S*)-oxoTCO–C1 (**5**) were adapted from routes for synthesis of (*R*)-oxoTCO (**6**) by Lambert *et al* [50] with some modifications, see below. The difference was the configuration of the initial glycidol starting material. (*R*)-glycidol was used for synthesis of (*S*)-oxoTCO–C1 (**5**), whereas (*S*)-glycidol was used for synthesis of (*R*)-oxoTCO (**6**). The intermediates for synthesis of **5** are enantiomers of corresponding intermediates for **6** and the spectra of intermediates for **5** matched those for **6** reported in the literature [50]**.** The synthetic routes adapted for **6** in this work had the same modifications as below for (*S*)-oxoTCO–C1 (**5**).

Modifications to Lambert *et al* [50] for the synthesis of (*S*)-oxoTCO–C1 (5):

a) For the synthesis of compound **17**, DCM was used as the solvent instead of DMF.

b) For the synthesis of compound **18**, 1.75 equivalents of allylmagnesium chloride was used instead of 1.2 equivalents.

c) For the synthesis of compound **19**, 3 equivalents of chloromethyl methyl ether was used instead of 2 equivalents and 10 mol% of 4-DMAP was used instead of 1 mol%.

d) For the synthesis of compound **20**, 0.5 equivalents of tin (IV) chloride was used instead of 5–6 equivalents.

e) For the synthesis of compound **21**, the complete removal of Ru metal from the product proved to be difficult; therefore, a two-step yield for synthesis of compound **22** was reported.

f) For the synthesis of compound **5**, the general photoisomerization procedure described above was used. 0.286 g of compound **22** in 1:1 ether/hexanes generated compound **5** (0.194 g, 68%) as a ~2.5:1 mixture of equatorial and axial isomers after 18 h of irradiation.

Compounds **23a** [77] and **23b** [78] have been reported previously.

Secondary alcohol **24a.** Compound **23a** (2.45 g, 7.50 mmol) and dilithium tetrachlorocuprate(II) (0.1 M in THF, 7.5 mL, 7.5 mmol) were dissolved in anhydrous THF (12 mL) under a nitrogen atmosphere. The solution was cooled to –30 ºC. Allylmagnesium chloride (1.7 M in THF, 7.5 mL, 12.8 mmol) was then added dropwise over 30 min. The reaction was stirred for an additional 30 min at –30 ºC before being allowed to warm to room temperature. The solution was diluted with ether (70 mL) and then quenched with saturated NH_4Cl (aq., 70 mL) slowly. The layers were separated and extracted with ether (3 × 70 mL). The organic layers were combined and washed with water and brine (100 mL each). The ether layer was dried with $MgSO_4$ and concentrated under reduced pressure. The crude material was purified by flash column chromatography (6–7% ethyl acetate in hexanes) to give compound **24a** as a colorless oil. ^{1}H NMR ($CDCl_3$, 500 MHz) δ 7.70-7.66 (m, 4H), 7.47-7.38 (m, 6H), 5.85 (ddt, *J* = 17.0 Hz, 10.2 Hz, 6.7 Hz, 1H), 5.05 (dq, *J* = 17.2 Hz, 1.7 Hz, 1H), 4.99-4.95 (m, 1H), 3.95-3.82 (m, 3H), 3.22 (d, *J* = 2.8 Hz, 1H), 2.27-2.09 (m, 2H), 1.77-1.49 (m, 4H), 1.06 (s, 9H). ^{13}C NMR ($CDCl_3$, 126 MHz) δ 138.77, [135.72, 135.70]*, [133.17, 133.08]*, [130.00, 129.97]*, 127.93, 114.72, 71.39, 63.67, 38.47, 36.76, 30.03, 26.96, 19.18. * indicates diastereotopic carbons. HRMS (DART) m/z: $[M+H]^+$ calcd. for $C_{23}H_{33}SiO_2^+$ 369.2244; found 369.2230.

Secondary alcohol **24b**. This compound was prepared analogously to **24a**. Epoxide **23b** (5.2 g, 15.3 mmol) generated 6.0 g (quant.) of compound **24b** as a colorless oil. ^{1}H NMR ($CDCl_3$, 500 MHz) δ 7.69-7.65 (m, 4H), 7.45-7.36 (m, 6H), 5.85 (ddt, *J* = 16.9 Hz, 10.1 Hz, 6.8 Hz, 1H), 5.05 (dq, *J* = 17.0 Hz, 1.7 Hz, 1H), 4.99-4.95 (m, 1H), 3.71-3.62 (m, 3H), 2.26-2.09 (m, 2H), 2.07-1.80 (br, s, 1H), 1.70-1.59 (m, 3H), 1.58-1.46 (m, 3H), 1.05 (s, 9H). ^{13}C NMR ($CDCl_3$, 126 MHz) δ 138.85, [135.74, 135.72]*, 133.80, 129.79, 127.81, 114.81, 71.22, 64.35, 36.62, 34.51, 30.28, 28.89, 26.98, 19.32. * indicates diastereotopic carbons. HRMS (DART) m/z: $[M+H]^+$ calcd. for $C_{24}H_{35}SiO_2^+$ 383.2401; found 383.2404.

Acetal **25a**. To an oven-dried scintillation vial, 4-dimethylaminopyridine (5 mg, 10 mol%), compound **24a** (146 mg, 0.40 mmol), DCM (1.5 mL), and DIEA (0.21 mL, 1.19 mmol) were added. The solution was cooled to 0 ºC, and chloromethyl methyl ether (90 µL, 1.19 mmol) was added dropwise. The reaction mixture was allowed to warm to room temperature and stirred for 20 h before dilution with DCM (6 mL) and quenching with water (6 mL). The layers were separated, and the aqueous layer was further extracted with DCM (2 × 6 mL). The organic layers were combined, washed with brine (10 mL), dried over $MgSO_4$, and concentrated under reduced pressure. The crude material was purified by flash column chromatography (6–7% ethyl acetate in hexanes) to give compound **25a** as a colorless oil (165 mg, quant.). ^{1}H NMR ($CDCl_3$, 500 MHz) δ 7.69-7.64 (m, 4H), 7.45-7.36 (m, 6H), 5.81 (ddt, *J* = 16.9 Hz, 10.3 Hz, 6.6 Hz, 1H), 5.02 (dq, *J* = 17.3 Hz, 1.7 Hz, 1H), 4.98-4.94 (m, 1H), 4.62 (q, *J* = 6.9 Hz, 2H), 3.82-3.71 (m, 3H), 3.32 (s, 3H), 2.18-2.04 (m, 2H), 1.75 (q, *J* = 6.3 Hz, 2H), 1.65-1.57 (m, 2H), 1.05 (s, 9H). ^{13}C NMR ($CDCl_3$, 126 MHz) δ 138.65, 135.71, 134.02, 129.73, 127.77, 114.72, 95.92, 74.57, 60.67, 55.66, 37.49, 34.13, 29.66, 27.01, 19.33. HRMS (DART) m/z: $[M+H]^+$ calcd. for $C_{25}H_{37}SiO_3^+$ 413.2506; found 413.2516.

Acetal **25b**. This compound was prepared analogously to **25a**. Secondary alcohol **24b** (2.2 g, 5.75 mmol) generated 2.13 g (87%) of compound **25b** as a colorless oil. ^{1}H NMR ($CDCl_3$, 500 MHz) δ 7.69-7.65 (m, 4H), 7.44-7.35 (m, 6H), 5.82 (ddt, *J* = 16.8 Hz, 10.1 Hz, 6.5 Hz, 1H), 5.03 (dq, *J* = 17.1 Hz, 1.7 Hz, 1H), 4.98-4.94 (m, 1H), 4.63 (d, *J* = 1.0 Hz, 2H), 3.67 (t, *J* = 5.0 Hz, 2H), 3.57 (tt, *J* = 5.6 Hz, 5.5Hz, 1H), 3.36 (s, 3H), 2.19-2.04 (m, 2H), 1.66-1.51 (m, 6H), 1.05 (s, 9H). ^{13}C NMR ($CDCl_3$, 126 MHz) δ 138.72, 135.72, 134.15, 129.68, 127.75, 114.71, 95.60, 76.95, 64.08, 55.68, 33.66, 30.56, 29.74, 28.35, 27.01, 19.36. HRMS (DART) m/z: $[M+H]^+$ calcd. for $C_{26}H_{39}SiO_3^+$ 427.2663; found 427.2663.

Ether diene **26a**. Compound **25a** (0.25 g, 0.61 mmol) and allyltrimethylsilane (0.192 mL, 1.21 mmol) were dissolved in anhydrous DCM (2.5 mL) under a nitrogen atmosphere. The solution was cooled to 0 ºC before dropwise addition of tin (IV) chloride (1 M in DCM, 0.30 mL, 0.30 mmol). The mixture was allowed to warm to room temperature and stirred for 2 h. The reaction was cooled to 0 ºC, diluted with DCM (10 mL), and quenched with saturated $NaHCO_3$ (aq) slowly. The layers were separated, and the aqueous layer was extracted with DCM (2 × 15 mL). The organic layers were combined, dried over $MgSO_4$, and concentrated under reduced pressure. The crude material was purified by flash column chromatography (6–7% ethyl acetate in hexanes) to give the title compound as a colorless oil (0.248 g, 97%). ^{1}H NMR ($CDCl_3$, 500 MHz) δ 7.71-7.64 (m, 4H), 7.45-7.36 (m, 6H), 5.80 (dtt, *J* = 17.0 Hz, 10.4 Hz, 6.6 Hz, 2H), 5.04 (ddq, *J* = 22.8 Hz, 17.1 Hz, 1.6 Hz, 2H), 5.02-4.93 (m, 2H), 3.82-3.69 (m, 2H), 3.53-3.40 (m, 3H), 2.27 (qt, J = 6.7 Hz, 1.30 Hz, 2H), 2.17-2.03 (m, 2H), 1.77-1.66 (m, 2H), 1.62-1.49 (m, 2H), 1.05 (s, 9H). ^{13}C NMR ($CDCl_3$, 126 MHz) δ 138.86, 135.71, 135.66, 134.08, 129.71, 127.76, 116.29, 114.60, 75.91, 68.62, 60.73, 37.28, 34.77, 33.65, 29.80, 27.02, 19.35. HRMS (DART) m/z: $[M+H]^+$ calcd. for $C_{27}H_{39}SiO_2^+$ 423.2714; found 423.2719.

Ether diene **26b**. This compound was prepared analogously to **26a**. Acetal **25b** (2.13 g, 5.00 mmol) generated 1.96 g (90%) of compound **26b** as a colorless oil. ^{1}H NMR ($CDCl_3$, 500 MHz) δ 7.70-7.65 (m, 4H), 7.45-7.35 (m, 6H), 5.80 (ddtd, *J* = 17.3 Hz, 10.1 Hz, 6.6 Hz, 1.3 Hz, 2H), 5.18 (ddq, *J* = 30.8 Hz, 17.3 Hz, 1.6 Hz, 2H), 5.05-4.93 (m, 2H), 3.69-3.65 (m, 2H), 3.49-3.40 (m, 2H), 3.26 (quint, *J* = 5.7 Hz, 1H), 2.30 (qt, J = 6.7 Hz, 1.50 Hz, 2H), 2.24-2.02 (m, 2H), 1.64-1.51 (m, 6H), 1.05 (s, 9H). ^{13}C NMR ($CDCl_3$, 126 MHz) δ 138.96, 135.72, 135.70, 134.20, 129.67, 127.74, 116.30, 114.56, 78.79, 68.36, 64.14, 34.82, 33.37, 30.13, 29.88, 28.45, 27.02, 19.37. HRMS (DART) m/z: $[M+H]^+$ calcd. for $C_{28}H_{41}SiO_2^+$ 437.2870; found 437.2878.

Oxo-cyclooctene **27a**. Compound **26a** (1.45 g, 3.43 mmol) was dissolved in DCM (650 mL) and the solution was heated to reflux before addition of Grubb's I catalyst (0.282 g, 0.343 mmol) in one portion. The mixture was stirred for 2.5 h under reflux before removal of DCM by rotary evaporation. The crude material was partially purified by flash column chromatography (6–7% ethyl acetate in hexanes to give the title compound as a brownish oil (1.40 g, containing Ru metal). The partially purified compound was used for the next deprotection step immediately.

Oxo-cyclooctene **27b**. This compound was prepared analogously to **27a**. Ether diene **26b** (1.38 g, 3.16 mmol) generated 1.22 g of compound **27b** (containing Ru metal) as a brownish oil. The partially purified compound was used for the next deprotection step immediately.

Oxo-cyclooctene primary alcohol **28a**. Tetrabutylammonium fluoride (1 M in THF, 10.3 mL, 10.3 mmol) was added to compound **27a** (1.40 g, containing Ru) at 0 ºC. The solution was allowed to warm to room temperature and stirred overnight. The reaction mixture was

diluted with ether (20 mL) and quenched slowly with saturated NH_4Cl (aq., 20 mL). The layers were separated, and the aqueous layer was extracted with ether (3 × 20 mL). The organic layers were combined, washed with brine (50 mL), dried over $MgSO_4$, and concentrated under reduced pressure. The crude material was purified by flash column chromatography (6–7% ethyl acetate in hexanes) to give the title compound as a colorless oil (0.297 g, 56% over two steps). ^{1}H NMR ($CDCl_3$, 500 MHz) δ 5.83-5.72 (m, 2H), 3.99-3.92 (m, 1H), 3.82-3.72 (m, 2H), 3.67-3.61 (m, 1H), 3.46-3.40 (m, 1H), 2.51-2.36 (m, 2H), 2.22-2.10 (m, 2H), 2.07-2.00 (m, 1H), 1.75-1.59 (m, 3H), 1.56-1.48 (m, 1H). ^{13}C NMR ($CDCl_3$, 126 MHz) δ 131.72, 128.59, 78.64 (app d), 71.45, 60.75 (app d), 38.90 (app d), 36.02, 29.35, 23.79. HRMS (DART) m/z: $[M+H]^+$ calcd. for $C_9H_{17}O_2^+$ 157.1223; found 157.1220.

Oxo-cyclooctene primary alcohol **28b**. This compound was prepared analogously to **28a**. Ether diene **27b** (1.22 g, containing Ru) generated 0.37 g of compound **28b** (69% over two steps) as a colorless oil. ^{1}H NMR ($CDCl_3$, 500 MHz) δ 5.82-5.70 (m, 2H), 3.99-3.92 (m, 1H), 3.68-3.59 (m, 2H), 3.41-3.31 (m, 2H), 2.52-2.36 (m, 2H), 2.14-1.97 (m, 2H), 1.94-1.79 (br, s, 1H), 1.76-1.22 (m, 6H). ^{13}C NMR ($CDCl_3$, 126 MHz) δ 131.75, 128.61, 79.81, 71.58, 63.21, 36.01, 33.56, 29.53, 29.15, 23.84. HRMS (DART) m/z: $[M+H]^+$ calcd. for $C_{10}H_{19}O_2^+$ 171.1380; found 171.1383.

(±)-oxoTCO–C2 (**7a**). The general photoisomerization procedure described above was used. 0.315 g compound **28a** in 1:1 ether/hexanes generated compound **7a** (0.088 g, 28%) as a ~2.9:1 mixture of equatorial and axial isomers after 17 h of irradiation. ^{1}H NMR (C_6D_6, 500 MHz) δ 5.82-5.68, 5.53-5.44 and 5.21-5.12 (m, 2H), 3.82-3.76 (m, 1H), 3.67-3.27 (m, 2H, mixed with peaks from minor isomer), 2.91-2.83 (m, 2H), 2.30-2.19 (m, 2H), 2.03-1.25 (m,

7H). ^{13}C NMR (C_6D_6, 126 MHz) Peaks due to major diastereomer: δ 140.64 (dn), 126.41 (dn), 82.88 (dn), 73.26 (u), 59.08 (u), 40.94 (u), 39.16 (u), 37.98 (u), 34.29 (u). Peaks due to minor diastereomer: δ 137.07 (dn), 132.69 (dn), 80.69 (dn), 72.92 (u), 60.00 (u), 42.61 (u), 33.07 (u), 27.95 (u), 27.67 (u). HRMS (DART) m/z: $[M+H]^+$ calcd. for $C_9H_{17}O_2^+$ 157.1223; found 157.1236.

(±)-oxoTCO–C3 (**7b**). The general photoisomerization procedure described above was used. 0.37 g compound **28b** in 1:1 ether/hexanes generated compound **7b** (0.251 g, 68%) as a ~2.7:1 mixture of equatorial and axial isomers after 17 h of irradiation. ^{1}H NMR (C_6D_6, 500 MHz) δ 5.83-5.72, 5.50-5.40 and 5.20-5.12 (m, 2H), 3.86-3.79 (m, 1H), 3.59-3.33 (m, 2H, mixed with peaks from minor isomer), 2.77-2.70 (m, 1H), 2.62-2.55 (m, 1H), 2.32-1.68 (m, 5H), 1.55-1.18 (m, 6H). ^{13}C NMR (C_6D_6, 126 MHz) Peaks due to major diastereomer: δ 140.75 (dn), 126.33 (dn), 84.84 (dn), 73.35 (u), 62.65 (u), 40.93 (u), 38.08 (u), 34.43 (u), 33.82 (u), 28.49 (u). Peaks due to minor diastereomer: δ 137.77 (dn), 131.66 (dn), 81.18 (dn), 71.20 (u), 62.28 (u), 42.32 (u), 34.31 (u), 30.96 (u), 29.44 (u), 28.26 (u). HRMS (DART) m/z: $[M+H]^+$ calcd. for $C_{10}H_{19}O_2^+$ 171.1380; found 171.1393.

Synthesis of the fluorogenic **Tz–BODIPY** has been reported previously [51].

BODIPY-alkyl-Tz. BODIPY-succinate (**29**) was synthesized as previously described [79]. Compound **29** (14 mg, 39 μmol), methyltetrazine-amine (Click Chemistry Tools, 9 mg, 39 μmol), EDC-HCl (15 mg, 77 μmol), and HOBt (12 mg, 77 μmol) were added into a flame-dried scintillation vial equipped with a stir bar under a nitrogen atmosphere. Dichloromethane (3 mL) and Hunig's base (40 μL) were then added to the vial. The solution was stirred overnight at room temperature before dilution with dichloromethane. The mixture was washed with 1 M

HCl, neutralized with $NaHCO_3$ (aq., saturated), and washed with brine. The organic layer was dried with $MgSO_4$ before concentration. The crude was purified with column chromatography (0–5% v/v MeOH in DCM) and subsequent normal-phase HPLC to give BODIPY-alkyl-Tz (14 mg, 67%) as a red solid. ^{1}H NMR ($CDCl_3$, 500 MHz) δ 8.50 (d, 2H, J = 8.0 Hz), 7.57 (s, 1H), 7.47 (d, 2H, J = 8.1 Hz), 7.09 (d, 1H, J = 4.3 Hz), 6.48 (t, 1H, J = 5.9 Hz), 6.44-6.41 (m, 1H), 6.34 (t, 1H, J = 6.2 Hz), 6.16 (s, 1H), 4.52 (d, 2H, J = 5.9 Hz), 3.48 (q, 2H, J = 7.0 Hz), 3.10-3.05 (m, 5H), 2.59-2.49 (m, 7H), 2.44 (s, 3H). ^{13}C NMR ($CDCl_3$, 126 MHz) δ 172.64, 172.25, 167.43, 163.84, 161.36, 145.29, 143.23, 142.49, 138.30, 134.17, 131.14, 128.49, 128.36, 124.26, 123.96, 116.18, 56.12, 43.47, 41.47, 31.69, 31.61, 21.31, 16.35, 15.17. The product was further characterized on reverse-phase HPLC (see chromatogram below) on Shimadzu LC-20AR HPLC equipped with an SPD20AV UV/Vis detector. Column: Epic Polar 5µ 120 Å, 25 cm X 4.6 mm, Catalog # 155291-EPO, Serial #271-15-84620. Channels: 495 nm and 553 nm. Solvent A: Water. Solvent B: Acetonitrile. Flow rate: 1 mL/min. The percent of solvent B is indicated by the red line.

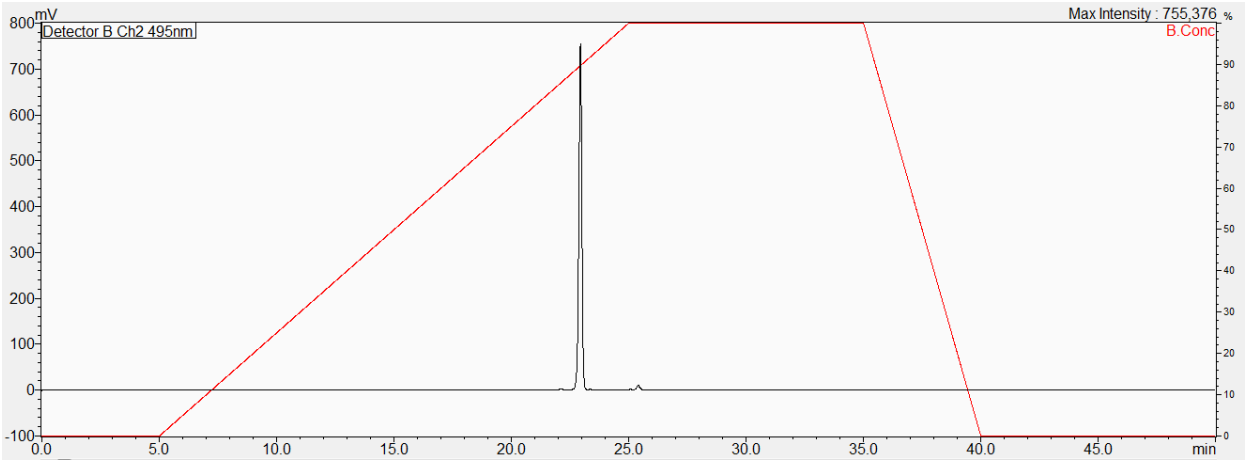

Figure 2.23: reverse-phase HPLC chromatogram of BODIPY-alkyl-Tz.

Acknowledgments

The author would like to acknowledge research contributions from the following researchers at Cornell University: Kane Wu, Reika Tei, Timothy W. Bumpus, Johnny Ye, and Jeremy M. Baskin. J.M.B. acknowledges support from the Arnold and Mabel Beckman Foundation (Beckman Young Investigator Award), the National Science Foundation (CAREER CHE-1749919), and the Alfred P. Sloan Foundation (Sloan Research Fellowship). D.L. and R.T. were supported by Cornell Fellowships, R.T. was additionally supported by a Funai Overseas Fellowship, and T.W.B. was supported by an NSF graduate research fellowship (DGE-1650441). This work made use of the Cornell University NMR Facility, which is supported in part by the NSF (CHE-1531632) and the Cornell University Biotechnology Resource Center Imaging Facility, which is supported in part by the NSF (DBI-1428922). We thank Joseph Fox and William Lambert (University of Delaware) for generously providing samples of oxoTCO reagents and for assisting with and advising on the synthesis of oxoTCO reagents, Alex Brown (Vanderbilt University) for providing isoform-selective PLD1 and PLD2 inhibitors (VU0359595 and VU0364739), Megan Gelsinger for assistance with statistical analysis, the Emr and Fromme labs for sharing equipment and reagents, Weizhi Yu for technical assistance, and members of the Baskin laboratory for helpful discussions.

References

1 Giepmans BNG, Adams SR, Ellisman MH, Tsien RY. The fluorescent toolbox for assessing protein location and function. *Science* 2006;**312**:217–24. https://doi.org/10.1126/science.1124618.

2 Oldach L, Zhang J. Genetically Encoded Fluorescent Biosensors for Live-Cell Visualization of Protein Phosphorylation. *Chem Biol* 2014;**21**:186–97. https://doi.org/10.1016/j.chembiol.2013.12.012.

3 Chakraborty K, Veetil AT, Jaffrey SR, Krishnan Y. Nucleic Acid–Based Nanodevices in Biological Imaging. *Annu Rev Biochem* 2016;**85**:349–73. https://doi.org/10.1146/annurev-biochem-060815-014244.

4 Chan J, Dodani SC, Chang CJ. Reaction-based small-molecule fluorescent probes for chemoselective bioimaging. *Nat Chem* 2012;**4**:973–84. https://doi.org/10.1038/nchem.1500.

5 Liu Y, Su Y, Wang X. Phosphatidic Acid-Mediated Signaling. *Lipid-mediated Protein Signal.* Dordrecht: Springer Netherlands; 2013. p. 159–76.

6 Selvy PE, Lavieri RR, Lindsley CW, Brown HA. Phospholipase D: enzymology, functionality, and chemical modulation. *Chem Rev* 2011;**111**:6064–119. https://doi.org/10.1021/cr200296t.

7 Shulga Y V., Topham MK, Epand RM. Regulation and functions of diacylglycerol kinases. *Chem Rev* 2011;**111**:6186–208. https://doi.org/10.1021/cr1004106.

8 Kang DW, Choi KY, Min DS. Functional Regulation of Phospholipase D Expression in Cancer and Inflammation. *J Biol Chem* 2014;**289**:22575–82. https://doi.org/10.1074/jbc.R114.569822.

9 Zhang Y, Frohman MA. Cellular and physiological roles for phospholipase D1 in cancer. *J Biol Chem* 2014;**289**:22567–74. https://doi.org/10.1074/jbc.R114.576876.

10 Oliveira TG, Di Paolo G. Phospholipase D in brain function and Alzheimer's disease. *Biochim Biophys Acta* 2010;**1801**:799–805. https://doi.org/10.1016/j.bbalip.2010.04.004.

11 Nelson RK, Frohman MA. Physiological and pathophysiological roles for phospholipase D. *J Lipid Res* 2015;**56**:2229–37. https://doi.org/10.1194/jlr.R059220.

12 Scott SA, Selvy PE, Buck JR, Cho HP, Criswell TL, Thomas AL, *et al.* Design of isoform-selective phospholipase D inhibitors that modulate cancer cell invasiveness. *Nat Chem Biol* 2009;**5**:108–17. https://doi.org/10.1038/nchembio.140.

13 Bruntz RC, Lindsley CW, Brown HA. Phospholipase D signaling pathways and phosphatidic acid as therapeutic targets in cancer. *Pharmacol Rev* 2014;**66**:1033–79. https://doi.org/10.1124/pr.114.009217.

14 Brown HA, Thomas PG, Lindsley CW. Targeting phospholipase D in cancer, infection and neurodegenerative disorders. *Nat Struct Mol Biol* 2017. https://doi.org/10.1038/nrd.2016.252.

15 Frohman MA. The phospholipase D superfamily as therapeutic targets. *Trends Pharmacol Sci* 2015;**36**:137–44. https://doi.org/10.1016/j.tips.2015.01.001.

16 Jang J-H, Lee CS, Hwang D, Ryu SH. Understanding of the roles of phospholipase D and phosphatidic acid through their binding partners. *Prog Lipid Res* 2012;**51**:71–81. https://doi.org/10.1016/j.plipres.2011.12.003.

17 Hammond SM, Jenco JM, Nakashima S, Cadwallader K, Gu Q, Cook S, *et al.* Characterization of two alternately spliced forms of phospholipase D1. Activation of the purified enzymes by phosphatidylinositol 4,5-bisphosphate, ADP-ribosylation factor, and Rho family monomeric GTP-binding proteins and protein kinase C-alpha. *J Biol Chem* 1997;**272**:3860–8. https://doi.org/10.1074/jbc.272.6.3860.

18 Colley WC, Sung TC, Roll R, Jenco J, Hammond SM, Altshuller Y, *et al.* Phospholipase D2, a distinct phospholipase D isoform with novel regulatory properties that provokes cytoskeletal reorganization. *Curr Biol* 1997;**7**:191–201. https://doi.org/10.1016/S0960-9822(97)70090-3.

19 Du G, Altshuller YM, Vitale N, Huang P, Chasserot-Golaz S, Morris AJ, *et al.* Regulation of phospholipase D1 subcellular cycling through coordination of multiple membrane association motifs. *J Cell Biol* 2003;**162**:305–15. https://doi.org/10.1083/jcb.200302033.

20 Sarri E, Pardo R, Fensome-Green A, Cockcroft S. Endogenous phospholipase D2 localizes to the plasma membrane of RBL-2H3 mast cells and can be distinguished from ADP ribosylation factor-stimulated phospholipase D1 activity by its specific

sensitivity to oleic acid. *Biochem J* 2003;**369**:319–29. https://doi.org/10.1042/BJ20021347.

21 Laulagnier K, Grand D, Dujardin A, Hamdi S, Vincent-Schneider H, Lankar D, *et al.* PLD2 is enriched on exosomes and its activity is correlated to the release of exosomes. *FEBS Lett* 2004;**572**:11–4. https://doi.org/10.1016/j.febslet.2004.06.082.

22 Antal CE, Newton AC. Tuning the signalling output of protein kinase C. *Biochem Soc Trans* 2014;**42**:1477–83. https://doi.org/10.1042/BST20140172.

23 Gallegos LL, Newton AC. Spatiotemporal dynamics of lipid signaling: protein kinase C as a paradigm. *IUBMB Life* 2008;**60**:782–9. https://doi.org/10.1002/iub.122.

24 Du G, Altshuller YM, Kim Y, Han JM, Ryu SH, Morris AJ, *et al.* Dual requirement for rho and protein kinase C in direct activation of phospholipase D1 through G protein-coupled receptor signaling. *Mol Biol Cell* 2000;**11**:4359–68. https://doi.org/10.1091/mbc.11.12.4359.

25 Mozzicato S, Joshi B V., Jacobson KA, Liang BT. Role of direct RhoA-phospholipase D1 interaction in mediating adenosine-induced protection from cardiac ischemia. *FASEB J* 2004;**18**:1–13. https://doi.org/10.1096/fj.03-0592fje.

26 Senogles SE, Everett PB. D3 dopamine receptor signals to activation of phospholipase D through a complex with Rho. *J Neurochem* 2010;**112**:963–71. https://doi.org/10.1111/j.1471-4159.2009.06508.x.

27 Powner DJ, Wakelam MJO. The regulation of phospholipase D by inositol phospholipids and small GTPases. *FEBS Lett* 2002;**531**:62–4. https://doi.org/10.1016/S0014-5793(02)03410-5.

28 Hughes WE, Larijani B, Parker PJ. Detecting Protein-Phospholipid Interactions. *J Biol Chem* 2002;**277**:22974–9. https://doi.org/10.1074/jbc.m201391200.

29 Kassas N, Tanguy E, Thahouly T, Fouillen L, Heintz D, Chasserot-Golaz S, *et al.* Comparative characterization of phosphatidic acid sensors and their localization during frustrated phagocytosis. *J Biol Chem* 2017;**292**:4266–79. https://doi.org/10.1074/jbc.M116.742346.

30 Kassas N, Tryoen-Tóth P, Corrotte M, Thahouly T, Bader M-F, Grant NJ, *et al.* Genetically encoded probes for phosphatidic acid. *Methods Cell Biol* 2012;**108**:445–59.

https://doi.org/10.1016/B978-0-12-386487-1.00020-1.

31 Zhang F, Wang Z, Lu M, Yonekubo Y, Liang X, Zhang Y, *et al.* Temporal Production of the Signaling Lipid Phosphatidic Acid by Phospholipase D2 Determines the Output of Extracellular Signal-Regulated Kinase Signaling in Cancer Cells. *Mol Cell Biol* 2013;**34**:84–95. https://doi.org/10.1128/MCB.00987-13.

32 Bumpus TW, Baskin JM. A Chemoenzymatic Strategy for Imaging Cellular Phosphatidic Acid Synthesis. *Angew Chem Int Ed* 2016;**55**:13155–8. https://doi.org/10.1002/anie.201607443.

33 Bumpus TW, Baskin JM. Clickable Substrate Mimics Enable Imaging of Phospholipase D Activity. *ACS Cent Sci* 2017;**3**:1070–7. https://doi.org/10.1021/acscentsci.7b00222.

34 Wong LH, Gatta AT, Levine TP. Lipid transfer proteins: the lipid commute via shuttles, bridges and tubes. *Nat Rev Mol Cell Biol* 2018. https://doi.org/10.1038/s41580-018-0071-5.

35 Yang Y, Lee M, Fairn GD. Phospholipid subcellular localization and dynamics. *J Biol Chem* 2018;**293**:6230–40. https://doi.org/10.1074/jbc.R117.000582.

36 Brown HA, Henage LG, Preininger AM, Xiang Y, Exton JH. Biochemical Analysis of Phospholipase D. *Methods Enzymol* 2007:49–87. https://doi.org/10.1016/S0076-6879(07)34004-4.

37 Philip F, Ha EE, Seeliger MA, Frohman MA. Measuring Phospholipase D Enzymatic Activity Through Biochemical and Imaging Methods. *Methods Enzymol* 2017;**583**:309–25. https://doi.org/10.1016/bs.mie.2016.09.041.

38 Bumpus TW, Liang FJ, Baskin JM. Ex Uno Plura: Differential Labeling of Phospholipid Biosynthetic Pathways with a Single Bioorthogonal Alcohol. *Biochemistry* 2018;**57**:226–30. https://doi.org/10.1021/acs.biochem.7b01021.

39 Rostovtsev V V, Green LG, Fokin V V, Sharpless KB. A stepwise huisgen cycloaddition process: copper(I)-catalyzed regioselective ‘ligation’ of azides and terminal alkynes. *Angew Chem Int Ed* 2002;**41**:2596–9. https://doi.org/10.1002/1521-3773(20020715)41:14<2596::AID-ANIE2596>3.0.CO;2-4.

40 Presolski SI, Hong VP, Finn MG. Copper-Catalyzed Azide-Alkyne Click Chemistry

for Bioconjugation. *Curr Protoc Chem Biol* 2011;**3**:153–62. https://doi.org/10.1002/9780470559277.ch110148.

41 Agard NJ, Prescher JA, Bertozzi CR. A strain-promoted [3 + 2] azide-alkyne cycloaddition for covalent modification of biomolecules in living systems. *J Am Chem Soc* 2004;**126**:15046–7. https://doi.org/10.1021/ja044996f.

42 Dommerholt J, Schmidt S, Temming R, Hendriks LJA, Rutjes FPJT, Van Hest JCM, *et al.* Readily accessible bicyclononynes for bioorthogonal labeling and three-dimensional imaging of living cells. *Angew Chem Int Ed* 2010;**49**:9422–5. https://doi.org/10.1002/anie.201003761.

43 Fujiwara T, Ritchie K, Murakoshi H, Jacobson K, Kusumi A. Phospholipids undergo hop diffusion in compartmentalized cell membrane. *J Cell Biol* 2002;**157**:1071–81. https://doi.org/10.1083/jcb.200202050.

44 Kusumi A, Tsunoyama TA, Hirosawa KM, Kasai RS, Fujiwara TK. Tracking single molecules at work in living cells. *Nat Chem Biol* 2014;**10**:524–32. https://doi.org/10.1038/nchembio.1558.

45 Nicolson GL. The Fluid - Mosaic Model of Membrane Structure: Still relevant to understanding the structure, function and dynamics of biological membranes after more than 40 years. *Biochim Biophys Acta - Biomembr* 2014;**1838**:1451–66. https://doi.org/10.1016/j.bbamem.2013.10.019.

46 Blackman ML, Royzen M, Fox JM. Tetrazine ligation: fast bioconjugation based on inverse-electron-demand Diels-Alder reactivity. *J Am Chem Soc* 2008;**130**:13518–9. https://doi.org/10.1021/ja8053805.

47 Devaraj NK, Weissleder R, Hilderbrand SA. Tetrazine-based cycloadditions: application to pretargeted live cell imaging. *Bioconjug Chem* 2008;**19**:2297–9. https://doi.org/10.1021/bc8004446.

48 Oliveira BL, Guo Z, Bernardes GJL. Inverse electron demand Diels-Alder reactions in chemical biology. *Chem Soc Rev* 2017;**114**:4764. https://doi.org/10.1039/c7cs00184c.

49 Su W, Yeku O, Olepu S, Genna A, Park J-S, Ren H, *et al.* 5-Fluoro-2-indolyl des-chlorohalopemide (FIPI), a phospholipase D pharmacological inhibitor that alters cell spreading and inhibits chemotaxis. *Mol Pharmacol* 2009;**75**:437–46.

https://doi.org/10.1124/mol.108.053298.

50 Lambert WD, Scinto SL, Dmitrenko O, Boyd SJ, Magboo R, Mehl RA, *et al.* Computationally guided discovery of a reactive, hydrophilic trans-5-oxocene dienophile for bioorthogonal labeling. *Org Biomol Chem* 2017;**15**:6640–4. https://doi.org/10.1039/C7OB01707C.

51 Carlson JCT, Meimetis LG, Hilderbrand SA, Weissleder R. BODIPY-tetrazine derivatives as superbright bioorthogonal turn-on probes. *Angew Chem Int Ed* 2013;**52**:6917–20. https://doi.org/10.1002/anie.201301100.

52 Lewis JA, Scott SA, Lavieri R, Buck JR, Selvy PE, Stoops SL, *et al.* Design and synthesis of isoform-selective phospholipase D (PLD) inhibitors. Part I: Impact of alternative halogenated privileged structures for PLD1 specificity. *Bioorg Med Chem Lett* 2009;**19**:1916–20. https://doi.org/10.1016/j.bmcl.2009.02.057.

53 Lavieri RR, Scott SA, Selvy PE, Kim K, Jadhav S, Morrison RD, *et al.* Design, synthesis, and biological evaluation of halogenated N-(2-(4-oxo-1-phenyl-1,3,8-triazaspiro[4.5]decan-8-yl)ethyl)benzamides: discovery of an isoform-selective small molecule phospholipase D2 inhibitor. *J Med Chem* 2010;**53**:6706–19. https://doi.org/10.1021/jm100814g.

54 Devaraj NK, Hilderbrand S, Upadhyay R, Mazitschek R, Weissleder R. Bioorthogonal turn-on probes for imaging small molecules inside living cells. *Angew Chem Int Ed* 2010;**49**:2869–72. https://doi.org/10.1002/anie.200906120.

55 Saheki Y, Camilli P De. Endoplasmic Reticulum – Plasma Membrane Contact Sites. *Annu Rev Biochem* 2017;**86**:659–84. https://doi.org/10.1146/annurev-biochem-061516-044932.

56 Schauder CM, Wu X, Saheki Y, Narayanaswamy P, Torta F, Wenk MR, *et al.* Structure of a lipid-bound extended synaptotagmin indicates a role in lipid transfer. *Nature* 2014;**510**:552–5. https://doi.org/10.1038/nature13269.

57 Falkenburger BH, Jensen JB, Hille B. Kinetics of M1 muscarinic receptor and G protein signaling to phospholipase C in living cells. *J Gen Physiol* 2010;**135**:81–97. https://doi.org/10.1085/jgp.200910344.

58 Falkenburger BH, Jensen JB, Hille B. Kinetics of PIP2 metabolism and KCNQ2/3

channel regulation studied with a voltage-sensitive phosphatase in living cells. *J Gen Physiol* 2010;**135**:99–114. https://doi.org/10.1085/jgp.200910345.

59 Plevin R, Cook SJ, Palmer S, Wakelam MJ. Multiple sources of sn-1,2-diacylglycerol in platelet-derived-growth-factor-stimulated Swiss 3T3 fibroblasts. Evidence for activation of phosphoinositidase C and phosphatidylcholine-specific phospholipase D. *Biochem J* 1991;**279**:559–65. https://doi.org/10.1042/bj2790559.

60 Yeo EJ, Kazlauskas A, Exton JH. Activation of phospholipase C-γ is necessary for stimulation of phospholipase D by platelet-derived growth factor. *J Biol Chem* 1994;**269**:27823–6. https://doi.org/10.1016/S0021-9258(18)46860-3.

61 Van Dijk MCM, Muriana FJG, De Widt J, Hilkmann H, Van Blitterswijk WJ. Involvement of phosphatidylcholine-specific phospholipase C in platelet- derived growth factor-induced activation of the mitogen-activated protein kinase pathway in rat-1 fibroblasts. *J Biol Chem* 1997;**272**:11011–6. https://doi.org/10.1074/jbc.272.17.11011.

62 Shome K, Rizzo MA, Vasudevan C, Andresen B, Romero G. The activation of phospholipase D by endothelin-1, angiotensin II, and platelet-derived growth factor in vascular smooth muscle A10 cells is mediated by small G proteins of the ADP-ribosylation factor family. *Endocrinology* 2000;**141**:2200–8. https://doi.org/10.1210/endo.141.6.7517.

63 Hess JA, Ross AH, Qiu RG, Symons M, Exton JH. Role of Rho family proteins in phospholipase D activation by growth factors. *J Biol Chem* 1997;**272**:1615–20. https://doi.org/10.1074/jbc.272.3.1615.

64 Pathre P, Shome K, Blumental-Perry A, Bielli A, Haney CJ, Alber S, *et al.* Activation of phospholipase D by the small GTPase Sar1p is required to support COPII assembly and ER export. *EMBO J* 2003;**22**:4059–69. https://doi.org/10.1093/emboj/cdg390.

65 Sanematsu F, Sanematsu F, Nishikimi A, Nishikimi A, Watanabe M, Watanabe M, *et al.* Phosphatidic acid-dependent recruitment and function of the Rac activator DOCK1 during dorsal ruffle formation. *J Biol Chem* 2013;**288**:8092–100. https://doi.org/10.1074/jbc.M112.410423.

66 Bumpus TW, Baskin JM. Greasing the Wheels of Lipid Biology with Chemical Tools.

Trends Biochem Sci 2018;**43**:970–83. https://doi.org/https://doi.org/10.1016/j.tibs.2018.09.011.

67 Yang J, Šečkute J, Cole CM, Devaraj NK. Live-cell imaging of cyclopropene tags with fluorogenic tetrazine cycloadditions. *Angew Chem Int Ed* 2012;**51**:7476–9. https://doi.org/10.1002/anie.201202122.

68 Erdmann RS, Takakura H, Thompson AD, Rivera-Molina F, Allgeyer ES, Bewersdorf J, *et al.* Super-resolution imaging of the Golgi in live cells with a bioorthogonal ceramide probe. *Angew Chem Int Ed* 2014;**53**:10242–6. https://doi.org/10.1002/anie.201403349.

69 Thompson AD, Bewersdorf J, Toomre D, Schepartz A. HIDE Probes: A New Toolkit for Visualizing Organelle Dynamics, Longer and at Super-Resolution. *Biochemistry* 2017;**56**:5194–201. https://doi.org/10.1021/acs.biochem.7b00545.

70 Chiapparino A, Maeda K, Turei D, Saez-Rodriguez J, Gavin AC. The orchestra of lipid-transfer proteins at the crossroads between metabolism and signaling. *Prog Lipid Res* 2016;**61**:30–9. https://doi.org/10.1016/j.plipres.2015.10.004.

71 Wong LH, Čopič A, Levine TP. Advances on the Transfer of Lipids by Lipid Transfer Proteins. *Trends Biochem Sci* 2017;**42**:516–30. https://doi.org/10.1016/j.tibs.2017.05.001.

72 Prinz WA. Bridging the gap: Membrane contact sites in signaling, metabolism, and organelle dynamics. *J Cell Biol* 2014;**205**:759–69. https://doi.org/10.1083/jcb.201401126.

73 Reinisch KM, De Camilli P. SMP-domain proteins at membrane contact sites: Structure and function. *Biochim Biophys Acta - Mol Cell Biol Lipids* 2016;**1861**:924–7. https://doi.org/10.1016/j.bbalip.2015.12.003.

74 Brailoiu E, Chakraborty S, Brailoiu GC, Unterwald EM, Abood ME, Taylor CW, *et al.* Choline Is an Intracellular Messenger Linking Extracellular Stimuli to IP3-Evoked Ca2+ Signals through Sigma-1 Receptors. *Cell Rep* 2019;**26**:330–7. https://doi.org/10.1016/j.celrep.2018.12.051.

75 Clark PG, Guidry EN, Chan WY, Steinmetz WE, Grubbs RH. Synthesis of a molecular charm bracelet via click cyclization and olefin metathesis clipping. *J Am Chem Soc*

2010;**132**:3405–12. https://doi.org/10.1021/ja9090337.

76 Li Z, Cai H, Hassink M, Blackman ML, Brown RCD, Conti PS, *et al.* Tetrazine-trans-cyclooctene ligation for the rapid construction of 18F labeled probes. *Chem Commun* 2010;**46**:8043–5. https://doi.org/10.1039/c0cc03078c.

77 Jamieson ML, Hume PA, Furkert DP, Brimble MA. Divergent reactivity via cobalt catalysis: An epoxide olefination. *Org Lett* 2016;**18**:468–71. https://doi.org/10.1021/acs.orglett.5b03514.

78 Kim J, Jeong W, Rhee YH. Flexible tetrahydropyran synthesis from homopropargylic alcohols using sequential Pd-Au catalysis. *Org Lett* 2017;**19**:242–5. https://doi.org/10.1021/acs.orglett.6b03532.

79 Alamudi SH, Satapathy R, Kim J, Su D, Ren H, Das R, *et al.* Development of background-free tame fluorescent probes for intracellular live cell imaging. *Nat Commun* 2016;**7**:. https://doi.org/10.1038/ncomms11964.

CHAPTER 3: Activity-based, bioorthogonal imaging of phospholipase D reveals spatiotemporal dynamics of GPCR–Gq signaling[1]

Abstract

Canonically, GPCR signaling is transient and confined to the plasma membrane (PM). Deviating from this paradigm, the parathyroid hormone receptor (PTHR1) stimulates sustained G_s signaling at endosomes. In addition to G_s, PTHR1 also activates G_q signaling. In contrast to the PTHR1–G_s pathway, the spatiotemporal dynamics of the G_q branch of PTHR1 signaling, and its relationship to G_s signaling, remain largely ill-defined. Recognizing that a downstream consequence of G_q signaling is the activation of phospholipase D (PLD) enzymes, we leveraged activity-based, bioorthogonal imaging tools for PLD signaling to specifically visualize and quantify the G_q branch of PTHR1 signaling. We established that PTHR1–G_q signaling is short-lived, exclusively at the PM, and antagonized by PTHR1 endocytosis. Our data support a model wherein G_q and G_s compete for ligand-bound receptors at the PM and more broadly highlight the utility of bioorthogonal tools for imaging PLDs as probes to visualize GPCR–G_q signaling.

[1] Currently in press as a brief communication by Dongjun Liang, Ross W. Cheloha, Tomoyuki Watanabe, Thomas J. Gardella, Jeremy M. Baskin in *Cell Chemical Biology*.

Introduction

The traditional paradigm for GPCR signaling involves transient, agonist-induced activation of heterotrimeric G proteins and second messenger production at the plasma membrane (PM), which terminates upon receptor internalization [1–3]. Classically, different second messengers are produced at the PM depending on the Gα subtype that is activated. For example, G_s activates adenylyl cyclase, producing cyclic AMP (cAMP), leading to protein kinase A signaling, whereas $G_{q/11}$ stimulates phospholipase Cβ (PLCβ) enzymes, inducing $PI(4,5)P_2$ hydrolysis to produce diacylglycerol (DAG) and inositol trisphosphate (IP_3), leading to protein kinase C (PKC) and Ca^{2+} signaling. Both G_s and G_q are primarily found in the cytosolic leaflet of the PM, though they can also be found at intracellular locations, along with downstream signaling proteins and second messengers [4,5].

Notably, recent work has identified that certain GPCRs, including opioid receptors [6], the β2-adrenergic receptor (β_2AR) [7], and the parathyroid hormone receptor 1 (PTHR1) [8–10], also signal, via G_s, from intracellular membranes after receptor-mediated endocytosis. In the case of PTHR1, such signaling occurs on endosomes following β-arrestin-induced, clathrin-mediated endocytosis of the ligand-bound GPCR [11]. This non-classical, endosomal signaling persists until V-ATPase-mediated endosomal acidification causes ligand dissociation, and subsequent receptor binding to the retromer complex enables eventual recycling to the PM [12–15]. Recent efforts to characterize whether GPCRs remain signaling-competent after internalization have used single-domain antibodies that bind to the receptor in its active conformation as biosensors [16]. Although this approach reveals the subcellular localizations of GPCRs in their active

conformations, it does not elucidate whether these GPCRs maintain the ability to signal via different pathways following internalization.

Sustained endosomal G_s signaling by both β_2AR and PTHR1 has proven physiologically significant for regulating distinct outcomes compared to when confined at the PM [17,18]. However, PTHR1, which has numerous functions in physiology of bone, kidney, and other tissues, has a more complex signaling landscape [19,20]. In addition to both PM and endosome-localized G_s–cAMP signaling, PTHR1 also activates the G_q–PLC axis, and such signaling is also physiologically relevant [21,22]. A longstanding question has been the extent of interplay between the G_q and G_s branches of PTHR1 signaling, which is fundamental to the understanding of diverse physiological functions under the control of PTHR1. Some evidence suggests that regulation of PTHR1–G_q signaling occurs within the kidney [23]. A recent study revealed that G_q signaling was required for subsequent prolonged, intracellular G_s-signaling, via a mechanism implicating G$\beta\gamma$ intracellular translocation and activation of PI3Kb [24].

Nevertheless, the spatiotemporal dynamics of PTHR1–G_q signaling and its full relationship to the G_s pathway remain incompletely understood. Here, we establish a chemical toolset for visualizing the G_q branch of GPCR signaling and apply it to elucidate the spatiotemporal dynamics of PTHR1–G_q signaling and clarify its relationship to G_s signaling. Our approach capitalizes upon the recognition that G_q/PLC signaling — via production of DAG and IP_3 to activate conventional PKCs — leads to stimulation of phospholipase D (PLD) enzymes (Fig. 3.1A). PLDs in turn produce phosphatidic acid (PA), a lipid second messenger that engages several effectors to influence membrane trafficking, cytoskeletal dynamics, and signaling [25,26].

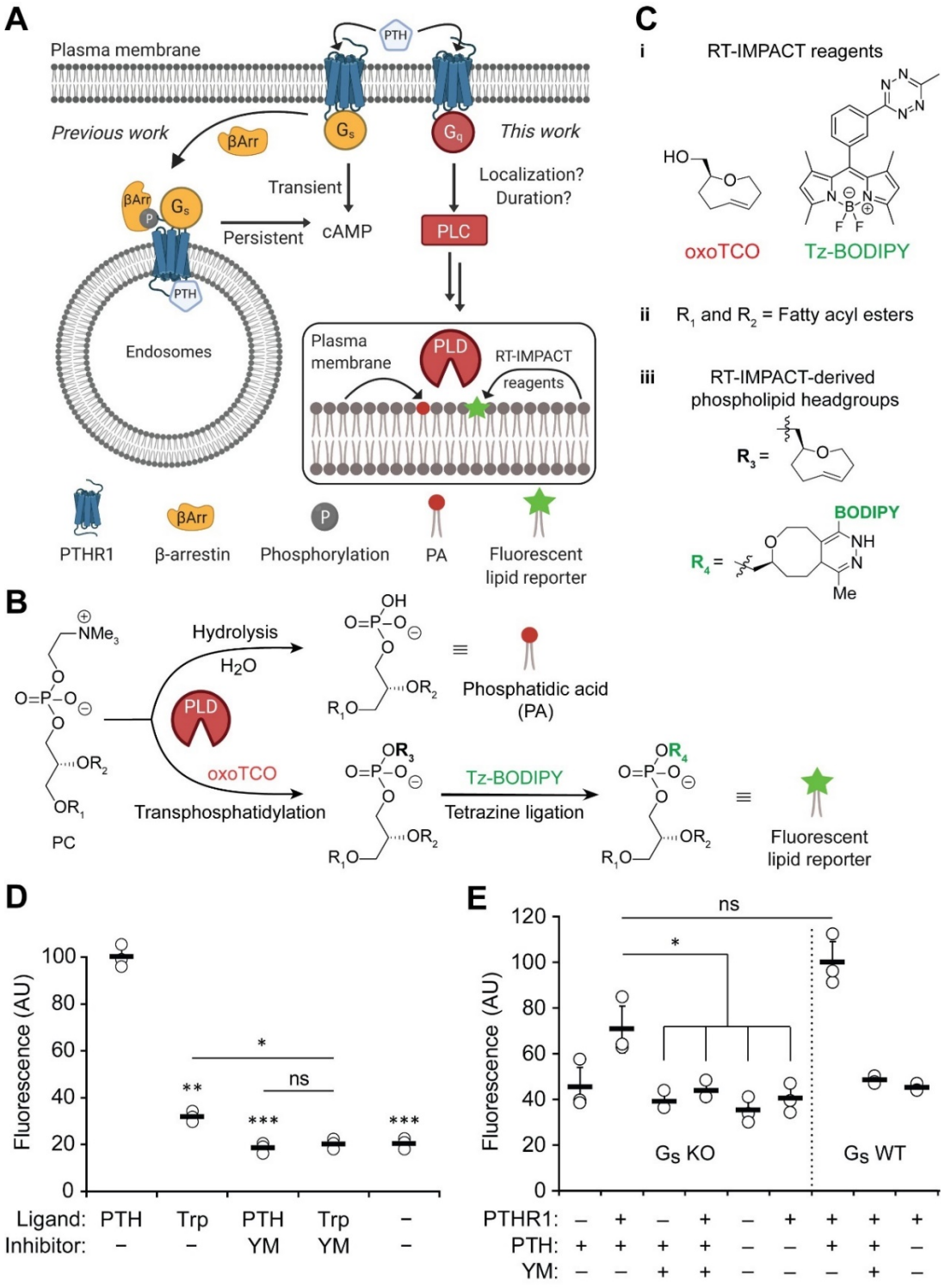

Figure 3.1: RT-IMPACT is a tool to quantify phospholipase D (PLD) activity elicited by PTHR1–G_q but not PTHR1–G_s signaling. (A) Schematic of PTHR1 signaling, illustrating how

RT-IMPACT could report on PTHR-dependent G_q signaling. (B–C) Schematic of (B) and chemical structures for (C) RT-IMPACT, a tool to visualize endogenous PLD signaling. (D–E) Flow cytometry of HEK 293 cells indicating the RT-IMPACT labeling depends upon PTHR1–G_q signaling. (D) HEK 293 cells stably expressing PTHR1 (hPTHR1-293) were incubated with oxoTCO and the indicated PTHR1 ligand for 5 min prior to a rinse and addition of Tz-BODIPY for 1 min, rinse, and flow cytometry analysis. Shown: mean BODIPY fluorescence (AU, arbitrary units). Where indicated, cells were treated with the G_q inhibitor YM-254890 (YM) or DMSO vehicle for 15 min prior to and during oxoTCO and PTHR1 activation step. PTH: PTH(1-34); Trp (G_s-selective agonist): PTH-Trp. (E) G_s knockout (KO) cells transfected with hPTHR1-HA were stained with AF647-conjugated α-PTHR1 antibody to identify transfected cells. Cells were labeled via RT-IMPACT as in (D). Flow cytometry was performed, gating on PTHR1-positive or -negative cells (left). Shown: mean BODIPY fluorescence. hPTHR1-293 cells (G_s WT) were analyzed concurrently (right). Asterisks above data denote significance compared to PTH without inhibitors. Asterisks above lines denote significance comparing the indicated groups. Error bars represent standard deviation. One-way ANOVA, Games-Howell post-hoc test: *$P < 0.05$, **P < 0.01 and ***$P < 0.001$; ns, not significant; n=3 for (D) and (E). See also Fig. 3.2.

We have developed bioorthogonal chemical tools to visualize and quantify PLD activity with organelle-level resolution [27,28]. These approaches harness the ability of PLD enzymes, which normally catalyze phosphatidylcholine hydrolysis to produce PA, to also produce phosphatidyl alcohol lipids via transphosphatidylation with exogenous primary alcohols [29]. Our tools, termed Imaging Phospholipase D Activity with Clickable Alcohols via

Transphosphatidylation (IMPACT), use bioorthogonally labeled alcohols as transphosphatidylation substrates, followed by click chemistry tagging of the resultant lipids in live cells with fluorescent groups (Fig. 3.1B) [27].

By using an alcohol and click chemistry partner capable of undergoing a rapid and fluorogenic inverse electron-demand Diels-Alder (IEDDA) cycloaddition, such labeling can be performed in real time (RT-IMPACT) [27,28]. In RT-IMPACT, the IEDDA-tagged lipids, prior to their trafficking to other organelle membranes, report on the localizations of endogenous PLD activity [27]. Because of the specific connection between G_q/PLC signaling and PLD activation, we reasoned that RT-IMPACT would enable us to visualize localizations and quantify the extent of PLD activity downstream of PTHR1–G_q signaling, reporting on the spatiotemporal dynamics of this branch of PTHR1 signaling.

Here, we first establish that RT-IMPACT is a selective reporter for PTHR1–G_q signaling, and we show that PTHR1–G_q signaling specifically activates the PLD1 isoform. We then reveal that PLD1 signaling downstream of PTHR1–G_q is transient and occurs exclusively at the PM. The timescale of this signaling matched that of the PM residence of the ligand-bound GPCR, and inhibition of endocytosis prolonged G_q and suppressed G_s signaling. These data suggest that G_q and G_s compete for PTHR1-mediated signaling upon ligand binding at the PM, hence giving rise to maximal levels of cAMP production after the termination of G_q signaling by receptor endocytosis. This work reveals insights into spatiotemporal control of signaling via different Gα subunits from the same GPCR and highlights how bioorthogonal tools to visualize PLD signaling can act as selective reporters of G_q signaling.

Results and Discussion

G_q, but not G_s, is required for PLD activation downstream of PTHR1

We began by determining the specificity of RT-IMPACT as a reporter for G_q-signaling downstream of PTHR1. During PTHR1 stimulation, we treated cells with a *trans*-cyclooctene alcohol (oxoTCO, Fig. 3.1C), in the presence or absence of PTHR1 ligands, to generate oxoTCO-containing lipids as transphosphatidylation products. After a rinse and IEDDA tagging with a fluorogenic tetrazine-BODIPY (Tz-BODIPY, Fig. 3.1C), cellular fluorescence was quantified by flow cytometry. To stimulate PTHR1, we first used PTH(1-34), comprising the N-terminal fragment of the parathyroid hormone (PTH), which strongly activates all downstream PTHR1-coupled Gα pathways. We found substantial PTH(1-34)-dependent RT-IMPACT labeling (Fig. 3.1D).

To determine whether RT-IMPACT reports on G_q versus G_s signaling, we treated HEK 293 cells stably expressing PTHR1 with PTH(1-34)-Trp1, a G_s-biased ligand that induces binding of the receptor exclusively to G_s [30], and found that this ligand exhibited only a very minimal activation of PLDs (Fig. 3.1D). Alternatively, we applied PTH(1-34) with YM-254890 [31,32], a G_q-selective inhibitor, and found no detectable PLD activity (Fig. 3.1D). These results are consistent with our previous work using these probes to distinguish PTHR1-dependent G_q vs. G_s signaling using fluorescence-based Ca^{2+} measurements as a readout [20,33]. To selectively activate G_q, we expressed PTHR1 in G_s knockout cells, and upon PTH stimulation, found a comparable level of PLD activity to that from PTH-stimulated, PTHR1-expressing wild-type cells (Figs. 3.1E and 3.2). These data indicate that G_q, and not G_s, is responsible for the

activation of PLDs downstream of PTH–PTHR1 signaling, likely via PLCβ enzymes, which hydrolyze $PI(4,5)P_2$ to generate DAG and IP_3 to activate PKCs, which upregulate PLDs.

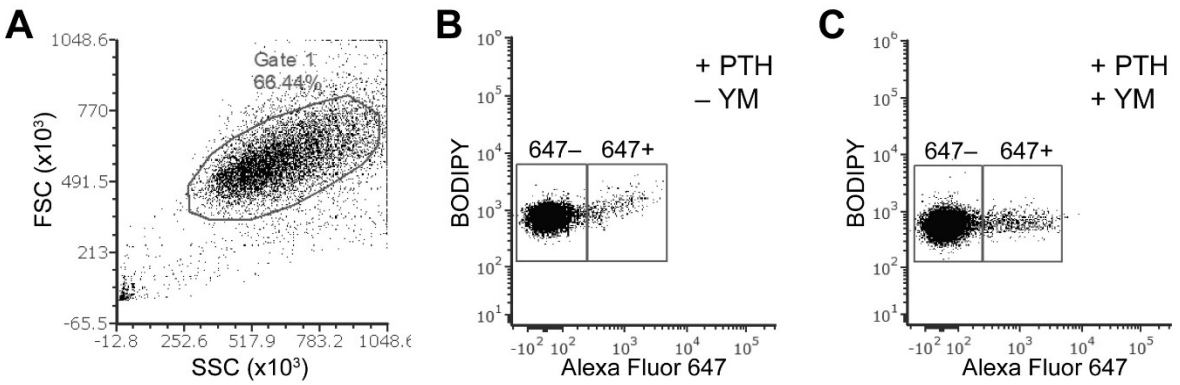

Figure 3.2: Gating strategy for two-color flow cytometry, related to Fig. 3.1. G_s KO HEK 293 cells were transfected with hPTHR1-HA, and after 24 h, cells were stained with Alexa Fluor 647-tagged anti-PTHR1 antibody (100 nM, 30 min at 4 ºC). Cells were incubated with PTH and/or YM-254890 (YM), and RT-IMPACT labeling was performed as described in the legend for Fig. 3.1. (A) Live cells were identified using the indicated gate, comparing forward scatter (FSC) and side scatter (SSC) analysis. Singlets were also gated for further analysis. (B and C) Identification of cells expressing PTHR1 (647+) and those not expressing PTHR1 (647–) from two-color scatter plots of Alexa Fluor 647 (hPTHR1) and BODIPY (RT-IMPACT) indicated gates in the +PTH/–YM (B) and +PTH/+YM (C) samples. Data shown in Fig. 3.1E (left) are BODIPY mean fluorescence intensities for the 647+ and 647– populations.

PTHR1 predominantly activates the PLD1 isoform at the PM

To characterize the nature of the PTHR1–G_q-induced PLD signaling, we used isoform-selective PLD inhibitors to determine which of the two PLD isoforms that generate PA via PC hydrolysis, PLD1 and PLD2, is responsible for PLD activity downstream of PTHR1. Using RT-

IMPACT followed by flow cytometry, we found that a PLD1-selective inhibitor (VU0359595, IC_{50}(PLD1) = 3.7 nM; IC_{50}(PLD2) = 6.4 μM) abrogated nearly all of the PTH-induced PLD activity, equivalent to a pan-PLD inhibitor (Fig. 3.3A). By contrast, a PLD2-selective inhibitor (VU0364739, IC_{50}(PLD1) = 1.5 μM; IC_{50}(PLD2) = 20 nM) had only a modest effect (Fig. 3.3A). Thus, PLD1 is responsible for the bulk of the PLD activity downstream of PTHR1, consistent with the established role of PLD1 as inducible by activated PKCs [29,34].

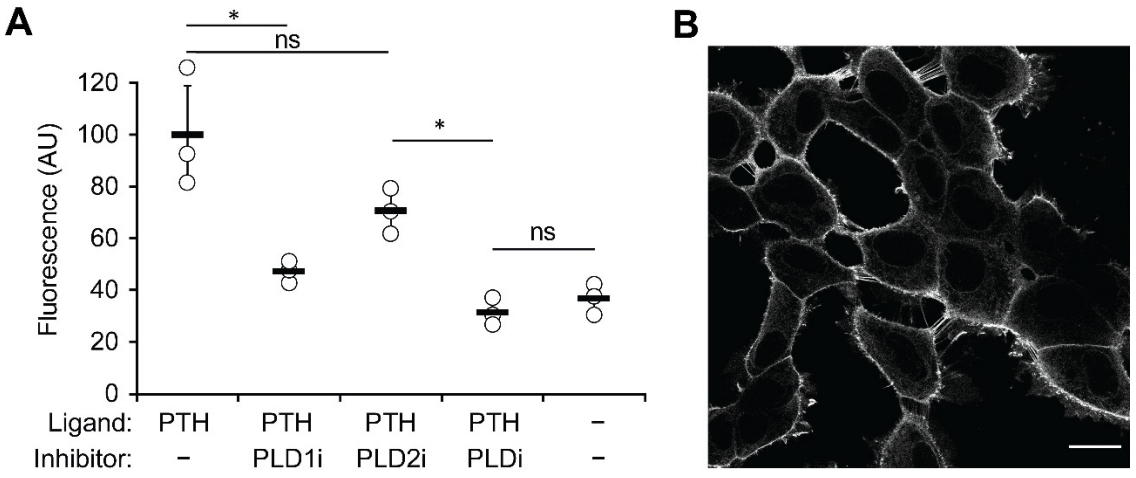

Figure 3.3: PTHR–G_q-induced PLD signaling is due predominantly to the PLD1 isoform and is localized at the PM. (A). Flow cytometry of PLD activity of hPTHR1-293 cells stimulated by PTH in the presence of pan- or isoform-selective PLD inhibitors. Cells were incubated with the indicated inhibitors (PLD1i, PLD1-selective VU0359595; PLD2i, PLD2-selective VU0364739; PLDi, pan-inhibitor FIPI) or DMSO for 30 min. PTH and oxoTCO were added for 5 min before rinsing, Tz-BODIPY addition, and flow cytometry analysis. Asterisks above lines denote significance comparing the indicated groups. Error bars represent standard deviation. One-way ANOVA, Games-Howell post-hoc test: *$P < 0.05$, **$P < 0.01$ and ***$P < 0.001$; ns, not significant; n=3. (B) Rea-time confocal microscopy of hPTHR1-293 cells

stimulated with PTH and labeled via RT-IMPACT to reveal localization of PTHR1-derived PLD signaling, showing 9 s post-addition of Tz-BODIPY. Experiments were performed similarly as previously described in Figs. 2.19B and 2.22B. Scale bar: 20 μm. See also Fig. 3.4.

We next sought to use RT-IMPACT to reveal the subcellular localization of the PTHR1–G_q-induced PLD signaling. Here, we performed a similar RT-IMPACT labeling with oxoTCO during PTH stimulation, rinsing, and then visualization of the fluorogenic IEDDA tagging reaction in real-time by time-lapse confocal microscopy. Because of the rapid kinetics of this IEDDA reaction, we could detect its fluorescent lipid products within seconds of administering Tz-BODIPY to cells, and such images reveal the localization of PLD-generated lipids prior to their subsequent trafficking. Using this technique, we found that PTHR1-induced PLD activity is exclusively at the PM (Figs. 3.3B and 3.4).

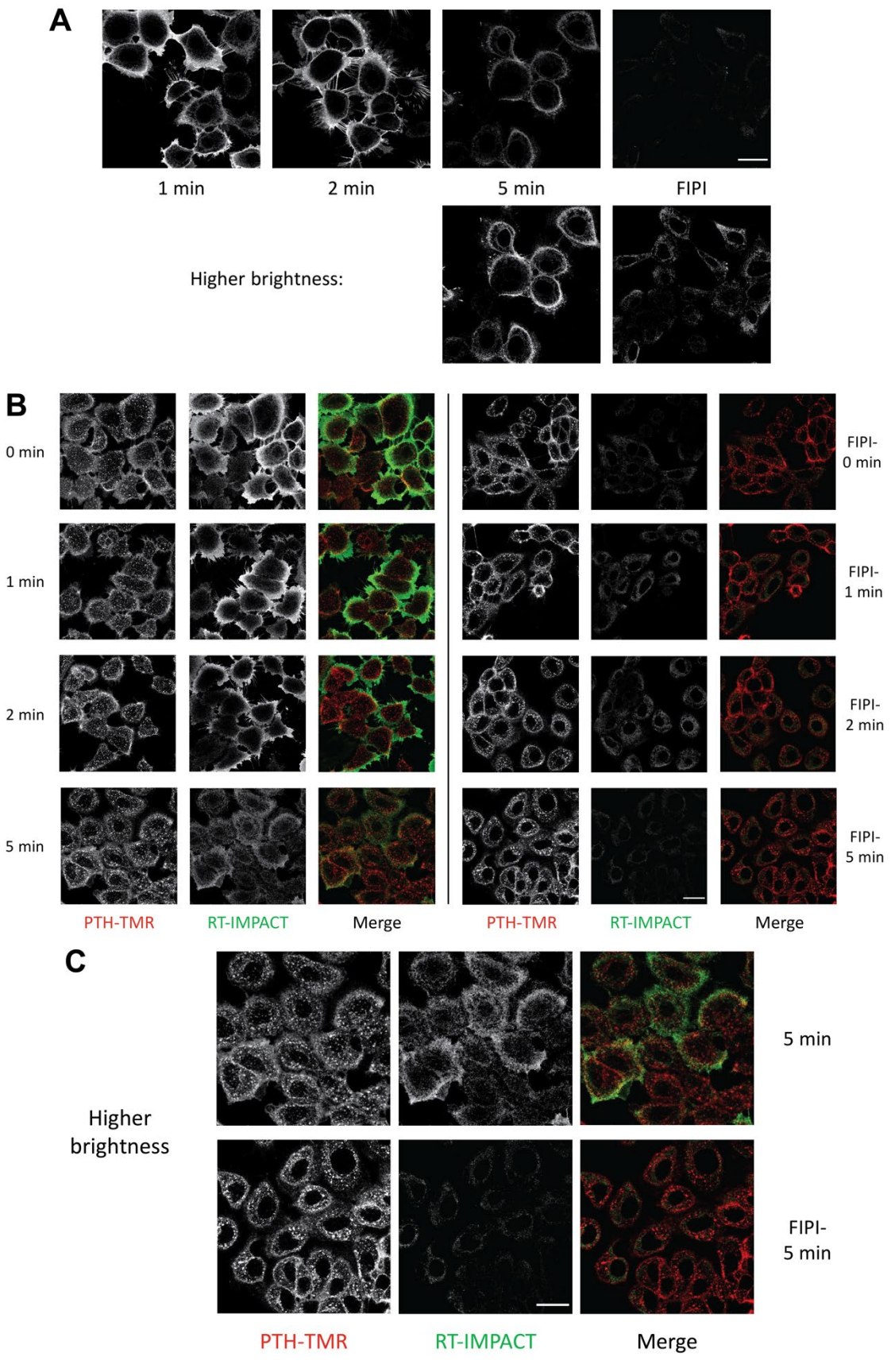
A
1 min
2 min
5 min
FIPI
Higher brightness:
B
0 min
1 min
2 min
5 min
FIPI-
0 min
FIPI-
1 min
FIPI-
2 min
FIPI-
5 min
PTH-TMR
RT-IMPACT
Merge
PTH-TMR
RT-IMPACT
Merge
C
Higher
brightness
5 min
FIPI-
5 min
PTH-TMR
RT-IMPACT
Merge

Figure 3.4: RT-IMPACT imaging reveals that PLD activity induced by PTH(1-34) and PTH-TMR is localized at plasma membrane, related to Fig. 3.3. hPTHR1-293 cells were stimulated with PTH(1-34) (A) or PTH-TMR (B–C) for the indicated periods of time (1–5 min) at 37 ºC before being labeled via RT-IMPACT to reveal the subcellular localization of PTHR1-derived PLD signaling. Where indicated, cells were treated with the pan-PLD inhibitor PLDi (FIPI, 750 nM) or DMSO vehicle for 30 min prior to and during the PTH and oxoTCO incubation step. Images showing RT-IMPACT fluorescence are at t = 9 s post-addition of Tz-BODIPY. All images in (A) and in (B–C) were acquired with the same microscope settings. For (A), images in the top row are processed identically, and in the bottom row, the 5 min and FIPI images are additionally shown at higher brightness levels to facilitate better visual assessment of the signal and background (due to the lower extent of RT-IMPACT labeling at the 5 min timepoint). Similarly, in (B–C), Images in (B) are all shown at the same brightness levels, and images in (C) are shown at higher brightness in the RT-IMPACT channel. Scale bars: 30 μm.

We have previously shown that platelet-derived growth factor receptor signaling induced PLD activity at intracellular membranes using RT-IMPACT [27]. Therefore, a lack of similar intracellular fluorescence following PTHR1 activation provides strong evidence of a restricted subcellular localization of PLD1 activation in this context. Though PLD1 localizes to many intracellular sites, it can translocate to the PM upon certain stimuli. In this setting, PTHR1–G_q signaling, which activates PLCβ to generate the PKC agonist diacylglycerol, would be expected to stimulate the activity of PLDs in this membrane.

RT-IMPACT reveals that PTHR1–G_q activation of PLDs is transient

In addition to the spatial aspects of PTHR1–G_q signaling, we also sought to use RT-IMPACT to elucidate the temporal dynamics of this pathway. The temporal resolution of RT-IMPACT is roughly 5 min, encompassing transphosphatidylation, rinsing, and IEDDA reaction. To quantify PTHR1–G_q signaling elicited by PTH agonism over time, we varied the time after PTH addition prior to oxoTCO addition by 5-min intervals. Flow cytometry of cells labeled via RT-IMPACT in this manner revealed that PLD activity downstream of PTHR1–G_q signaling was transient, peaking within the first five minutes and rapidly returned to basal levels within 10 min of exposure to PTH (Figs. 3.5A and 3.6). This finding aligns with previous work showing that PTHR1–G_q signaling induces a transient release of calcium into the cytoplasm that reverts to basal levels within a few minutes [20,35].

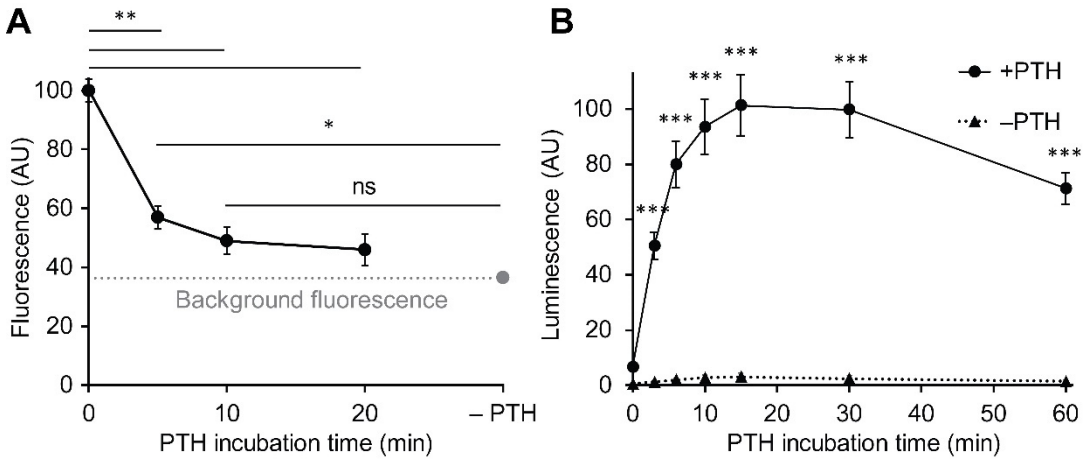

Figure 3.5: PLD activation downstream of PTHR1–G_q signaling is transient, in contrast to persistent PTHR1–G_s signaling. (A) Flow cytometry of hPTHR1-293 cells, showing extent of PLD activity following PTH addition. hPTHR1-293 cells were stimulated with PTH for 0–20 min, followed by oxoTCO addition for 5 min, rinsing, Tz-BODIPY addition, and flow cytometry. Gray: background fluorescence in the absence of PTH. (B) Levels of cAMP from hPTHR1-293 cells stably expressing cAMP GloSensor after addition of PTH (solid line; circles)

or control (dashed line; triangles). In (A), asterisks above lines denote significance comparing the indicated groups. In (B), asterisks above groups represent significance comparing the +/– PTH conditions at each timepoint. Error bars represent standard deviation. One-way ANOVA, Games-Howell post-hoc test: *$P < 0.05$, **$P < 0.01$ and ***$P < 0.001$; ns, not significant; n=3 for (A) and n=4 for (B). See also Fig. 3.6.

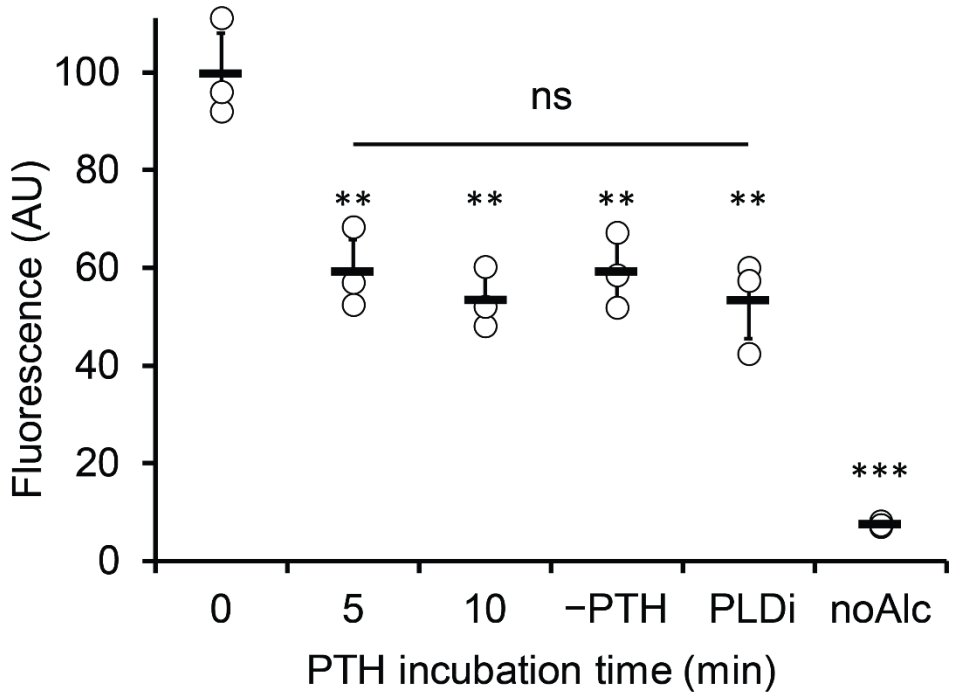

Figure 3.6: Flow cytometry analysis using RT-IMPACT reagents reveals desensitization of PLD activities downstream of PTHR1-G_q, related to Fig. 3.5. Flow cytometry analysis of hPTHR1-293 cells, showing extent of PLD activity in the 10 min following the addition of PTH. hPTHR1-293 cells were stimulated with PTH for the indicated period of time (0–10 min), followed by RT-IMPACT labeling by addition of oxoTCO for 5 min in the continued presence of PTH, rinsing, addition of Tz-BODIPY, and analysis by flow cytometry. Shown is the BODIPY mean fluorescence intensity (AU, arbitrary units). Where indicated, cells were treated

with the pan-PLD inhibitor PLDi (FIPI, 750 nM) or DMSO vehicle for 30 min prior to and during oxoTCO and PTHR1 activation step. NoAlc: negative control with no oxoTCO present throughout experiment. Asterisks directly above data groups denote statistical significance compared to PTH without the presence of inhibitors. Asterisks above horizontal lines denote statistical significance comparing the indicated data groups, and error bars represent standard deviation. One-way ANOVA with Games-Howell post-hoc test: *$P < 0.05$, **P < 0.01 and ***$P < 0.001$; ns, not significant; n=3.

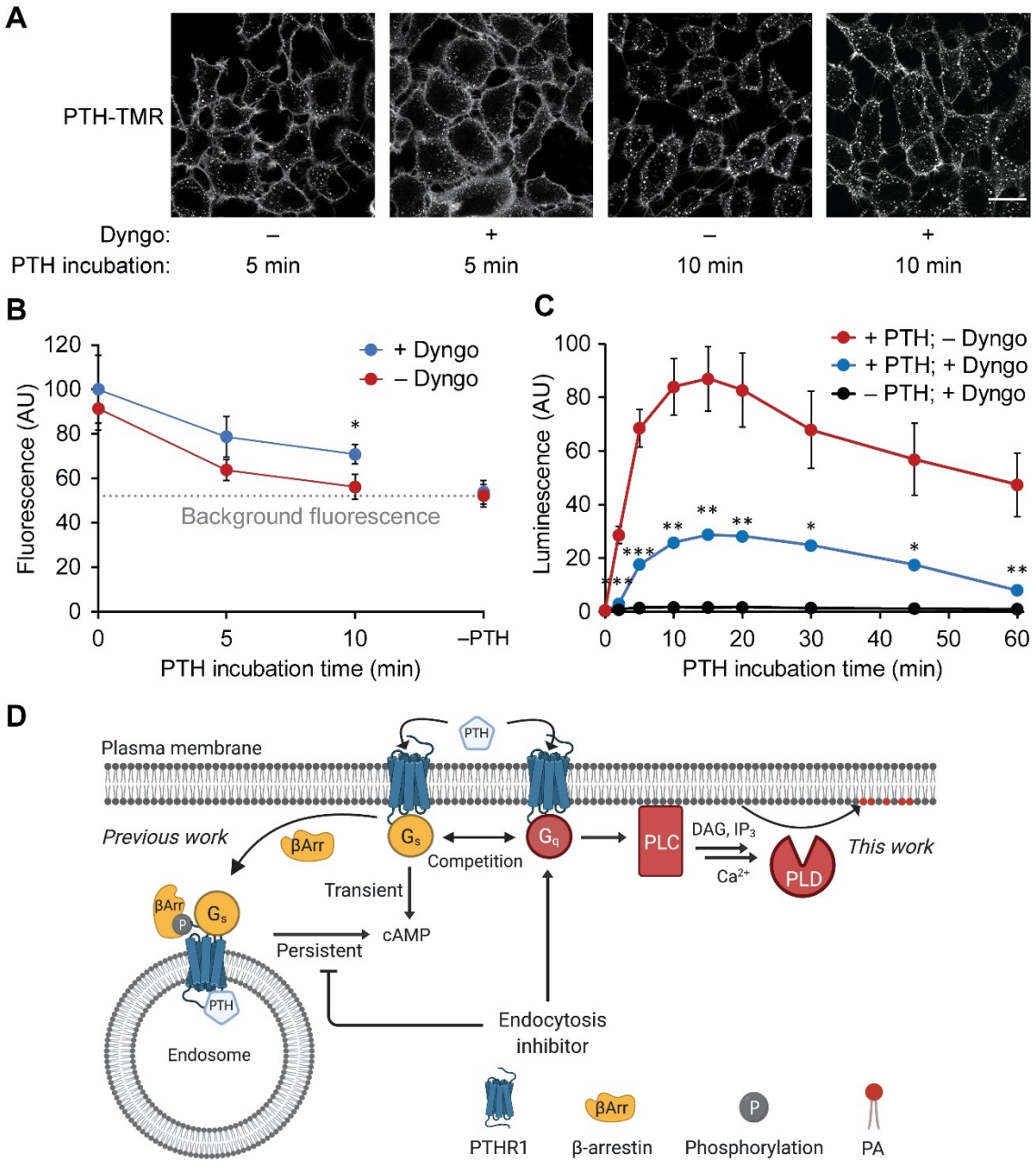

Figure 3.7: Inhibition of PTHR1 endocytosis prolongs PLD activation through G_q and reduces G_s/cAMP signaling. (A) Confocal microscopy of hPTHR1-293 cells treated with rhodamine-PTH (PTH-TMR) for 5–10 min. Cells were treated with Dyngo-4a or DMSO vehicle 15 min prior to and during ligand addition. Scale bar: 30 µm. (B) Flow cytometry of hPTHR1-293 cells, showing extent of PLD activity over 20 min after the PTH addition +/– Dyngo addition.

hPTHR1-293 cells were incubated with Dyngo or vehicle for 15 min, stimulated with PTH for 0–20 min in the presence of Dyngo or vehicle, followed by addition of oxoTCO (5 min) in the presence of PTH and Dyngo or vehicle, rinsing, addition of Tz-BODIPY, and flow cytometry. Shown: mean BODIPY fluorescence. Gray: background fluorescence in the absence of PTH. (C) Timecourse of cAMP levels in hPTHR1-293 cells stably expressing cAMP GloSensor. Dyngo or vehicle was added 15 min prior to and during the PTH labeling step. (D) Model indicating competition between G_q and G_s signaling downstream of PTHR1. In (B–C), asterisks above data denote significance comparing blue and red data points (+ vs. – Dyngo in the presence of PTH). Error bars represent standard deviation. One-way ANOVA, Games-Howell post-hoc test: *$P < 0.05$; **$P < 0.01$; ***$P < 0.001$; ns, not significant; n=3 for (B) and n=4 for (C). See also Fig. 3.8.

By contrast, PTHR1–G_s signaling was, as expected, delayed and sustained, peaking at 15 min post-PTH application and persisting for at least 60 min, as measured by a cAMP-based biosensor assay (Fig. 3.5B) [36]. This short-lived G_q activation is in line with the classical model of GPCR signaling, wherein ligand-bound receptors are rapidly phosphorylated and internalized via binding to β-arrestins, which terminates most GPCR signaling processes but prolongs G_s signaling in the case of PTHR1.

Despite such rapid deactivation of PTHR1–G_q signaling within 10 min of PTH stimulation, the observed PLD activity at various timepoints (1, 2, and 5 min) post-addition of either PTH or rhodamine-tagged PTH (PTH-TMR), to visualize PTH–PTHR1 complexes, was predominantly at the PM even before complete desensitization (Fig. 3.4), suggesting that G_q activation of PLD was confined to the PM in this context. Importantly, our findings reinforce

and are complementary to a recent report that G_q activation is critical for prolonged endosomal G_s signaling through the recruitment of β-arrestins [24].

Receptor endocytosis antagonizes PTHR1–G_q-elicited PLD activity

The above data reveal a stark contrast between the spatiotemporal dynamics of PTHR1-induced G_q and G_s signaling, with the former transient and at the PM and the latter being sustained and largely from endosomes [13]. Typically, ligand-bound GPCRs are internalized via interaction with β-arrestin and subsequent clathrin-mediated endocytosis [37,38]. We hypothesized that receptor-mediated endocytosis might act as a key control point for the switch from G_q to G_s signaling [13]. To test this idea, we perturbed the endocytosis of PTHR1 and investigated effects on the amplitudes and kinetics of G_q and G_s signaling.

First, we tested the effects of blocking endocytosis by treating cells with Dyngo-4a, an inhibitor of dynamin [17,39,40], a GTPase required for clathrin-mediated endocytosis. We established conditions under which Dyngo-4a reduced the endocytosis of PTHR1, by visualizing PTH–PTHR1 complexes by confocal microscopy in cells treated with PTH-TMR. At 5–10 min after PTH-TMR addition, we found that Dyngo-4a led to substantially reduced internalization of PTHR1–PTH-TMR complexes (Fig. 3.7A). We then found that Dyngo-4a treatment led to prolonged G_q activation compared to control, as assessed by flow cytometry of RT-IMPACT-labeled cells (Fig. 3.7B). By contrast, under these same conditions, the magnitude of PTHR1–G_s signaling was significantly reduced (Fig. 3.7C). Moreover, the same inhibitory effect of Dyngo-4a on G_s signaling was confirmed in human osteosarcoma cells, which express physiological levels of PTHR1 (Fig. 3.8A), although we were unable to detect Ca^{2+} responses by fura-2 or PLD activity by IMPACT, following PTH stimulation in these cells, speaking to a

possible combination of factors, including a limited sensitivity of the method, low levels of PTHR1 expression, and a more modest stimulation of G_q, compared to G_s, by PTHR1 [41] (Fig. 3.8B and 3.8C).

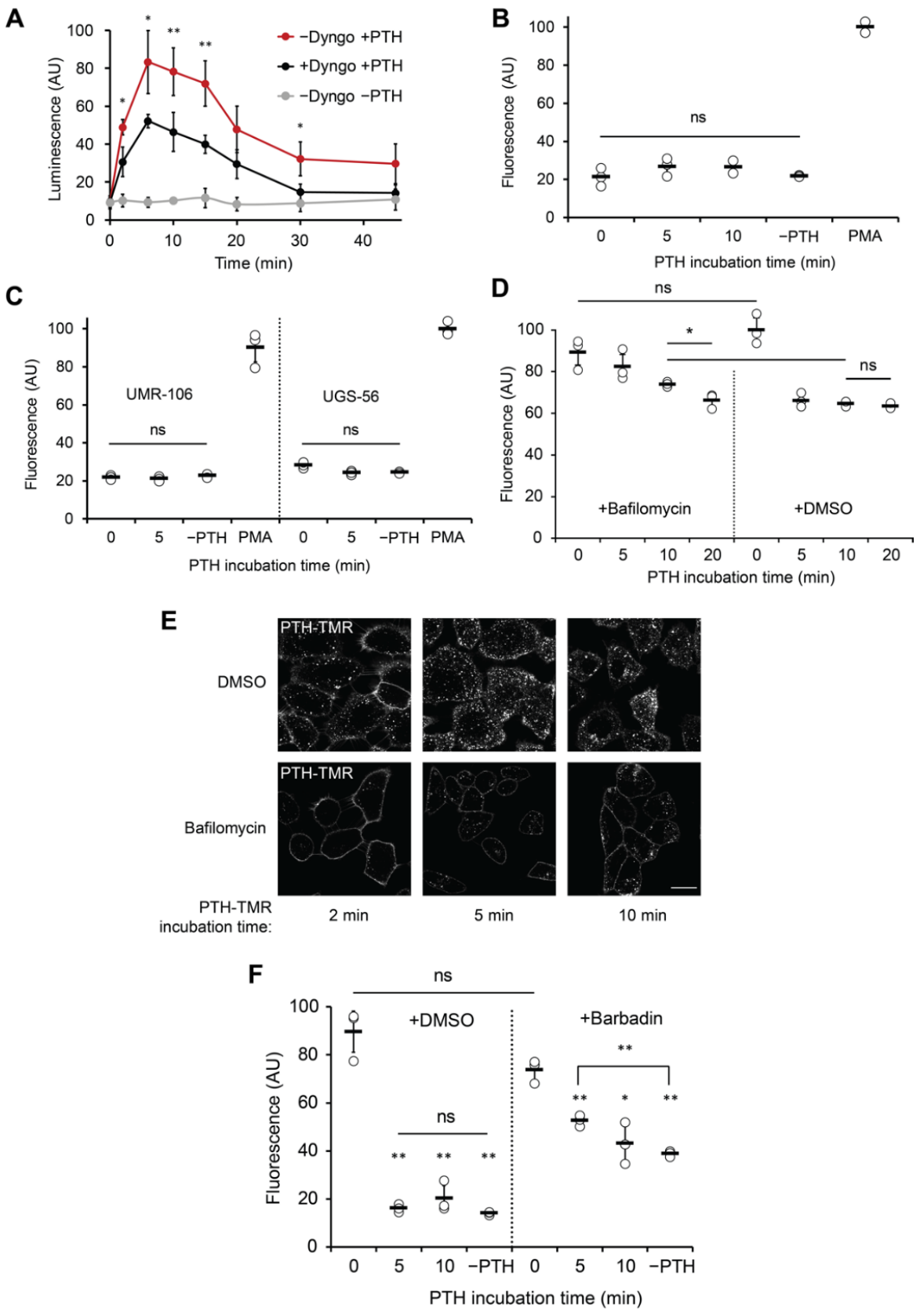
A
Luminescence (AU)
Time (min)
−Dyngo +PTH
+Dyngo +PTH
−Dyngo −PTH
B
Fluorescence (AU)
ns
PTH incubation time (min)
−PTH
PMA
C
UMR-106
UGS-56
ns
PTH incubation time (min)
D
ns
*
+Bafilomycin
+DMSO
PTH incubation time (min)
E
PTH-TMR
DMSO
Bafilomycin
PTH-TMR incubation time:
2 min
5 min
10 min
F
+DMSO
+Barbadin
ns
**
PTH incubation time (min)

Figure 3.8: Effects of endocytosis perturbation on PTHR1 signaling in various cell lines, related to Figure 4. (A) Quantification of cAMP production in SGS-72 cells (SaOS-2 human osteosarcoma cells engineered to express the split luciferase-based GloSensor) at various timepoints post-addition of PTH or control. Dyngo-4a (30 μM) or vehicle (DMSO) was added 15 min prior to and during the PTH labeling step. cAMP levels were measured using the GloSensor assay. Asterisks directly above data points denote statistical significance comparing the black and red data points (+Dyngo vs. –Dyngo in the presence of PTH). (B) Flow cytometry analysis of PLD activities of SaOS-2 cells under stimulation of PTH(1-34) or phorbol 12-myristate 13-acetate (PMA). Cells were stimulated with PTH(1-34) for the indicated amount of time and then labeled by IMPACT via addition of azidopropanol in the continued presence of PTH for 5 min, addition of BCN-BODIPY, rinsing, and analysis by flow cytometry [28]. Where indicated, PMA (100 nM) was added to the cells together with azidopropanol as a positive control for IMPACT and to verify expression of PLDs in these cells. Plotted are mean fluorescence intensities of BODIPY fluorescence. (C) Flow cytometry analysis of PLD activities of UMR-106 rat osteosarcoma cells and UGS-56 cells (UMR-106 cells stably expressing cAMP GloSensor) stimulated by either PTH(1-34) or PMA. Cells were labeled as described in (B). Asterisks directly above data groups denote statistical significance compared to 0 min within the same group (+DMSO or +Barbadin). Asterisks above horizontal lines denote statistical significance comparing the indicated two data groups. Error bars represent standard deviation. One-way ANOVA with Games-Howell post-hoc test: $*P < 0.05$ and $**P < 0.01$; ns, not significant; n=4 for (A) and n=3 for (B) and (C). (D–E) Bafilomycin A1 attenuates PTHR1 endocytosis and prolongs PLD activity downstream of PTHR1–Gq signaling. (D) Shown is flow cytometry analysis of hPTHR1-293 cells treated with Bafilomycin A1 or DMSO vehicle

for 16 h and then stimulated with PTH for the indicated amount of time prior to RT-IMPACT. Cells were then labeled by RT-IMPACT by addition of oxoTCO in the continued presence of PTH for 5 min, rinsing, addition of Tz-BODIPY, and analysis by flow cytometry. Plotted are mean fluorescence intensities of BODIPY fluorescence. Asterisks above horizontal lines denote statistical significance comparing the indicated two points. (In particular, note significant differences between (i) Bafilomycin 10 min and Bafilomycin 20 min and (ii) Bafilomycin 10 min and DMSO 10 min.) Error bars represent standard deviation. One-way ANOVA with Games-Howell post-hoc test: *$P < 0.05$; ns, not significant; n=3. (E) Confocal microscopy analysis of hPTHR1-293 cells treated with PTH-TMR for 2, 5, or 10 min. As indicated, cells were treated with DMSO vehicle (top) or Bafilomycin A1 (bottom) 16 h prior to and during ligand addition. PTH-TMR was added to the cells for 20 s, followed by two quick rinses with PBS and confocal microscopy analysis of cells kept at 37 ºC, with images acquired at 2, 5, and 10 min timepoints. Scale bar: 20 μm. (F) The β-arrestin inhibitor Barbadin prolongs PLD activity downstream of PTHR1–G_q signaling. Shown is flow cytometry analysis of hPTHR1-293 cells treated with Barbadin or DMSO vehicle for 30 min and then stimulated with PTH for the indicated periods of time prior to IMPACT. Cells were then labeled by addition of azidopropanol in the continued presence of PTH for 5 min, addition of BCN-BODIPY, rinsing and analysis by flow cytometry [28]. Plotted are mean fluorescence intensities of BODIPY fluorescence. Asterisks directly above data groups denote statistical significance compared to 0 min within the same group (+DMSO or +Barbadin). Asterisks above horizontal lines denote statistical significance comparing the indicated two data groups. Error bars represent standard deviation. One-way ANOVA with Games-Howell post-hoc test: *$P < 0.05$ and **$P < 0.01$; ns, not significant; n=3.

To account for any potential off-target effects of Dyngo-4a [42,43], we corroborated these findings by perturbing endocytosis using two independent methods. First, we treated cells with Bafilomycin A1 (BafA1), an inhibitor of the V-ATPase responsible for endosomal acidification. Prolonged BafA1 treatment, by preventing endosomal maturation to lysosomes, has the ultimate effect of diminishing endocytosis [15,44]. Similar to Dyngo-4a, BafA1 potentiated G_q-induced PLD signaling (Fig. 3.8D and 3.8E). Alternatively, we perturbed clathrin-mediated endocytosis through acute inhibition of β-arrestins by the pharmacological inhibitor Barbadin, which blocks interactions between β-arrestin and the clathrin adaptor protein AP2 to prevent endocytosis of β_2AR [45]. Consistent with the Dyngo-4a and BafA1 experiments, Barbadin treatment prolonged PTHR1-depedent PLD activation (Fig. 3.8F).

Collectively, these results support a model wherein the PTHR1–G_q pathway is restricted to the PM. Under physiological conditions, this branch of PTHR1 signaling is short-lived and is terminated upon endocytosis of PTHR1, within 5–10 min of ligand binding. By contrast, the G_s-cAMP pathway occurs on both membranes. At the PM, a brief burst of G_s signaling, immediately following PTHR1 activation, has been reported, but the bulk of G_s signaling is now appreciated to occur at early endosomes, peaking at ~15 min and lasting for more than 1 hour.

These observations can be explained by a model wherein G_q and G_s compete for binding to PTH-bound PTHR1 receptors at the PM, where both pathways are active upon initial ligand binding (Fig. 3.7D). Phosphorylation and subsequent β-arrestin-mediated endocytosis of PTHR1 terminates PTHR1–G_q signaling, leading ultimately to PTHR1 signaling at endosomes via the G_s-cAMP pathway, such that maximal cAMP levels correlate with the termination of

G_q-induced PLD signaling. The pharmacological perturbations of receptor endocytosis, which enhance G_q signaling and attenuate G_s signaling, further supports this model of a competitive relationship between G_q and G_s signaling in this system.

Conclusion

We have established that RT-IMPACT, an activity-based, bioorthogonal method for visualizing PLD signaling, can be used to selectively image and quantify GPCR–G_q signaling. We applied RT-IMPACT to elucidate the spatiotemporal dynamics of G_q signaling downstream of PTHR1, an important GPCR in physiology and disease that signals through multiple Gα proteins at diverse subcellular locations. Following PTH binding, PLD activity downstream of PTHR1–G_q signaling occurs transiently and exclusively at the PM. Perturbations of receptor endocytosis prolonged such G_q signaling and reduced G_s signaling, which predominantly occurs on endosomes, supporting a model for competition between G_q and G_s for binding to the activated receptor. These data reinforce that G_q and G_s signaling downstream of PTHR1 activation exhibit vastly different spatiotemporal behavior, and such dynamics may be critical for the distinct physiological outcomes of these signaling pathways. More generally, our study underscores the value of applying bioorthogonal imaging methods for tracking PLD activity to understand the regulation of diverse signaling pathways that intersect with PLD signaling.

Methods and materials

Key resources table

REAGENT or RESOURCE	SOURCE	IDENTIFIER
Antibodies		
Anti-PTHR1-Alexa Fluor 647 nanobody	Laboratory of Ross Cheloha	VHH_{PTHR}, described in [35]
Chemicals, Peptides, and Recombinant Proteins		
Bafilomycin A1	Cayman Chemical	Cat# 11038
Barbadin	MedChem Express	Cat# HY-119706
D-luciferin	Gold Bio	Cat# L-123-250
Dyngo-4a	Selleck Chem	Cat# S7163
FIPI	Cayman Chemical	Cat# 13563
PLD1i	Laboratory of Alex Brown	VU0359595
PLD2i	Laboratory of Alex Brown	VU0364739
Phorbol 12-myristate 13-acetate (PMA)	Santa Cruz Biotechnology	Cat# sc-3576
PTH(1-34) (PTH)	GenScript	Cat# RP01001
PTH(1-34) Trp1 (PTH-Trp)	Massachusetts General Hospital Peptide/Protein Core Facility	Sequence: WVSEIQLMHNLGKHLNSMERVEWLRKKLQDVHNF-CO_2H
PTH-K13-TMR (PTH-TMR)	Massachusetts General Hospital Peptide/Protein Core Facility	Sequence: SVSEIQLMHNLGK(5-carboxytetramethylrhodamine)HLNSMERVEWLRKKLQDVHNF-CO_2H

YM-254890	Focus Biomolecules	Cat# 10-1590-0100
Critical Commercial Assays		
GloSensor cAMP responsive luciferase stably expressed in HEK 293	Promega	pGloSensor™-22F, # E2301, described in [36]
Experimental Models: Cell Lines		
hPTHR1-HEK 293 containing GloSensor (293-PTHR1)	ATCC	CRL-11268 base cell line (HEK 293). Stable hPTHR1-HEK 293 expressing GloSensor plasmid originally described in [46]
G_s KO-HEK 293	G_s knockout achieved using CRISPR-Cas9	Described in [47]
SaOS-2	ATCC	HTB-85, human osteosarcoma
SGS-72	ATCC	SaOS-2 cells stably expressing GloSensor [48]
UMR-106	ATCC	CRL-1661, Rat osteosarcoma
UGS-56	ATCC	UMR-106 cells stably expressing GloSensor [49]
Recombinant DNA		
hPTHR1-HA plasmid	Gardella Lab, custom plasmid (VectorBuilder). HA inserted into exon 2	Gardella lab plasmid #906
Software and Algorithms		
ImageJ	NIH	https://imagej.nih.gov/ij/

General materials and methods

See Key Resources Table for sources for reagents, cell lines, etc. All imaging experiments were performed on a Zeiss LSM 800 confocal laser scanning microscope equipped with 40X 1.4 NA Plan Apochromat objectives, 405, 488, 561, and 640 nm solid-state lasers, and two GaAsP PMT detectors, using the Zeiss Zen Blue 2.3 software. All image analysis was performed using FIJI/ImageJ. Flow cytometry experiments, except for Figs. 3.1E and 3.2, was performed on a BD Accuri C6 flow cytometer, and analysis was performed using the BD Accuri C6 analysis software. Flow cytometry experiment for Figs. 3.1E and 3.2 was performed on a Thermo Fisher Attune NxT Flow Cytometer equipped with 405, 488, 561, 637 nm lasers using 480 and 647 dual lasers. Luminescence measurements were performed using a Tecan Infinite M1000 Microplate Reader (cat # 30034301).

Cell culture

HEK 293 cells that stably express human PTHR1 and cAMP GloSensor (293-PTHR1 cells) and HEK 293 G_s knockout cells that stably express GloSensor (i.e. G_s KO cells), Osteosarcoma cells UMR-106 and SaOS-2, and corresponding cells that stably express cAMP GloSensor UGS-56 (for UMR-106) and SGS-72 (for SaOS-2) were grown in DMEM (Dulbecco's modified Eagle medium) supplemented with 10% FBS and 1% penicillin/streptomycin and were maintained in a 5% CO_2, moisture-saturated atmosphere at 37 ºC. Cell densities were maintained between 10^5 and 1.6 x 10^6 cells/mL. For cell labeling experiments, all buffers or media were warmed to 37 ºC or room temperature prior to addition to cells unless otherwise noted, and incubations were done at 37 ºC unless otherwise specified.

RT-IMPACT labeling with oxoTCO for live-cell imaging and flow cytometry analysis

HEK 293-PTHR1 cells or G_s KO cells (150,000 cells) were seeded on 35-mm glass-bottom imaging dishes (MatTek) for 24 h prior to experiments. Rinses after oxoTCO incubation were performed in DMEM supplemented with FBS and P/S. Where indicated, the cells were then transfected with the indicated plasmid using Lipofectamine 2000 as per the manufacturer's instructions. One day after seeding (or transfection, if any), cells were first treated with the indicated PLD inhibitor (PLDi [FIPI], 750 nM; PLD1i [VU0359595], 250 nM; PLD2i [VU0364739], 350 nM; 30 min), YM-254890 (1 μM, 15 min), Dyngo-4a (30 μM, 15 min, serum-free), or corresponding DMSO vehicle in media at 37 ºC. The working concentrations of PTH(1-34) (PTH), PTH-Trp (Trp) and PTH-TMR were 50 nM and that of PMA was 100 nM. The appropriate stimulus was then added to the media for the indicated periods of time (0–20 min). Subsequently, freshly prepared oxoTCO (3 mM) together with the respective stimulus and PLD inhibitor/DMSO in media (100 μL) were carefully added to cover the central glass well. <u>*Cautionary note:*</u> *oxoTCOs are reported to have limited water stability* [50]*. Therefore, all aqueous oxoTCO solutions (e.g., those in DMEM-containing media) were used within 20 min of their generation. For example, we dissolved oxoTCO in 200 μL of DMEM with PLD inhibitor/DMSO and respective stimulus and used it only for two consecutive replicates rather than make a single stock solution for an entire day of experiments at the beginning of the day.* The dish was incubated for 5 min, the treatment media was aspirated, the cells were rinsed with PBS (1 mL) briefly, and the cells were then rinsed in DMEM (500 μL) for 1 min at 37 ºC. The media was aspirated and replaced with Tz–BODIPY (0.33 μM) in PBS (100 μL) for 1 min, which was further aspirated and replaced with 100 μL Tyrode's-HEPES buffer. Cells were

imaged immediately afterwards. Multicolor images were obtained in two-channel, line-switching mode. Z stacks were taken with 0.45 μm sectioning. For flow cytometry analysis, cells were instead seeded in 24 well-plates (125,000 cells/well) and labeled as described above. Following the final aspiration of Tz–BODIPY, cells were lifted with trypsin, transferred to 96-well plates, rinse twice with cold PBS + 0.5% FBS by centrifugation at 500 x g, and analyzed by flow cytometry. For the experiment shown in Fig. 3.1E, an extra step of incubation of anti-PTHR1-Alexa Fluor 647 nanobodies (100 nM) at 4 ºC in the dark for 30 min before oxoTCO incubation steps. At least 10,000 live cells were analyzed for each well in all flow cytometry experiments, as determined by forward/side scatter analysis for all experiments and additional gating for the experiment shown in Fig. 3.1E (see Fig. 3.2).

For Fig. 3.8B–D, azidopropanol (10 mM) and BCN-BODIPY (1 mM) was used in place of oxoTCO in place of Tz-BODIPY, respectively. Detailed procedures can be found elsewhere [28]. PMA (100 nM), where indicated, was added to the cells together with azidopropanol with no prior incubation. Barbadin (100 μM, serum-free), where indicated, was present 30 min before experiment. The incubation of BCN-BODIPY was performed at 37 ºC for 10 min followed by rinsing in Tyrode's-HEPES buffer at 37 ºC for 10 min and triple rinses in PBS prior to trypsinization.

Luciferase assays of cAMP production

Procedures were adopted from previously published protocols [51]. Monolayers of HEK 293 cells stably expressing PTHR1 were seeded on a 96-well plate 24 h before experiments. Dyngo-4a (30 μM) or corresponding DMSO vehicle, where indicated, was incubated with the cells in serum-free media for 15 min at 37 ºC prior to the experiment. The cells were incubated

with D-luciferin (0.5 mM) for 30 min at room temperature until the luminescence achieved a steady baseline. PTH ligands (50 nM) were then added to the wells and luminescence recorded by a Tecan Infinite M1000 Microplate Reader at the indicated time points.

Imaging of PTH-TMR to visualize PTHR1 endocytosis

293-PTHR1 cells (150,000 cells) were seeded on 35-mm glass-bottom imaging dishes (MatTek) for 24 h prior to experiments. Dyngo-4a (30 μM), where indicated, was incubated with the cells in serum-free media for 15 min at 37 ºC prior to the experiment. PTH-TMR (50 nM) was added to cells for 20 s, followed by three PBS rinses and imaging, with excitation by the 561 nm laser.

RT-IMPACT imaging of the localization of PLD activity

Real-time IMPACT using oxoTCO ((*S*)-oxoTCO–C1) and Tz-BODIPY was performed as described previously [27,28]. Briefly, freshly prepared oxoTCO (3 mM) together with the PTH(1-34) or PTH-TMR (50 nM) in media (100 μL) were carefully added to cover the central glass well. The dish was incubated for 5 min, the treatment media was aspirated, the cells were rinsed with PBS (1 mL) briefly, and the cells were then rinsed in DMEM (500 μL) for 1 min at 37 ºC. The media was replaced with 100 μL of Tyrode's-HEPES buffer to cover the center of the glass bottom and the dish was mounted on the microscope. The cells to be imaged were quickly located and time-lapse imaging with an interval of 3 s (488 nm, for PTH(1-34) or 6 s (488 nm and 561 nm, for PTH-TMR) and duration of 3 min begun. Tz-BODIPY (100 μL, 1 μM in PBS) was added dropwise but quickly to the center of the dish during acquisition. The image

shown in Fig. 3.3B represents the 9-s timepoint post-addition of Tz-BODIPY. The RT-IMPACT experiment was repeated four times, yielding similar localizations.

Statistics and reproducibility

All imaging experiments show representative images from experiments performed in at least three biological replicates on different days, where each replicate refers to a single dish of cells with approximately 15 cells in the field of view, whose parameters were all determined and averaged for the data point for that dish. Exact numbers of replicate experiments and sample sizes are provided in each figure legend. For experiments involving quantification of comparisons between more than two independent groups, significance was calculated using one-way ANOVA, followed by Games-Howell post-hoc test (for samples of unequal variance).

Acknowledgments

The author acknowledges research contributions from Ross W. Cheloha (National Institute of Health), Tomoyuki Watanabe (Chugai Pharmaceutical Company, Japan) and Thomas J. Gardella (Harvard Medical School). J.M.B. acknowledges support from NSF CAREER (CHE-1749919), Beckman Young Investigator, and Sloan Research Fellowship awards. T.J.G. acknowledges support from the NIH (P01DK011794). D.L. was supported by a Cornell Fellowship. R.W.C was supported by a CRI Irvington Postdoctoral Fellowship. Schematics were created with BioRender.com. We thank the Baskin lab for helpful discussions, Kane Wu for technical assistance, and the Emr, Fromme, and Yu labs at Cornell University for use of equipment.

References

1 L. Mohan M, T. Vasudevan N, K. Gupta M, E. Martelli E, V. Naga Prasad S. G-Protein Coupled Receptor Resensitization - Appreciating the Balancing Act of Receptor Function. *Curr Mol Pharmacol* 2013;**5**:350–61. https://doi.org/10.2174/1874467211205030004.

2 Irannejad R, Von Zastrow M. GPCR signaling along the endocytic pathway. *Curr Opin Cell Biol* 2014:109–16. https://doi.org/10.1016/j.ceb.2013.10.003.

3 Pavlos NJ, Friedman PA. GPCR Signaling and Trafficking: The Long and Short of It. *Trends Endocrinol Metab* 2017:213–26. https://doi.org/10.1016/j.tem.2016.10.007.

4 Mohammad Nezhady MA, Rivera JC, Chemtob S. Location Bias as Emerging Paradigm in GPCR Biology and Drug Discovery. *IScience* 2020. https://doi.org/10.1016/j.isci.2020.101643.

5 Marrari Y, Crouthamel M, Irannejad R, Wedegaertner PB. Assembly and trafficking of heterotrimeric G proteins. *Biochemistry* 2007:7665–77. https://doi.org/10.1021/bi700338m.

6 Stoeber M, Jullié D, Lobingier BT, Laeremans T, Steyaert J, Schiller PW, *et al.* A Genetically Encoded Biosensor Reveals Location Bias of Opioid Drug Action. *Neuron* 2018;**98**:963–976.e5. https://doi.org/10.1016/j.neuron.2018.04.021.

7 Irannejad R, Tomshine JC, Tomshine JR, Chevalier M, Mahoney JP, Steyaert J, *et al.* Conformational biosensors reveal GPCR signalling from endosomes. *Nature* 2013;**495**:534–8. https://doi.org/10.1038/nature12000.

8 Ferrandon S, Feinstein TN, Castro M, Wang B, Bouley R, Potts JT, *et al.* Sustained cyclic AMP production by parathyroid hormone receptor endocytosis. *Nat Chem Biol* 2009;**5**:734–42. https://doi.org/10.1038/nchembio.206.

9 Cheloha RW, Gellman SH, Vilardaga JP, Gardella TJ. PTH receptor-1 signalling - Mechanistic insights and therapeutic prospects. *Nat Rev Endocrinol* 2015:712–24. https://doi.org/10.1038/nrendo.2015.139.

10 Sutkeviciute I, Clark LJ, White AD, Gardella TJ, Vilardaga JP. PTH/PTHrP Receptor Signaling, Allostery, and Structures. *Trends Endocrinol Metab* 2019:860–74. https://doi.org/10.1016/j.tem.2019.07.011.

11 Luttrell LM, Lefkowitz RJ. The role of β-arrestins in the termination and transduction of G-protein-coupled receptor signals. *J Cell Sci* 2002;**115**:455–65. https://doi.org/10.1242/jcs.115.3.455.

12 Vilardaga JP, Gardella TJ, Wehbi VL, Feinstein TN. Non-canonical signaling of the PTH receptor. *Trends Pharmacol Sci* 2012:423–31. https://doi.org/10.1016/j.tips.2012.05.004.

13 Feinstein TN, Wehbi VL, Ardura JA, Wheeler DS, Ferrandon S, Gardella TJ, *et al.* Retromer terminates the generation of cAMP by internalized PTH receptors. *Nat Chem Biol* 2011;**7**:278–84. https://doi.org/10.1038/nchembio.545.

14 Wehbi VL, Stevenson HP, Feinstein TN, Calero G, Romero G, Vilardaga JP. Noncanonical GPCR signaling arising from a PTH receptor-arrestin-Gβγ complex. *Proc Natl Acad Sci U S A* 2013;**110**:1530–5. https://doi.org/10.1073/pnas.1205756110.

15 Gidon A, Al-Bataineh MM, Jean-Alphonse FG, Stevenson HP, Watanabe T, Louet C, *et al.* Endosomal GPCR signaling turned off by negative feedback actions of PKA and v-ATPase. *Nat Chem Biol* 2014;**10**:707–9. https://doi.org/10.1038/nchembio.1589.

16 Cheloha RW, Harmand TJ, Wijne C, Schwartz TU, Ploegh HL. Exploring cellular biochemistry with nanobodies. *J Biol Chem* 2020;**295**:15307–27. https://doi.org/10.1074/jbc.REV120.012960.

17 Tsvetanova NG, von Zastrow M. Spatial encoding of cyclic AMP signaling specificity by GPCR endocytosis. *Nat Chem Biol* 2014;**10**:1061–5. https://doi.org/10.1038/nchembio.1665.

18 White AD, Fang F, Jean-Alphonse FG, Clark LJ, An HJ, Liu H, *et al.* Ca2+ allostery in PTH-receptor signaling. *Proc Natl Acad Sci U S A* 2019;**116**:3294–9. https://doi.org/10.1073/pnas.1814670116.

19 Wein MN, Kronenberg HM. Regulation of bone remodeling by parathyroid hormone. *Cold Spring Harb Perspect Med* 2018;**8**:. https://doi.org/10.1101/cshperspect.a031237.

20 Sato T, Verma S, Khatri A, Dean T, Goransson O, Gardella TJ, *et al.* Comparable initial engagement of intracellular signaling pathways by parathyroid hormone receptor ligands teriparatide, abaloparatide, and long-acting PTH . *JBMR Plus* 2020. https://doi.org/10.1002/jbm4.10441.

21 Abou-Samra AB, Juppner H, Force T, Freeman MW, Kong XF, Schipani E, *et al.* Expression cloning of a common receptor for parathyroid hormone and parathyroid hormone-related peptide from rat osteoblast-like cells: A single receptor stimulates intracellular accumulation of both cAMP and inositol trisphosphates and increases intracel. *Proc Natl Acad Sci U S A* 1992;**89**:2732–6. https://doi.org/10.1073/pnas.89.7.2732.

22 Guo J, Chung U Il, Kondo H, Bringhurst FR, Kronenberg HM. The PTH/PTHrP receptor can delay chondrocyte hypertrophy in vivo without activating phospholipase C. *Dev Cell* 2002;**3**:183–94. https://doi.org/10.1016/S1534-5807(02)00218-6.

23 Capuano P, Bacic D, Roos M, Gisler SM, Stange G, Biber J, *et al.* Defective coupling of apical PTH receptors to phospholipase C prevents internalization of the Na+-phosphate cotransporter NaP i-IIa in Nherf1-deficient mice. *Am J Physiol - Cell Physiol* 2007;**292**:. https://doi.org/10.1152/ajpcell.00126.2006.

24 White AD, Jean-Alphonse FG, Fang F, Peña KA, Liu S, König GM, *et al.* Gq/11-dependent regulation of endosomal cAMP generation by parathyroid hormone class B GPCR. *Proc Natl Acad Sci U S A* 2020;**117**:7455–60. https://doi.org/10.1073/pnas.1918158117.

25 Selvy PE, Lavieri RR, Lindsley CW, Brown HA. Phospholipase D: enzymology, functionality, and chemical modulation. *Chem Rev* 2011;**111**:6064–119. https://doi.org/10.1021/cr200296t.

26 Nelson RK, Frohman MA. Physiological and pathophysiological roles for

phospholipase D. *J Lipid Res* 2015;**56**:2229–37. https://doi.org/10.1194/jlr.R059220.

27 Liang D, Wu K, Tei R, Bumpus TW, Ye J, Baskin JM. A real-time click chemistry imaging approach reveals stimulus-specific subcellular locations of phospholipase D activity. *Proc Natl Acad Sci U S A* 2019;**116**:15453–62. https://doi.org/10.1073/pnas.1903949116.

28 Bumpus TW, Liang D, Baskin JM. IMPACT: Imaging phospholipase D activity with clickable alcohols via transphosphatidylation. *Methods Enzymol* 2020:75–94. https://doi.org/10.1016/bs.mie.2020.04.037.

29 Brown HA, Henage LG, Preininger AM, Xiang Y, Exton JH. Biochemical Analysis of Phospholipase D. *Methods Enzymol* 2007:49–87. https://doi.org/10.1016/S0076-6879(07)34004-4.

30 Gardella TJ, Vilardaga JP. International union of basic and clinical pharmacology. XCIII. The parathyroid hormone receptors—family B G protein–coupled receptors. *Pharmacol Rev* 2015;**67**:310–37. https://doi.org/10.1124/pr.114.009464.

31 Takasaki J, Saito T, Taniguchi M, Kawasaki T, Moritani Y, Hayashi K, *et al.* A novel Gαq/11-selective inhibitor. *J Biol Chem* 2004;**279**:47438–45. https://doi.org/10.1074/jbc.M408846200.

32 Nishimura A, Kitano K, Takasaki J, Taniguchi M, Mizuno N, Tago K, *et al.* Structural basis for the specific inhibition of heterotrimeric Gq protein by a small molecule. *Proc Natl Acad Sci U S A* 2010;**107**:13666–71. https://doi.org/10.1073/pnas.1003553107.

33 Roszko KL, Bi R, Gorvin CM, Bräuner-Osborne H, Xiong XF, Inoue A, *et al.* Knockin mouse with mutant Gα11 mimics human inherited hypocalcemia and is rescued by pharmacologic inhibitors. *JCI Insight* 2017;**2**:. https://doi.org/10.1172/jci.insight.91079.

34 Hu T, Exton JH. Mechanisms of regulation of phospholipase D1 by protein kinase Ca. *J Biol Chem* 2003;**278**:2348–55. https://doi.org/10.1074/jbc.M210093200.

35 Cheloha RW, Fischer FA, Woodham AW, Daley E, Suminski N, Gardella TJ, *et al.*

Improved GPCR ligands from nanobody tethering. *Nat Commun* 2020;**11**:. https://doi.org/10.1038/s41467-020-15884-8.

36 Binkowski BF, Butler BL, Stecha PF, Eggers CT, Otto P, Zimmerman K, *et al.* A luminescent biosensor with increased dynamic range for intracellular cAMP. *ACS Chem Biol* 2011;**6**:1193–7. https://doi.org/10.1021/cb200248h.

37 Shukla AK, Xiao K, Lefkowitz RJ. Emerging paradigms of β-arrestin-dependent seven transmembrane receptor signaling. *Trends Biochem Sci* 2011:457–69. https://doi.org/10.1016/j.tibs.2011.06.003.

38 Lefkowitz RJ. G protein-coupled receptors: III. New roles for receptor kinases and β-arrestins in receptor signaling and desensitization. *J Biol Chem* 1998:18677–80. https://doi.org/10.1074/jbc.273.30.18677.

39 Harper CB, Martin S, Nguyen TH, Daniels SJ, Lavidis NA, Popoff MR, *et al.* Dynamin inhibition blocks botulinum neurotoxin type A endocytosis in neurons and delays botulism. *J Biol Chem* 2011;**286**:35966–76. https://doi.org/10.1074/jbc.M111.283879.

40 McCluskey A, Daniel JA, Hadzic G, Chau N, Clayton EL, Mariana A, *et al.* Building a better dynasore: The dyngo compounds potently inhibit dynamin and endocytosis. *Traffic* 2013;**14**:1272–89. https://doi.org/10.1111/tra.12119.

41 Inoue A, Raimondi F, Kadji FMN, Singh G, Kishi T, Uwamizu A, *et al.* Illuminating G-Protein-Coupling Selectivity of GPCRs. *Cell* 2019;**177**:1933–1947.e25. https://doi.org/10.1016/j.cell.2019.04.044.

42 Preta G, Cronin JG, Sheldon IM. Dynasore - Not just a dynamin inhibitor. *Cell Commun Signal* 2015. https://doi.org/10.1186/s12964-015-0102-1.

43 Park RJ, Shen H, Liu L, Liu X, Ferguson SM, De Camilli P. Dynamin triple knockout cells reveal off target effects of commonly used dynamin inhibitors. *J Cell Sci* 2013;**126**:5305–12. https://doi.org/10.1242/jcs.138578.

44 Kozik P, Hodson NA, Sahlender DA, Simecek N, Soromani C, Wu J, *et al.* A human genome-wide screen for regulators of clathrin-coated vesicle formation reveals an

unexpected role for the V-ATPase. *Nat Cell Biol* 2013;**15**:50–60. https://doi.org/10.1038/ncb2652.

45 Beautrait A, Paradis JS, Zimmerman B, Giubilaro J, Nikolajev L, Armando S, *et al.* A new inhibitor of the β-arrestin/AP2 endocytic complex reveals interplay between GPCR internalization and signalling. *Nat Commun* 2017;**8**:. https://doi.org/10.1038/ncomms15054.

46 Maeda A, Okazaki M, Baron DM, Dean T, Khatri A, Mahon M, *et al.* Critical role of parathyroid hormone (PTH) receptor-1 phosphorylation in regulating acute responses to PTH. *Proc Natl Acad Sci U S A* 2013;**110**:5864–9. https://doi.org/10.1073/pnas.1301674110.

47 Stallaert W, Van Der Westhuizen ET, Schönegge AM, Plouffe B, Hogue M, Lukashova V, *et al.* Purinergic receptor transactivation by the β2-adrenergic receptor increases intracellular Ca2+ in nonexcitable cells. *Mol Pharmacol* 2017;**91**:533–44. https://doi.org/10.1124/mol.116.106419.

48 Cheloha RW, Watanabe T, Dean T, Gellman SH, Gardella TJ. Backbone Modification of a Parathyroid Hormone Receptor-1 Antagonist/Inverse Agonist. *ACS Chem Biol* 2016;**11**:2752–62. https://doi.org/10.1021/acschembio.6b00404.

49 Daley EJ, Khatri A, Dean T, Vilardaga JP, Zaidi SA, Katritch V, *et al.* Ligand-dependent effects of methionine-8 oxidation in parathyroid hormone peptide analogues. *Endocrinol (United States)* 2021;**162**:1–14. https://doi.org/10.1210/endocr/bqaa216.

50 Lambert WD, Scinto SL, Dmitrenko O, Boyd SJ, Magboo R, Mehl RA, *et al.* Computationally guided discovery of a reactive, hydrophilic: Trans -5-oxocene dienophile for bioorthogonal labeling. *Org Biomol Chem* 2017;**15**:6640–4. https://doi.org/10.1039/c7ob01707c.

51 Cheloha RW, Maeda A, Dean T, Gardella TJ, Gellman SH. Backbone modification of a polypeptide drug alters duration of action in vivo. *Nat Biotechnol* 2014;**32**:653–5. https://doi.org/10.1038/nbt.2920.

CHAPTER 4: Direct visualization of plasma membrane-to-ER phospholipid trafficking mediated by extended synaptotagmins using bioorthogonally tagged fluorescent lipids

Abstract

It has long been known that different organelles consist of distinctive lipid compositions. The relative stability of lipid compositions for specific organelle membranes, or lipid homeostasis, is tightly regulated in a healthy cell. The dynamic process of lipid homeostasis is crucial for maintaining both membrane integrity and proper organelle functions and is achieved via the classical vesicular pathways as well as the emerging, non-vesicular pathways. However, the mechanisms of many non-vesicular pathways mediated by lipid transfer proteins acting at membrane contact sites remain poorly understood. Here, we utilized RT-IMPACT, a bioorthogonal toolset for imaging phospholipase D activities, to install unnatural fluorescent lipids on the plasma membrane and examined the effects of expression of specific lipid transfer proteins on the trafficking events from plasma membrane (PM) to endoplasmic reticulum (ER). Specifically, we found that RNAi-based knockdown of extended synaptotagmin family proteins (ESyt1/2/3) located at PM-ER contact sites reduce trafficking rates of fluorescent lipids from PM to ER. Furthermore, such effects can be fully rescued by expressing RNAi-resistant ESyt1 constructs, indicating that the expression of ESyt1/2/3 is important for non-vesicular trafficking from PM to ER. In addition, we designed an ESyt1-OMP25 chimeric construct and found that it led to a substantial increase in lipid trafficking towards mitochondria. Moreover, mutations in the lipid transfer domain of ESyt1 completely

abrogated such effects, suggesting that the functional lipid transfer domain of ESyt1 is essential for the fluorescent lipids to be transported to the mitochondria. Taken together, these data reveal that the extended synaptotagmins are responsible for non-vesicular trafficking events of unnatural, RT-IMPACT-derived lipids mediated at PM-ER contact sites. We expect this study to have broader implications on the non-specificity of lipid-binding in ESyts and potentially other SMP-domain containing proteins and their general role as gatekeeper for lipid homeostasis. Finally, it highlights an unanticipated application of RT-IMPACT beyond visualization of PLD signaling pathways, to directly visualize the spatiotemporal dynamics of intracellular bulk phospholipid transport.

Introduction

Membrane partitioning is a defining feature of eukaryotic cells. Subcellular membranes form compartmentalized regions within the cells, or organelles, to facilitate certain biochemical pathways. All organelle membranes are primarily composed of lipids. Different organelle membranes have distinctive lipid compositions. In a healthy cell, this differential distribution of lipid compositions is dynamically maintained, and disruptions are constantly restored. Cells maintain such dynamic lipid homeostasis for essential organelle functions and proper membrane signaling events. It has long been known that the differential lipid compositions can be maintained by two broad mechanisms, namely local lipid metabolism, which degrades or converts starting lipids to other products, and lipid trafficking, which transfers lipids from the place of biosynthesis to the membrane of destination.

Lipid trafficking can be divided into two categories, vesicular and non-vesicular trafficking. Vesicular trafficking is mediated by membrane invagination and fusion events, such as clathrin-mediated endocytosis. Non-vesicular trafficking is achieved by lipid transfer proteins (LTPs) acting at membrane contact sites (MCSs) where the two membranes of different organelles (heterotypic) or the same organelle (homotypic) form areas of close appositions. MCSs have been known in the literature for many decades [1], but the molecular identities of many that tether and maintain two membranes in close appositions have only been revealed in recent years [2,3].

Heterotypic MCSs that have been well characterized frequently involves the ER, which forms extensive contacts with virtually all organelles in the cell, including ER-mitochondria, ER-PM, ER-Golgi, etc [4]. Because the ER is the primary the site of synthesis for many lipids

and intermediary organelle for lysosomal degradation, ER-associated MCSs are crucial for non-vesicular lipid trafficking events in and out of the ER. Among these, PM-ER contact sites have been shown to be especially important for calcium uptake [5] and lipid homeostasis on the PM [6].

Extended synaptotagmins (EStyts) are newly characterized ER-PM tethering proteins that facilitate formation of ER-PM contacts [7–9]. In addition to their tethering function, ESyts are also lipid transfer proteins that help to maintain lipid homeostasis at the PM [10]. There are three members of ESyt protein family, ESyt1, ESyt2 and ESyt3. They are all ER-resident proteins and can form homo- or heterodimers that mediate ER-PM contacts. All three proteins consist of an N-terminal hydrophobic stretch that inserts into the ER, a cytosolic synaptotagmin-like mitochondrial lipid binding protein (SMP) domain followed by multiple C2 domains [11]. The SMP domain is a lipid-binding module that are responsible for lipid exchange between the two membranes at PM-ER contact sites[7]. The multiple C2 domains serve as Ca^{2+}-sensing switch for the lipid-binding activities of SMP domain and they are also responsible for $PI(4,5)P_2$ binding in the PM [10]. In cells, knockdown/knockout of ESyts results in a substantial decrease in the number of ER-PM contacts as well as defects in diacylglycerol (DAG) removal from the plasma membrane, suggesting that they are important for maintaining lipid homeostasis on the PM [10].

The lipid transfer activities of ESyts have been extensively characterized by in vitro liposomal assays, which showed broad selectivity of the SMP domains towards many lipids, including unnatural fluorophore-tagged lipids [10]. Nevertheless, it remains unclear whether the non-specific lipid transfer activity is pertinent to removal of unnatural lipids from the plasma membrane in cells. With the RT-IMPACT method established and characterized in the previous chapters, we then devoted our efforts towards understanding such lipid trafficking events that

we observed in real-time imaging in Chapter 2. To test whether ESyts are responsible for this process, we utilized RT-IMPACT, which selectively attaches fluorophores to lipid products produced by endogenous phospholipase D enzymes, to generate unnatural fluorescent lipids at the PM in live cells. We then used time-lapse imaging and fluorescence colocalization to quantitatively analyze the effects of ESyts on the trafficking of these reporter lipids towards the ER. We found that knockdown of expressions of ESyts by RNAi dramatically reduced the trafficking rates of reporter lipids, and such effects could be fully rescued by expressing RNAi-resistant ESyt1 construct. Furthermore, expression of a protein chimera composed of the SMP domain of ESyt1 and mitochondria-targeting sequence OMP25 led to substantial trafficking of the reporter lipids towards mitochondria. Such trafficking events are much less pronounced in cells transfected with mutant chimera where the SMP domains are unable to bind to lipids. In sum, these data implicate important functions of ESyts in non-vesicular lipid trafficking events at PM-ER contact sites in response to unnatural perturbations and the broad scope of lipid recognition that characterizes such processes.

Results and Discussion

Knockdown of ESyts reduces trafficking rates of fluorescent lipids from PM to ER

We have demonstrated in the previous two chapters, RT-IMPACT resolves PLD activities in real-time under live-cell conditions by virtue of the fast chemical kinetics and fluorogenic behavior. On that note, it can also visualize the otherwise elusive non-vesicular lipid trafficking from PM to ER with high temporal resolution. Therefore, we proposed to use PM-to-ER trafficking half-lives of unnatural fluorescent lipids generated by RT-IMPACT as the readout to verify whether the potential candidate LTPs are responsible for non-vesicular trafficking events recorded in real-time. We selected ESyts as the prime candidate for their potential role in facilitating lipid trafficking at PM-ER contacts because of their reported lipid transfer activities and the non-selective lipid-binding affinity reported previously [6,12].

We first tested RNAi-based knockdown (KD) to examine whether the expression of ESyts can have a significant effect on lipid trafficking. We obtained RNAi oligos for all three members of the ESyt family and tested the efficiency of RNAi-KD by western blot (Figure 4.1A). Because ESyt3 is minimally expressed under physiological conditions, ESyt1/2 double KD is usually as effective as ESyt1/2/3 triple KD [6]. Figure 4.1A shows that RNAi-KDs of ESyt1 and ESyt2 were highly effective, which can then be used for analysis by real-time imaging.

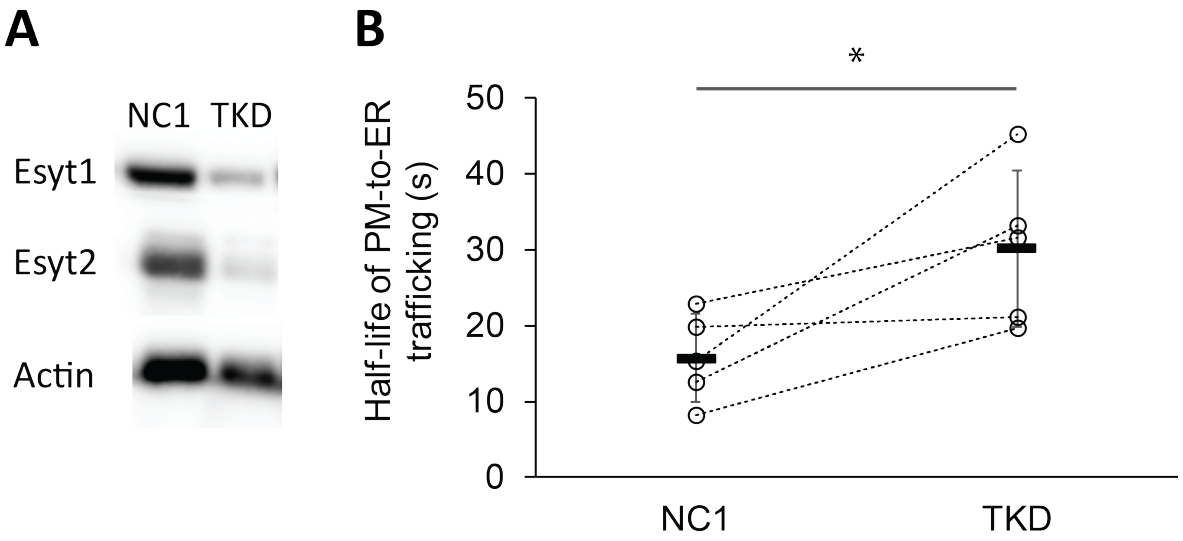

Figure 4.1. Knockdown of expressions of ESyts increase apparent trafficking half-lives of RT-IMPACT derived lipids from PM to ER. (A) Western blot analysis showing efficiency of ESyt1/2/3 RNAi on the expression levels of ESyt1 and ESyt2. HEK 293 cells were harvested 72 h after RNAi. (B) Plot of trafficking half-lives of RT-IMPACT-derived lipids from PM to ER in HEK 293 cells treated with either control or ESyt1/2/3 RNAi. HEK 293 cells were first treated with ESyt1/2/3 RNAi (TKD) or negative control RNAi (NC1) for 72 h before experiments. Cells were then treated with PMA, (S)-oxoTCO–C1 and ER-tracker Red at 37 ºC for 5 min and rinsed for 1 min prior to time-lapse imaging. PM-to-ER trafficking half-lives were measured by real-time imaging as described in Figure 2.18. Dotted lines indicate pairing of data points. Student's t-test (paired two-tailed distribution): * $p < 0.05$.

Next, we used RT-IMPACT coupled with PMA to stimulate PLD activities to synthesize unnatural fluorescent lipids in live cells and measured trafficking rates with or without ESyt1/2/3 triple KD by RNAi. As reported in Chapter 2, PMA results in major translocation of PLD enzymes towards PM, where PLDs are activated and the lipid products tagged by RT-IMPACT reagents. Therefore, under such conditions, a substantial amount of

fluorescently tagged lipids will be exclusively generated at the plasma membrane. Afterwards, as observed in Fig. 2.17B, these lipids are quickly internalized over time through non-vesicular pathways presumably acting at PM-ER contact sites. With co-staining of an ER-marker, such trafficking events can be recorded in a time-lapse movie and further characterized by mono-exponential half-lives measuring the change of fluorescence colocalization of reporter lipids with ER over time.

Under ESyt1/2/3 triple KD conditions, we found that the trafficking half-lives in HEK 293 cells showed a significant increase to an average of ~30 s for KD, as compared to ~16 s for cells treated with control RNAi (Figs 4.1A and 4.6, left two lanes), indicating a significant decrease in trafficking rates upon KD of ESyts. This result is consistent with previous reports that ESyts facilitate lipid transfer between PM and ER membranes and KD of ESyts inhibit the removal of DAG from PM to the ER. The incomplete inhibition of non-vesicular trafficking by RNAi-based knockdown could be due to residual amounts of ESyts present after RNAi treatment, or due to other lipid transfer proteins acting at ER-PM contacts that have similar functions as ESyts. It is also worth noting that these rapid trafficking rates are typical for non-vesicular lipid trafficking [13,14], as the vesicular pathway is usually much slower.

Re-expressing ESyt1 fully rescues the trafficking defects

We then further tested whether such trafficking defects can be rescued by reintroducing ESyts into RNAi-treated cells. To test this idea, we engineered a miRFP-ESyt1 plasmid that is RNAi-resistant, as verified by western blot (Fig. 4.2). ESyt1 is an ER-resident protein and is reported to form homodimers at ER-PM contacts. When we co-expressed miRFP-ESyt1 with the ER-marker Sec61β-mRFP in RNAi-treated cells, we indeed observed strong colocalization

of ESyt1 with the ER-marker. Furthermore, the ER-marker showed enhanced localization at cortical ER (Fig. 4.5), where the ER membrane is in close proximity with the PM to form contact sites. This finding agreed with the literature that overexpression of ESyt1 favors formation of cortical ER as well as significant translocation of ER-markers towards cortical ER [7].

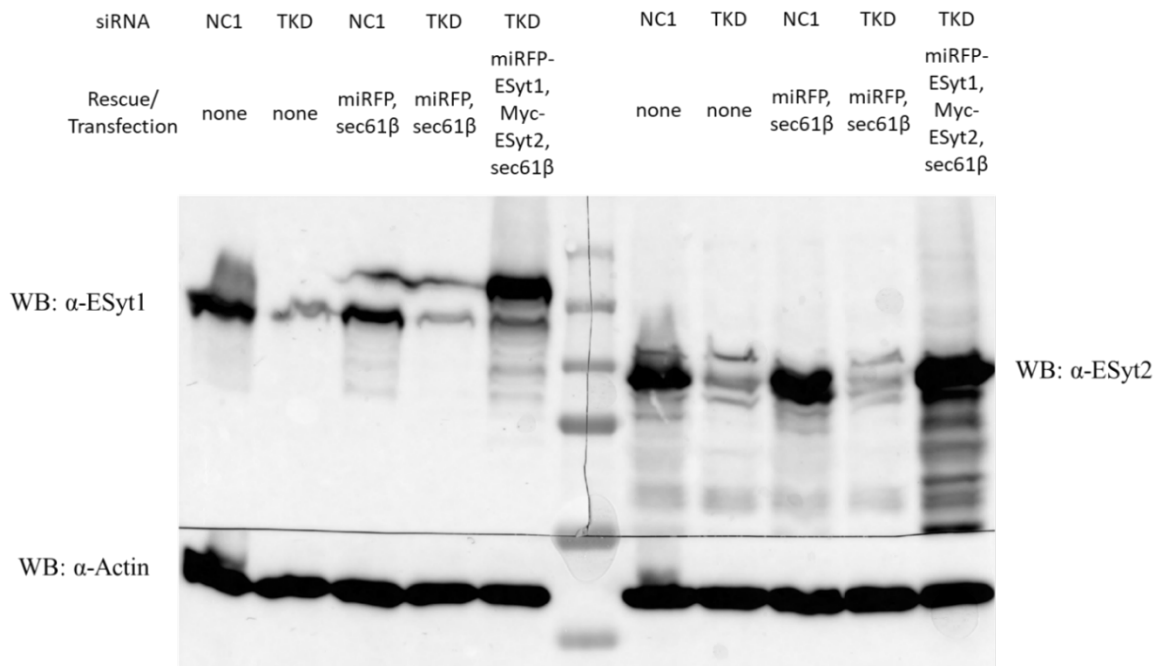

Fig. 4.2: Western blot analysis of expression level of ESyts with RNAi-knockdown and rescue. HEK 293 cells were harvested 72 h after RNAi (24 h after plasmid transfection/rescue) for western blot analysis.

Under these conditions, the ESyt-RNAi-treated cells that were rescued with miRFP-ESyt1 (Fig. 4.5) construct showed enhanced trafficking rates than those transfected with miRFP empty vector (Fig. 4.4). Moreover, the average trafficking half-life of rescued cells (~14 s) resembles that of control-RNAi treated cells (~17 s) (Figs. 4.3, 4.5 and 4.6). Taken together,

these data indicate that the trafficking rates of unnatural fluorescent reporter lipids derived from RT-IMPACT are strongly correlated with expression levels of ESyts.

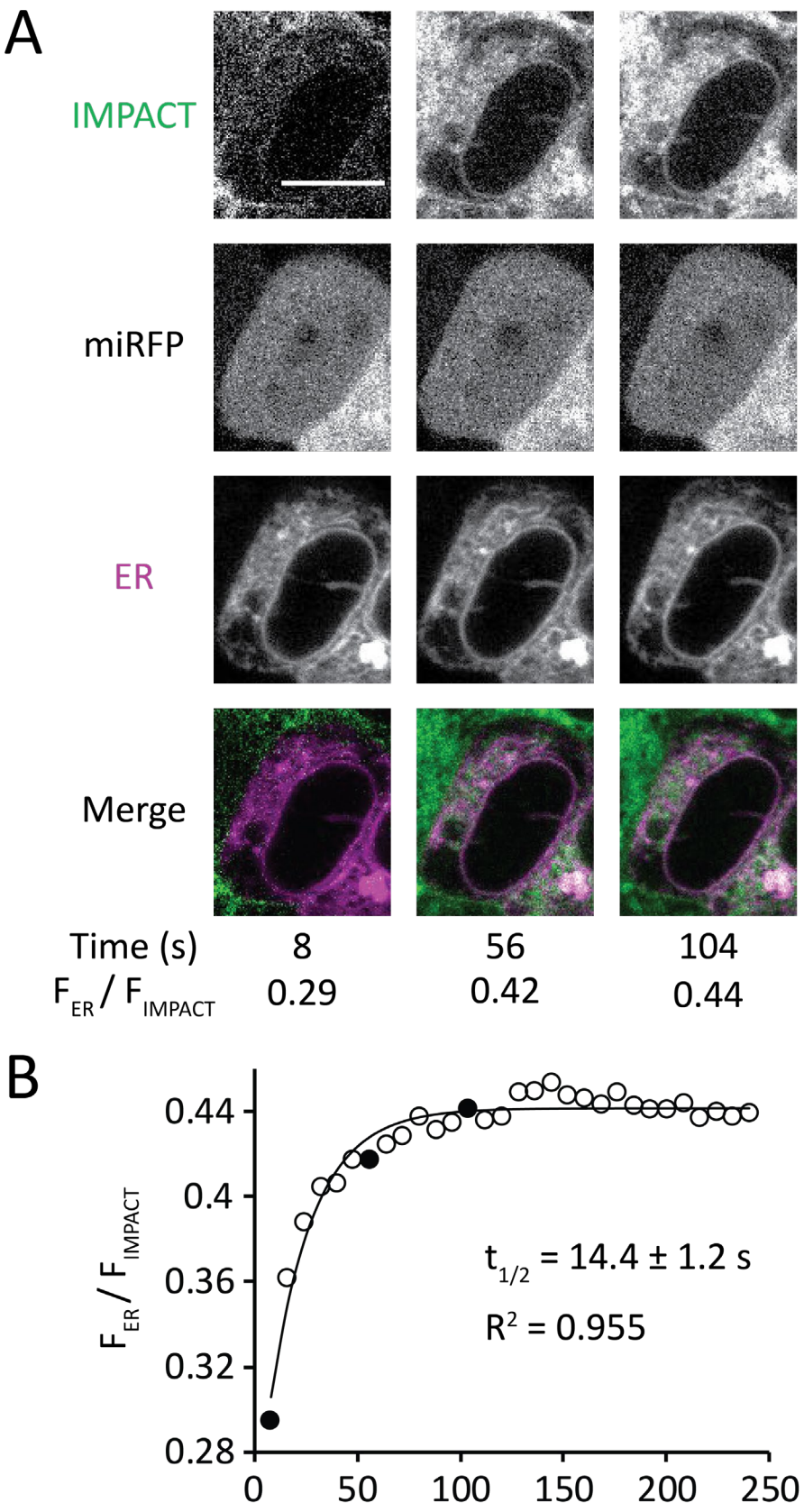
A
IMPACT
miRFP
ER
Merge
Time (s)
8
56
104
F_ER / F_IMPACT
0.29
0.42
0.44
B
0.44
0.4
0.36
0.32
0.28
F_ER / F_IMPACT
t_1/2 = 14.4 ± 1.2 s
R² = 0.955
0
50
100
150
200
250

Figure 4.3: Representative real-time imaging measurements of trafficking half-lives of control RNAi-treated cells (NC1). HEK 293 cells were treated with control RNAi (NC1) 72 h before experiment and transfected with Sec61β-mRFP (ER-marker) and miRFP 24 h before experiment. Cells were treated with PMA and (S)-oxoTCO–C1 at 37 ºC for 5 min and rinsed for 1 min prior to time-lapse imaging. (A) Representative images of a 3-color time-lapse movie at indicated time points after addition of Tz-BODIPY. Merge of IMPACT (green) and ER marker (magenta) was shown, where colocalization appears as white color. Ratios of IMPACT-derived fluorescence that overlaps with ER (F_{ER}) over total IMPACT fluorescence (F_{IMPACT}) were calculated for each time point. (B) Exponential fitting of kinetics of PM-to-ER trafficking. F_{ER}/F_{IMPACT} was plotted against time. Circles are raw data points, and the curve indicates an exponential fit. Filled circles correspond to F_{ER}/F_{IMPACT} ratios for the images shown in (A). R^2 indicates the coefficient of determination of the fit and $t_{1/2}$ indicates average half-life of internalization. Scale bar: 10 μm.

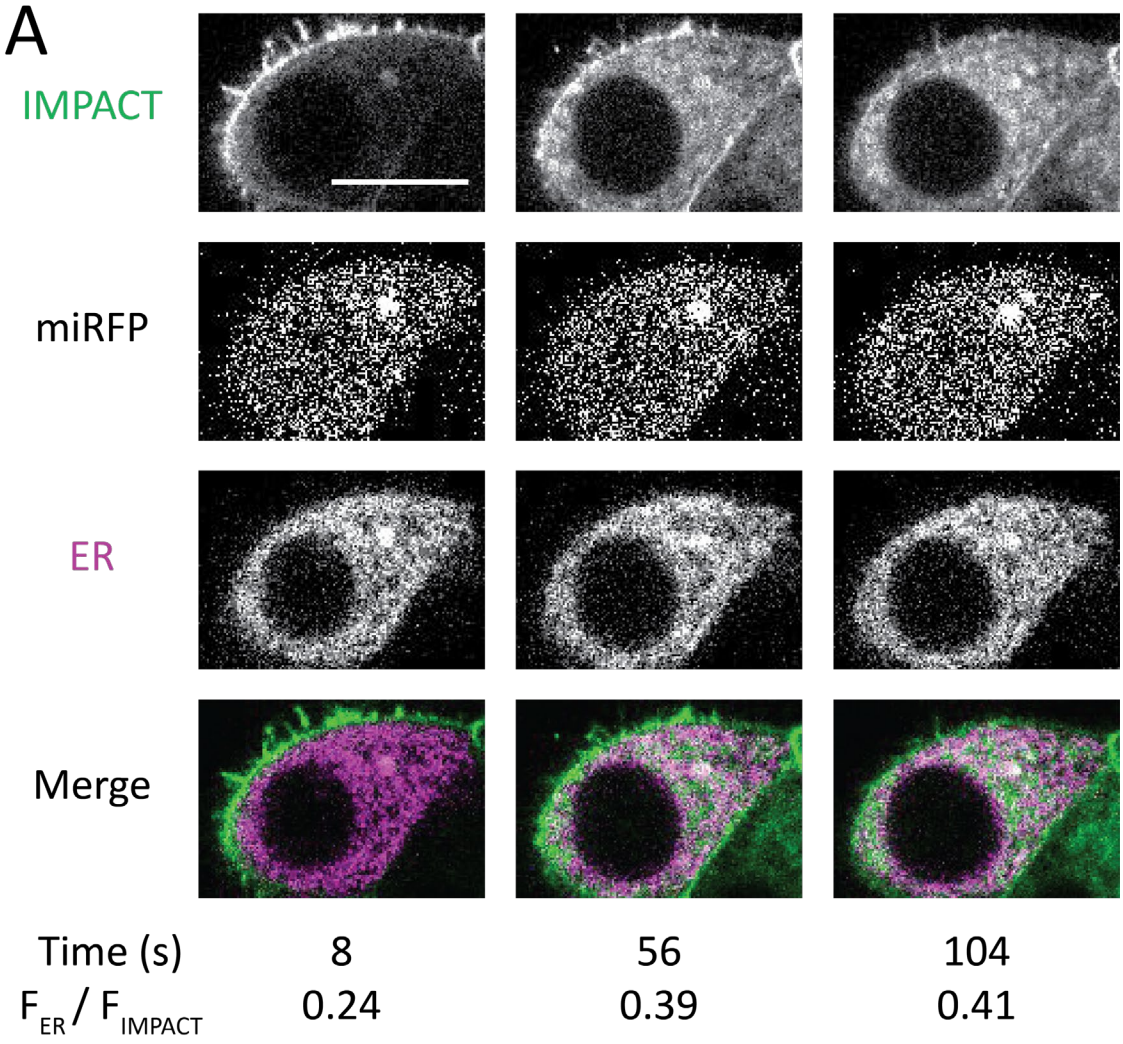
A
IMPACT
miRFP
ER
Merge
Time (s)
8
56
104
F_ER / F_IMPACT
0.24
0.39
0.41

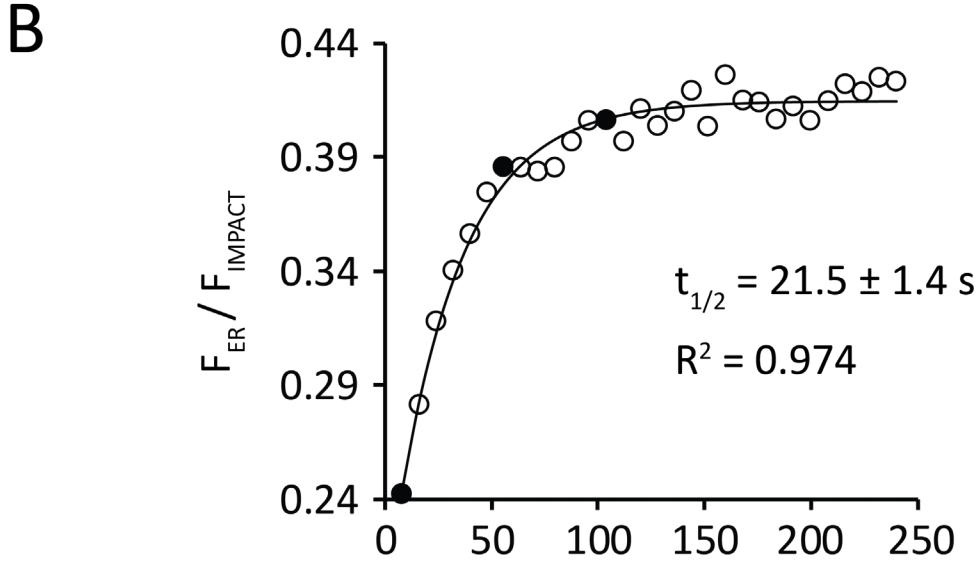
B
0.44
0.39
0.34
0.29
0.24
F_ER / F_IMPACT
0
50
100
150
200
250
t_1/2 = 21.5 ± 1.4 s
R² = 0.974

Figure 4.4: Representative real-time imaging measurements of trafficking half-lives of ESyt1/2/3 RNAi-treated cells (TKD). HEK 293 cells were treated with ESyt1/2/3 RNAi (TKD) 72 h before experiment and transfected with Sec61β-mRFP (ER-marker) and miRFP 24 h before experiment. Cells were treated with PMA and (S)-oxoTCO–C1 at 37 ºC for 5 min and rinsed for 1 min prior to time-lapse imaging. (A) Representative images of a 3-color time-lapse movie at indicated time points after addition of Tz-BODIPY. Merge of IMPACT (green) and ER marker (magenta) was shown, where colocalization appears as white color. Ratios of IMPACT-derived fluorescence that overlaps with ER (F_{ER}) over total IMPACT fluorescence (F_{IMPACT}) were calculated for each time point. (B) Exponential fitting of kinetics of PM-to-ER trafficking. F_{ER}/F_{IMPACT} was plotted against time. Circles are raw data points, and the curve indicates an exponential fit. Filled circles correspond to F_{ER}/F_{IMPACT} ratios for the images shown in (A). R^2 indicates the coefficient of determination of the fit and $t_{1/2}$ indicates average half-life of internalization. Scale bar: 10 μm.

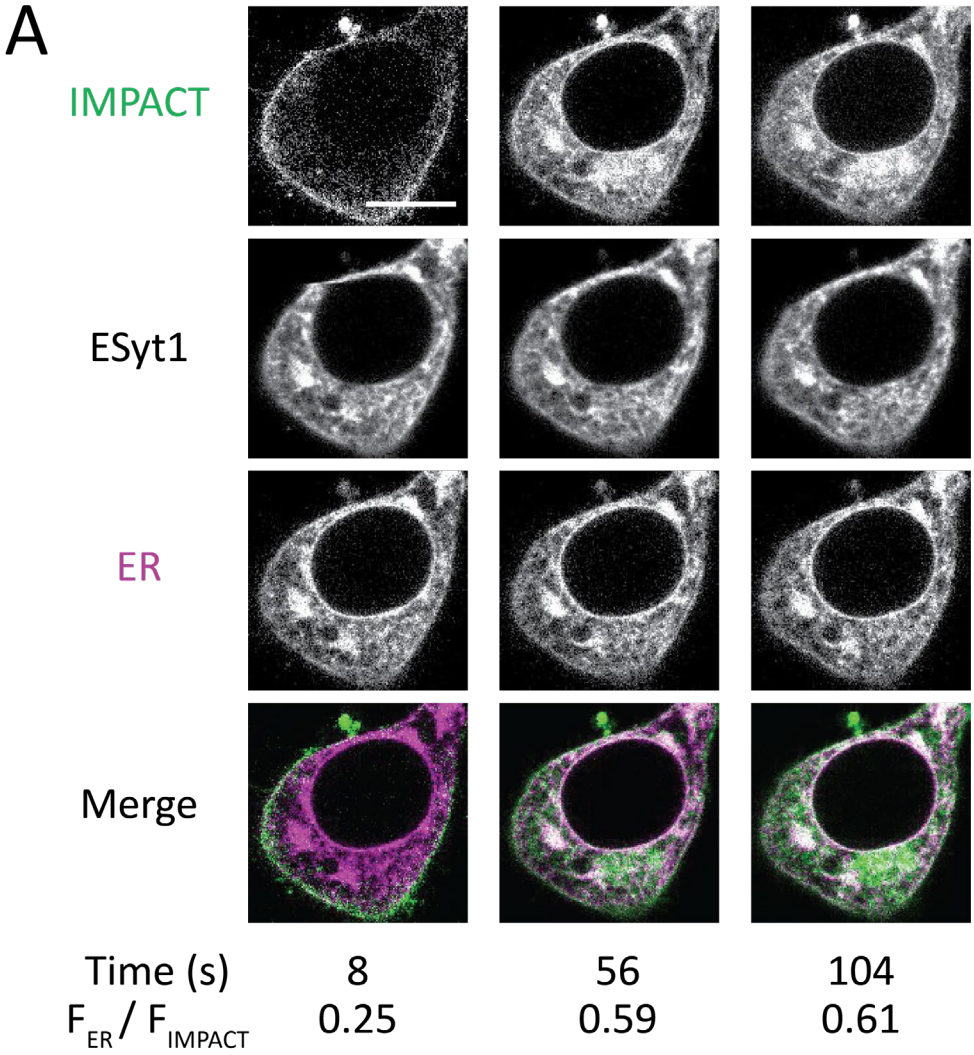
A
IMPACT
ESyt1
ER
Merge
Time (s) 8 56 104
F ER / F IMPACT 0.25 0.59 0.61
B
0.64
0.54
0.44
0.34
0.24
F ER / F IMPACT
t 1/2 = 8.66 ± 0.66 s
R2 = 0.965
0 50 100 150 200 250

Figure 4.5: Representative real-time imaging measurements of trafficking half-lives of ESyt1/2/3 RNAi-treated cells rescued with miRFP-ESyt1 (Rescue). HEK 293 cells were treated with ESyt1/2/3 RNAi (TKD) 72 h before experiment and transfected with Sec61β-mRFP (ER-marker) and miRFP-ESyt1 24 h before experiment. Cells were treated with PMA and (S)-oxoTCO–C1 for 5 min at 37 ºC and rinsed for 1 min prior to time-lapse imaging. (A) Representative images of a 3-color time-lapse movie at indicated time points after addition of Tz-BODIPY. Merge of IMPACT (green) and ER marker (magenta) was shown, where colocalization appears as white color. Ratios of IMPACT-derived fluorescence that overlaps with ER (F_{ER}) over total IMPACT fluorescence (F_{IMPACT}) were calculated for each time point. (B) Exponential fitting of kinetics of PM-to-ER trafficking. F_{ER}/F_{IMPACT} was plotted against time. Circles are raw data points, and the curve indicates an exponential fit. Filled circles correspond to F_{ER}/F_{IMPACT} ratios for the images shown in (A). R^2 indicates the coefficient of determination of the fit and $t_{1/2}$ indicates average half-life of internalization. Scale bar: 10 μm.

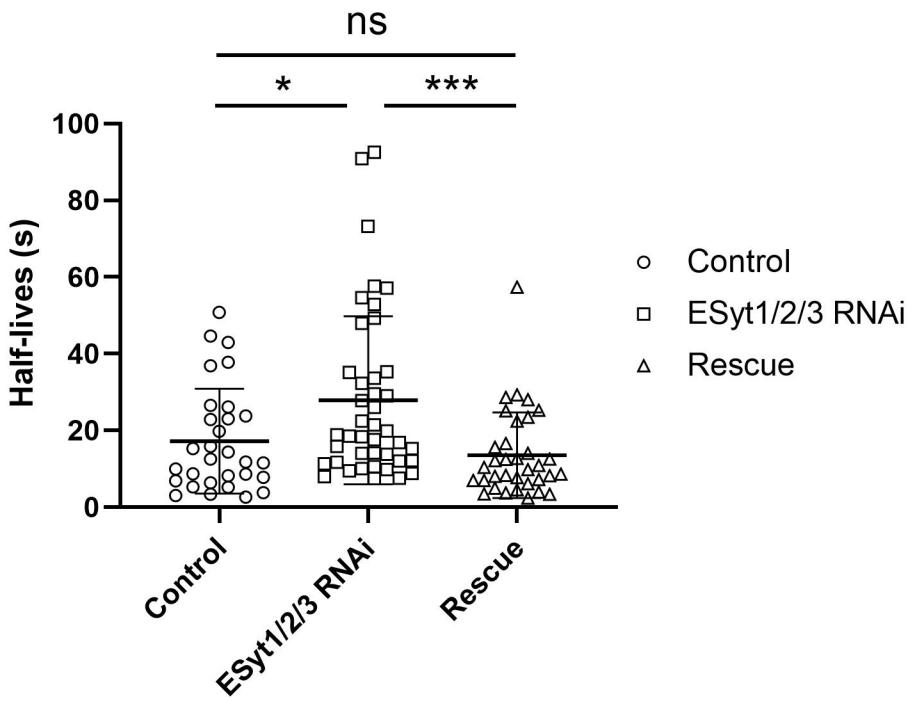

Figure 4.6: PM-to-ER trafficking half-lives are highly dependent on expression levels of ESyts. Scatter plot shows quantification of half-lives for individual transfected cells measured in same ways as in Figs. 4.3 to 4.6. Data points of each group were obtained from at least three biological replicates on different days, with each replicate referring to an imaging dish with 15-30 cells in focus and 2-10 transfected HEK 293 cells. Each data point refers to quantification of an individual transfected cell. Mean (middle bar) ± standard deviation (error bars) was shown for each group of data. One-way ANOVA, Games-Howell *post hoc* test: *$p < 0.05$, **$p < 0.01$, and ***$p < 0.001$; ns, not significant. Asterisks above lines denote significance comparing the indicated groups.

ESyt1-OMP25 construct is an artificial tether for ER-mitochondria contacts

Because ESyts are both tethers and LTPs functioning at PM-ER contacts, it may be difficult to attribute the effects of expression on trafficking rates to their lipid transfer activities or tethering functions which promote the formation of contacts. We sought to further dissect these two possibilities by reconstituting the transfer activities with a different organelle membrane.

In Chapter 2, fluorescent reporter lipids derived from RT-IMPACT showed strong colocalizations with many organelles, especially ER and Golgi. However, these reporter lipids did not show extensive colocalization with mitochondria through extended periods of time. Therefore, we proposed to engineer an ESyt-based artificial tether at ER-mitochondria contact sites to examine whether the lipid trafficking can be reconstituted towards mitochondria. Because the C2C, C2D and C2E domains of ESyt1 are responsible for PI(4,5)P_2-binding on the plasma membrane [11], only these domains need to be swapped with a mitochondria-targeting sequence (Fig. 4.7A, top).

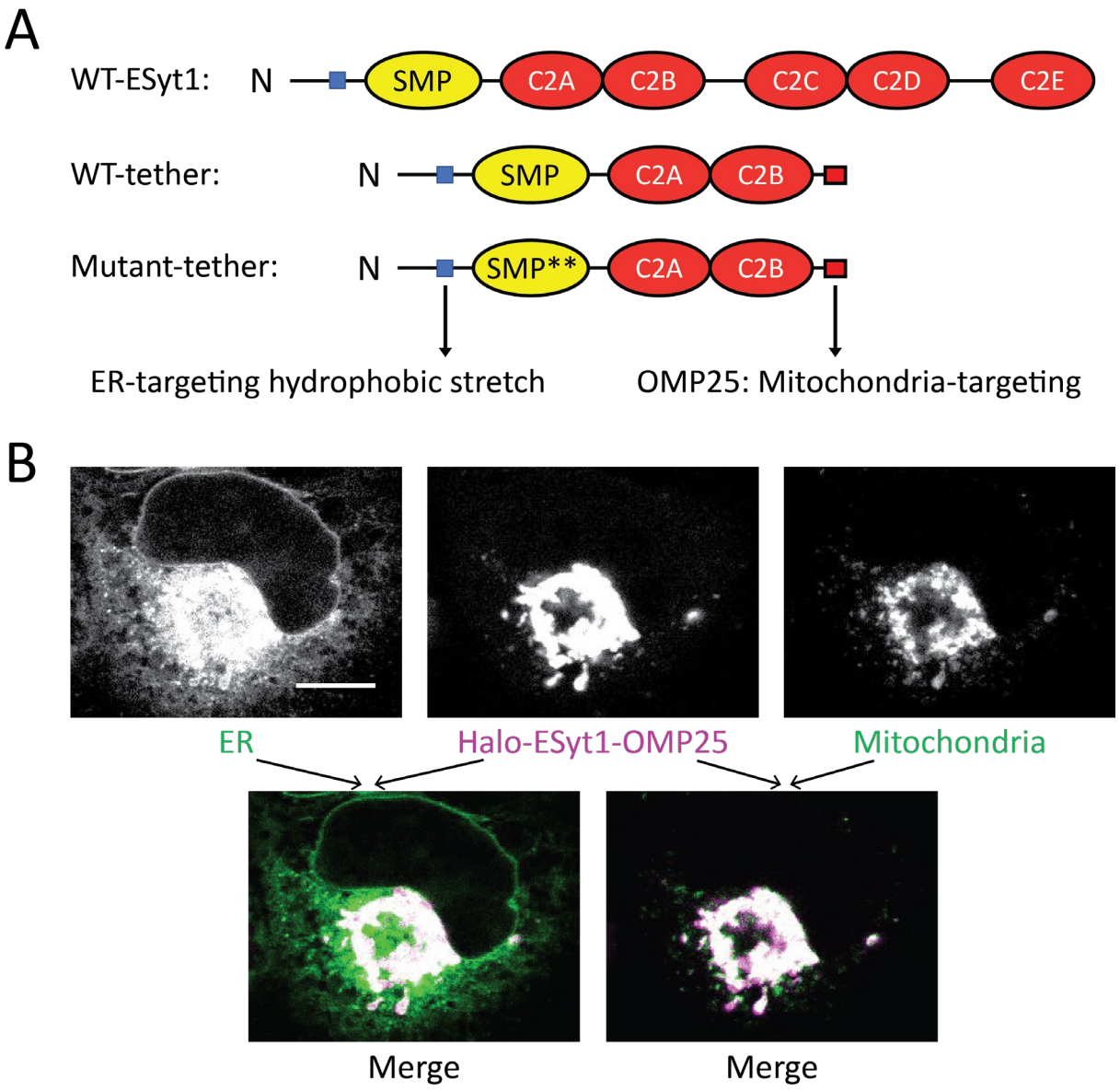

Figure 4.7: Protein engineering ESyt1 allows construction of a chimera tethering protein at ER-mitochondria contacts. (A) Domain maps of WT-ESyt1 and designed artificial ER-mitochondria WT- and Mutant-tethers ESyt1-OMP25. Asterisks indicate V169W and L308W point mutations introduced in the SMP domain for Mutant-tether. (B) Fluorescence microscopy analysis showing localizations of WT-tether at ER-mitochondria contacts. HeLa cells were transfected with Halo-ESyt1-OMP25 (WT-tether) 24 h before experiments. Cells were then

treated with HaloTag-JF635, ER-tracker Green and Mitoview 405 for 5 min at 37 ºC and rinsed for 1 min before imaging. Merged image on the left was an overlay of ER-tracker (green) and WT-tether (magenta), while on the right was of Mitoview 405 (green) and WT-tether (magenta). Colocalizations in merge appear as white color. Scale bar: 10 μm.

It follows that the design of artificial tether consists of the bulk ESyt1 protein including the N-terminal ER insertion sequence of ESyt1, the SMP domain as well as C2A and C2B domains, followed by the OMP25 transmembrane helix, a short mitochondrial targeting sequence at the C-terminus. As a result, this tether is cloned with HaloTag on the N-terminus and named Halo-ESyt1-OMP25 (WT-tether) (Fig. 4.7A, middle). As a negative control, we also cloned the mutant tether, Halo-ESyt1*-OMP25 (Mutant-tether) (Fig. 4.7A, bottom) with two point mutations in the SMP domain (V169W and L308W) of ESyt1 that eliminates its lipid-binding activities [6]. We then expressed the construct in HeLa cells and observed that the tether, without much disruption of membrane morphology, indeed colocalized with both ER and mitochondria, with stronger colocalization with the latter (Fig. 4.7B). These data indicate that the WT-tether is highly enriched in ER-mitochondria contact sites.

Expression of ESyt1-OMP25 leads to substantial fluorescent lipid trafficking towards mitochondria

Next, we tested whether the expression of tether could reconstitute transfer activities of unnatural lipids between ER and mitochondria membranes. Fluorescence colocalization analysis showed that cells transfected with WT-tether showed stronger colocalizations between reporter lipids and mitochondria than those transfected with Mutant-tether, which have similar extent of colocalization with non-transfected cells (Fig. 4.8A). We further tested whether the

tether would increase the apparent trafficking rates of fluorescent lipids towards ER and mitochondrial membranes using their respective markers. We found that although the extent of colocalization was stronger for WT-tether-expressing cells overall (Figs 4.8 and 4.9), the trafficking half-lives were unaltered by the tether (Figs. 4.10, 4.11 and 4.12). This result shows that the analysis of ER to mitochondria trafficking by measurements of half-lives (Fig. 4.12) might not fully reflect the lipid-trafficking activities by the tethers, as revealed by measurements of absolute values of Pearson's coefficients (Fig. 4.9). The limitations of half-life measurements could reveal the limitation of measuring kinetics with diffraction-limited confocal for assessing ER-to-mitochondria trafficking of fluorescent lipids. Nevertheless, these data hint at correlations between the integrity of SMP domain and observed lipid transfer activities of ESyt1-derived tether at ER-mitochondria contacts.

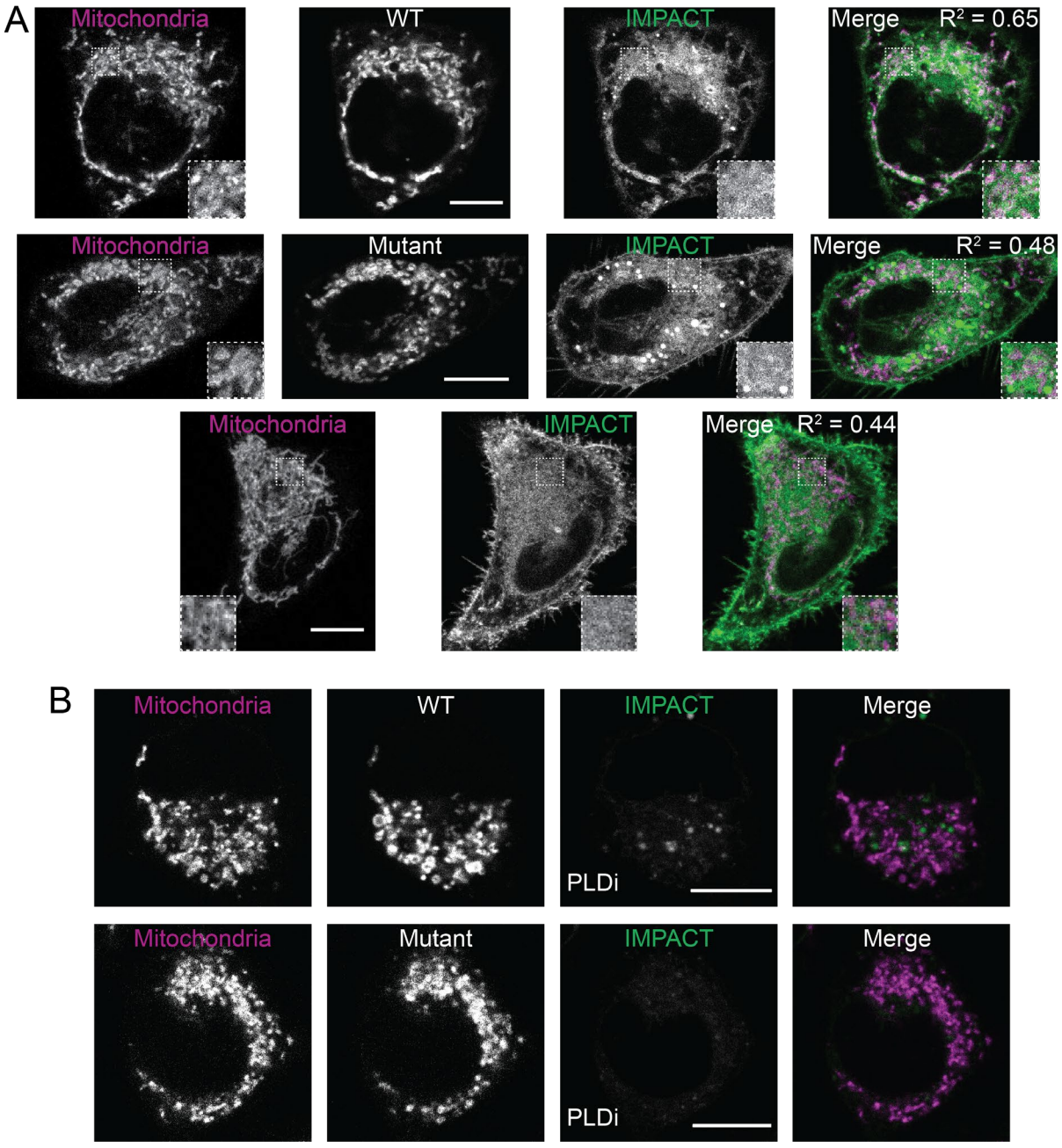

Figure 4.8: ESyt1-based artificial tether increases trafficking of RT-IMPACT derived lipids towards mitochondria. (A) Fluorescence microscopy analysis showing colocalizations between RT-IMPACT-derived lipids and mitochondria. HeLa cells were transfected with WT- (WT, top) or Mutant-tether (Mutant, middle), compared to no transfection (bottom) 24 h before

experiments. Cells were then treated with PMA, (S)-oxoTCO–C1, HaloTag-JF635, and Mitoview 405 at 37 ºC for 5 min and rinsed for 1 min prior to tagging with Tz-BODIPY for 1 min, followed by immediate imaging. Merged images show overlay of RT-IMPACT (green) and Mitoview 405 (magenta), where colocalizations appear as white color. Pearson's correlation coefficient (R^2) were calculated for the two channels in Merge. Dimensions of squares of zoom-in images: 5 × 5 μm^2. Scale bars: 10 μm. (B) Fluorescence microscopy analysis showing localizations of WT-tether and Mutant-tether at ER-mitochondria contacts and specificity of RT-IMPACT-derived lipids by PLD activities. HeLa cells were transfected with WT- (WT, top) or Mutant-tether (Mutant, bottom) 24 h before experiments. Cells were then treated with FIPI (pan-PLD inhibitor) in DMSO for 30 min, followed by incubation with PMA, (S)-oxoTCO–C1, HaloTag-JF635, and Mitoview 405 at 37 ºC for 5 min and rinsed for 1 min prior to tagging with Tz-BODIPY for 1 min before imaging. Merged image was an overlay of IMPACT (green) and Mitoview 405 (magenta). Colocalizations in merge appear as white color. Scale bars: 10 μm.

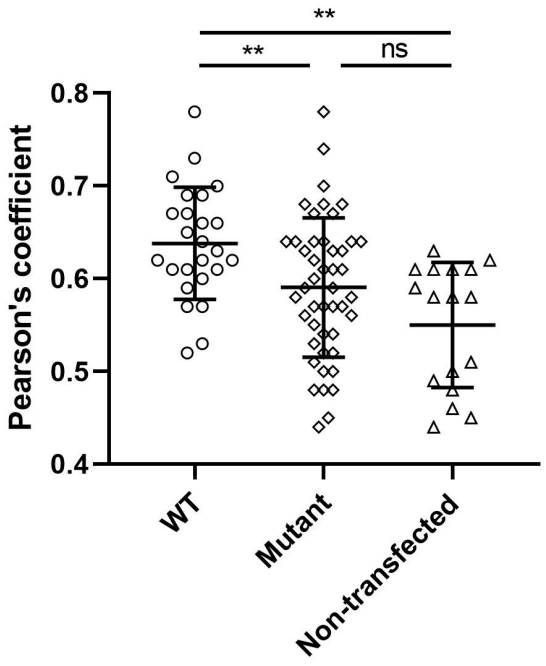

Figure 4.9: Expression of WT-tether leads to trafficking of RT-IMPACT-derived lipid towards mitochondria. Scatter-plot quantification of effects of WT- and Mutant-tether on trafficking of RT-IMPACT-derived fluorescent lipids towards mitochondria. Scatter plot shows quantification of Pearson's coefficient for individual transfected HeLa cells measured in same ways as in Fig. 4.8A. Data points of WT and Mutant were obtained from at least three biological replicates on different days, with each replicate referring to an imaging dish with 15-30 cells in focus and 2-10 transfected cells. Each data point refers to quantification of an individual transfected cell. For Non-transfected group, each data point represents a biological replicate (one imaging dish) with 15-30 cells in focus and the parameters for all cells were averaged and recorded as one data point. Mean (middle bar) ± standard deviation (error bars) was shown for each group of data. One-way ANOVA, Games-Howell *post hoc* test: *$p < 0.05$, **$p < 0.01$, and ***$p < 0.001$; ns, not significant. Asterisks above lines denote significance comparing the indicated groups.

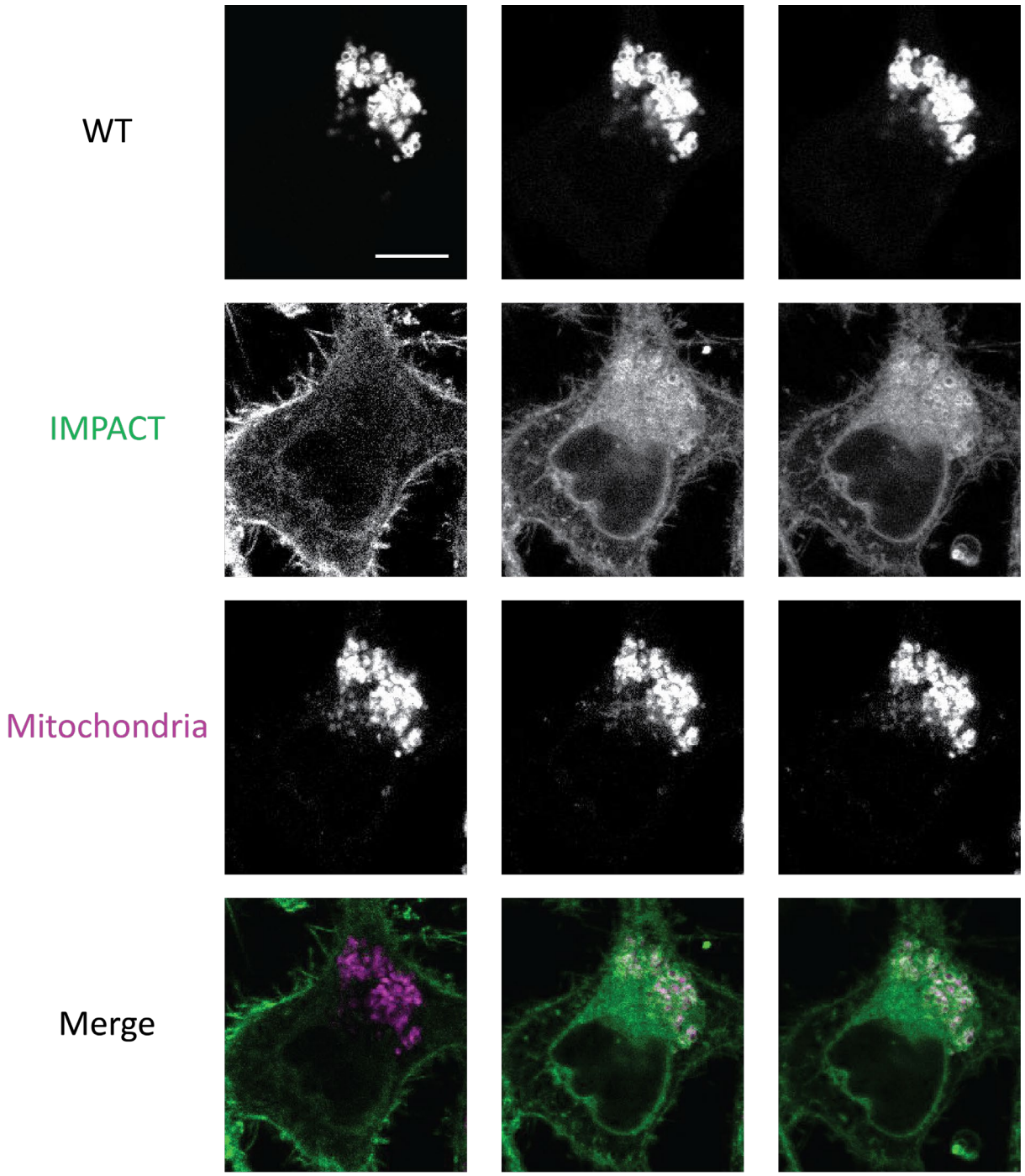
WT
IMPACT
Mitochondria
Merge
Time (s)
10
70
130
Pearson's coefficient
−0.01
0.57
0.66

Figure 4.10: WT-tether increases extent of trafficking of RT-IMPACT-derived lipids towards mitochondria. Representative real-time imaging measurements of colocalization coefficients of WT-tether (WT)-transfected cells. HeLa cells were transfected with WT-tether 24 h before experiment. Cells were treated with Mitoview 405, ER-tracker Red, PMA and (S)-oxoTCO–C1 at 37 ºC for 5 min and rinsed for 1 min prior to time-lapse imaging. Representative images of a 3-color time-lapse movie were shown at indicated time points after addition of Tz-BODIPY. Merge of IMPACT (green) and Mitoview 405 (magenta) was shown, where colocalization appears as white color. Pearson's correlation coefficients between IMPACT and Mitoview 405 were calculated at indicated time points. Scale bar: 10 μm.

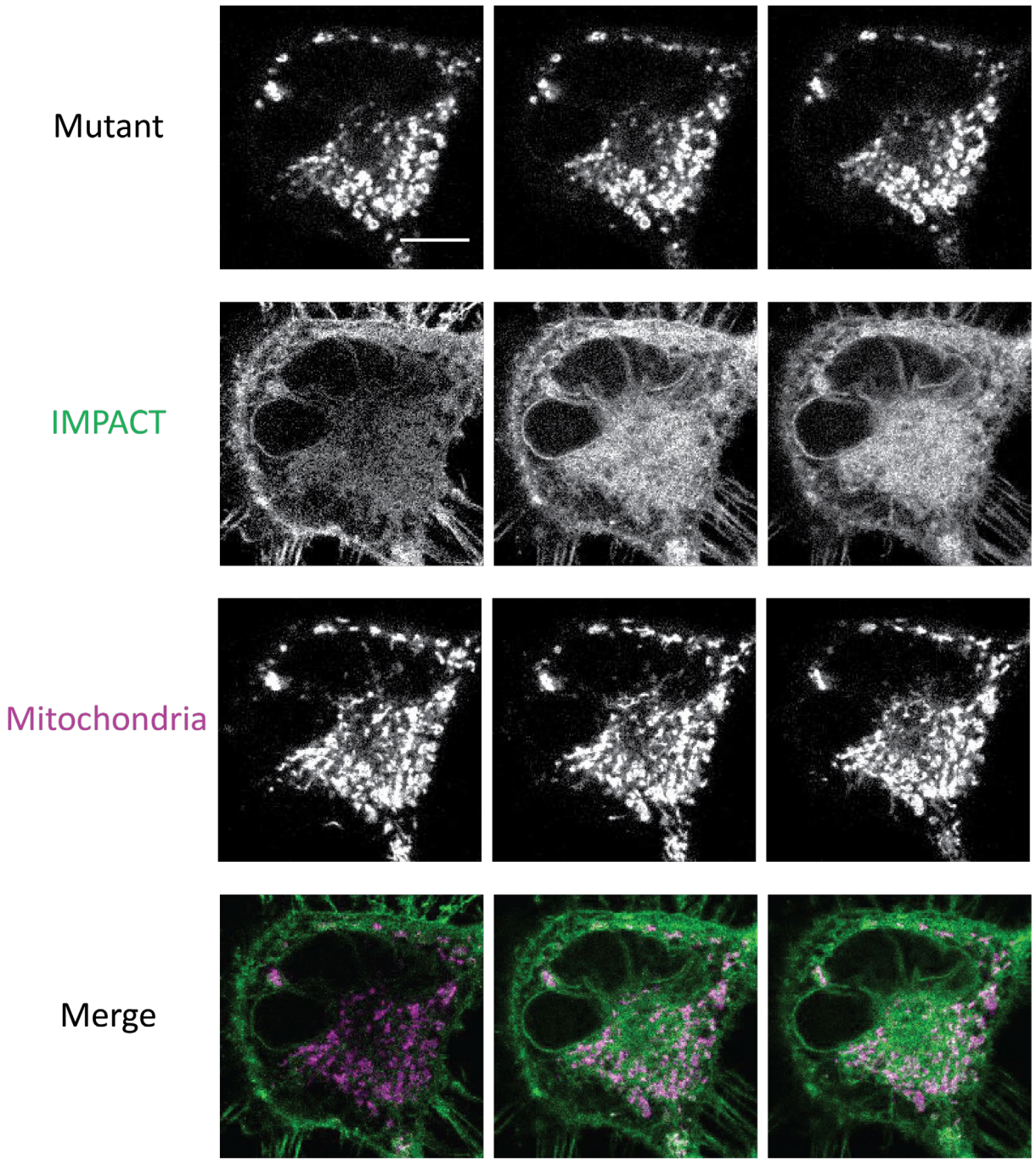
Mutant
IMPACT
Mitochondria
Merge
Time (s)
10
70
130
Pearson's coefficient
0.17
0.49
0.55

Figure 4.11: Mutant-tether barely increases extent of trafficking of RT-IMPACT-derived lipids towards mitochondria. Representative real-time imaging measurements of colocalization coefficients of Mutant-tether (Mutant)-transfected cells. HeLa cells were transfected with Mutant-tether 24 h before experiment. Cells were treated with Mitoview 405, ER-tracker Red, PMA and (S)-oxoTCO–C1 at 37 ºC for 5 min and rinsed for 1 min prior to time-lapse imaging. Representative images of a 3-color time-lapse movie were shown at indicated time points after addition of Tz-BODIPY. Merge of IMPACT (green) and Mitoview 405 (magenta) was shown, where colocalization appears as white color. Pearson's correlation coefficients between IMPACT and Mitoview 405 were calculated at indicated time points. Scale bar: 10 μm.

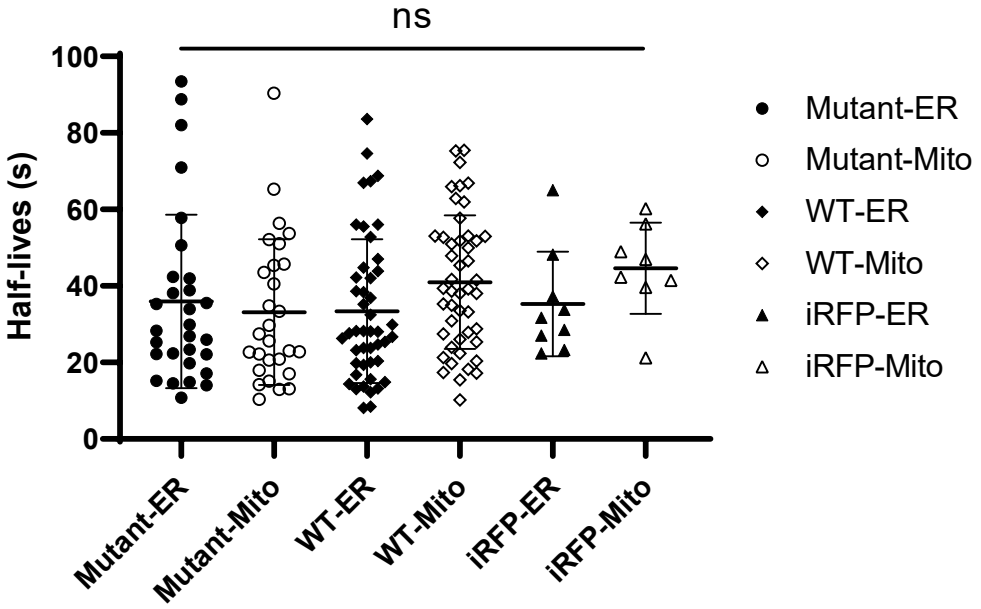

Figure 4.12: Expression of artificial ER-mitochondria tethers does not affect trafficking half-lives towards ER or mitochondria. WT, Mutant and iRFP: Cells were transfected with WT- (WT), Mutant-tether (Mutant) or miRFP (iRFP) 24 h before experiments. ER and Mito: Trafficking half-lives for individual transfected cells were measured in similar ways as in Figs.

4.3 to 4.6, plotting F_{ER}/F_{IMPACT} with ER-marker (ER) or F_{Mito}/F_{IMPACT} with Mitoview (Mito) against time. The data were then fitted with a mono-exponential decay curve to give trafficking half-lives towards ER (ER) or mitochondria (Mito), plotted in this scatter plot. Data points of each group were obtained from at least three biological replicates on different days, with each replicate referring to an imaging dish with 15-30 cells in focus and 2-10 transfected HeLa cells. Each data point refers to quantification of an individual transfected cell. Mean (middle bar) ± standard deviation (error bars) was shown for each group of data. One-way ANOVA, Games-Howell *post hoc* test: *$p < 0.05$, **$p < 0.01$, and ***$p < 0.001$; ns, not significant. Asterisks above lines denote significance comparing the indicated groups.

Taken together, these data strongly suggest that the ESyt1-based artificial tether localizes at ER-mitochondria contacts and that the tether is sufficient for establishing lipid transfer activities between the ER and mitochondria. Moreover, because the lipid transfer activity of the tether is dependent on the integrity of the SMP domain, it can be inferred that, in addition to its tethering functions, lipid transfer functions of ESyt1 at respective ER-PM or ER-mitochondria contacts are major contributors to the enhanced lipid transfer behavior of unnatural fluorescent lipids between organelles *in cellulo*.

In summary, we have demonstrated that the extended synaptotagmins (ESyts) are ER-PM tethering proteins with lipid transfer activities acting at contact sites. The lipid transfer activities of ESyts not only serve as a means to remove specific lipids (e.g., DAG) from the plasma membrane, but also have broader implications in maintaining lipid homeostasis for cells to cope with unnatural perturbations, such as doping PM with unnatural fluorescent lipids derived from RT-IMPACT labeling. Using RNAi-KD and rescue experiments, we have shown

that cells react to these unnatural reporter lipids by trafficking them from PM to ER, in part, via ESyts that are both tethers and LTPs acting at ER-PM contacts. Further, expression of an artificial tether made from ESyts with an altered localization at ER-mitochondria contacts leads to enhanced trafficking of unnatural lipids towards mitochondria, and such trafficking is dependent on lipid-transfer activities of the SMP domain. Taken together, these data indicate that ESyts are both tethers and non-specific LPTs at PM-ER contacts that can remove unnatural fluorescent lipids from PM to ER, with the SMP domain essential for their lipid transfer activities. We expect our findings to shed light on the physiological significance of the non-specificity of lipid recognition of ESyts and certain other lipid transfer proteins. We also foresee RT-IMPACT to find applications in installing fluorescent reporter lipids on targeted membranes in general, possibly in combination with engineered, optogenetic PLDs [15], as well as searching for new candidates of lipid transfer proteins and quantifying their activities in living cells.

Methods and materials

Reagents and resources

RNAi for ESyt1 were purchased from Dharmacon (Cat # J-010652-06-0010). Anti-ESyt1 antibody was purchased from Sigma-Aldrich (Cat # HPA016858). RNAi for ESyt2 was purchased from Integrated DNA Technologies (Cat # HSC.RNAI.N020728.12.5). Anti-ESyt2 antibody was purchased from Sigma-Aldrich (Cat # HPA002132). RNAi for ESyt3 was purchased from Integrated DNA Technologies (Cat # HSC.RNAI.N031913.12.6). Anti-ESyt3 antibody was purchased from Sigma-Aldrich (Cat # HPA039200). Lipofectamine 2000 (Cat # 11668019) and Lipofectamine RNAiMAX (Cat # 13778150) were purchased from ThermoFisher. FIPI was purchased from Cayman Chemical (Cat # 13563). Phorbol 12-myristate 13-acetate (PMA) was purchased from ChemCruz (Cat # SC-3576). Mitoview 405 was purchased from Biotium (Cat # 70070). ER-tracker green (Cat # E34251) and ER-tracker red (Cat # E34250) were purchased from ThermoFisher. HaloTag-JF635 was synthesized according to previous protocols [16].

General imaging methods

All imaging experiments were performed on a Zeiss LSM 800 confocal laser scanning microscope equipped with 40X 1.4 NA Plan Apochromat objectives, 405, 488, 561, and 640 nm solid-state lasers, and two GaAsP PMT detectors, using the Zeiss Zen Blue 2.3 software. All image analysis was performed using FIJI/ImageJ.

Fluorescence colocalization imaging with RT-IMPACT reagents using oxoTCO ((S)-oxoTCO–C1) and Tz-BODIPY (Figs. 4.8 and 4.9)

Briefly, HeLa or HEK cells (150,000 cells) were seeded on 35-mm glass-bottom imaging dishes (MatTek) for 24 h prior to experiments. Where indicated, the cells were then transfected with RNAi coupled with Lipofectamine RNAiMAX (24 h after seeding), and/or the indicated plasmid with Lipofectamine 2000 (24 h after RNAi or 24 h before imaging/harvesting) as per the manufacturer's instructions. 72 h after RNAi (or 24 h after plasmid transfection, if any), cells were first treated with the indicated PLD inhibitor PLDi (FIPI) at 750 nM, or corresponding DMSO vehicle in media at 37 ºC. (Cells for Western blot analysis were also harvested after 72 h of RNAi.) Subsequently, freshly prepared oxoTCO (3 mM) together with PMA (100 nM) and PLD inhibitor/DMSO in media (100 µL) were carefully added to cover the central glass well.

Cautionary note: oxoTCOs are reported to have limited water stability [17]. Therefore, all aqueous oxoTCO solutions (e.g., those in DMEM-containing media) were used within 20 min of their generation. For example, we dissolved oxoTCO in 200 µL of DMEM with PLD inhibitor/DMSO and respective stimulus and used it only for two consecutive replicates rather than make a single stock solution for an entire day of experiments at the beginning of the day.

The dish was incubated for 5 min, the treatment media was aspirated, the cells were rinsed with PBS (1 mL) briefly, and the cells were then rinsed in DMEM (500 µL) for 1 min at 37 ºC. (Rinses after oxoTCO incubation were performed in DMEM supplemented with 10% FBS and 1% P/S (media).) The media was aspirated and replaced with 100 µL Tyrode's-HEPES buffer. Cells were imaged immediately afterwards. Multicolor images were obtained in two-channel, line-switching mode. Z stacks were taken with 0.45 µm sectioning.

Real-time imaging of trafficking half-lives with RT-IMPACT reagents

Real-time IMPACT using oxoTCO ((*S*)-oxoTCO–C1) and Tz-BODIPY and was performed as described previously [18–20]. Briefly, freshly prepared oxoTCO (3 mM) together with PMA (100 nM) in media (100 µL) were carefully added to cover the central glass well of the imaging dish. The dish was incubated for 5 min, the treatment media was aspirated, the cells were rinsed with PBS (1 mL) briefly, and the cells were then rinsed in media (500 µL) for 1 min at 37 ºC. The media was replaced with 100 µL of PBS buffer to cover the center of the glass bottom and the dish was mounted on the microscope. The cells to be imaged were quickly located and time-lapse imaging with an interval of 8 s (Figs. 4.1B, 4.3 to 4.6), or 10 s (Fig. 4.10 to 4.12), and duration of 4 min begun. Tz-BODIPY (100 µL, 1 µM in PBS) was added dropwise but quickly to the center of the dish during acquisition. The percentage of total IMPACT fluorescence (488 channel) that colocalizes with a mask of ER-marker (561 nm) channel (F_{ER}/F_{IMPACT}) were measured in ImageJ for each time point. For Figs. 4.1B, 4.3 to 4.6, F_{ER}/F_{IMPACT} vs. time was then fitted with a mono-exponential decay function [$y = A_1 * \exp(-x/t_1) + y_0$] using Origin Pro 8, with the half-life equal to [$\ln(2) * t_1$]. For Figs. 4.8 to 4.12, Pearson correlation coefficients between IMPACT/ER and/or IMPACT/Mitochondria channels were measured by ImageJ. The collections of half-lives and Pearson coefficients were plotted as scatter plots (Figs 4.6, 4.9 and 4.12) using GraphPad Prism 8.

Cell culture

HEK 293 and HeLa cells were grown in DMEM (Dulbecco's modified Eagle medium) supplemented with 10% FBS, 1% penicillin/streptomycin (HEK 293 cells were additionally supplemented with 1 mM sodium pyruvate) were maintained in a 5% CO2, moisture-saturated atmosphere at 37 ºC. Cell densities were maintained between 10^5 and 1.6 x 10^6 cells/mL. For

cell labeling experiments, all buffers or media were warmed to 37 ºC or room temperature prior to addition to cells, and incubations were done at 37 ºC.

Primers and cloning

EGFP-ESyt1 plasmid [7] was obtained from De Camilli lab at Yale University. In all PCR reactions, Phusion High-Fidelity DNA Polymerase (New England Biolabs, Cat # M0530S) was used for amplifying fragments. PfuUltra High-fidelity DNA Polymerase (Agilent Technologies, Cat # 600382) was used for site-directed mutagenesis. Gibson assembly was performed using Gibson Assembly HiFi 1 Step Starter Kit (Synthetic Genomics, Cat # GA1100-S).

miRFP-ESyt1 was cloned by PCR and ligated by 3-component Gibson assembly. miRFP fragment was amplified from pmiRFP-N1 vector (Addgene Cat # 79987) by Gib-miRFP-F (taagcttggtaccgagctcgATGGTAGCAGGTCATGCCTC) and Gib-miRFP-AgeI-(ESyt1)-R (atcgctccataccggtGCTCTCAAGCGCGGTGATC). ESyt1 fragment was amplified from EGFP-ESyt1 plasmid by Gib-AgeI-ESyt1-(miRFP)-F (ccgcgcttgagagcaccggtATGGAGCGATCTCCAGGAG) and Gib-ESyt1-R (tccaccacactggactagtgCTAGGAGCTGCCCTTGTC). pcDNA5-FRT-TO (ThermoFisher Cat # V652020) was digested by BamHI. The digested plasmid was then ligated with miRFP and ESyt1 fragments by Gibson assembly.

The RNAi-resistance of miRFP-ESyt1 was further achieved by introducing 6 silent point mutations in the region targeted by the RNAi oligos using site-directed mutagenesis and the following primers (targeted nucleotides are shown in uppercase: ESyt1_siRNA-res_S, ctgggccaggtgaaactgactctgtggtaTtaTTCCgaGgagcgaaagctggtcagcattgttc; ESyt1_siRNA-res_AS, gaacaatgctgaccagctttcgctcCtcGGAAtaAtaccacagagtcagtttcacctggcccag) [7].

Halo-ESyt1 was cloned by PCR and ligated by two-component Gibson assembly. The Halo-TEV fragment was amplified from HaloTag-TEVsite_pcDNA5.FRT Plasmid (obtained from Hollopeter lab at Cornell University) by (AgeI)-GFP-C1-AgeI-Halo-F (cgtcagatccgctagcgctaaccggtgccaccatggcagaaatcggtactg) and (SalI)-GFPC1-GGSG-Halo-R (ctcctggagatcgctccatgcctgatccaccgttatcgctctgaaagtacag). EGFP-ESyt1 plasmid was digested using AgeI and SalI. The digested plasmid was then ligated together with the Halo-TEV fragment using Gibson assembly.

Halo-ESyt1-OMP25 was cloned by PCR and ligated by two-component Gibson assembly. GGS-OMP25-MCS fragment was amplified from mCherry-OMP25 plasmid (obtained from De Camilli lab at Yale University) using OMP25-MCS_fwd (gccccacctcgacccagatctcgagctcaaggtg) and OMP25-MCS_rev (tttgtgaaatttgtgatgctattgctttatttgtaaccattataagc). AgeI-ESyt1-C2AB fragment was amplified from Halo-ESyt1 plasmid using AgeI-E1-C2AB_F (gcatcacaaatttcacaaataaagcatttttttc) and AgeI-E1-C2AB_R (gggtcgaggtggggcatc). These two fragments were then ligated together by using Gibson assembly.

Halo-ESyt1*-OMP25 was further cloned by site-directed mutagenesis using primer sets E-Syt1_L308W_MF (tgccttcctcgtgttgcccaaccgatggctggtgccccttgtgcctgaccttcaagatgt), E-Syt1_ L308W _MR (acatcttgaaggtcaggcacaaggggcaccagccatcggttgggcaacacgaggaaggca), E-Syt1_V169W_MF (tctggctgaaactgtggctccggcttggaggggatctaacccccatctgcaaacatttac) and E-Syt1_V169W_MR (gtaaatgtttgcagatgggggttagatcccctccaagccggagccacagtttcagccaga) [6].

Statistics and reproducibility

All imaging experiments show representative images from experiments performed in at least three biological replicates on different days, where each replicate refers to a dish of cells with approximately 15-30 cells in total and 2-10 transfected cells in the field of view. For imaging with transfected cells, measurements were made on individual transfected cells, with each transfected cell being a data point in Figs. 4.6, 4.9 (left two lanes) and 4.12. For imaging experiments with non-transfected cells, each dish contains approximately 15-30 cells in total and the parameters for all cells were averaged and recorded as one data point for Figs. 4.1B and 4.9 (right lane). Exact numbers of replicate experiments and sample sizes are provided in each figure legend. For experiments involving quantification of comparisons between two independent groups (Fig. 4.1B), student's t-test (paired two-tailed distribution) with unequal variance was used to calculated p-values. For experiments involving quantification of comparisons between more than two independent groups (Figs. 4.6, 4.9 and 4.12), p-values were calculated using one-way ANOVA, followed by Games-Howell post-hoc test (for samples of unequal variance).

References

1 Bernhard W, Rouiller C. Close topographical relationship between mitochondria and ergastoplasm of liver cells in a definite phase of cellular activity. *J Biophys Biochem Cytol* 1956;**2**:73–8. https://doi.org/10.1083/jcb.2.4.73.

2 Scorrano L, De Matteis MA, Emr S, Giordano F, Hajnóczky G, Kornmann B, *et al.* Coming together to define membrane contact sites. *Nat Commun* 2019;**10**:. https://doi.org/10.1038/s41467-019-09253-3.

3 Gatta AT, Levine TP. Piecing Together the Patchwork of Contact Sites. *Trends Cell Biol* 2017:214–29. https://doi.org/10.1016/j.tcb.2016.08.010.

4 Eisenberg-Bord M, Shai N, Schuldiner M, Bohnert M. A Tether Is a Tether Is a Tether: Tethering at Membrane Contact Sites. *Dev Cell* 2016:395–409. https://doi.org/10.1016/j.devcel.2016.10.022.

5 Wu MM, Buchanan JA, Luik RM, Lewis RS. Ca2+ store depletion causes STIM1 to accumulate in ER regions closely associated with the plasma membrane. *J Cell Biol* 2006;**174**:803–13. https://doi.org/10.1083/jcb.200604014.

6 Saheki Y, Bian X, Schauder CM, Sawaki Y, Surma MA, Klose C, *et al.* Control of plasma membrane lipid homeostasis by the extended synaptotagmins. *Nat Cell Biol* 2016;**18**:504–15. https://doi.org/10.1038/ncb3339.

7 Giordano F, Saheki Y, Idevall-Hagren O, Colombo SF, Pirruccello M, Milosevic I, *et al.* PI(4,5)P2-Dependent and Ca2+-Regulated ER-PM interactions mediated by the extended synaptotagmins. *Cell* 2013;**153**:1494. https://doi.org/10.1016/j.cell.2013.05.026.

8 Min SW, Chang WP, Südhof TC. E-Syts, a family of membranous Ca2+-sensor proteins with multiple C2 domains. *Proc Natl Acad Sci U S A* 2007;**104**:3823–8. https://doi.org/10.1073/pnas.0611725104.

9 Fernández-Busnadiego R, Saheki Y, De Camilli P. Three-dimensional architecture of extended synaptotagmin-mediated endoplasmic reticulum-plasma membrane contact sites. *Proc Natl Acad Sci U S A* 2015;**112**:E2004–13. https://doi.org/10.1073/pnas.1503191112.

10 Bian X, Saheki Y, De Camilli P. Ca2+ releases E-Syt1 autoinhibition to couple ER-

plasma membrane tethering with lipid transport. *EMBO J* 2018;**37**:219–34. https://doi.org/10.15252/embj.201797359.

11 Saheki Y, De Camilli P. The Extended-Synaptotagmins. *Biochim Biophys Acta - Mol Cell Res* 2017:1490–3. https://doi.org/10.1016/j.bbamcr.2017.03.013.

12 Schauder CM, Wu X, Saheki Y, Narayanaswamy P, Torta F, Wenk MR, *et al.* Structure of a lipid-bound extended synaptotagmin indicates a role in lipid transfer. *Nature* 2014;**510**:552–5. https://doi.org/10.1038/nature13269.

13 Wong LH, Gatta AT, Levine TP. Lipid transfer proteins: the lipid commute via shuttles, bridges and tubes. *Nat Rev Mol Cell Biol* 2019:85–101. https://doi.org/10.1038/s41580-018-0071-5.

14 Wong LH, Čopič A, Levine TP. Advances on the Transfer of Lipids by Lipid Transfer Proteins. *Trends Biochem Sci* 2017;**42**:516–30. https://doi.org/10.1016/j.tibs.2017.05.001.

15 Tei R, Baskin JM. Spatiotemporal control of phosphatidic acid signaling with optogenetic, engineered phospholipase Ds. *J Cell Biol* 2020;**219**:. https://doi.org/10.1083/jcb.201907013.

16 Grimm JB, Muthusamy AK, Liang Y, Brown TA, Lemon WC, Patel R, *et al.* A general method to fine-tune fluorophores for live-cell and in vivo imaging. *Nat Methods* 2017;**14**:987–94. https://doi.org/10.1038/nmeth.4403.

17 Lambert WD, Scinto SL, Dmitrenko O, Boyd SJ, Magboo R, Mehl RA, *et al.* Computationally guided discovery of a reactive, hydrophilic trans-5-oxocene dienophile for bioorthogonal labeling. *Org Biomol Chem* 2017;**15**:6640–4. https://doi.org/10.1039/C7OB01707C.

18 Bumpus TW, Liang D, Baskin JM. IMPACT: Imaging phospholipase D activity with clickable alcohols via transphosphatidylation. *Methods Enzymol* 2020:75–94. https://doi.org/10.1016/bs.mie.2020.04.037.

19 Liang D, Wu K, Tei R, Bumpus TW, Ye J, Baskin JM. A real-time click chemistry imaging approach reveals stimulus-specific subcellular locations of phospholipase D activity. *Proc Natl Acad Sci U S A* 2019;**116**:15453–62. https://doi.org/10.1073/pnas.1903949116.

20 Liang D, Cheloha RW, Watanabe T, Gardella TJ, Baskin JM. Activity-based, bioorthogonal imaging of phospholipase D reveals spatiotemporal dynamics of GPCR-Gq signaling. *Cell Chem Biol* 2021. https://doi.org/10.1016/j.chembiol.2021.05.020.

CHAPTER 5: Concluding remarks and outlook

Epilogue

Cells synthesize specific signaling molecules at precise subcellular locations to regulate cellular behaviors. It is therefore of utter importance to visualize the production of these signaling agents with high spatiotemporal resolution to understand the physiological consequences of these molecules. Phosphatidic acid (PA) is a pleiotropic signaling lipid that are responsible for cell migration, proliferation, inflammatory responses, and many other cellular behaviors. Overall, it is a strong signal for cell survival. Therefore, cancer cells frequently upregulate the production of PA for their aggressive division and metastatic behaviors. Among major biosynthetic pathways of PA, excessive production through phospholipase D (PLD) enzymes is commonly associated with cancer cell growth. However, the lack of faithful toolsets to image PLD activities in live cells has been a bottleneck that has limited our understanding of PA biosynthesis and signaling. For example, traditional biochemical methods to quantify PLD activities cannot report with single-cell resolution. In addition, tagging fluorescent proteins to PLDs does not necessarily reflect on their enzymatic activities. Lastly, even the most faithful PA biosensors developed to date rely on coincidence detection, limiting their reliability, and these biosensors cannot differentiate nascent PA molecules made specifically from a particular pathway. Having considered the limitations of exciting biochemical assays, we therefore turned our perspective to chemical biology tools to develop faithful reporters for PLD-mediated PA biosynthesis.

In Chapter 2, the author discusses the design, synthesis and validation of a bioorthogonal chemistry-based imaging approach, termed RT-IMPACT, to visualize PLD activities in real-time under live-cell conditions. It is demonstrated that RT-IMPACT is a highly faithful and sensitive reporter for PLD activities through fluorescence detection. Next, we show that virtues of fast chemical kinetics and fluorogenic behaviors of the fluorophore enable a real-time imaging method of endogenous PLD enzymes. Further, the utilities of RT-IMPACT probes are showcased by revealing real-time localizations of PLD activities downstream of various stimuli such as phorbol esters, G protein-coupled receptors and receptor tyrosine kinases. Lastly, the trafficking process of reporter lipids from plasma membrane to ER membrane happening during real-time imaging are characterized with short half-lives that are typical for non-vesicular pathways.

In Chapter 3, the author applies RT-IMPACT probes to analyze parathyroid hormone receptor signaling. Specifically, PLD activities, as measured by RT-IMPACT derived fluorescence, is directly downstream of Gq signaling pathway. Further, although the Gs pathway follows a non-canonical persistent signaling regime at endosomes, the Gq pathway is confined to the plasma membrane and is transient in nature. Lastly, pharmacological inhibition of endocytosis of receptors enhances Gq signaling and largely attenuates the Gs pathway, indicating a competitive relationship between these signaling pathways.

In Chapter 4, the author characterizes the activities of a family of lipid transfer proteins, namely the extended synaptotagmins (ESyts). The experimental design capitalizes on the ability of RT-IMPACT to generate PLD-derived fluorescent lipids on the plasma membrane (PM) and quantify trafficking dynamics towards intracellular membranes with

high temporal resolution. With RNAi-based knockdown and rescue experiments, a positive correlation between expression of ESyts and PM-to-ER trafficking rates is established. Next, the trafficking activities are reconstituted between the ER-Mitochondrial membranes with lipid transfer domain (SMP) of ESyt1 fused to a mitochondria-targeting sequence. These results demonstrate that the SMP domains of ESyts are responsible for removal of unnatural fluorescent lipids from the PM and may have broader implications in its role in maintaining lipid homeostasis in general.

Finally, in this concluding chapter, the author summarizes the significance of this work, highlights the outstanding questions in the field and provides potential directions for future research.

Potential improvement of real-time IMPACT toolset

Chapter 2 describes the limitations of the original IMPACT strategy being the low temporal resolution, which renders the localizations of PLD-derived fluorescent lipids unable to reflect original locations of PLD activities due to lipid trafficking events. Such drawbacks motivated the author to develop a real-time variant of IMPACT (RT-IMPACT) to visualize PLD activities with significantly improved spatiotemporal resolutions. The RT-IMPACT strategy is largely enabled by 1. The fast tetrazine ligation between trans-Cyclooctenes (TCOs) and fluorogenic tetrazines (Tz) and 2. The hydrophilicity of oxoTCOs compared to traditional carbocyclic TCOs. Despite these desirable properties, RT-IMPACT still has some limitations, including difficult synthetic procedures for oxoTCO, lower sensitivity and lower aqueous stability compared to original IMPACT, fast but suboptimal chemical kinetics as compared to lipid trafficking. Therefore, chemists could potentially optimize the RT-

IMPACT strategy even further by designing more hydrophilic variants of TCOs, faster-reacting, diversely-emitting and even caged/latent Tz that can be activated upon photoirradiation to allow for better visualization of PLD enzyme activities with enhanced signal-to-background and lipid trafficking events in real-time.

In addition to oxoTCO, another recently developed hydrophilic derivative of TCO-based clickable handle is aTCO [1], with a tertiary alcohol group appended at axial position of the quaternary carbon of the eight-membered ring, where the alkyl chain that sits on the equatorial position can be highly variable and further derivatized. The advantage of using aTCO-derived primary alcohol as potential PLD substrates for RT-IMPACT is that the synthetic procedures can be reduced to 4 steps as compared to 7 steps for oxoTCOs. Furthermore, the alkyl handle of aTCO can be more easily functionalized with different types of linkages between the primary alcohol group and the aTCO ring, as compared to a short methylene linkage in the (*S*)-oxoTCO−C1 molecule. This flexibility allows for screening of optimal linkages that results in higher aqueous stability of the molecule and better substrate recognition by PLD enzymes.

Besides, optimizations of Tz-fluorophore conjugate are also feasible, in light of recent advances of synthetic efforts. Improvement of chemical kinetics of tetrazine ligation can be achieved by replacing the methyl group that is para-to the fluorophore group with electron withdrawing groups (EWGs), such as 2-pyridyl-group or even a hydrogen atom (H), can increase the rate of tetrazine ligation [2,3]. Therefore, a potential future direction to optimize the reactivities of tetrazine is design, synthesis and characterization of H- and other EWG-substituted Tz-fluorophore conjugate [4]. However, the improvement on reactivity/chemical

kinetics could sacrifice the stability of tetrazines further, especially in cellular context [4,5]. Fortunately, recent computationally guided design yielded a highly reactive yet stable DHP-substituted tetrazine with >90% retained over 10 h at 37 °C in cellular media [6]. This type of design would allow researchers to generate highly stable yet reactive Tz-fluorophore conjugates for prolonged applications.

Furthermore, an even better approach to overcome the issue of stabilities for tetrazine is perhaps to take advantage of newly developed caged/latent tetrazines that can be activated with exogenous control such as photoirradiation. *In situ* photocatalytic oxidation of dihydrotetrazines − the precursor for reactive tetrazines – with far-red light has been reported to enable selective conjugation with TCOs with deep tissue penetration in *in vivo* settings [7,8]. In addition, visible light-activated photouncaging of dihydrotetrazines has been described recently, allowing for selective photopharmacology and precision medicine at single-cell levels [9]. These caged/latent strategies for designing tetrazine-fluorophore conjugate should enable applications requiring prolonged incubation of tetrazines in cellular conditions for imaging PLD activities in real-time. The *in situ* generation of reactive tetrazines will also overcome the potential issue of slow fluorophore diffusion across clusters of cells with a simple step of pre-incubation of caged tetrazines. The enhanced stability and selective uncaging will also allow 3D-organoid imaging through multiple layers of cells in real-time, with relevance to *in vivo* context.

Another way to boost the utilities of tetrazines in biological contexts is to utilize the full spectrum of fluorophores coupled to tetrazines to enable multiplexed imaging with other fluorescent outputs. For example, blue- [10], red- [11]and far-red- [12,13] emitting fluorogenic

tetrazines have been reported. These tetrazines could be applied to multicolor RT-IMPACT imaging where the green channel is occupied by another fluorophore, or to label PLD activities downstream of multiple stimuli at the same time.

CRISPR-Cas9-based high-throughput screening of activators of PLD enzymes

PLD enzymes intersect with many important signaling pathways and are regulated by many different protein interacting partners, many of which are well-characterized through detailed mechanistic studies, such as mTORC signaling. Whereas traditional biochemical assays are capable of characterizing specific biochemical pathways, systematic profiling of regulators for proteins of interests (POIs) can be hard to achieve. The CRISPR-Cas9 system has received tremendous attention as a versatile tool for gene editing and expression control since its first discovery as a bacterial immune system [14–16]. One major advantage of CRISPR-Cas9 is its high-throughput capacity to discover novel candidates as regulators for POIs. With properly designed single-guide (sg) RNAs, potential activators/inhibitors of POIs can be identified with appropriate phenotypic readouts such as fluorescence [17,18], cell proliferation [19] and survival [20,21].

Therefore, one potential future direction for understanding the PLD signaling network is to utilize CRISPR-Cas9-based high-throughput screening coupled with the IMPACT strategy as a fluorescent readout. Cells expressing with CRISPR-Cas9 constructs can be subjected to transfections with sgRNA libraries, followed by treatments of IMPACT probes to fluorescently tag PLD activities. These labeled cells can then be sorted by fluorescence-activated cell sorting (FACS) for separation of cells that display either highly active or inactive PLD activities. Through next-generation sequencing and comparison of sgRNA

abundances in different populations of sorted and unsorted cells, potential regulators of PLDs can then be identified [19,22].

As a cautionary note, although RT-IMPACT can faithfully report localizations of PLD-dependent activities in living cells, it is worth noting that significant synthetic capabilities and efforts are needed to access the RT-IMPACT reagents. Furthermore, the relatively low stability and substrate efficiency of oxoTCOs [23], as compared to azidopropanol in original IMPACT strategy, render RT-IMPACT inapplicable towards long-term treatment in cellular assays. Due to these limiting factors, the original IMPACT based on azidopropanol as PLD substrates is a better candidate for high-throughput screening of novel activators/inhibitors for PLD enzymes in a cellular context. Consequently, RT-IMPACT is more suitable for detailed, mechanistic analyses of real-time localizations of PLD activities in a low-throughput manner for validation of target gene hits from CRISPR screens.

Investigation of G_q signaling pathways in the context of non-canonical G_s-signaling

The primary motivation for the work in Chapter 3 was that the G_q-signaling pathway under PTHR1 activation was understudied, due to lack of available activity-based tools, as compared to heavy research efforts spent on understanding non-canonical G_s signaling using faithful biosensors for cAMP production. The author took initiative to study the G_q pathway using the novel chemical tools described in Chapter 2, RT-IMPACT, to unveil a competitive relationship between the G_q and G_s pathways.

With the recently characterized interactions between 148 GPCRs and all 11 unique Gα protein subunits [24], researchers could explore space of many other receptors that activate both G_s and G_q, where the G_s follows the non-canonical signaling at endosomes and the G_q

pathway remains largely unexplored. Among them, dopamine D1 receptor (D1R) [25], β_2-adrenergic receptor (β_2AR) [26], and Pituitary adenylate cyclase 1 receptor (PAC1R) [27] are all promising candidates reported to follow the non-canonical signaling for G_s and on the other hand show considerable binding affinity towards G_q. Therefore, a potential future research direction would be to investigate the role of G_q signaling and its relationship with G_s pathway downstream of these receptors, in a spatiotemporally resolved manner similar to Chapter 3.

Further characterizations of lipid transfer proteins at membrane contact sites

In Chapter 4, extended synaptotagmins (ESyts) are characterized by its contribution towards lipid trafficking events of unnatural reporter lipids from PM to ER in live cells. However, future experiments characterizing *in vitro* lipid transfer activities of ESyts could be performed to consolidate such findings. For example, De Camilli and coworkers have reported purification of a large fraction of ESyt1 (93-1104 out of 1104 amino acid sequence) [28] and lipid-binding and lipid-transfer activities have been extensively characterized with NBD-tagged PE as the fluorescent reporter. With *in vitro* liposome tethering assays, the transfer activities of ESyt1 can be characterized quantitatively. As an alternative assay, native-gel electrophoresis can be used to visualize protein-binding to fluorescent lipids under native conditions. Future research efforts could execute similar experiments to further confirm the lipid-binding and transferring activities of ESyts under *in vitro* conditions, serving as complementary evidence for real-time lipid trafficking data in live cells.

In Chapter 4, knockdown of expression of ESyts only results in partial inhibition of the observed transport of unnatural fluorescent lipids from PM to ER. It follows that another potential application of RT-IMPACT includes the identification and characterization of other

lipid transfer proteins that contribute to such processes. In principle, any proteins that influence PM-to-ER trafficking half-lives can be identified by targeted RNAi-based screening based on time-lapse imaging, similar to the rationale described in Chapter 4. Automated adaptions could in principle be made to achieve high-throughput efficiency for data analysis and target identifications of this process [29–31]. Consequently, with more and more lipid transfer proteins and their activities characterized by RT-IMPACT, researchers can gradually build a holistic profile of them acting at PM-to-ER contacts.

Furthermore, with the recently developed optogenetic control of PLD enzyme activities [32], selective organelle-targeted synthesis of PLD-derived fluorescent lipids can be achieved. Therefore, the optogenetic toolset should greatly extend possibilities of studying lipid-trafficking events originating from various organelle membranes of choice, including PM, lysosomes, ER and Golgi, without being limited to lipid transports at PM-to-ER contacts as achieved by phorbol ester stimulation of PLDs. Potential lipid-transfer activities acting at understudied membrane contacts can then be selectively visualized under the microscope, in ways similar to real-time imaging performed in Chapter 4.

References

1 Pigga JE, Rosenberger JE, Jemas A, Boyd SJ, Dmitrenko O, Xie Y, *et al.* General, Divergent Platform for Diastereoselective Synthesis of trans-Cyclooctenes with High Reactivity and Favorable Physiochemical Properties. *Angew Chem Int Ed* 2021;**60**:14975–80. https://doi.org/10.1002/anie.202101483.

2 Blackman ML, Royzen M, Fox JM. Tetrazine ligation: fast bioconjugation based on inverse-electron-demand Diels-Alder reactivity. *J Am Chem Soc* 2008;**130**:13518–9. https://doi.org/10.1021/ja8053805.

3 Hamasaki A, Ducray R, Boger DL. Two novel 1,2,4,5-tetrazines that participate in inverse electron demand Diels-Alder reactions with an unexpected regioselectivity. *J Org Chem* 2006;**71**:185–93. https://doi.org/10.1021/jo051832o.

4 Karver MR, Weissleder R, Hilderbrand SA. Synthesis and evaluation of a series of 1,2,4,5-tetrazines for bioorthogonal conjugation. *Bioconjug Chem* 2011;**22**:2263–70. https://doi.org/10.1021/bc200295y.

5 Oliveira BL, Guo Z, Bernardes GJL. Inverse electron demand Diels-Alder reactions in chemical biology. *Chem Soc Rev* 2017;**114**:4764. https://doi.org/10.1039/c7cs00184c.

6 Svatunek D, Wilkovitsch M, Hartmann L, Houk KN, Mikula H. Uncovering the key role of distortion in tetrazine ligations guides the design of bioorthogonal tools with high reactivity and superior stability. *ChemRxiv* 2021. https://doi.org/http://dx.doi.org/10.33774/chemrxiv-2021-vnwzk.

7 Wang C, Zhang H, Zhang T, Zou X, Wang H, Rosenberger JE, *et al.* Enabling in Vivo Photocatalytic Activation of Rapid Bioorthogonal Chemistry by Repurposing Silicon-Rhodamine Fluorophores as Cytocompatible Far-Red Photocatalysts. *J Am Chem Soc* 2021;**143**:10793–803. https://doi.org/10.1021/jacs.1c05547.

8 Jemas A, Xie Y, Pigga JE, Caplan JL, Ende CW, Fox JM. Catalytic Activation of Bioorthogonal Chemistry with Light (CABL) Enables Rapid , Spatiotemporally-controlled Labeling and No-Wash , Subcellular 3D-Patterning in Live Cells using Long Wavelength Light. *ChemRxiv* 2021. https://doi.org/10.33774/chemrxiv-2021-2s0d6.

9 Liu L, Zhang D, Johnson M, Devaraj NK. Light-activated tetrazines enable live-cell spatiotemporal control of bioorthogonal reactions. *BioRxiv* 2020:2020.12.01.405423.

https://doi.org/10.1101/2020.12.01.405423.

10 Meimetis LG, Carlson JCT, Giedt RJ, Kohler RH, Weissleder R. Ultrafluorogenic coumarin-tetrazine probes for real-time biological imaging. *Angew Chem Int Ed* 2014;**53**:7531–4. https://doi.org/10.1002/anie.201403890.

11 Wu H, Yang J, Šečkutė J, Devaraj NK. In Situ Synthesis of Alkenyl Tetrazines for Highly Fluorogenic Bioorthogonal Live-Cell Imaging Probes. *Angew Chemie* 2014;**126**:5915–9. https://doi.org/10.1002/ange.201400135.

12 Lukinavičius G, Umezawa K, Olivier N, Honigmann A, Yang G, Plass T, *et al.* A near-infrared fluorophore for live-cell super-resolution microscopy of cellular proteins. *Nat Chem* 2013;**5**:132–9. https://doi.org/10.1038/nchem.1546.

13 Werther P, Yserentant K, Braun F, Grußmayer K, Navikas V, Yu M, *et al.* Bio-orthogonal Red and Far-Red Fluorogenic Probes for Wash-Free Live-Cell and Super-resolution Microscopy. *ACS Cent Sci* 2021;**7**:1561–71. https://doi.org/10.1021/acscentsci.1c00703.

14 Ran FA, Hsu PD, Wright J, Agarwala V, Scott DA, Zhang F. Genome engineering using the CRISPR-Cas9 system. *Nat Protoc* 2013;**8**:2281–308. https://doi.org/10.1038/nprot.2013.143.

15 Cong L, Ran FA, Cox D, Lin S, Barretto R, Habib N, *et al.* Multiplex genome engineering using CRISPR/Cas systems. *Science* 2013;**339**:819–23. https://doi.org/10.1126/science.1231143.

16 Horvath P, Barrangou R. CRISPR/Cas, the immune system of Bacteria and Archaea. *Science* 2010:167–70. https://doi.org/10.1126/science.1179555.

17 Klann TS, Black JB, Chellappan M, Safi A, Song L, Hilton IB, *et al.* CRISPR-Cas9 epigenome editing enables high-throughput screening for functional regulatory elements in the human genome. *Nat Biotechnol* 2017;**35**:561–8. https://doi.org/10.1038/nbt.3853.

18 Zhou Y, Zhu S, Cai C, Yuan P, Li C, Huang Y, *et al.* High-throughput screening of a CRISPR/Cas9 library for functional genomics in human cells. *Nature* 2014;**509**:487–91. https://doi.org/10.1038/nature13166.

19 Shifrut E, Carnevale J, Tobin V, Roth TL, Woo JM, Bui CT, *et al.* Genome-wide

CRISPR Screens in Primary Human T Cells Reveal Key Regulators of Immune Function. *Cell* 2018;**175**:1958–1971.e15. https://doi.org/10.1016/j.cell.2018.10.024.

20 Wang T, Wei JJ, Sabatini DM, Lander ES. Genetic screens in human cells using the CRISPR-Cas9 system. *Science* 2014;**343**:80–4. https://doi.org/10.1126/science.1246981.

21 Koike-Yusa H, Li Y, Tan EP, Velasco-Herrera MDC, Yusa K. Genome-wide recessive genetic screening in mammalian cells with a lentiviral CRISPR-guide RNA library. *Nat Biotechnol* 2014;**32**:267–73. https://doi.org/10.1038/nbt.2800.

22 Shalem O, Sanjana NE, Zhang F. High-throughput functional genomics using CRISPR-Cas9. *Nat Rev Genet* 2015:299–311. https://doi.org/10.1038/nrg3899.

23 Bumpus TW, Liang D, Baskin JM. IMPACT: Imaging phospholipase D activity with clickable alcohols via transphosphatidylation. *Methods Enzymol* 2020:75–94. https://doi.org/10.1016/bs.mie.2020.04.037.

24 Inoue A, Raimondi F, Kadji FMN, Singh G, Kishi T, Uwamizu A, *et al.* Illuminating G-Protein-Coupling Selectivity of GPCRs. *Cell* 2019;**177**:1933–1947.e25. https://doi.org/10.1016/j.cell.2019.04.044.

25 Kotowski SJ, Hopf FW, Seif T, Bonci A, von Zastrow M. Endocytosis Promotes Rapid Dopaminergic Signaling. *Neuron* 2011;**71**:278–90. https://doi.org/10.1016/j.neuron.2011.05.036.

26 Irannejad R, Tomshine JC, Tomshine JR, Chevalier M, Mahoney JP, Steyaert J, *et al.* Conformational biosensors reveal GPCR signalling from endosomes. *Nature* 2013;**495**:534–8. https://doi.org/10.1038/nature12000.

27 Merriam LA, Baran CN, Girard BM, Hardwick JC, May V, Parsons RL. Pituitary adenylate cyclase 1 receptor internalization and endosomal signaling mediate the pituitary adenylate cyclase activating polypeptide-induced increase in guinea pig cardiac neuron excitability. *J Neurosci* 2013;**33**:4614–22. https://doi.org/10.1523/JNEUROSCI.4999-12.2013.

28 Saheki Y, Bian X, Schauder CM, Sawaki Y, Surma MA, Klose C, *et al.* Control of plasma membrane lipid homeostasis by the extended synaptotagmins. *Nat Cell Biol* 2016;**18**:504–15. https://doi.org/10.1038/ncb3339.

29 Wang C, Lu T, Emanuel G, Babcock HP, Zhuang X. Imaging-based pooled CRISPR screening reveals regulators of lncRNA localization. *Proc Natl Acad Sci U S A* 2019;**166**:10842–51. https://doi.org/10.1073/pnas.1903808116.

30 Neumann B, Held M, Liebel U, Erfle H, Rogers P, Pepperkok R, *et al.* High-throughput RNAi screening by time-lapse imaging of live human cells. *Nat Methods* 2006;**3**:385–90. https://doi.org/10.1038/nmeth876.

31 Neumann B, Walter T, Hériché JK, Bulkescher J, Erfle H, Conrad C, *et al.* Phenotypic profiling of the human genome by time-lapse microscopy reveals cell division genes. *Nature* 2010;**464**:721–7. https://doi.org/10.1038/nature08869.

32 Tei R, Baskin JM. Spatiotemporal control of phosphatidic acid signaling with optogenetic, engineered phospholipase Ds. *J Cell Biol* 2020;**219**:. https://doi.org/10.1083/jcb.201907013.

APPENDIX:

^{1}H and ^{13}C NMR Spectra for CHAPTER 2

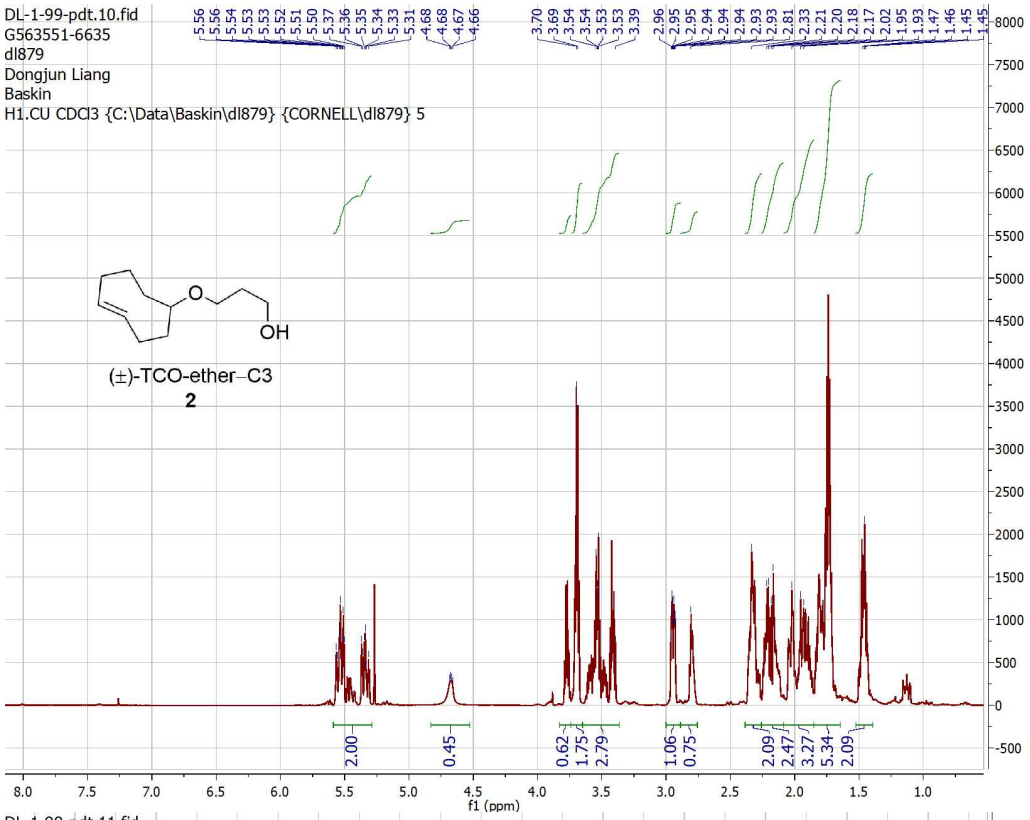
DL-1-99-pdt.10.fid
G563551-6635
dl879
Dongjun Liang
Baskin
H1.CU CDCl3 {C:\Data\Baskin\dl879} {CORNELL\dl879} 5
O
OH
(±)-TCO-ether–C3
2
f1 (ppm)

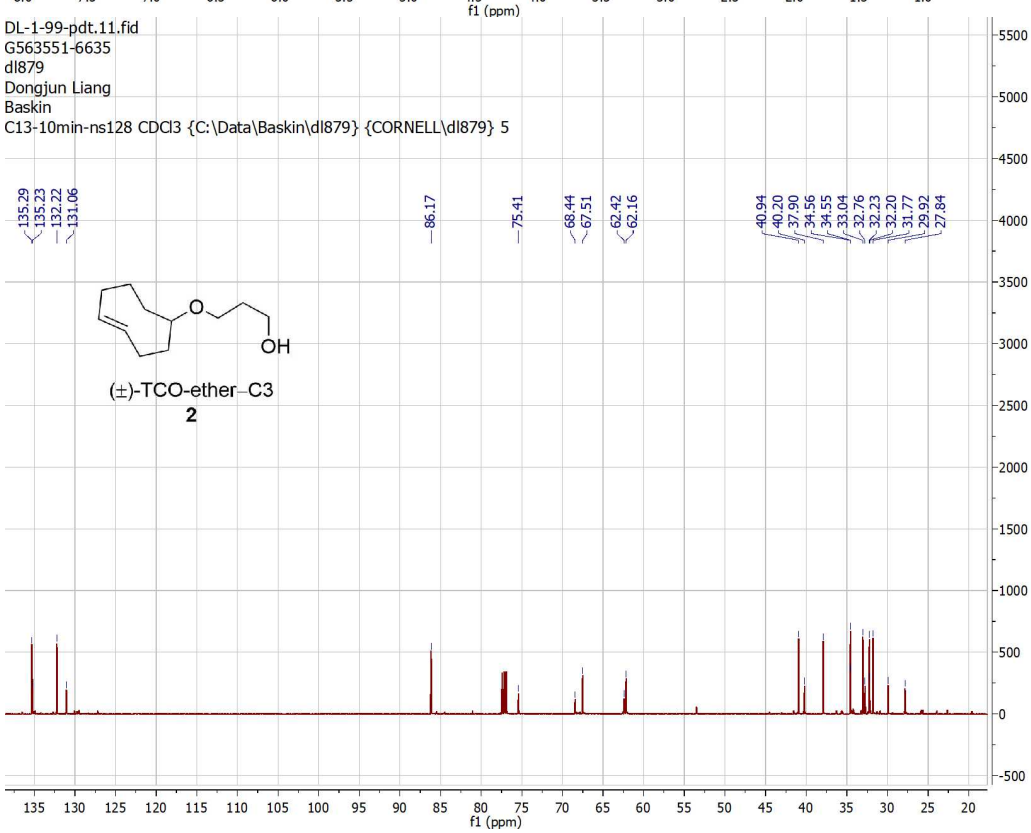
DL-1-99-pdt.11.fid
G563551-6635
dl879
Dongjun Liang
Baskin
C13-10min-ns128 CDCl3 {C:\Data\Baskin\dl879} {CORNELL\dl879} 5
O
OH
(±)-TCO-ether–C3
2
f1 (ppm)

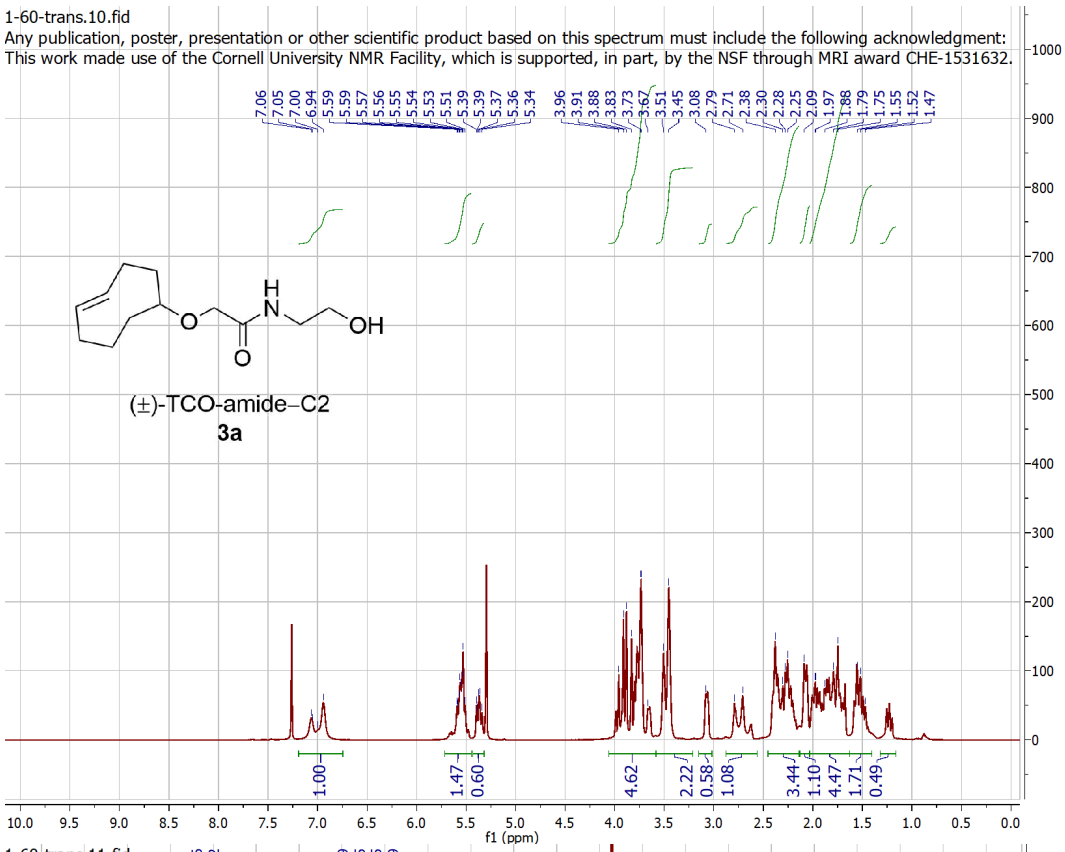
1-60-trans.10.fid
Any publication, poster, presentation or other scientific product based on this spectrum must include the following acknowledgment:
This work made use of the Cornell University NMR Facility, which is supported, in part, by the NSF through MRI award CHE-1531632.
(±)-TCO-amide–C2
3a
f1 (ppm)

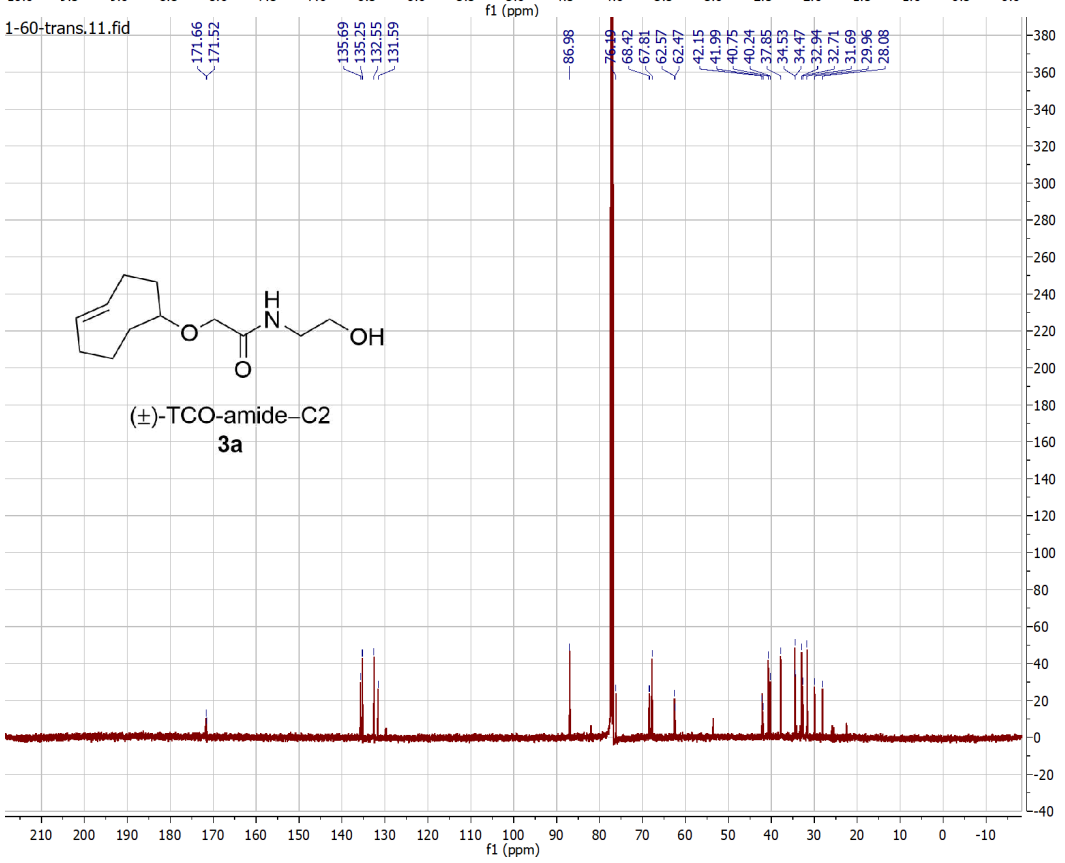
1-60-trans.11.fid
(±)-TCO-amide–C2
3a
f1 (ppm)

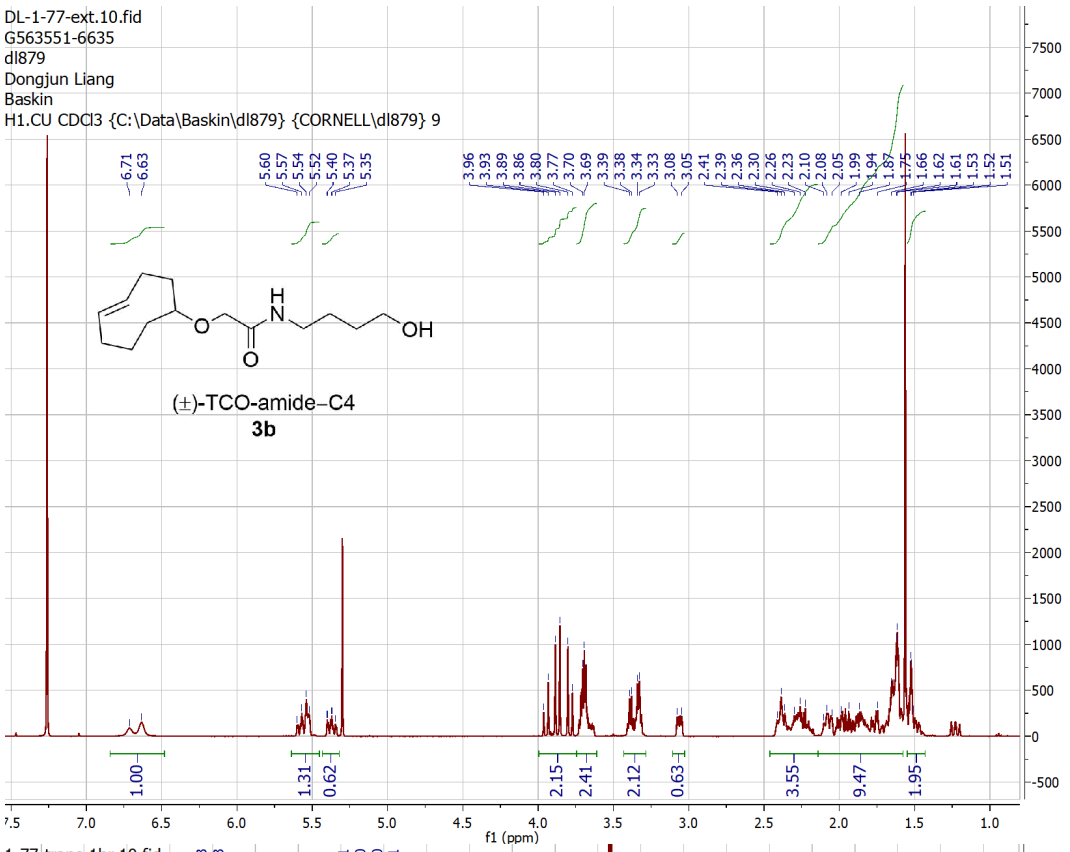
DL-1-77-ext.10.fid
G563551-6635
dl879
Dongjun Liang
Baskin
H1.CU CDCl3 {C:\Data\Baskin\dl879} {CORNELL\dl879} 9
6.71
6.63
5.60
5.57
5.54
5.52
5.40
5.37
5.35
3.96
3.93
3.89
3.86
3.80
3.77
3.70
3.69
3.39
3.38
3.34
3.33
3.08
3.05
2.41
2.39
2.36
2.30
2.26
2.23
2.10
2.08
2.05
1.99
1.94
1.87
1.75
1.66
1.62
1.61
1.53
1.52
1.51
H
N
O
O
OH
(±)-TCO-amide–C4
3b
1.00
1.31
0.62
2.15
2.41
2.12
0.63
3.55
9.47
1.95
f1 (ppm)

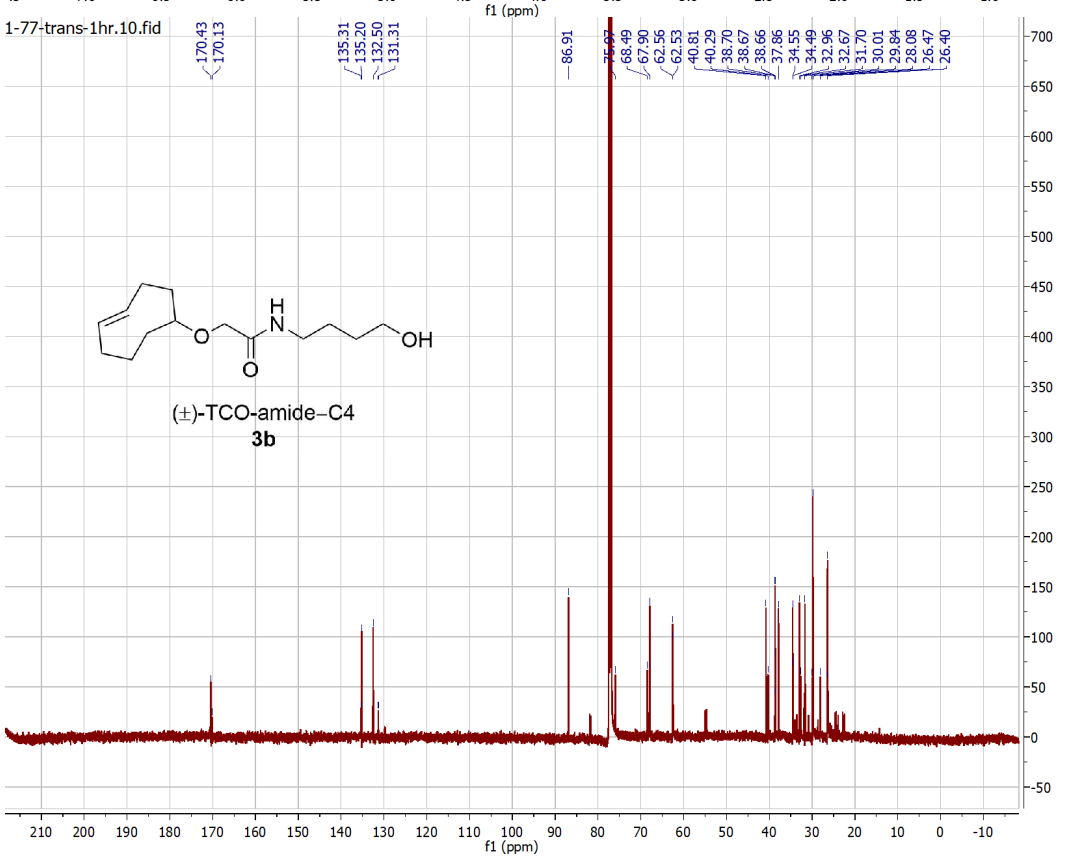
1-77-trans-1hr.10.fid
170.43
170.13
135.31
135.20
132.50
131.31
86.91
75.97
68.49
67.90
62.56
62.53
40.81
40.29
38.70
38.67
38.66
37.86
34.55
34.49
32.96
32.67
31.70
30.01
29.84
28.08
26.47
26.40
H
N
O
O
OH
(±)-TCO-amide–C4
3b
f1 (ppm)

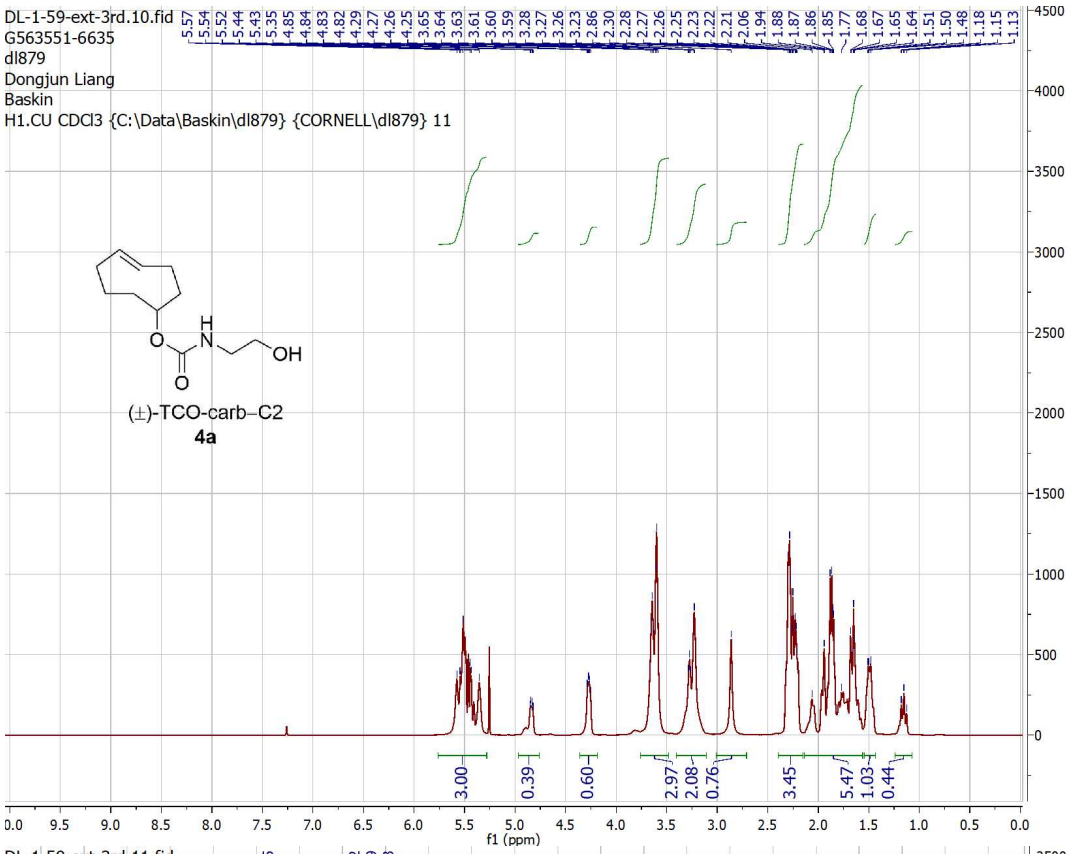
DL-1-59-ext-3rd.10.fid
G563551-6635
dl879
Dongjun Liang
Baskin
H1.CU CDCl3 {C:\Data\Baskin\dl879} {CORNELL\dl879} 11
(±)-TCO-carb–C2
4a
f1 (ppm)

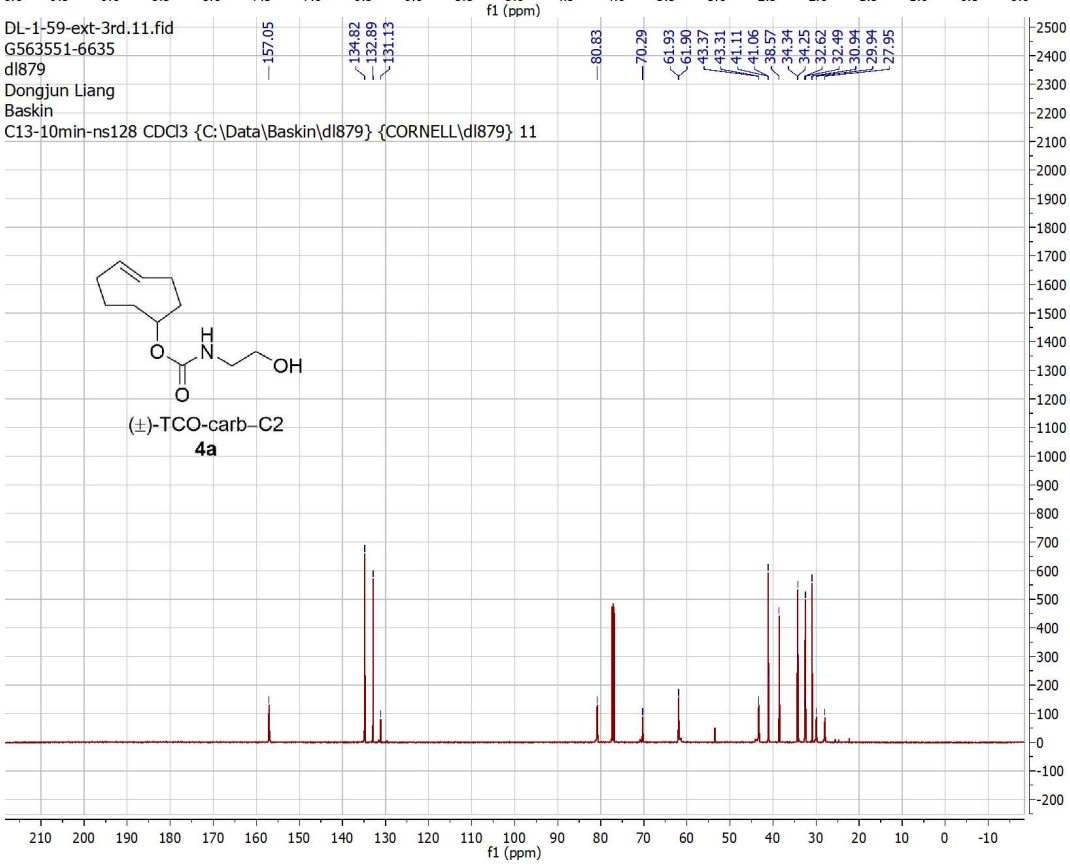
DL-1-59-ext-3rd.11.fid
G563551-6635
dl879
Dongjun Liang
Baskin
C13-10min-ns128 CDCl3 {C:\Data\Baskin\dl879} {CORNELL\dl879} 11
(±)-TCO-carb–C2
4a
f1 (ppm)

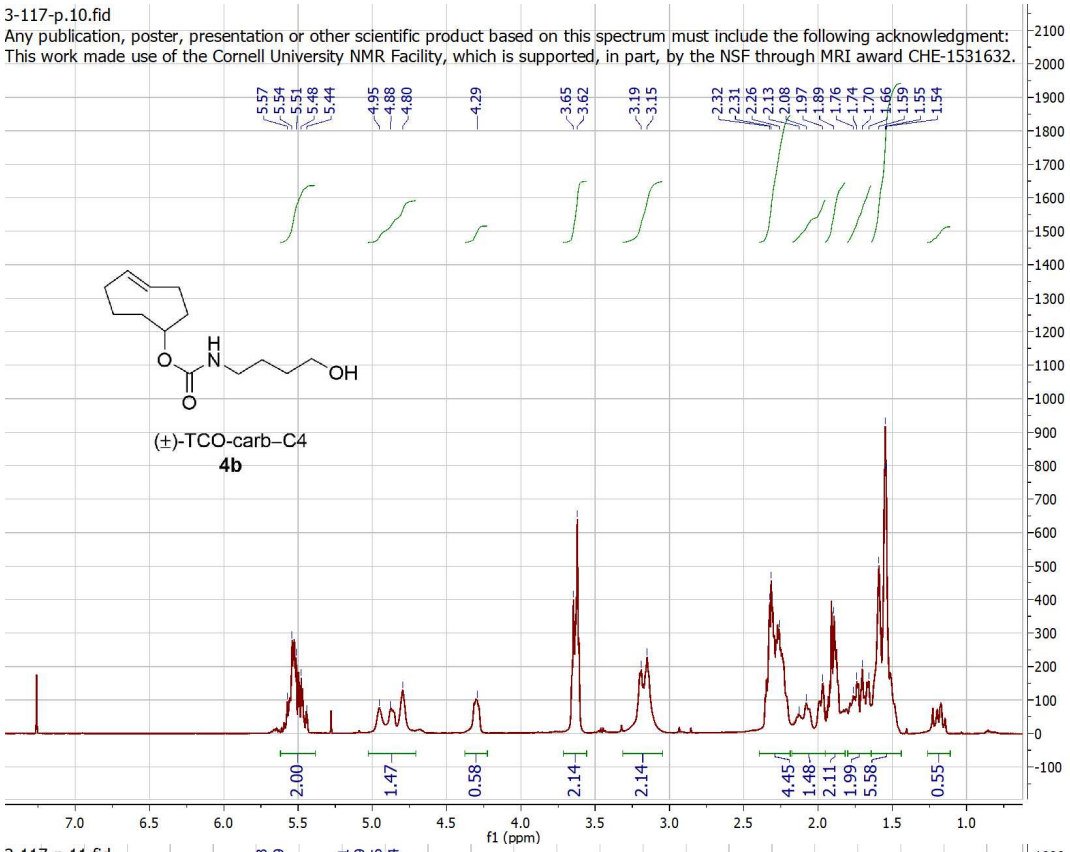
3-117-p.10.fid
Any publication, poster, presentation or other scientific product based on this spectrum must include the following acknowledgment:
This work made use of the Cornell University NMR Facility, which is supported, in part, by the NSF through MRI award CHE-1531632.
5.57
5.54
5.51
5.48
5.44
4.95
4.88
4.80
4.29
3.65
3.62
3.19
3.15
2.32
2.31
2.26
2.13
2.08
1.97
1.89
1.76
1.74
1.70
1.66
1.59
1.55
1.54
H
N
O
O
O
OH
(±)-TCO-carb–C4
4b
2.00
1.47
0.58
2.14
2.14
4.45
1.48
2.11
1.99
5.58
0.55
f1 (ppm)

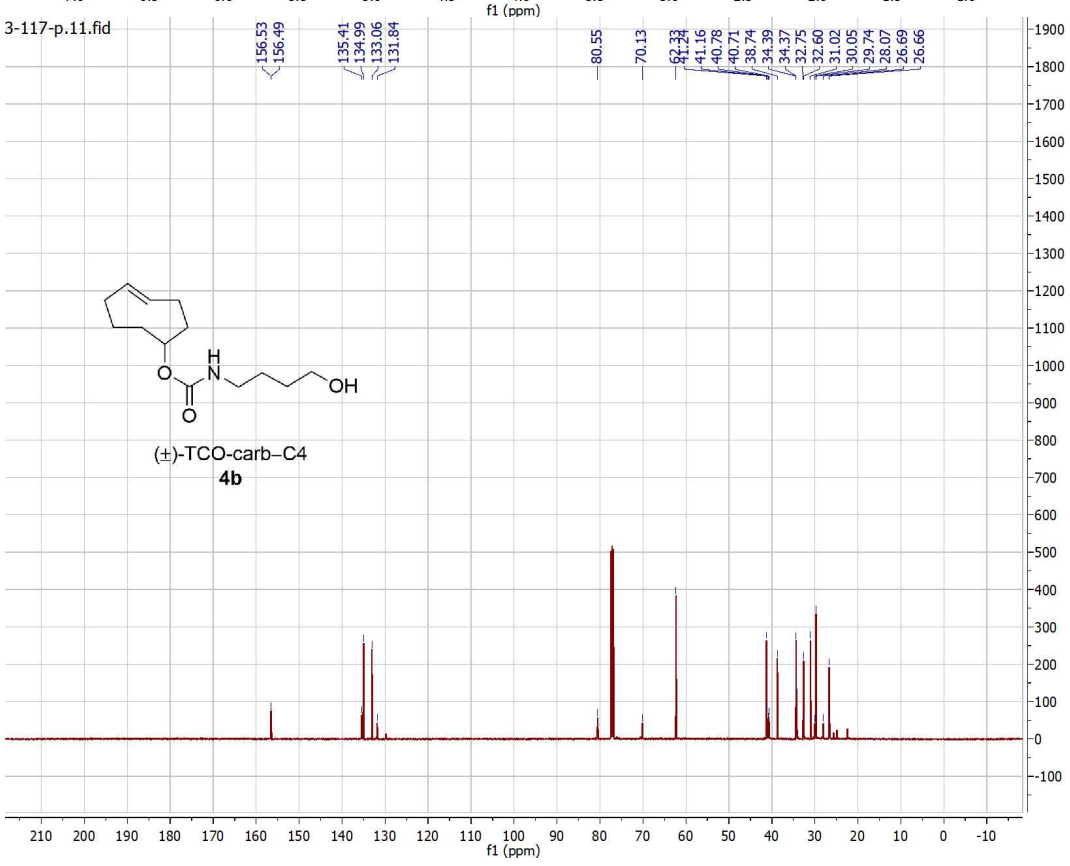
3-117-p.11.fid
156.53
156.49
135.41
134.99
133.06
131.84
80.55
70.13
62.33
41.24
41.16
40.78
40.71
38.74
34.39
34.37
32.75
32.60
31.02
30.05
29.74
28.07
26.69
26.66
H
N
O
O
O
OH
(±)-TCO-carb–C4
4b
f1 (ppm)

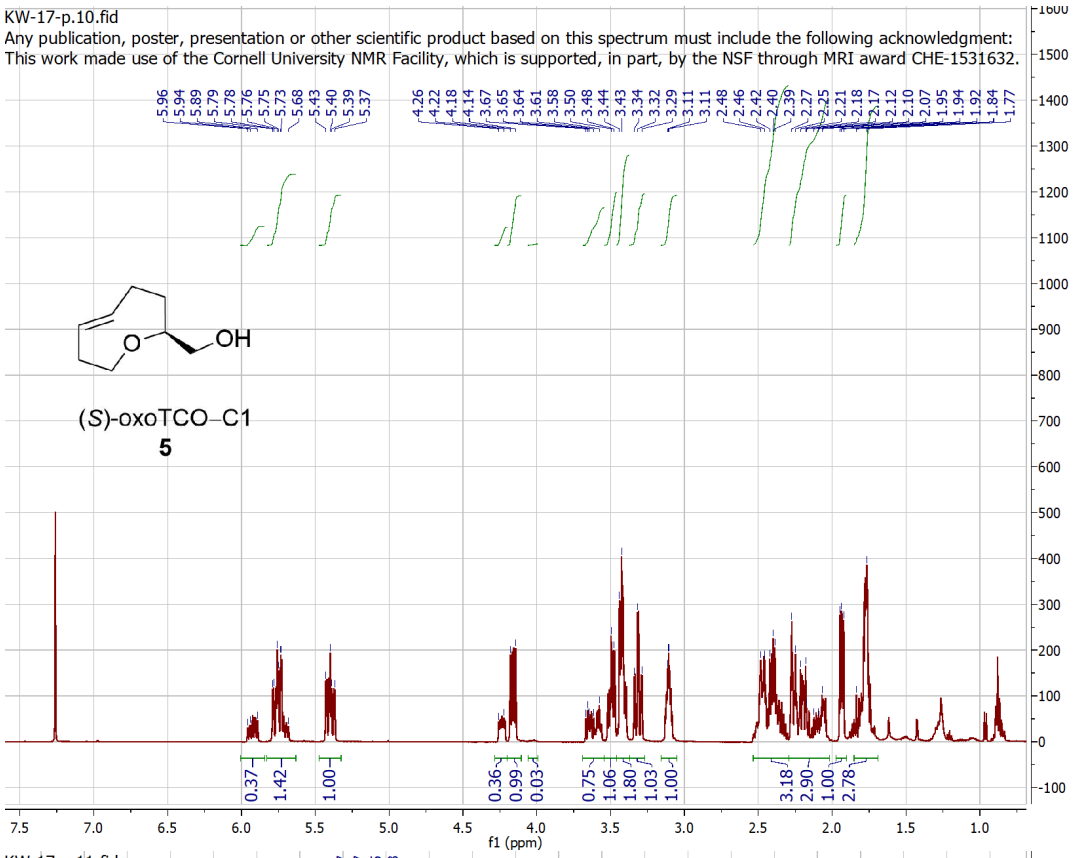
KW-17-p.10.fid
Any publication, poster, presentation or other scientific product based on this spectrum must include the following acknowledgment:
This work made use of the Cornell University NMR Facility, which is supported, in part, by the NSF through MRI award CHE-1531632.
OH
(S)-oxoTCO–C1
5
f1 (ppm)

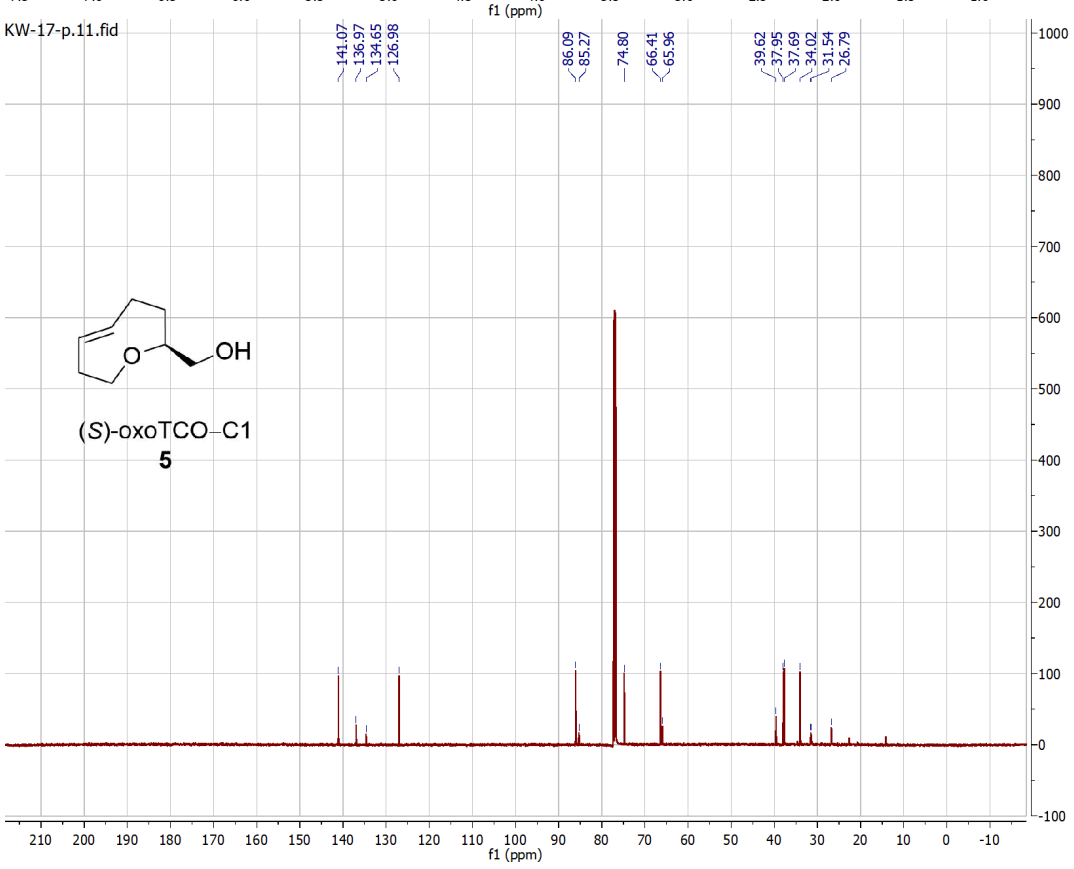
KW-17-p.11.fid
OH
(S)-oxoTCO–C1
5
f1 (ppm)

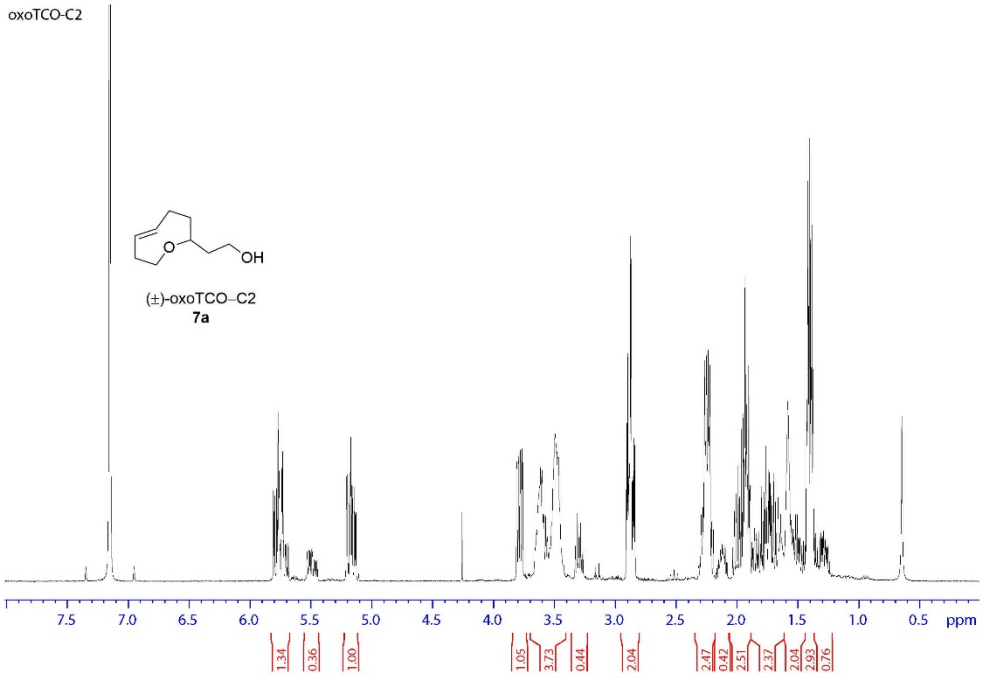
oxoTCO-C2
OH
(±)-oxoTCO-C2
7a
7.5 7.0 6.5 6.0 5.5 5.0 4.5 4.0 3.5 3.0 2.5 2.0 1.5 1.0 0.5 ppm
1.34 0.36 1.00 1.05 3.73 0.44 2.04 2.47 0.42 2.51 2.37 2.04 2.93 0.76

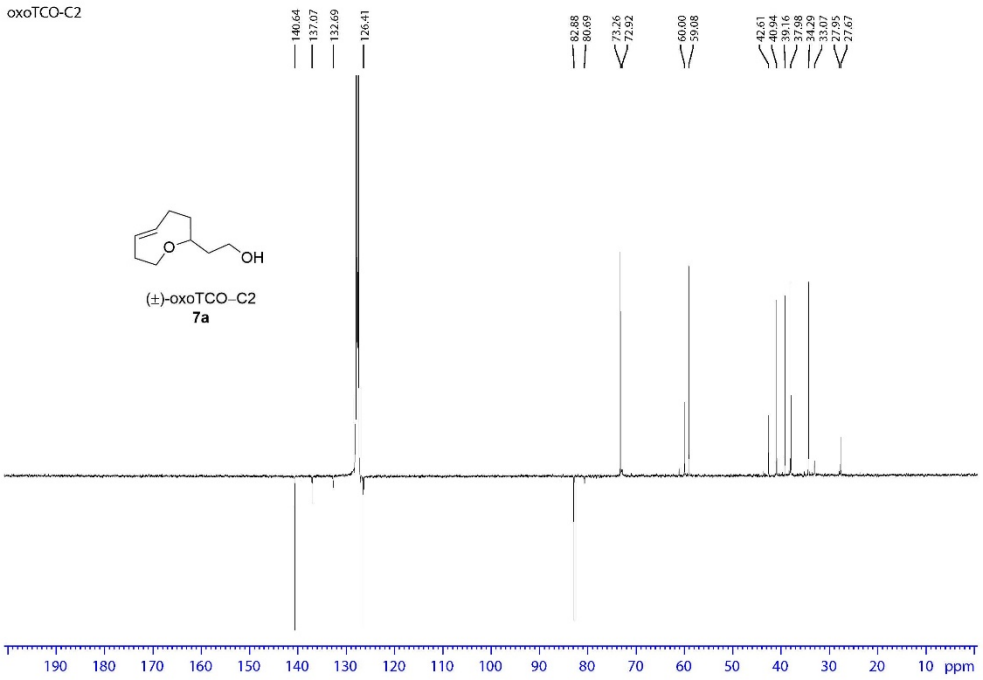
oxoTCO-C2
140.64
137.07
132.69
126.41
82.88
80.69
73.26
72.92
60.00
59.08
42.61
40.94
39.16
37.98
34.29
33.07
27.95
27.67
OH
(±)-oxoTCO-C2
7a
190 180 170 160 150 140 130 120 110 100 90 80 70 60 50 40 30 20 10 ppm

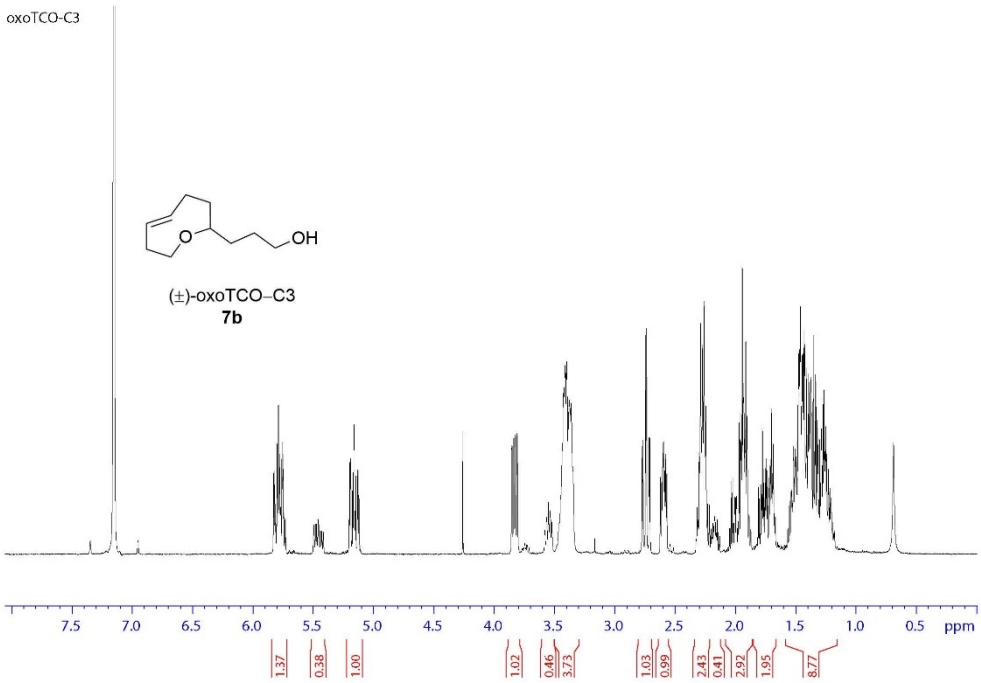
oxoTCO-C3
OH
(±)-oxoTCO–C3
7b
7.5 7.0 6.5 6.0 5.5 5.0 4.5 4.0 3.5 3.0 2.5 2.0 1.5 1.0 0.5 ppm
1.37 0.38 1.00 1.02 0.46 3.73 1.03 0.99 2.43 0.41 2.92 1.95 8.77

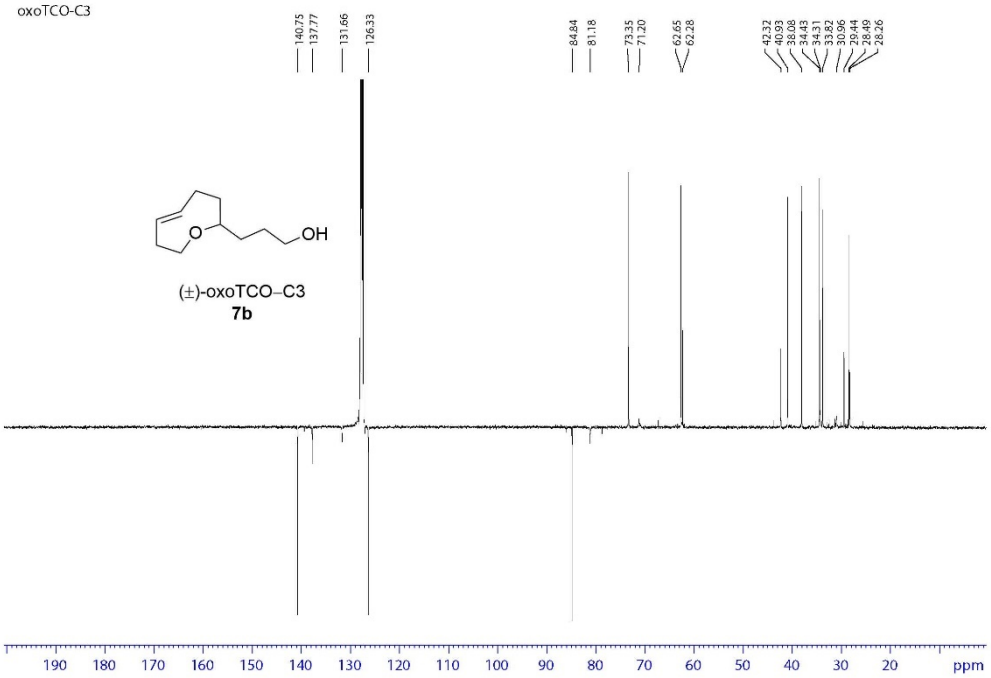
oxoTCO-C3
140.75
137.77
131.66
126.33
84.84
81.18
73.35
71.20
62.65
62.28
42.32
40.93
38.08
34.43
34.31
33.32
30.96
29.44
28.49
28.26
OH
(±)-oxoTCO–C3
7b
190 180 170 160 150 140 130 120 110 100 90 80 70 60 50 40 30 20 ppm

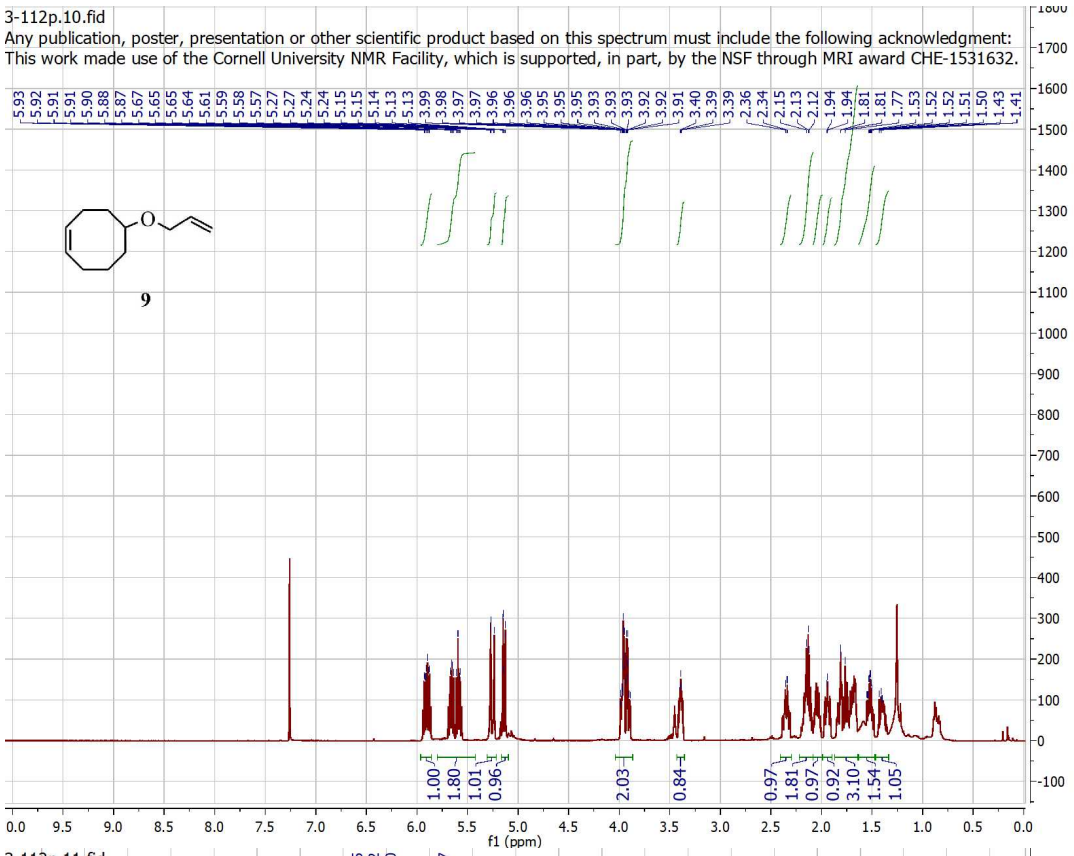
3-112p.10.fid
Any publication, poster, presentation or other scientific product based on this spectrum must include the following acknowledgment:
This work made use of the Cornell University NMR Facility, which is supported, in part, by the NSF through MRI award CHE-1531632.
9
f1 (ppm)

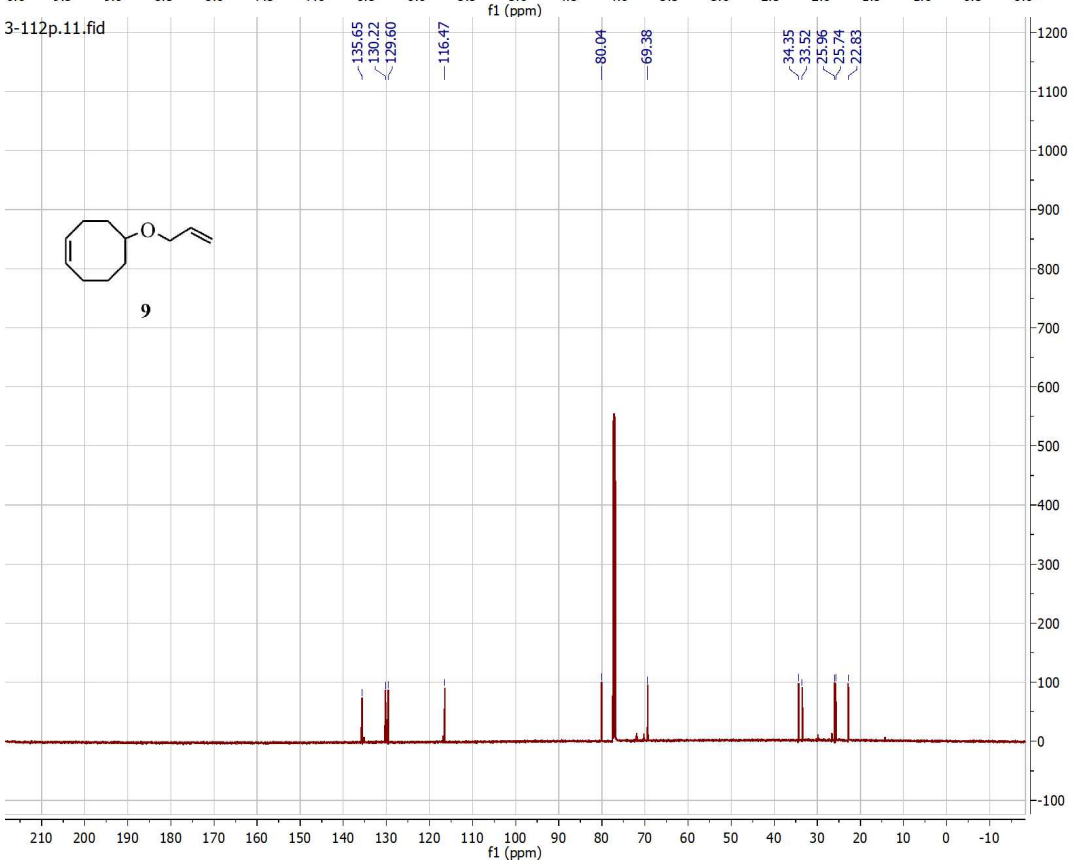
3-112p.11.fid
135.65
130.22
129.60
116.47
80.04
69.38
34.35
33.52
25.96
25.74
22.83
9
f1 (ppm)

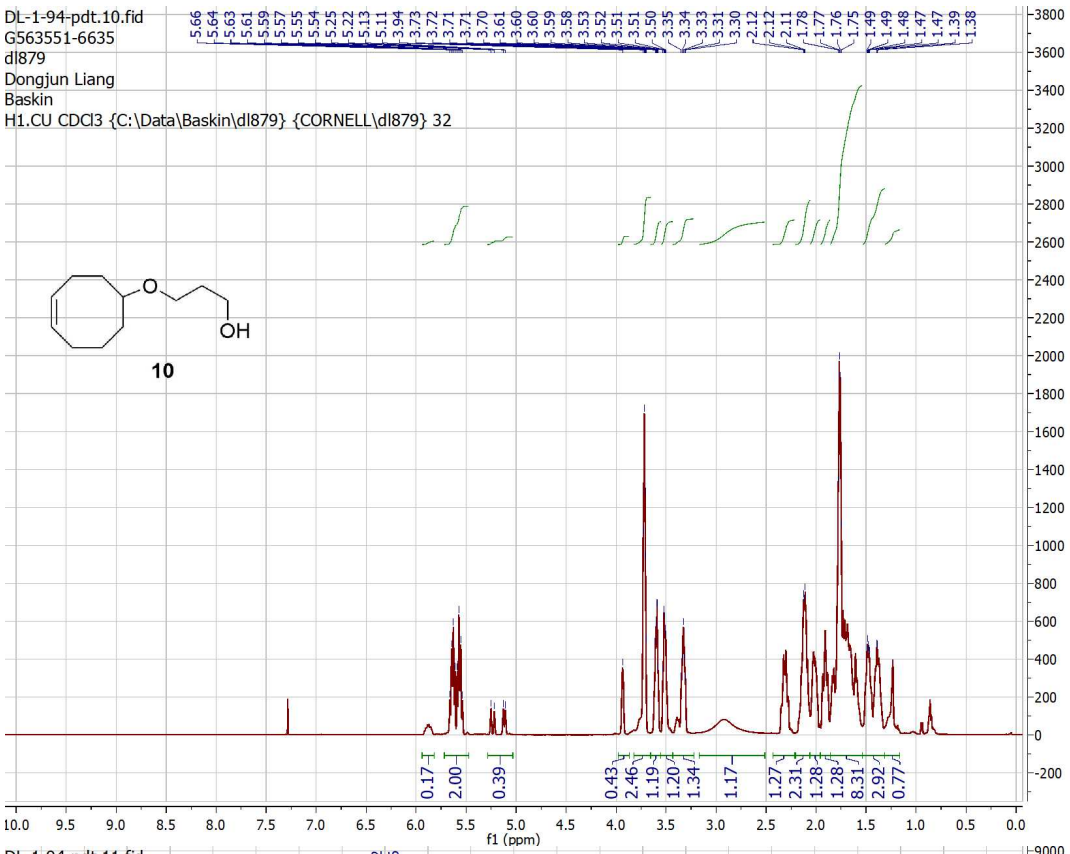
DL-1-94-pdt.10.fid
G563551-6635
dl879
Dongjun Liang
Baskin
H1.CU CDCl3 {C:\Data\Baskin\dl879} {CORNELL\dl879} 32
10
f1 (ppm)

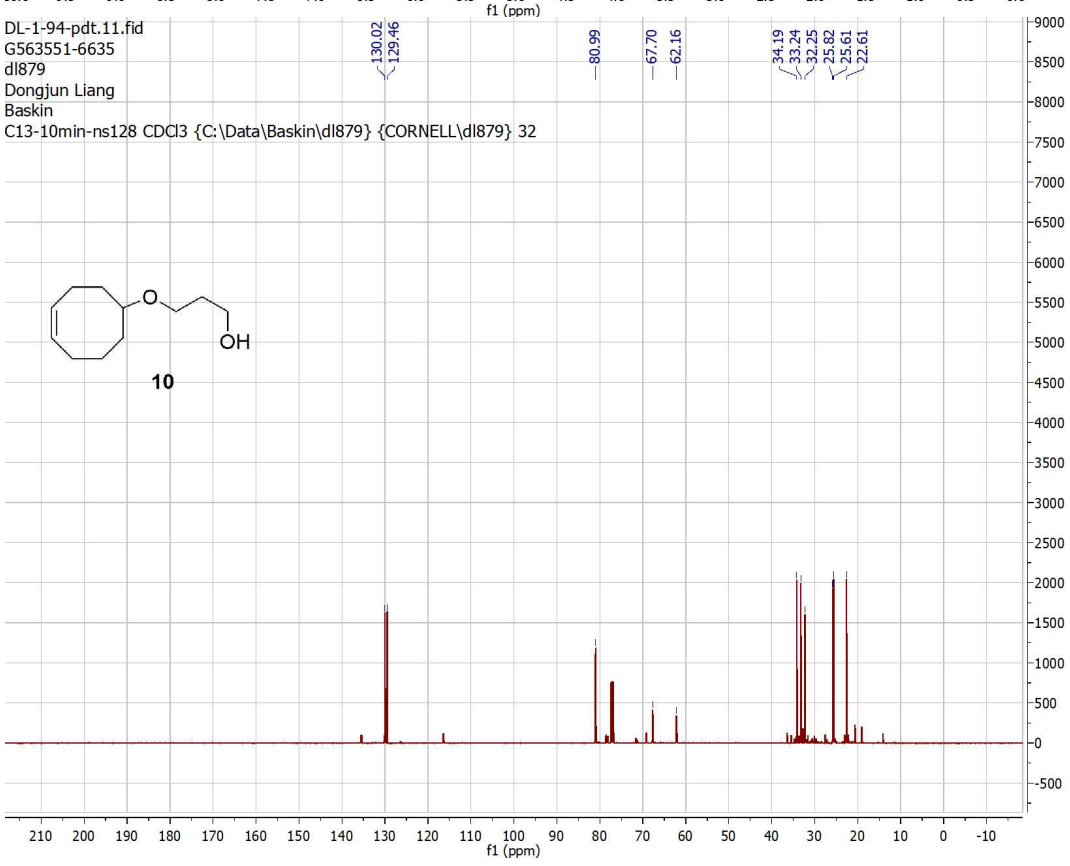
DL-1-94-pdt.11.fid
G563551-6635
dl879
Dongjun Liang
Baskin
C13-10min-ns128 CDCl3 {C:\Data\Baskin\dl879} {CORNELL\dl879} 32
10
f1 (ppm)

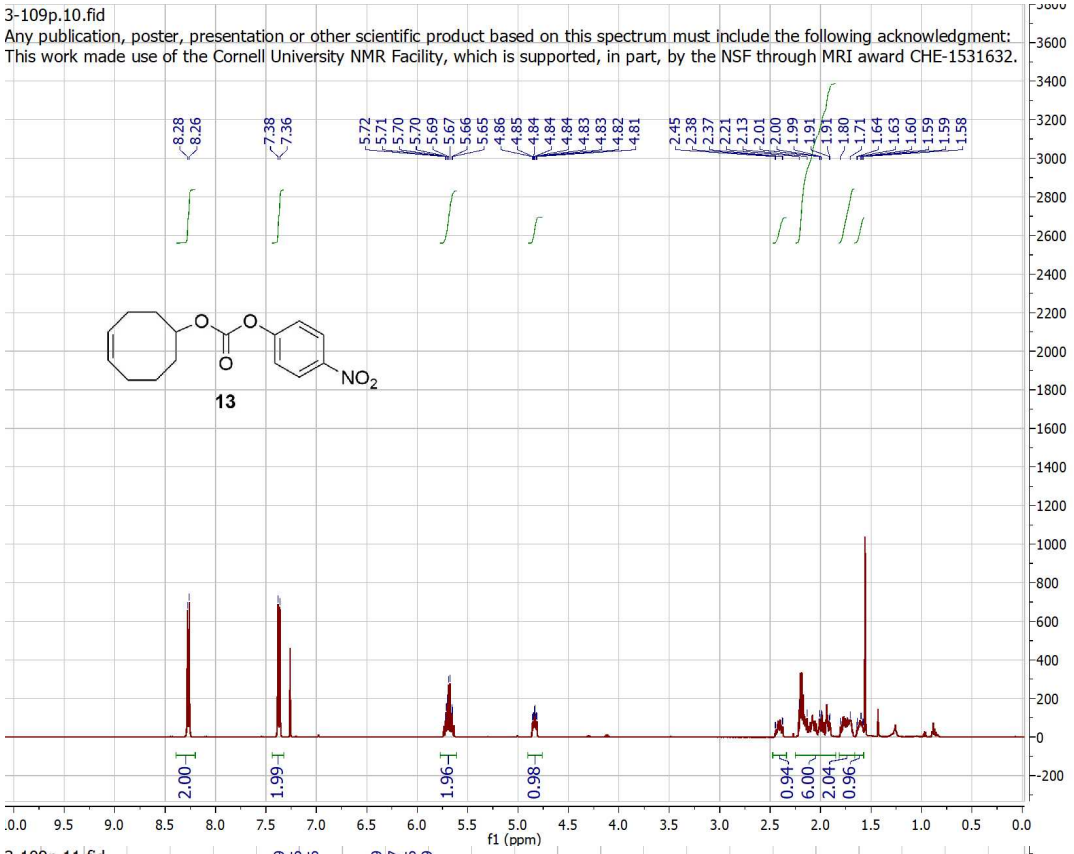
3-109p.10.fid
Any publication, poster, presentation or other scientific product based on this spectrum must include the following acknowledgment:
This work made use of the Cornell University NMR Facility, which is supported, in part, by the NSF through MRI award CHE-1531632.
8.28
8.26
7.38
7.36
5.72
5.71
5.70
5.69
5.67
5.66
5.65
4.86
4.85
4.84
4.84
4.84
4.83
4.83
4.82
4.81
2.45
2.38
2.37
2.21
2.13
2.01
2.00
1.99
1.91
1.91
1.80
1.71
1.64
1.63
1.60
1.59
1.59
1.58
O
O
O
NO2
13
2.00
1.99
1.96
0.98
0.94
6.00
2.04
0.96
f1 (ppm)

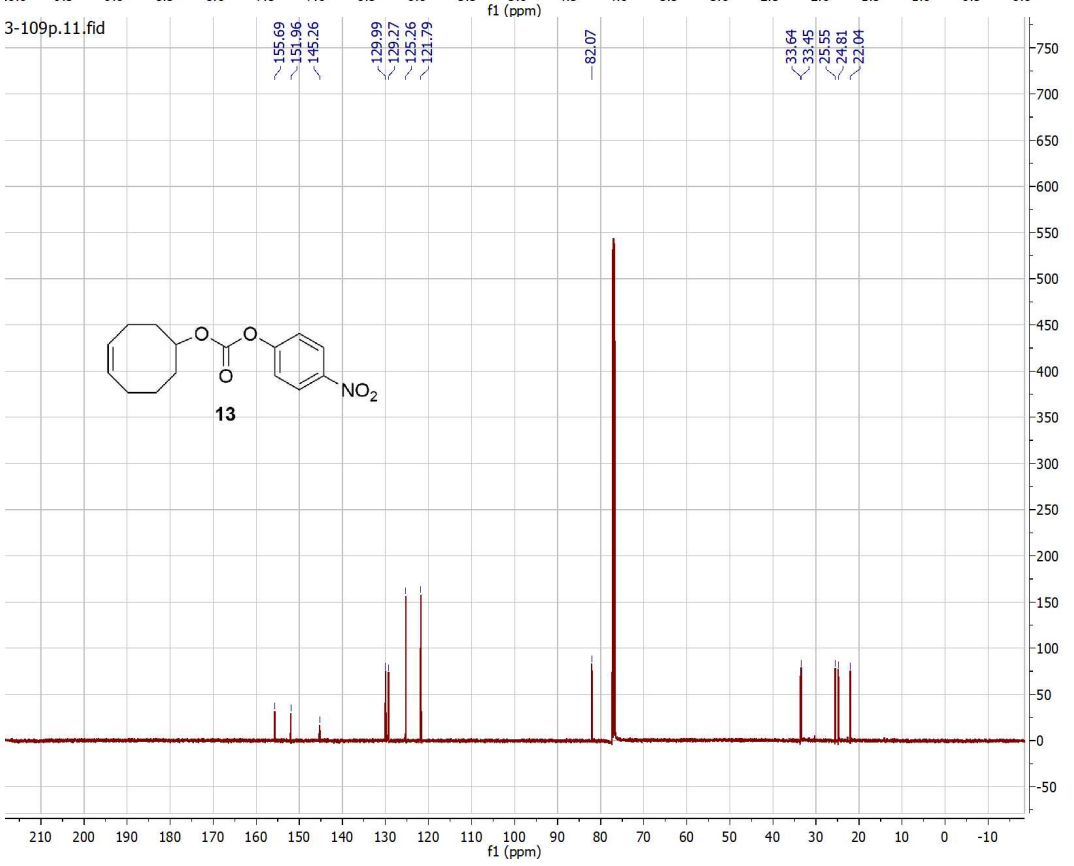
3-109p.11.fid
155.69
151.96
145.26
129.99
129.27
125.26
121.79
82.07
33.64
33.45
25.55
24.81
22.04
O
O
O
NO2
13
f1 (ppm)

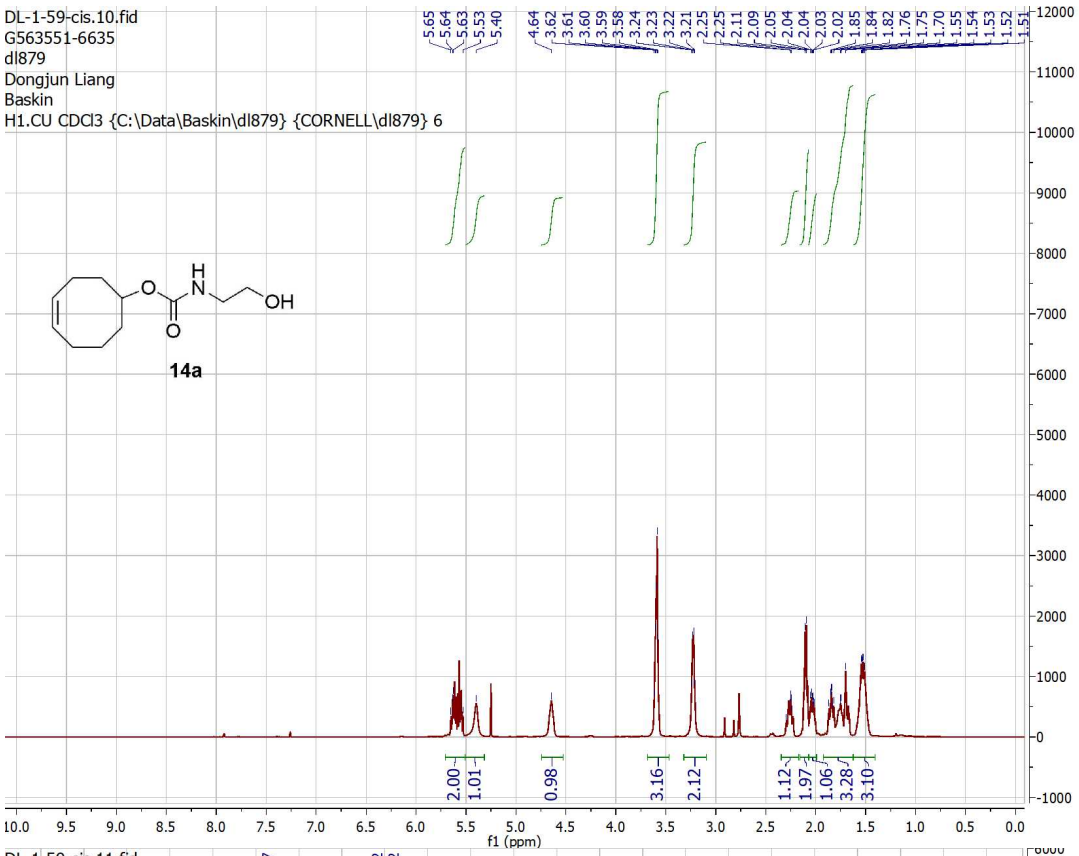
DL-1-59-cis.10.fid
G563551-6635
dl879
Dongjun Liang
Baskin
H1.CU CDCl3 {C:\Data\Baskin\dl879} {CORNELL\dl879} 6
5.65
5.64
5.63
5.53
5.40
4.64
3.62
3.61
3.60
3.59
3.58
3.24
3.23
3.22
3.21
2.25
2.11
2.09
2.05
2.04
2.04
2.03
2.02
1.85
1.84
1.82
1.76
1.75
1.70
1.55
1.54
1.53
1.52
1.51
H
N
O
O
OH
14a
2.00
1.01
0.98
3.16
2.12
1.12
1.97
1.06
3.28
3.10
f1 (ppm)

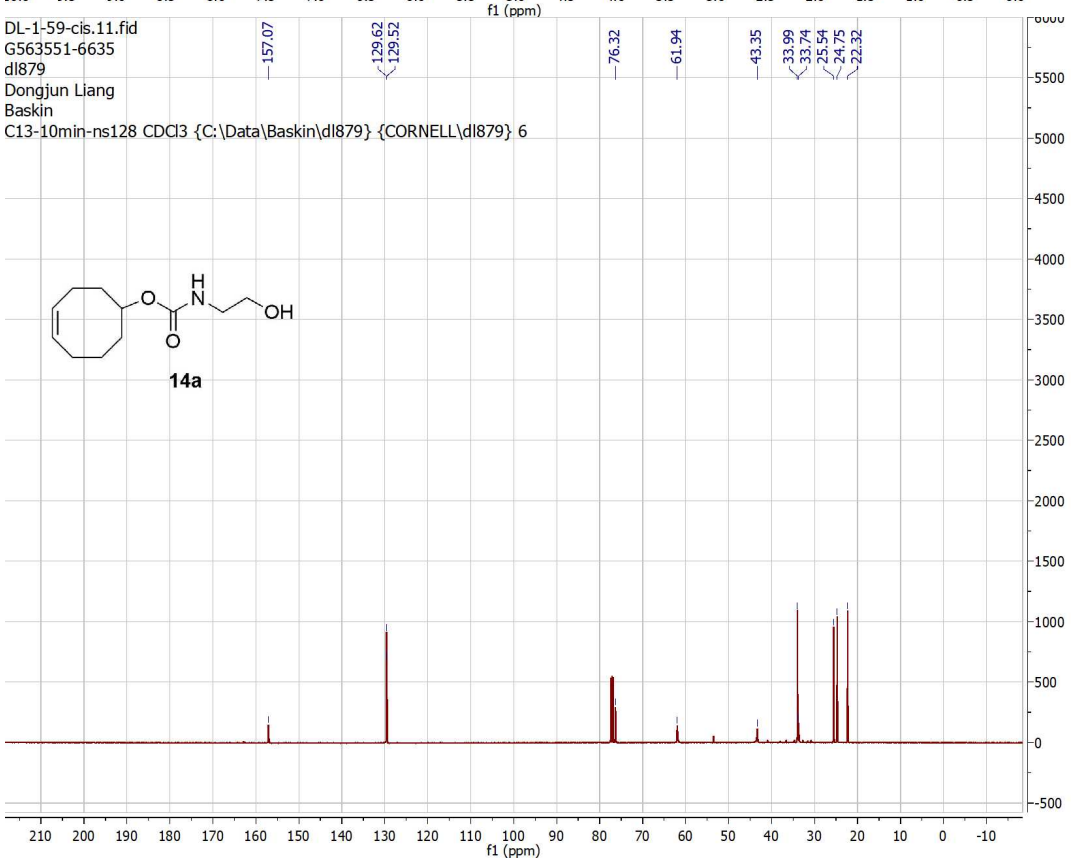
DL-1-59-cis.11.fid
G563551-6635
dl879
Dongjun Liang
Baskin
C13-10min-ns128 CDCl3 {C:\Data\Baskin\dl879} {CORNELL\dl879} 6
157.07
129.62
129.52
76.32
61.94
43.35
33.99
33.74
25.54
24.75
22.32
H
N
O
O
OH
14a
f1 (ppm)

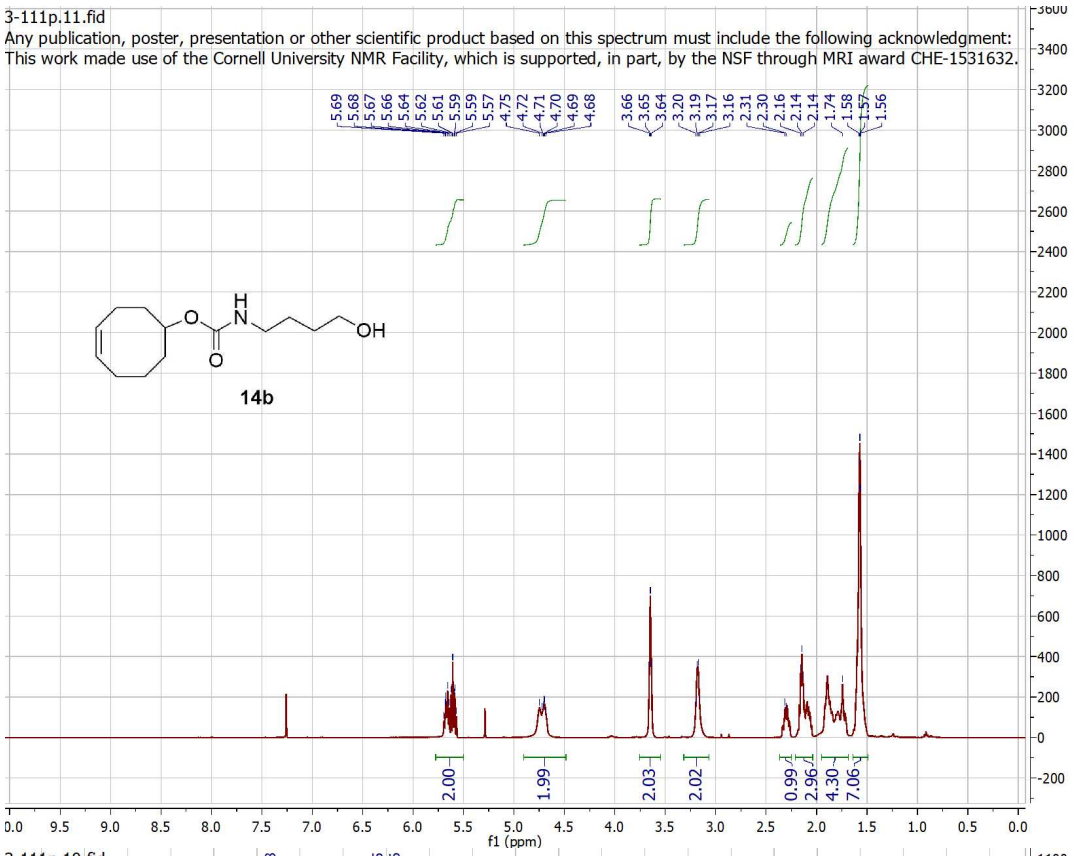
3-111p.11.fid
Any publication, poster, presentation or other scientific product based on this spectrum must include the following acknowledgment:
This work made use of the Cornell University NMR Facility, which is supported, in part, by the NSF through MRI award CHE-1531632.
14b
f1 (ppm)

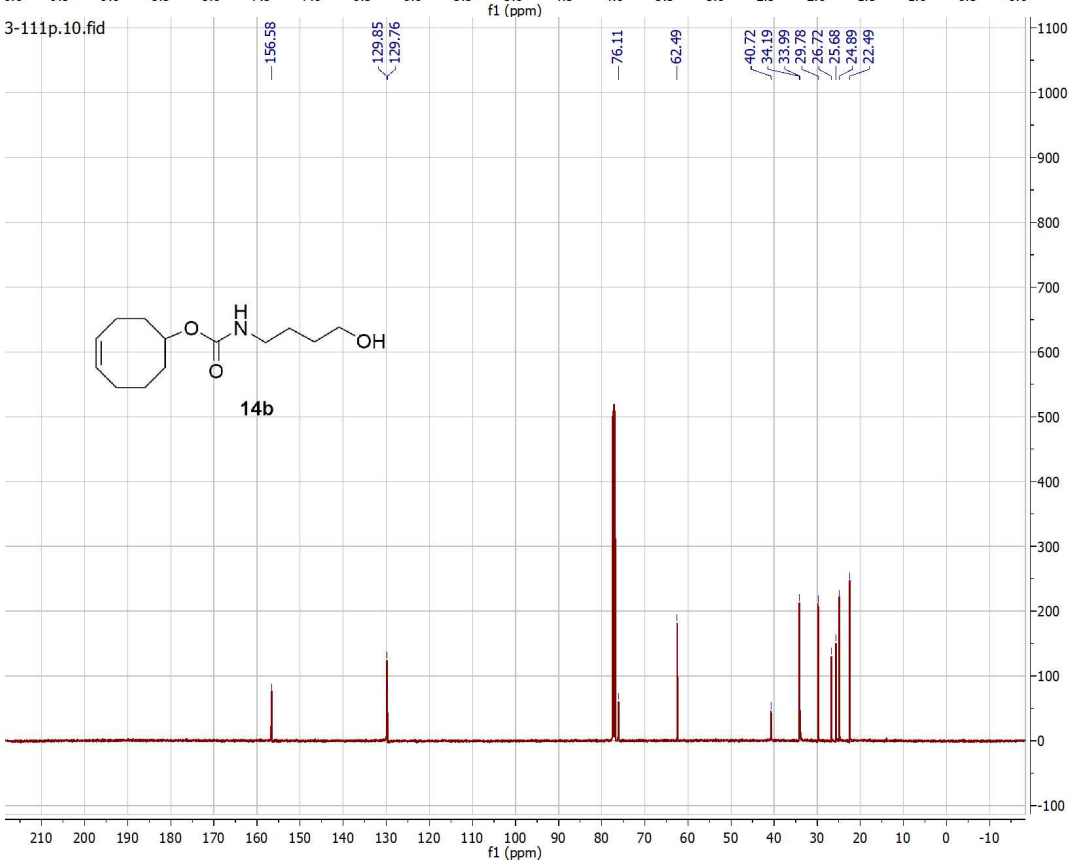
3-111p.10.fid
14b
f1 (ppm)

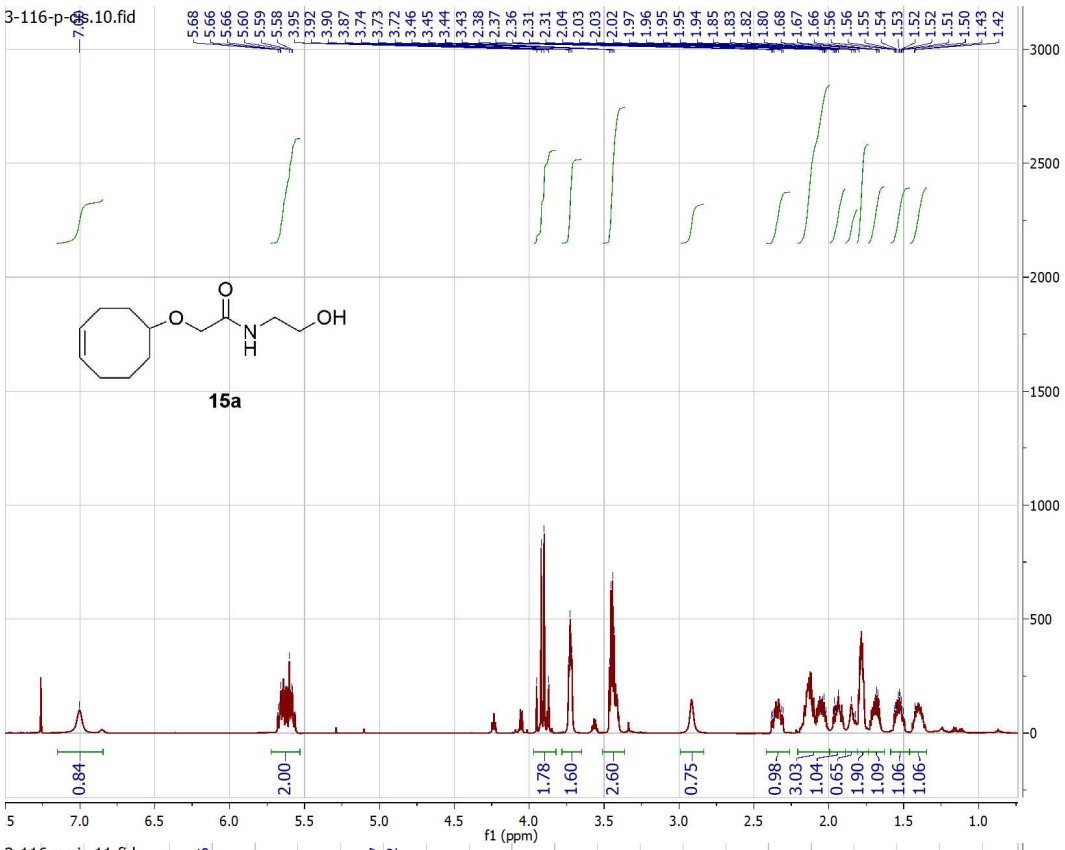
3-116-p-cis.10.fid
O
O
N
H
OH
15a
f1 (ppm)

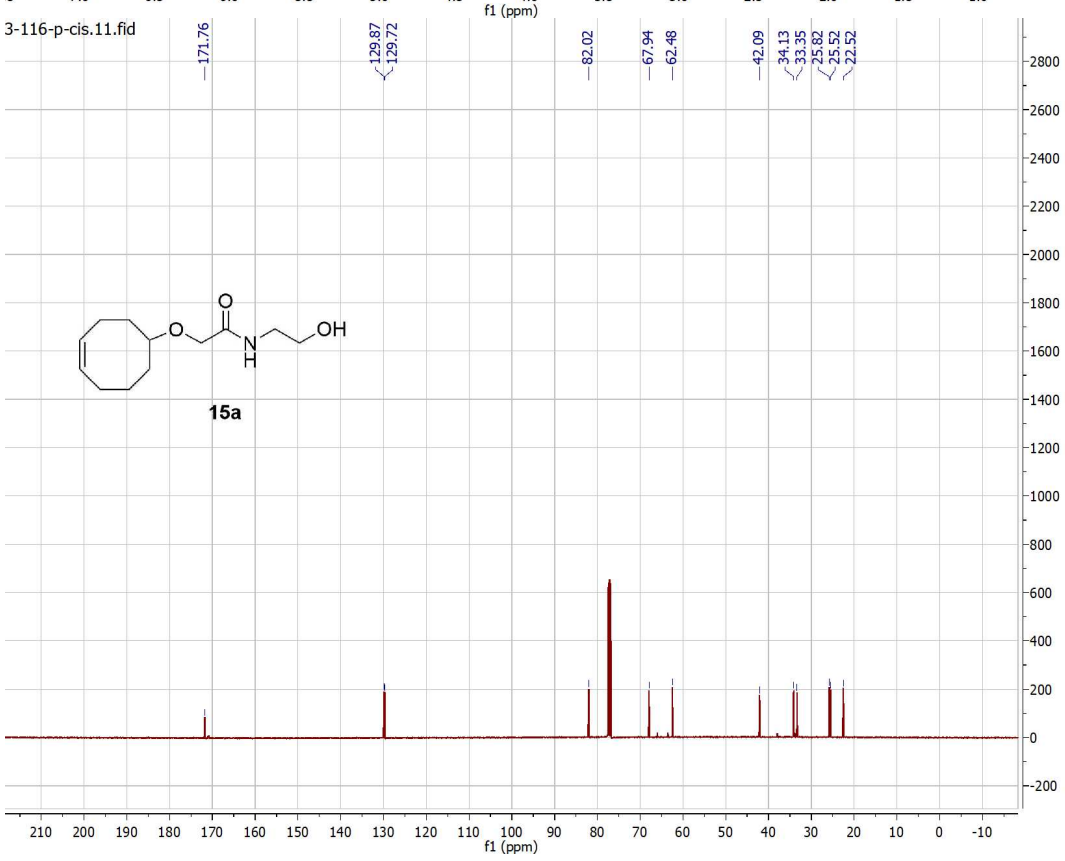
3-116-p-cis.11.fid
O
O
N
H
OH
15a
f1 (ppm)

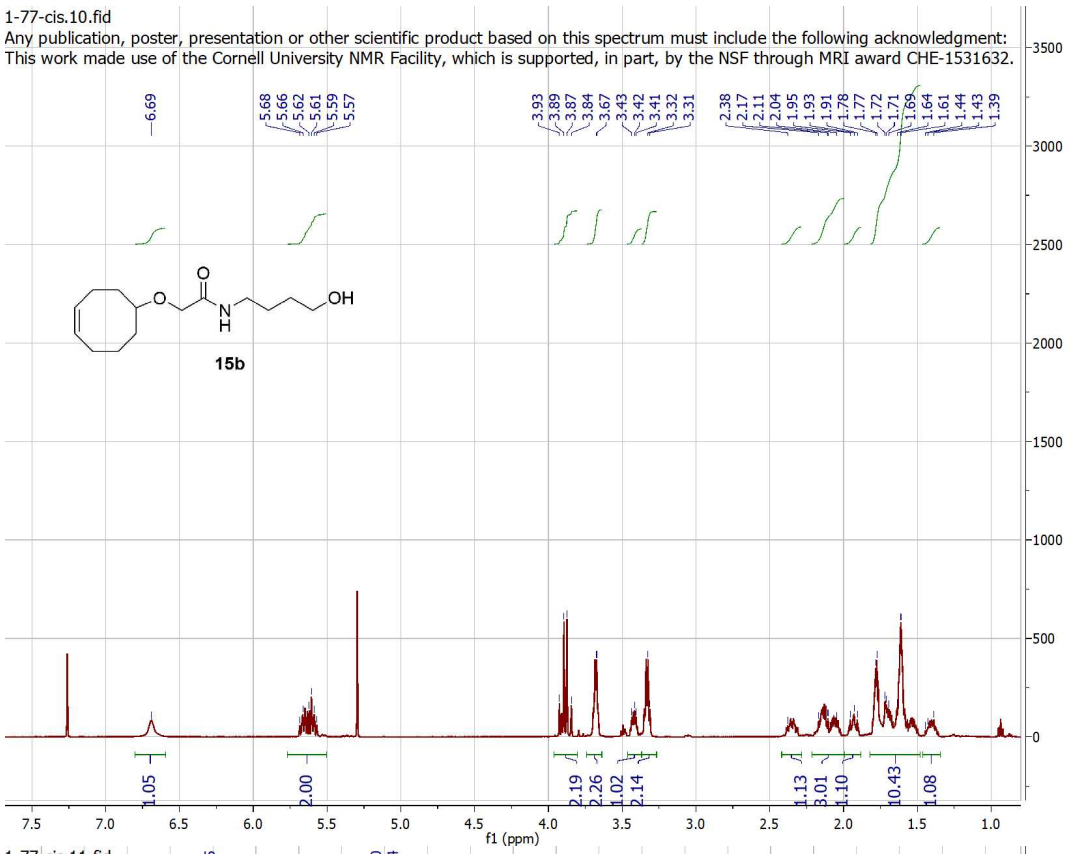
1-77-cis.10.fid
Any publication, poster, presentation or other scientific product based on this spectrum must include the following acknowledgment:
This work made use of the Cornell University NMR Facility, which is supported, in part, by the NSF through MRI award CHE-1531632.
6.69
5.68
5.66
5.62
5.61
5.59
5.57
3.93
3.89
3.87
3.84
3.67
3.43
3.42
3.41
3.32
3.31
2.38
2.17
2.11
2.04
1.95
1.93
1.91
1.78
1.77
1.72
1.71
1.69
1.64
1.61
1.44
1.43
1.39
O
O
N
H
OH
15b
1.05
2.00
2.19
2.26
1.02
2.14
1.13
3.01
1.10
10.43
1.08
f1 (ppm)

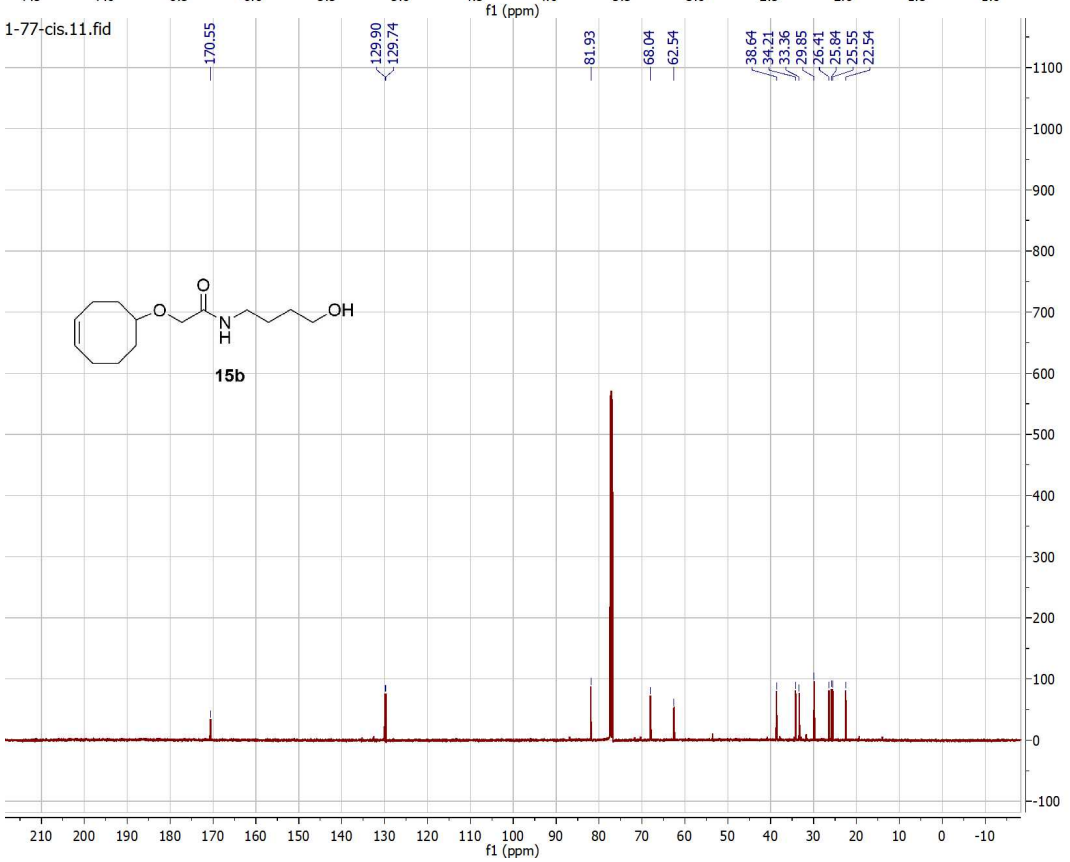
1-77-cis.11.fid
170.55
129.90
129.74
81.93
68.04
62.54
38.64
34.21
33.36
29.85
26.41
25.84
25.55
22.54
O
O
N
H
OH
15b
f1 (ppm)

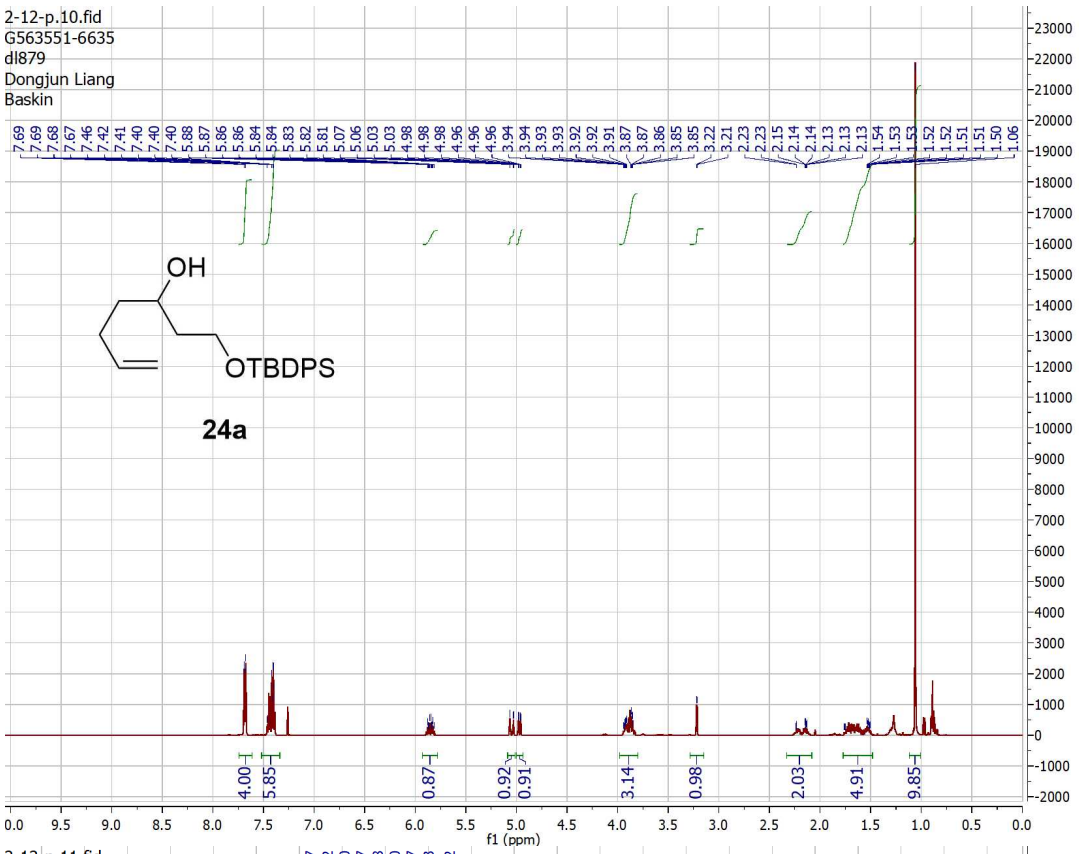
2-12-p.10.fid
G563551-6635
dl879
Dongjun Liang
Baskin
OH
OTBDPS
24a
f1 (ppm)

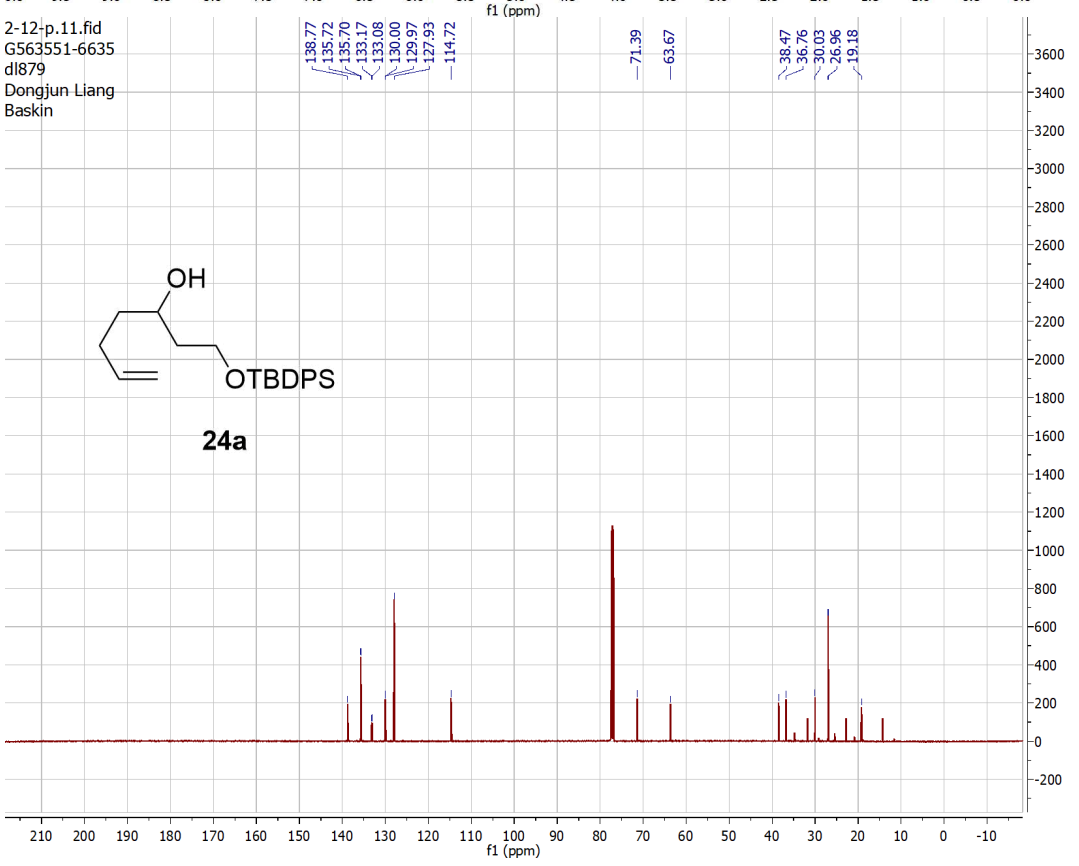
2-12-p.11.fid
G563551-6635
dl879
Dongjun Liang
Baskin
OH
OTBDPS
24a
f1 (ppm)

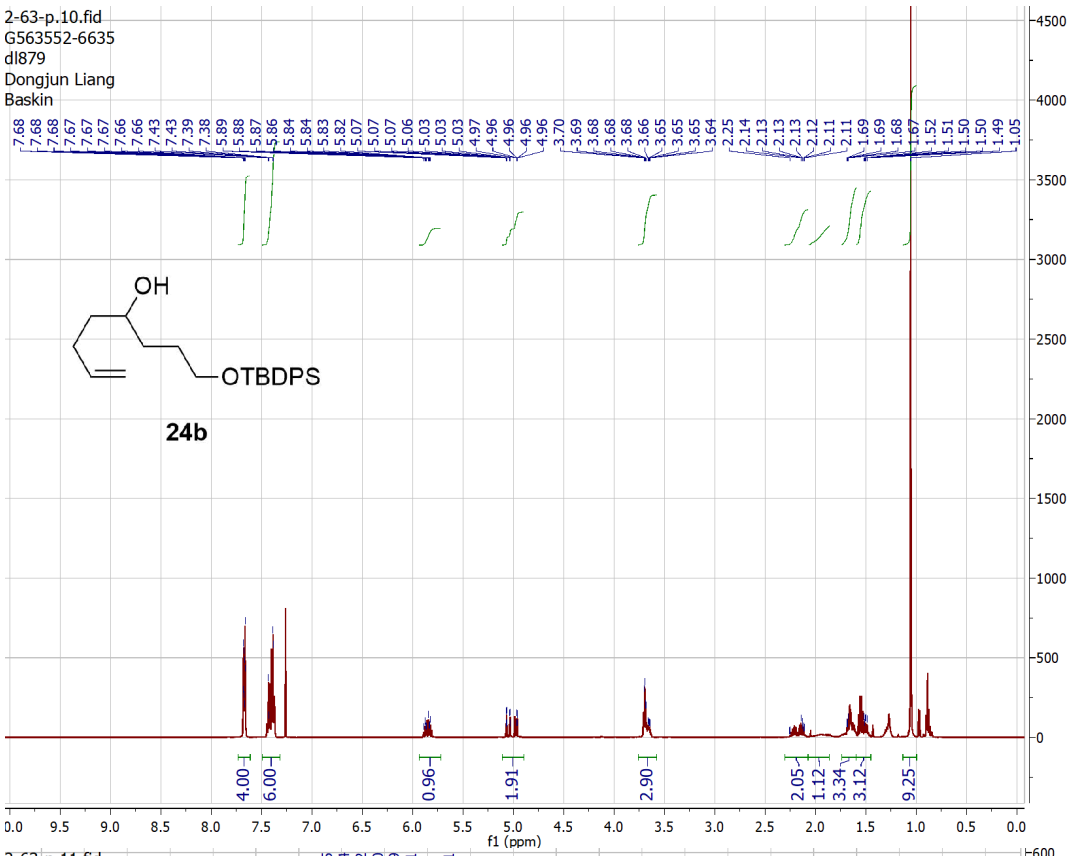
2-63-p.10.fid
G563552-6635
dl879
Dongjun Liang
Baskin
OH
OTBDPS
24b
4.00
6.00
0.96
1.91
2.90
2.05
1.12
3.34
3.12
9.25
f1 (ppm)

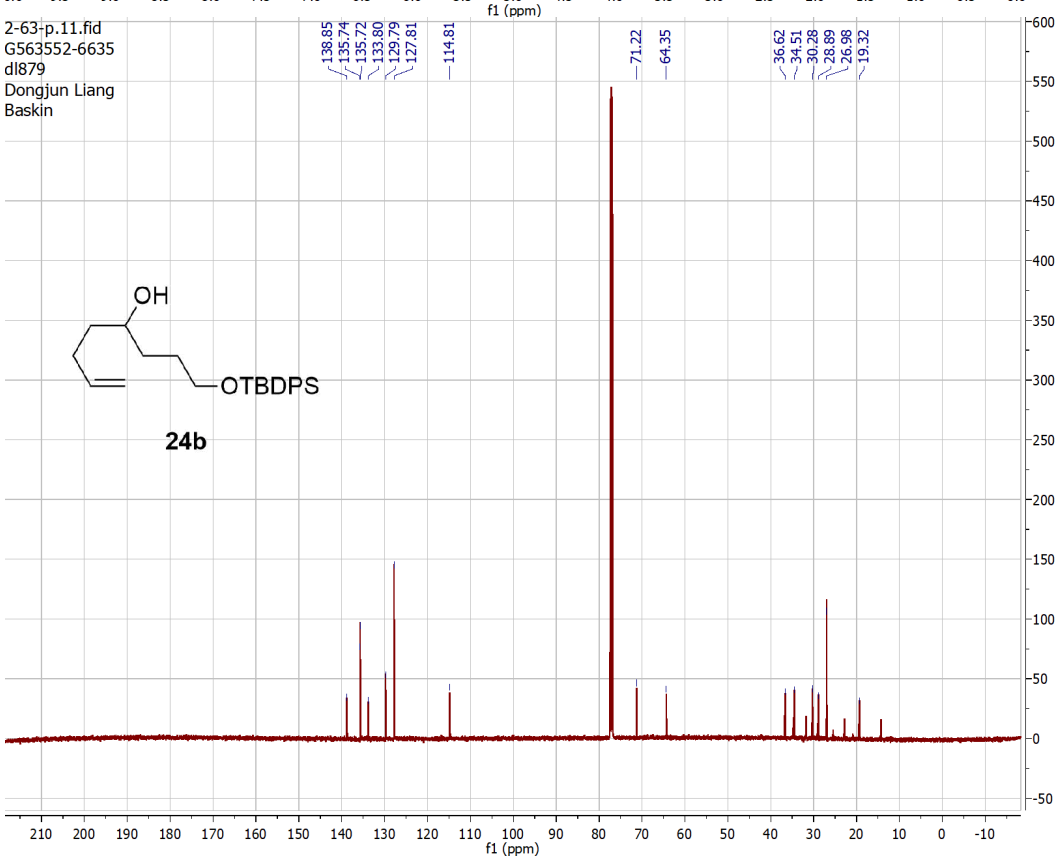
2-63-p.11.fid
G563552-6635
dl879
Dongjun Liang
Baskin
138.85
135.74
135.72
133.80
129.79
127.81
114.81
71.22
64.35
36.62
34.51
30.28
28.89
26.98
19.32
OH
OTBDPS
24b
f1 (ppm)

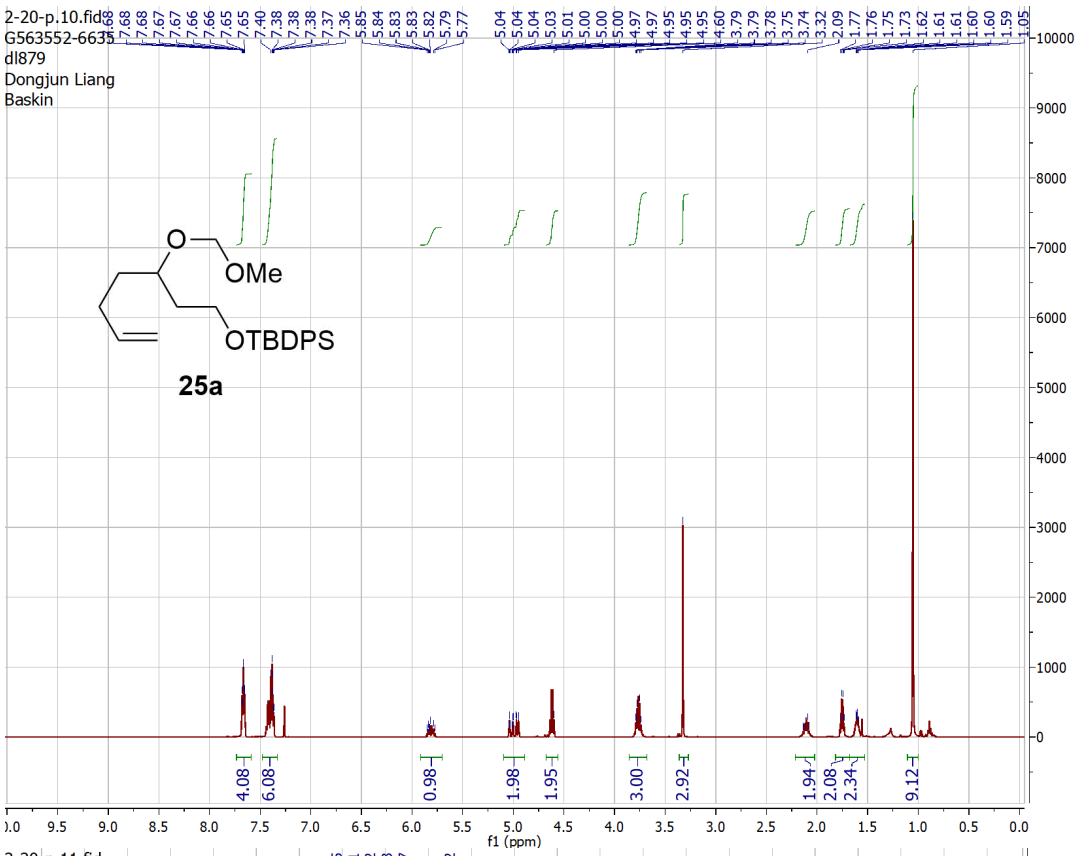
2-20-p.10.fid
G563552-6635
dl879
Dongjun Liang
Baskin
O
OMe
OTBDPS
25a
4.08
6.08
0.98
1.98
1.95
3.00
2.92
1.94
2.08
2.34
9.12
f1 (ppm)

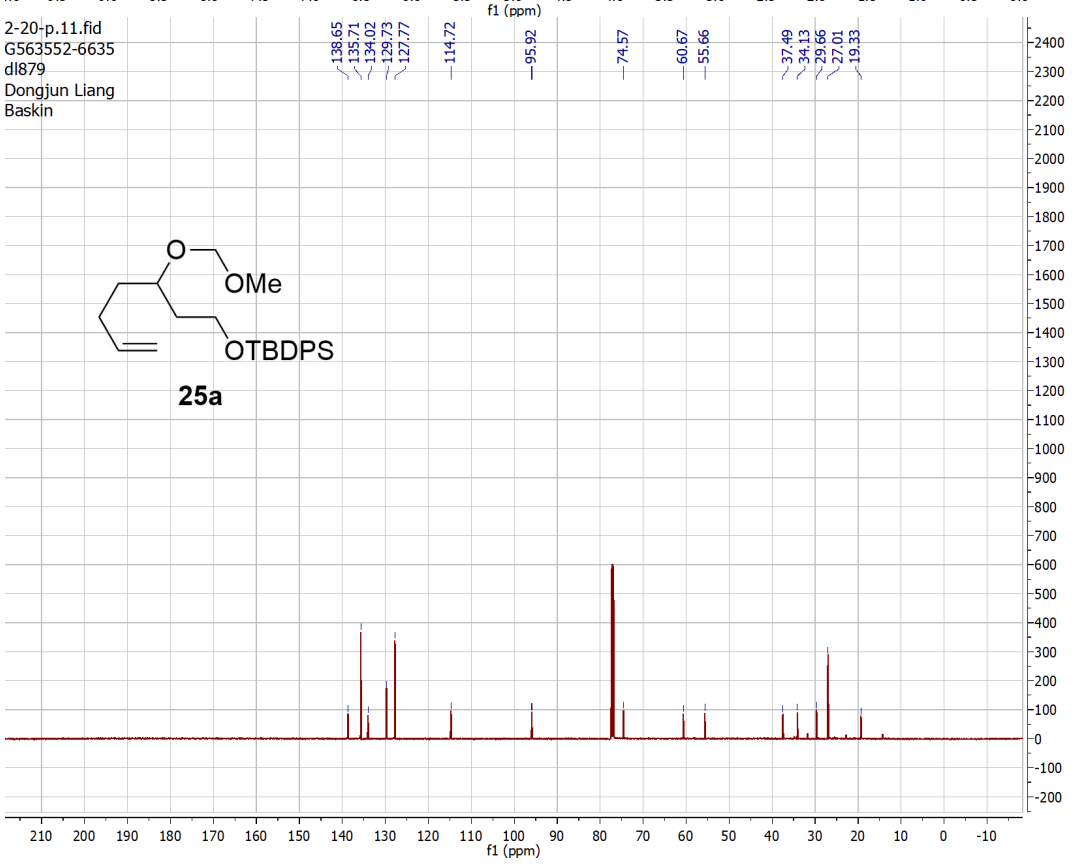
2-20-p.11.fid
G563552-6635
dl879
Dongjun Liang
Baskin
138.65
135.71
134.02
129.73
127.77
114.72
95.92
74.57
60.67
55.66
37.49
34.13
29.66
27.01
19.33
O
OMe
OTBDPS
25a
f1 (ppm)

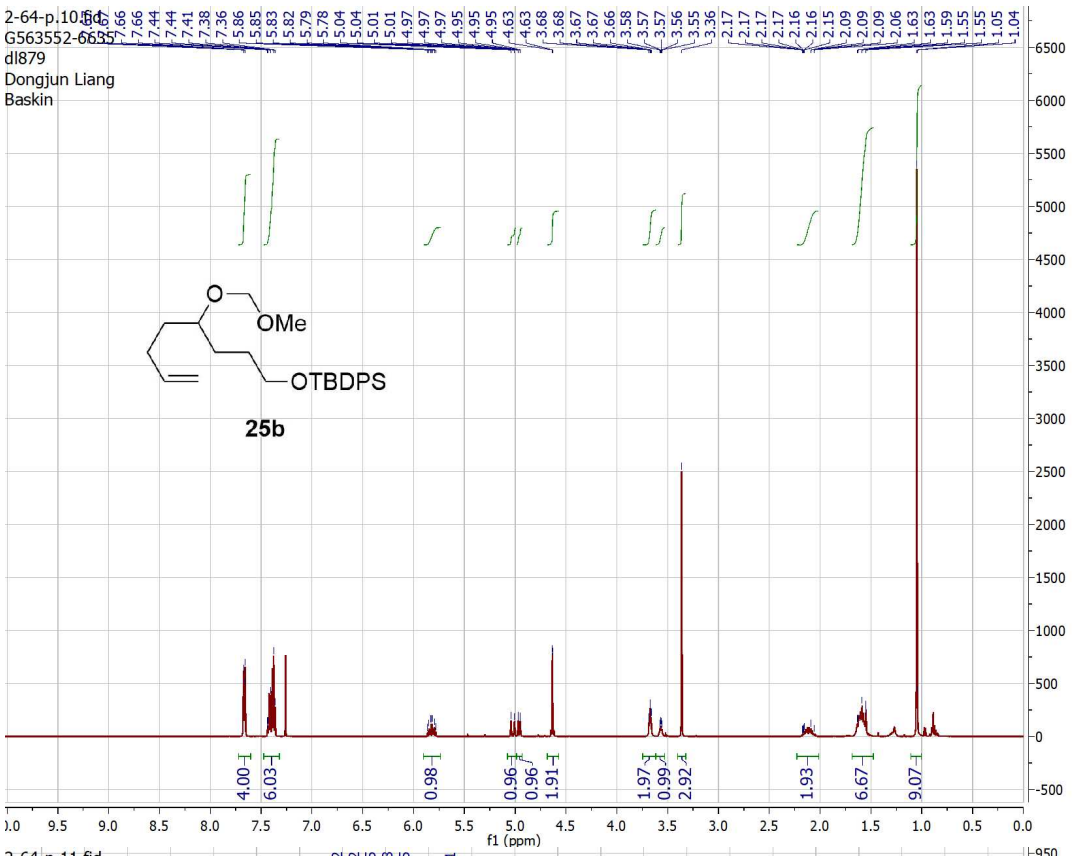
2-64-p.10.fid
G563552-6635
dl879
Dongjun Liang
Baskin
OMe
OTBDPS
25b
4.00
6.03
0.98
0.96
0.96
1.91
1.97
0.99
2.92
1.93
6.67
9.07
f1 (ppm)

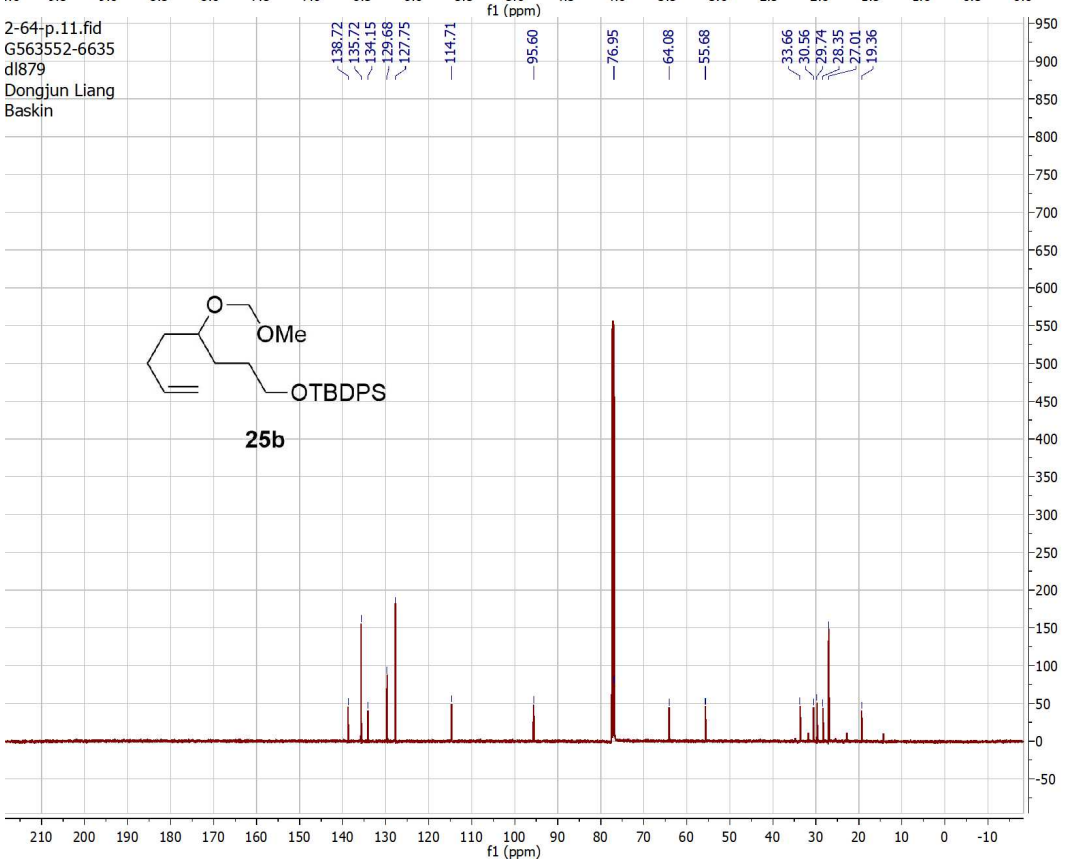
2-64-p.11.fid
G563552-6635
dl879
Dongjun Liang
Baskin
138.72
135.72
134.15
129.68
127.75
114.71
95.60
76.95
64.08
55.68
33.66
30.56
29.74
28.35
27.01
19.36
OMe
OTBDPS
25b
f1 (ppm)

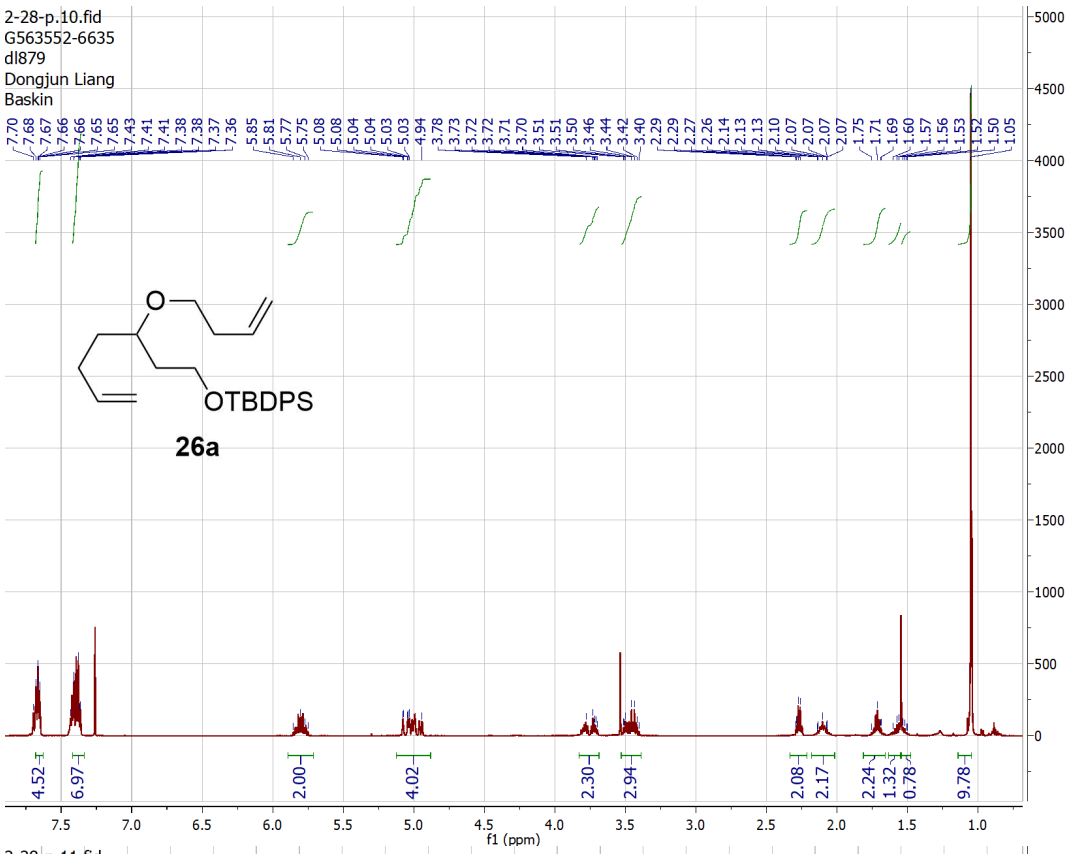
2-28-p.10.fid
G563552-6635
dl879
Dongjun Liang
Baskin
OTBDPS
26a
f1 (ppm)

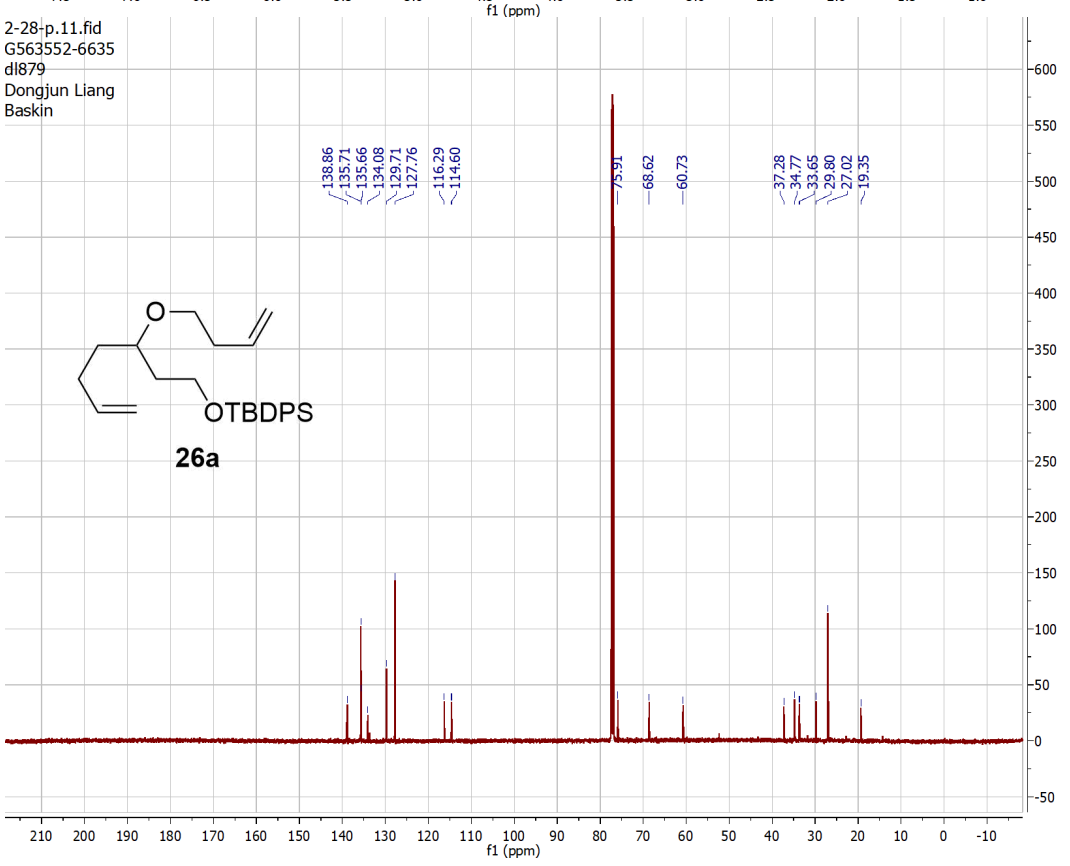
2-28-p.11.fid
G563552-6635
dl879
Dongjun Liang
Baskin
OTBDPS
26a
f1 (ppm)

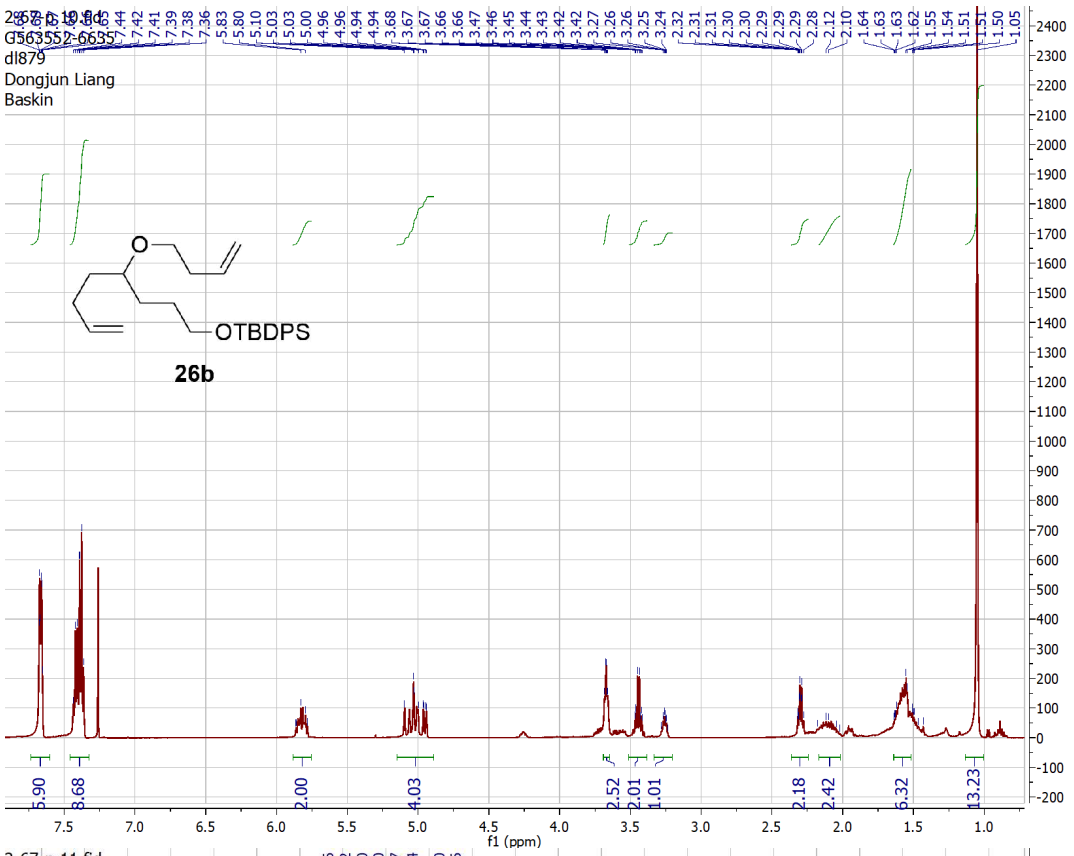
2-67-p.10.fid
G563552-6635
dl879
Dongjun Liang
Baskin
OTBDPS
26b
f1 (ppm)

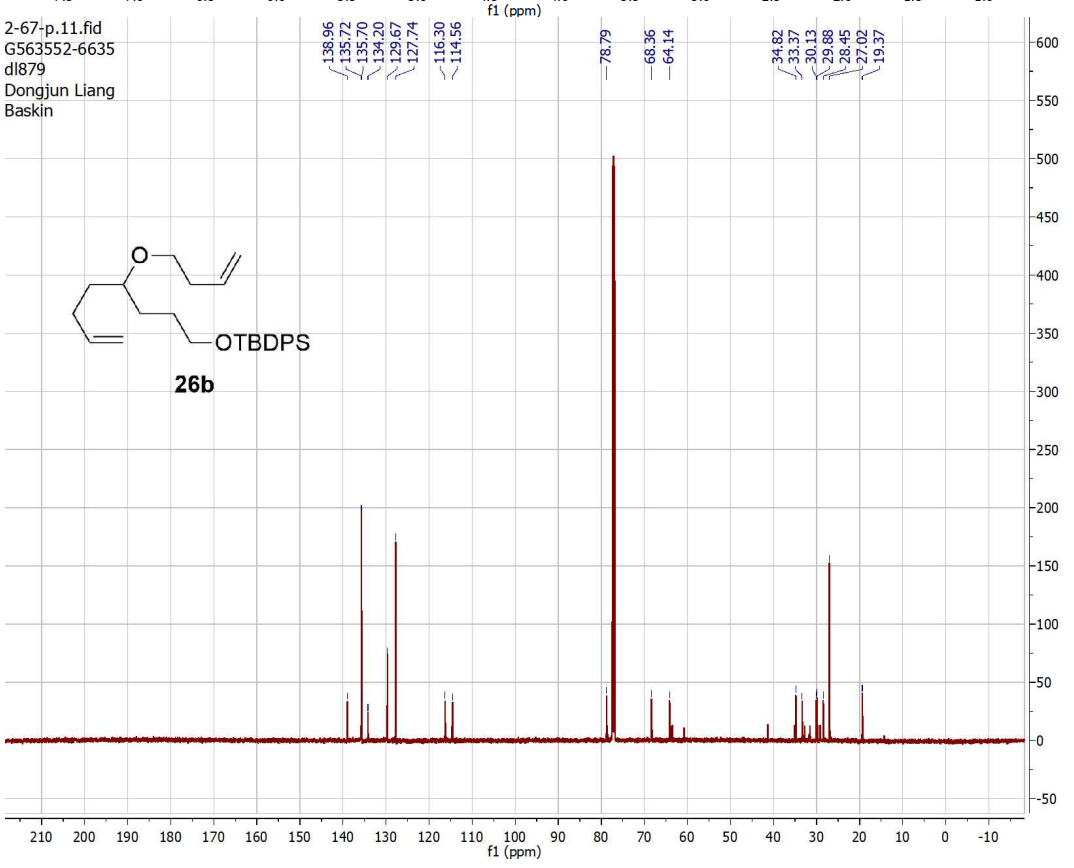
2-67-p.11.fid
G563552-6635
dl879
Dongjun Liang
Baskin
OTBDPS
26b
f1 (ppm)

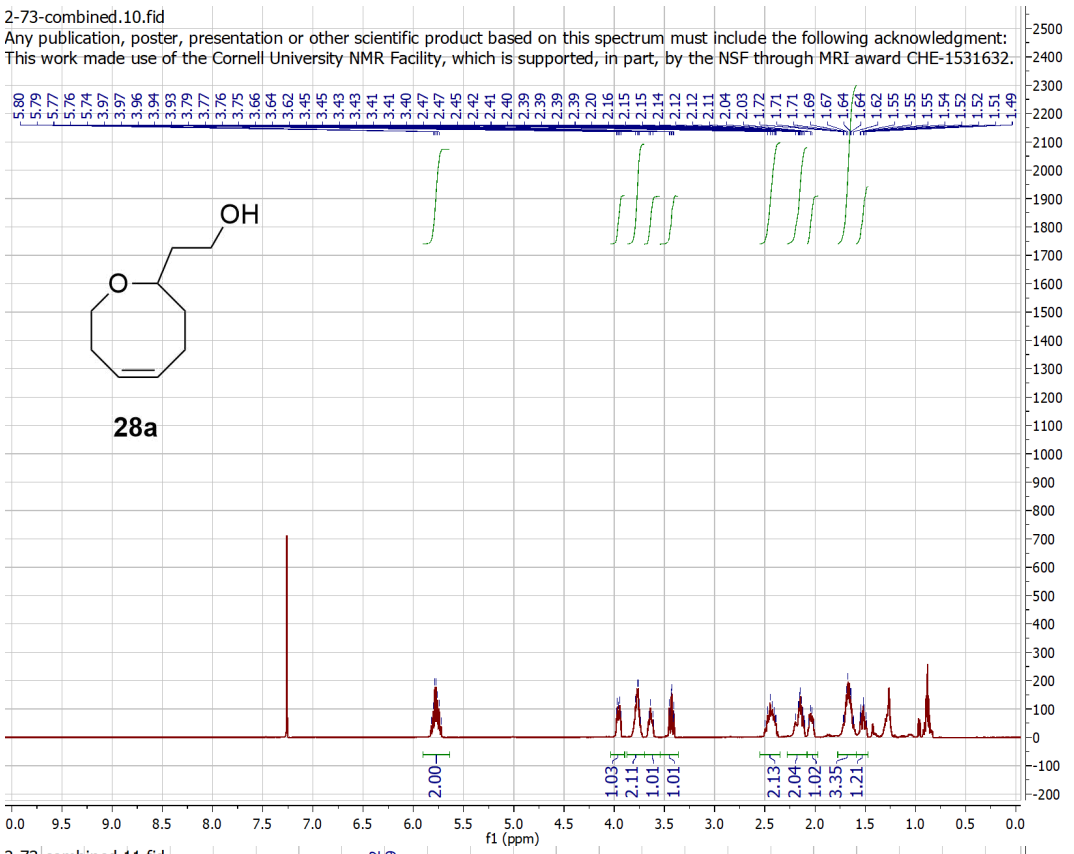
2-73-combined.10.fid
Any publication, poster, presentation or other scientific product based on this spectrum must include the following acknowledgment:
This work made use of the Cornell University NMR Facility, which is supported, in part, by the NSF through MRI award CHE-1531632.
OH
O
28a
f1 (ppm)

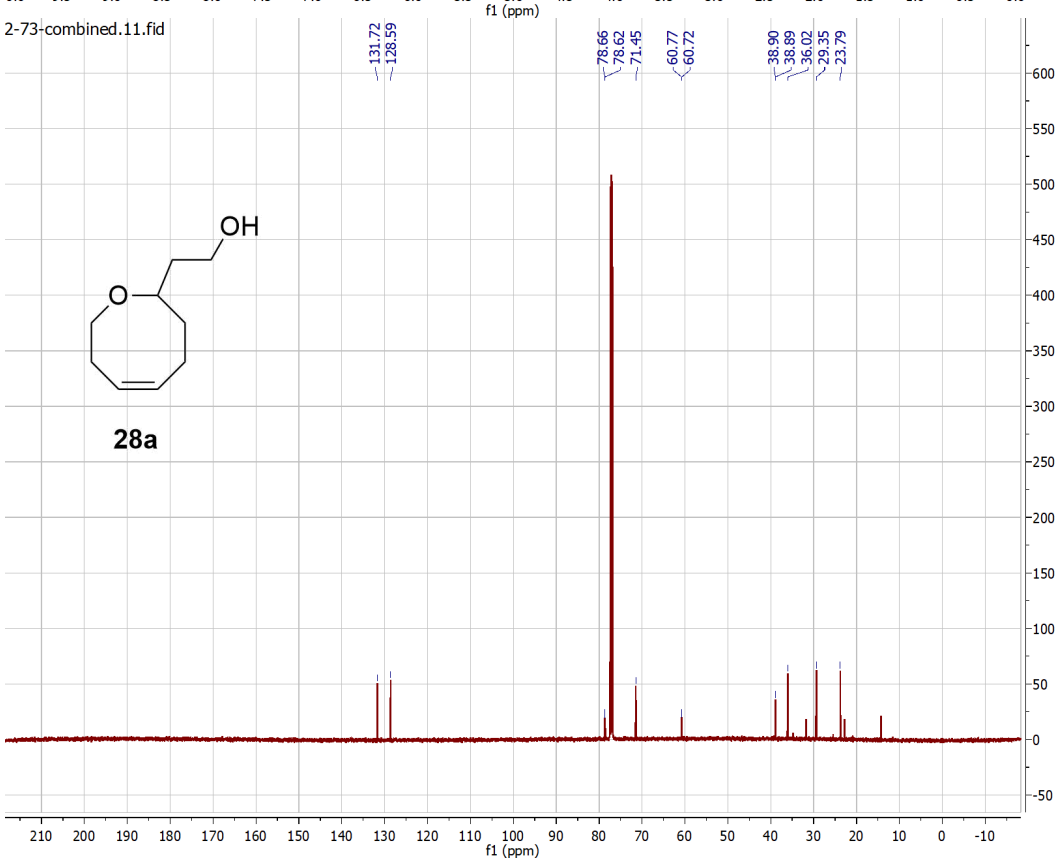
2-73-combined.11.fid
131.72
128.59
78.66
78.62
71.45
60.77
60.72
38.90
38.89
36.02
29.35
23.79
OH
O
28a
f1 (ppm)

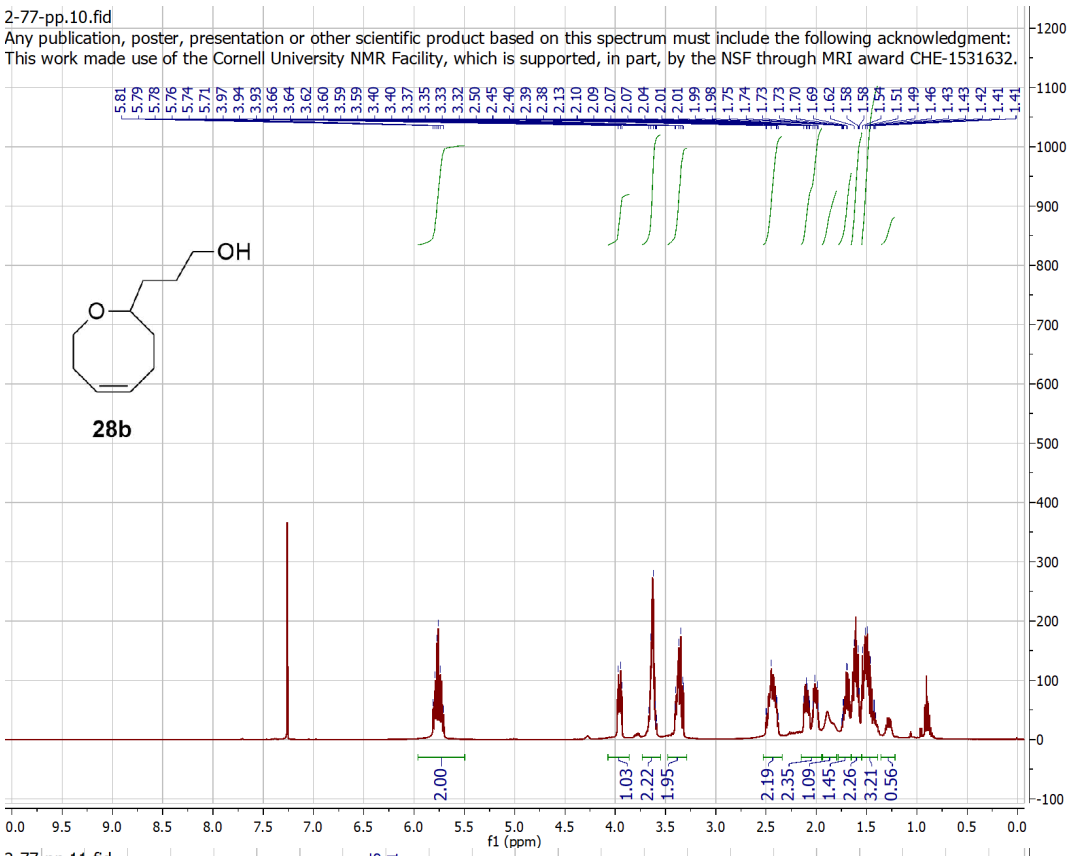
2-77-pp.10.fid
Any publication, poster, presentation or other scientific product based on this spectrum must include the following acknowledgment:
This work made use of the Cornell University NMR Facility, which is supported, in part, by the NSF through MRI award CHE-1531632.
OH
O
28b
f1 (ppm)

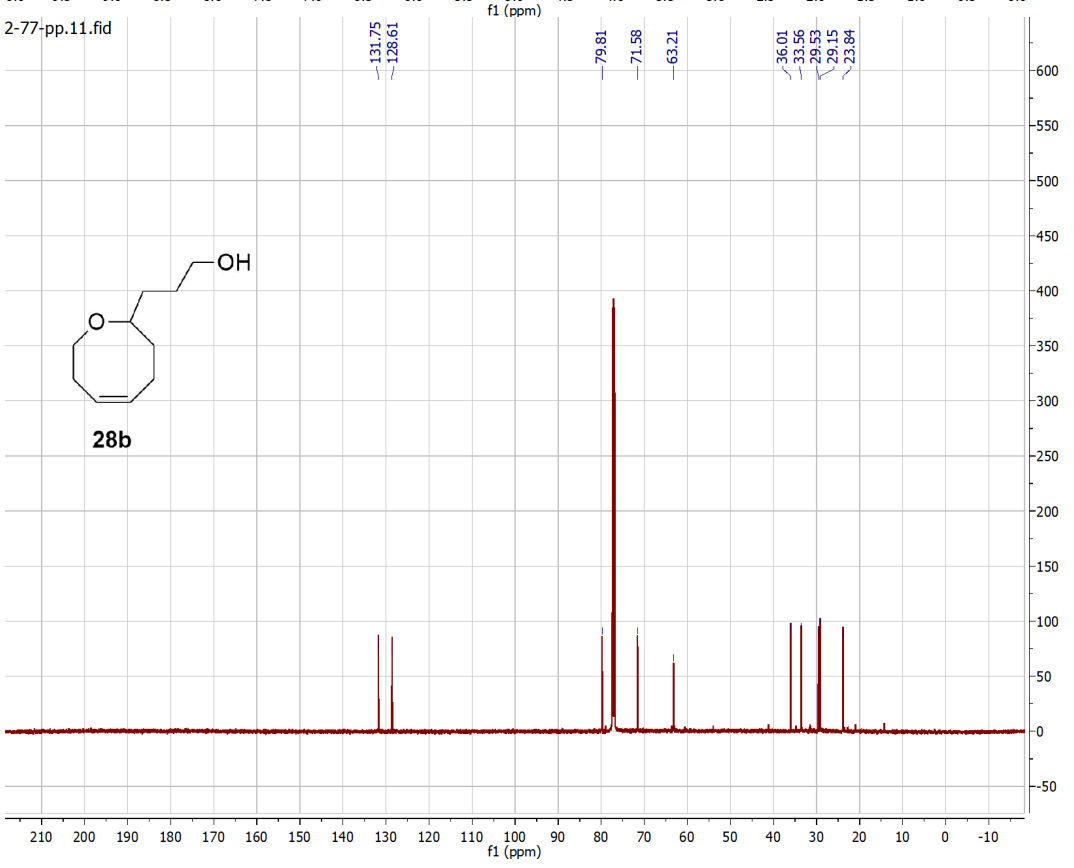
2-77-pp.11.fid
131.75
128.61
79.81
71.58
63.21
36.01
33.56
29.53
29.15
23.84
OH
O
28b
f1 (ppm)

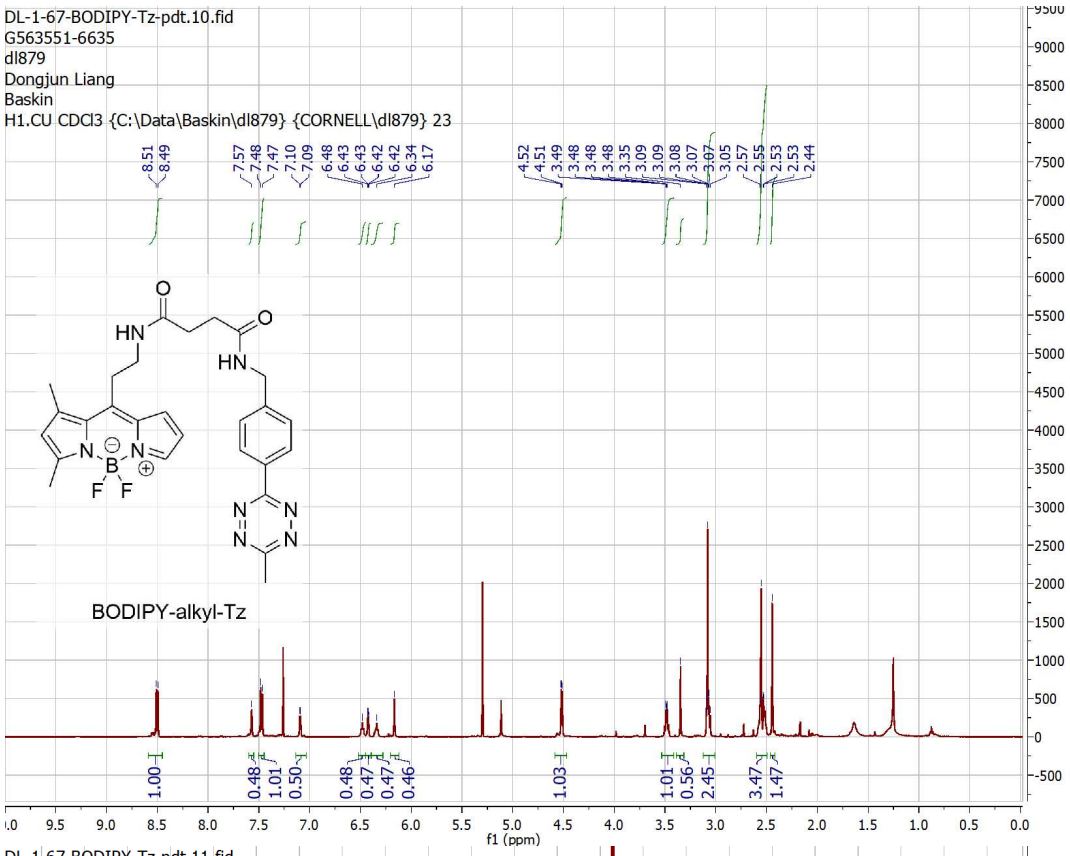
DL-1-67-BODIPY-Tz-pdt.10.fid
G563551-6635
dl879
Dongjun Liang
Baskin
H1.CU CDCl3 {C:\Data\Baskin\dl879} {CORNELL\dl879} 23
BODIPY-alkyl-Tz
f1 (ppm)

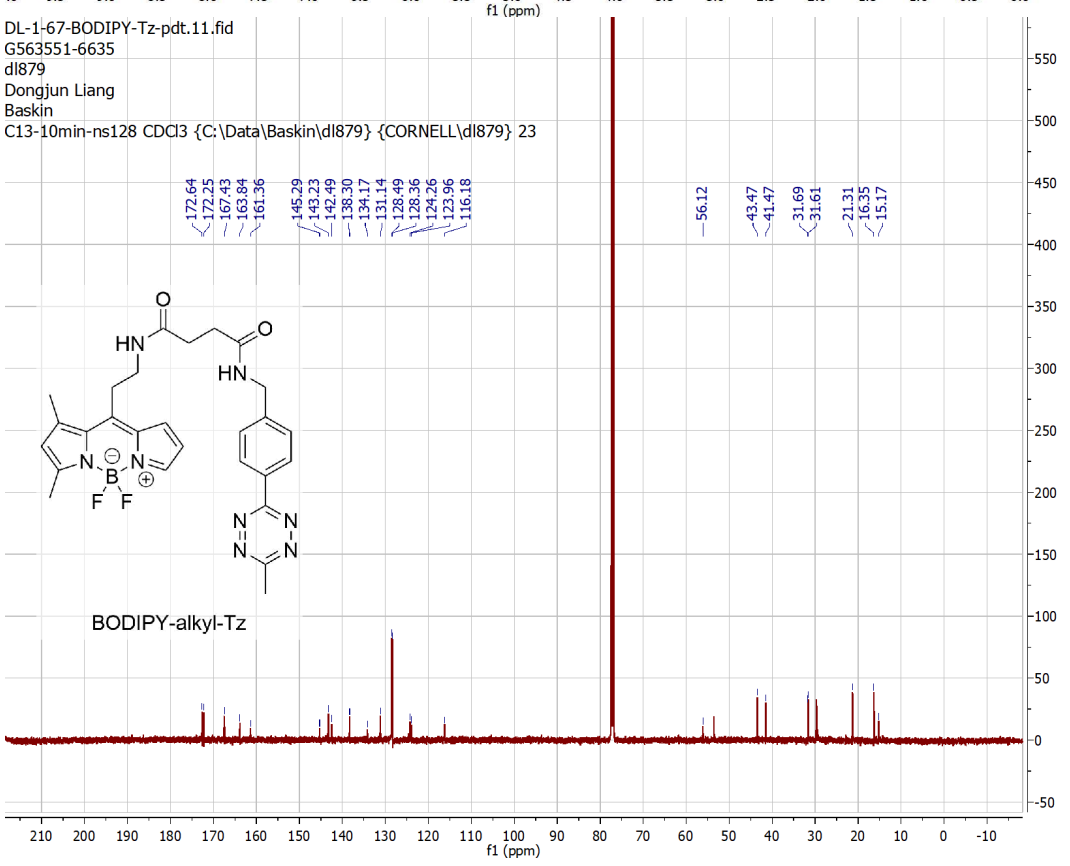
DL-1-67-BODIPY-Tz-pdt.11.fid
G563551-6635
dl879
Dongjun Liang
Baskin
C13-10min-ns128 CDCl3 {C:\Data\Baskin\dl879} {CORNELL\dl879} 23
BODIPY-alkyl-Tz
f1 (ppm)